Graz University of Technology

Numerical Modelling of Chemistry, Radiation and Transient Heating Characteristics in High Temperature Processes

von

Rene Prieler

als

DISSERTATION

zur Erlangung des akademischen Grades

DOKTOR DER TECHNISCHEN WISSENSCHAFT

der Studienrichtung

MASCHINENBAU

am Institut für Wärmetechnik angefertigt

Begutachter:

Univ.-Prof. Dipl.-Ing. Dr.techn. Christoph Hochenauer

Prof. Dr. rer. nat. habil. Amsini Sadiki

August 2016

Eidesstattliche Erklärung

Ich erkläre an Eides statt, dass ich die vorliegende Arbeit selbstständig verfasst, andere als die angegebenen Quellen/Hilfsmittel nicht benutzt und die den benutzten Quellen wörtlich und inhaltlich, entnommenen Stellen als solche kenntlich gemacht habe.

Graz, August 2016 .....

Abstract

Oxygen enhanced combustion (OEC) techniques are supposed to be a fuel saving alternative to conventional air-fired combustion. Due to the reduction or removal of nitrogen from the combustion system, higher flame temperatures and radiation intensity can be achieved in a combustion chamber. Additionally, more heat is available in OEC to maintain heating, melting and annealing processes etc. in industrial unit operations. The use of OEC is currently limited to a few applications because of the cost of oxygen and the expense for adapting the existing firing systems.

The main aim of the present study is the investigation of OEC with natural gas experimentally and numerically in a lab-scale furnace, which can be operated under air-fired conditions and different oxygen concentrations in the oxidant (N_2/O_2 mixture). The experimental part of the investigation revealed the benefits of OEC in furnaces for high temperature processes above 1000 °C and also provided measured data such as temperature and heat fluxes to validate different numerical models. By comparison with measured data, different numerical approaches for turbulence modelling, chemistry in the main reaction zone as well as different radiation models are investigated for their applicability in 3D CFD simulations of air-fuel combustion and OEC. The goal was the development of a time efficient CFD model, suitable for a wide range of oxygen enrichment up to the combustion of natural gas with pure oxygen. Furthermore, the applicability of the CFD model developed for different furnace dimensions (optical thickness) as well as burner types is crucial. Hence, the CFD model was further tested on an industrial walking hearth furnace, which was used for reheating steel billets. The coupling of the gas phase combustion and transient heating of the billets was considered by an iterative solution procedure. Results gained on the industrial walking hearth furnace finally prove the positive effect of OEC on high temperature processing.

Due to the experiments in the lab-scale furnace, fuel savings and an increase of the process efficiency especially at low oxygen enrichment levels between 21 % O_2 (air) and 30 % O_2 in the oxidant were detected. The experimental results suggested that also small amounts of additional oxygen can be sufficient for significant improvements on the combustion efficiency and heat transfer in the lab-scale furnace. Besides the measured heat fluxes and fuel consumption, the temperatures in the furnace showed close accordance to the results of CFD simulations using a skeletal reaction mechanism. This reaction mechanism is considering 17 species (including radicals and intermediate species) and was applied in conjunction with the steady flamelet model (SFM). Since experiments and simulations on the lab-scale furnace showed a close agreement, this developed CFD model was used to simulate the industrial

walking hearth furnace. The furnace was operated under air-fired conditions and OEC with 25 % O_2 in the oxidant. CFD simulation and data from the experimental test run confirmed the increase in the efficiency of the reheating process. It was found that natural gas consumption was reduced by approximately 8 % compared to air-fired conditions with consistent product quality.

Kurzfassung

Die sauerstoffangereicherte Verbrennung (Oxygen Enhanced Combustion – OEC) stellt eine brennstoffsparende Alternative zu konventioneller Feuerung mit Luft dar. Durch die Reduzierung des Stickstoffanteils im Oxidator können höhere Flammentemperaturen und Strahlungsintensitäten in einer Brennkammer erreicht werden. Somit steht mehr Wärme in der Brennkammer für Schmelz-, Aufheiz- oder Glühprozesse zur Verfügung und die Abgasverluste können minimiert werden. Die Anwendung von OEC ist noch limitiert, da zusätzliche Kosten für den Sauerstoff und eventuelle Umbauarbeiten an bereits bestehenden Anlagen nötig sind.

Das Ziel der vorliegenden Arbeit war die experimentelle und numerische Untersuchung von OEC mit Erdgas in einem Versuchsofen, welcher mit Luft als auch verschiedenen Anreicherungsstufen des Oxidators (N_2/O_2-Mischung) betrieben werden kann. Der experimentelle Teil der Arbeit zeigte die Vorteile der OEC in Öfen für Hochtemperaturprozesse über 1000 °C, wobei auch wichtige Messdaten wie Temperaturen und Wärmeströme für die Validierung verschiedener numerischer Modelle ermittelt wurden. Durch Vergleich mit Messdaten sollen die numerischen Ansätze für Turbulenzmodellierung, Beschreibung der Reaktionen in der Flamme sowie des Strahlungstransports auf ihre Anwendbarkeit für 3D CFD Simulationen unter OEC Bedingungen und Verbrennung mit Luft untersucht werden. Dadurch soll ein recheneffizientes CFD Modell entwickelt werden, welches für ein breites Spektrum an Sauerstoffanreicherung bis hin zur Verbrennung von Erdgas mit Reinsauerstoff anwendbar ist. Des Weiteren wurde bei der Untersuchung der Verbrennungsmodelle auf die Anwendbarkeit für verschiedene Ofengrößen (optische Dichten) sowie unterschiedliche Brennertypen geachtet. Das entwickelte CFD-Modell wurde in weiterer Folge an einem industriellen Hubbalkenofen für die Wiedererwärmung von Stahlknüppeln angewendet. Die Koppelung zwischen dem transienten Aufheizen der Knüppel und dem Wärmetransports in der Gasphase wurde durch einen iterativen Lösungsalgorithmus berücksichtigt. Schlussendlich sollen die erzielten Daten und Ergebnisse vom Hubbalkenofen die positiven Effekte von OEC für Hochtemperaturanwendungen auch unter industriellen Bedingungen bestätigen.

Durch die Experimente am Versuchsofen konnte sowohl eine Brennstoffeinsparung als auch eine Erhöhung des Ofenwirkungsgrades, vor allem im Bereich niedriger Anreicherungsstufen zwischen 21 % O_2 (Luft) und 30 % O_2 im Oxidator, festgestellt werden. Somit können auch kleine Mengen an zusätzlichem Sauerstoff ausreichen, um eine deutliche Optimierung des Verbrennungsprozesses und Wärmetransports im Versuchsofen zu bewerkstelligen. Neben

den gemessenen Wärmeströmen und Brennstoffverbrauch, zeigten auch die Temperaturen eine gute Übereinstimmung mit den Ergebnissen der CFD Simulation, bei welcher ein skeletal-Reaktionsmechanismus verwendet wurde. Dieser Mechanismus betrachtet 17 Spezies (inklusive Radikale und Zwischenspezies) und wurde in Kombination mit dem Steady Flamelet Model (SFM) angewendet. Da dieses CFD Modell die gemessenen Daten im Versuchsofen gut wiedergeben konnte, wurde es auch für die Simulation des Hubbalkenofens verwendet. In den Versuchen wurde der Ofen bei konventioneller Verbrennung mit Luft als auch mit OEC (25 % O_2) betrieben. Die durchgeführten Simulationen und Versuche bestätigten die Erhöhung des Prozesswirkungsgrades für den Erwärmungsvorgang. Der Erdgaseinsatz konnte, im Verglich zur Verbrennung mit Luft als Oxidator, um ca. 8 % verringert werden.

Acknowledgements

I’m very grateful to have had the opportunity to work on this PhD thesis in close cooperation with Messer Austria GmbH, where scientific and practical work is combined. I would like to thank Davor Spoljaric and Dr. Martin Demuth for the financial support and continuous supervision I was given at the Messer Austria test facility in Gumpoldskirchen. Furthermore, many thanks to Burkhardt Holleis, Dasen Karmelic and Johannes Rauch for their experience with field work in industry. I would also like to extend my thanks to the Austrian Research Promotion Agency (FFG) for their financial support.

During my employment at the Institute of Thermal Engineering, the deep knowledge of all staff members in their fields of expertise has been very helpful in relation to many numerical and experimental issues. I wish to express my gratitude to my supervisor at the Institute, Prof. Christoph Hochenauer, for his valuable input and experience in combustion modelling. Special thanks to Prof. Amsini Sadiki for reviewing and supervising the writing of this thesis. I would also like to thank all of my colleagues at the Institute for their input and constructive feedback. Of all involved, special thank goes to Johannes Wurm, for the interesting conversations in the office, where many ideas were born. Furthermore, I would like to thank Dr. Petr Bělohradský for giving me the opportunity to explore the burner test facility at Brno University of Technology.

Finally, my deepest gratitude is also due to my family, for the energy and support they have given me throughout my entire education and my life. This thesis would not have been completed without their help.

Contents

Nomenclature

A	Area
A, B	Model parameters for EDM
A, B, C, D	Representing reactants and products in a chemical reaction
A/F	Air-fuel ratio
a	Absorption coefficient
$a_1, a_2, \ldots$	Polynomial coefficients
a_{ki}	Number of atoms of the element i in the component (molecule) k
$a_{\varepsilon,i}$	Emissivity weighting factor
$b_{\varepsilon,i,j}$	Emissivity gas temperature polynomial coefficient
$C_\mu, C_{1\varepsilon}, C_{2\varepsilon}, C_{3\varepsilon}, C_1, C_2$	Model parameters for turbulence modelling with standard and realizable k-epsilon model
C_d, C_g	Model parameters for the SFM
c	Molar density or concentration
c_p	Specific heat capacity
$D_k, D_{k,T}$	Mass diffusion coefficient for laminar/turbulent and thermal (Soret) diffusion
E, e	Energy
E_A, E_f, E_b	Activation energy (forward and backward reaction)
$E_i, E_q, \overline{E_\iota}$	Relative error and average relative error
$E_{i,rel}^{sens}$	Sensitivity coefficient
F/A	Fuel-air ratio
$f, \bar{f}, \overline{f^2}$	Mixture fraction, mean mixture fraction and mixture fraction variance
$G, \Delta G_R^0$	Free energy (Gibbs function) and standard free reaction energy
G_b	Generation of turbulent kinetic energy due to gradients of the mean velocity
G_k	Generation of turbulence due to buoyancy
G_r	Incident radiation
$\vec{g}, g_i$	Gravitational vector or component i of the gravitational vector
$H, \overline{H}, h$	Enthalpy or mean enthalpy
ΔH_R	Reaction enthalpy
ΔH_R^0	Standard reaction enthalpy

H_u	Lower heating value
h, h_1, h_2	Grid cell size
I	Radiation intensity or identity matrix
$\vec{J}$	Diffusive flux
K, K_c, K_p	Equilibrium constant (expressed by the concentration or pressure)
k	Rate coefficient of a reaction; Turbulent kinetic energy
k_0	Pre-exponential factor or frequency factor
L	Length (scale)
$M, \overline{M}$	Molecular weight, molecular weight of a gas mixture
m	Mass
n	Number of moles; Refractive index
$\vec{n}$	Unit normal vector
p	Pressure; Order of algorithm accuracy
Pr_t	Turbulent Prandtl number
$p(f)$	Probability density function of the mixture fraction
$\dot{Q}, \dot{q}$	Heat flux, specific heat flux
Q	Heat
R	Universal gas constant
r	Reaction rate; Refinement factor
S	Entropy; Model parameter for realizable k-epsilon model
Sc_t	Turbulent Schmidt number
$\vec{s}, \overrightarrow{s'}$	Direction vector and direction of scattered radiation
s, s_{gl}	Beam length and mean beam length
T, T_b, T_u	Temperature, Temperature of burnt and unburnt gases
t, t^*	Time and time scale
U	Internal energy
V	Volume
$\tilde{V}$	Diffusion velocity
$u, v, w, \vec{v}$	Velocity components and vector for the Cartesian coordinate system
X	Mole fraction
$x, y, z, \vec{x}$	Coordinates and vector for Cartesian coordinate system

Y	Mass fraction
Y_i^*	Fine scale mass fraction
Z_i	Elemental mass fraction of element i

Greek letters

α	Heat transfer coefficient; Parameter for PDF generation
β	Coefficient of thermal expansion; Parameter for PDF generation
Γ	Diffusion coefficient
δ	Single Dirac PDF
δ_{ij}	Kronecker delta
ε	Emissivity; Turbulent dissipation rate
η	Reaction progress variable; Model parameter for realizable k-epsilon model
λ	Thermal conductivity; Air-to-fuel equivalence ratio
μ, μ_t	Dynamic viscosity and turbulent viscosity
$\bar{\mu}$	Chemical potential
$\mu_{i,k}$	Mass fraction of element i in the component k
ν	Kinematic viscosity
ν', ν''	Stoichiometric coefficients of the reactants and products
ξ^*	Length fraction
ρ, ρ_∞	Density and density at the inlet
σ	Stefan-Boltzmann constant
σ_s	Scattering coefficient
τ	Stress tensor
Φ	Equivalence ratio (fuel-to-air equivalence ratio); Phase function
$\phi, \bar{\phi}, \phi'$	Instantaneous, mean and fluctuating value of a transport value
χ	Scalar dissipation
ω	Production/destruction rate (source or sink term)

Subscripts and superscripts

^{0}	Standard conditions
air	Air
b	Backward reaction; Burnt gases
$black$	Black body

$coarse$	Coarse grid
$cold$	Cold surface
$exact$	Approximation of the exact value during Richardson extrapolation
f	Forward reaction
$fuel$	Fuel
$fine$	Fine grid
g	Gas
hot	Hot surface
i	Element; Control variable; Number of fictive gas in the WSGGM
$irrev$	Irreversible process
j	Control variable
k	Component
max	Maximum value
ox	Oxidant
r	Reaction
rad	Radiation
rev	Reversible process
s	Surface (wall)
$stoich$	Stoichiometric conditions
$total$	Total amount

List of abbreviations

BUT	Brno University of Technology
CFD	Computational Fluid Dynamics
CSTR	Continuous Stirred Tank Reactor
CV	Control Volume
DNS	Direct Numerical Simulation
DOM	Discrete Ordinates Model
EDC	Eddy Dissipation Concept
EDM	Eddy Dissipation Model
FGM	Flamelet Generated Manifold
IFRF	International Flame Research Foundation

LBL	Line-by-Line Model
LES	Large Eddy Simulation
MIEC	Mixed Ionic and Electronic Conductor
OEC	Oxygen Enhanced Combustion
PDF	Probability Density Function
RANS	Reynolds-averaged Navier-Stokes
RKE	Realizable k-epsilon Model
RSM	Reynolds Stress Model
RTE	Radiative Transfer Equation
SNB	Statistical Narrow Band Model
WSGGM	Weighted-Sum-of-Grey-Gases Model

1 Introduction

Nowadays, the combustion of fossil fuels, such as natural gas, oil and coal, is still a key process for several industrial applications, including power generation, transportation and heating processes. In the steel, cement and glass industries, unit operations for heating and melting require a huge amount of energy, typically provided through the combustion of hydrocarbons. The anthropogenic greenhouse gas, carbon dioxide (CO_2) is a product of the combustion of fossil fuels, which are responsible for approximately 85 % of global energy production [1]. In order to slow down global warming, the reduction of CO_2 emissions in industry and transportation has been identified as a crucial factor. In 2000, the total amount of CO_2 emissions was determined to be 23.5 Gt/a [2]. CO_2 emissions of large scale plants with more than 0.1 $MtCO_2$/a are listed in Table 1. This represents approximately 60 % of the total emissions.

Table 1
Processes or industrial activities of worldwide large stationary CO_2 sources with emissions more than 0.1 $MtCO_2$/a [2].

Process	**Number of sources**	**Emissions [$MtCO_2$/a]**
Fossil fuels		
Power	4,942	10,539
Cement production	1,175	932
Refineries	638	798
Iron and steel industry	269	646
Petrochemical industry	470	379
Oil and gas processing	not available	50
Other sources	90	33
Biomass		
Bioethanol and bioenergy	303	91
Total	7,887	13,466

In addition to the production of CO_2 during gas phase combustion, in high temperature processes, it can also arise from chemical reactions within the furnace load. For example, in cement clinker formation, CO_2 is also formed by the calcination process in the furnace or kiln. Manickam et al. [3] determined that 68% of the total amount of CO_2 in the flue gas is formed through the calcination process. Furthermore, in the glass industry, a huge amount of CO_2 is produced, not only by combustion: the glass bath during the melting process emits 30 to 36 % of the overall CO_2 emissions [4]. Capturing CO_2 for future storage or utilisation can

prevent the release of carbon into the atmosphere. Carbon capturing processes include post combustion and pre combustion capturing, as well as oxy-fuel combustion and oxygen enhanced combustion (see Fig. 1). Post combustion capturing uses different unit operations, such as absorption by chemical solvents, adsorption, cryogenic separation etc., to capture the CO_2 (e.g. Rabensteiner et al. [5; 6; 7]). In pre combustion, the fuel is converted in a reactor with steam and/or air (oxygen) to a syngas, mainly consisting of CO and H_2. In a second stage, the CO is used with additional steam to maintain the water-gas-shift reaction to produce H_2 and CO_2. After this step, the hydrogen can be used as fuel for the combustion after separation from CO_2. Oxy-fuel combustion uses pure oxygen as the oxidant for power generation, heating and melting processes. A mixture of O_2 and recirculated flue gas can also be used as an oxidant in oxy-fuel combustion. For use in industrial processes, air is commonly mixed with additional pure oxygen to increase the O_2 concentration in the oxidant. This procedure is known as oxygen enhanced combustion (OEC). Cuellar-Franca and Azapagic [8] have summarized the effect of carbon capturing and the processing of CO_2 by storage and utilisation.

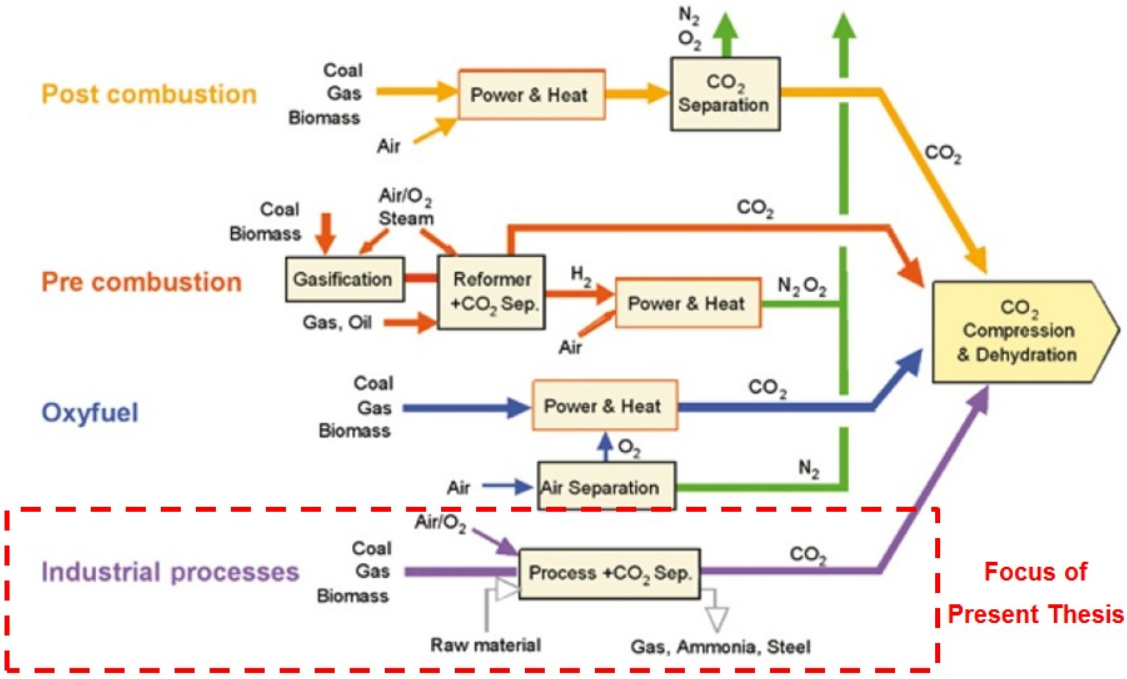

Fig. 1. Carbon capturing processes [2].

Furthermore, in future process operations, the availability and cost of fossil fuels have to be taken into account, and represent a major factor for many industrial sectors. Therefore, driven by these economic and environmental issues, many efforts are being made to increase the furnace efficiency of high temperature processes. In this thesis, the applicability of OEC is investigated, by means of experiments, for use in several industrial sectors to improve the

process efficiency. A numerical approach should be developed in order to predict the temperature, species concentrations and other transport phenomena in OEC. The positive effects of OEC on the process efficiency and heat transfer in industrial furnaces are examined by means of experiments and simulations in the following sections.

1.1 State of the art – Process optimisation

In the past, test runs were necessary for the optimization of industrial scale furnaces, in order to determine the effect of different operating conditions on the efficiency and product quality in heating and melting processes. Since test runs on large scale furnaces represent additional costs, experiments should be avoided. In recent years, computational methods have evolved for the prediction of combustion processes and heat transfer in furnaces. Thus, numerical analyses are used with increasing regularity for the investigation of combustion and radiation in high temperature applications. Computational methods are able to provide detailed insight into temperature distribution and species concentrations in furnaces, especially when measurement techniques are limited due to high temperatures and challenging accessibility. Numerical methods for combustion processes can be subdivided, as displayed in Fig. 2. Computational fluid dynamics (CFD) is commonly used to investigate the transport phenomena in combustion, solving the governing transport equations. Since local information about the scalars (temperature, species, etc.) is predicted with a high spatial resolution, more calculation time is needed in CFD simulations. Reactor network analysis (RNA) uses a combination of plug-flow (PF) and continuous stirred tank reactors (CSTR) to analyse the flow field, temperatures and species concentrations in a combustion chamber. Each reactor represents a region of the chamber where the detailed set of chemical reactions is solved with low computational effort. Ponsich et al. [9] carried out the RNA for a glass melting furnace, and compared the calculated residence time in the furnace with CFD simulations. A hybrid method is a two-step simulation procedure where the fluid flow and main species, such as CO_2, H_2O, CO, etc., are considered by CFD in a first step. Then, a reactor network is created based on the results of the CFD simulation. Detailed chemistry can be considered in the RNA with low computational demand, including intermediate species like radicals or NO_x. This method was successfully applied by Falcitelli et al. [4] for two glass melting furnaces.

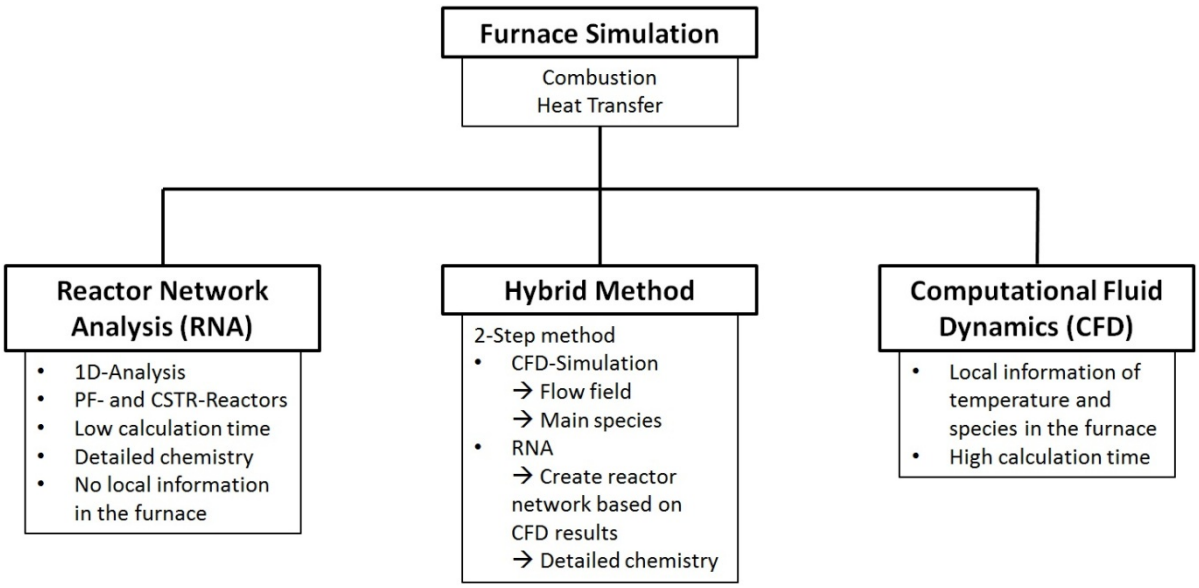

Fig. 2. Numerical methods for furnace simulation.

Since a CFD approach to predicting OEC will be developed in this thesis, a small overview of CFD modelling of combustion processes is given in this paragraph. The main focus was the oxy-coal combustion and OEC for different applications in industry (e.g. glass, aluminium, etc.). Many experimental and numerical investigations have already been done for a huge number of operating conditions in lab-scale furnaces. Considering the combustion of natural gas with pure oxygen for glass melting furnaces, test runs on a lab-scale furnace have been carried out by Leicher and Giese [10]. Measured temperatures and species concentrations were compared to CFD results. Stallinger [11] used the experimental results from [10] for comparison with CFD simulations of an oxy-fuel glass melting furnace. In the aluminium industry, Furu et al. [12] carried out several experiments and CFD simulations on a small scale furnace to predict the heat transfer to aluminium samples. The heat transfer was determined for air-fuel and oxy-fuel conditions for further application in aluminium melting. Not only furnaces for different industrial applications have been tested, but also pilot scale furnaces with various fuels. Al-Abbas and Naser [13; 14] published experiments and CFD results of a 100 kW furnace lignite and propane. The results of co-firing of biomass in a 0.5 MW furnace were published by Naser and Bhuiyan in [15]. Temperatures and species concentrations can also be calculated with high accuracy for large scale furnaces or boilers with CFD simulations (e.g. steam cracking [16], ethylene cracking [17] and a rotary kiln furnace for cement production [18]). Thus, the local prediction of relevant thermo-physical information in the furnace can be achieved by available commercial or free CFD codes without test runs. A more detailed overview of CFD modelling of OEC can be found in [19].

The optimization of a high temperature process is not only restricted to the gas phase combustion and energy efficiency, which can be calculated by CFD simulations. The desired product quality after discharging from the furnace must also be achieved. Basically, in the steel, glass and cement industries, the product quality is determined by temperature uniformity and the target temperature after discharging, as well as the chemical composition of the load (cement, glass, etc.). The chemical reactions in the load and at the surface depend on the temperature and combustion environment. With regard to steel reheating, the oxide scale layer formation during the reheating process can lead to a significant mass loss of 1-2 % [20]. The effect of temperature and combustion environments on the scale layer growth was determined by Sobotka [21], who also investigated aluminium and copper alloys by means of experiments in a lab-scale furnace. Similar experiments had already been done in a Lindberg horizontal tube furnace, and these were compared with a literature review [22]. Due to the varying thermal properties of a scale layer (consisting of different stable oxides) compared to the basic material, the transient heating of the material is affected [23]. The condition of the scale layer is also important for the transportation of the product to subsequent processing steps, such as deformation on a rolling mill [24]. Therefore the transient heating characteristic has to be considered in detail for an accurate prediction of the temperature distribution of the load and at the surface. Heat transfer through convection, and especially by radiation, is associated with the local surface temperature of the load. As a consequence, the coupling of the gas phase combustion, heat transfer and transient heating of the load is important for the numerical investigation of high temperature processes (see Fig. 3).

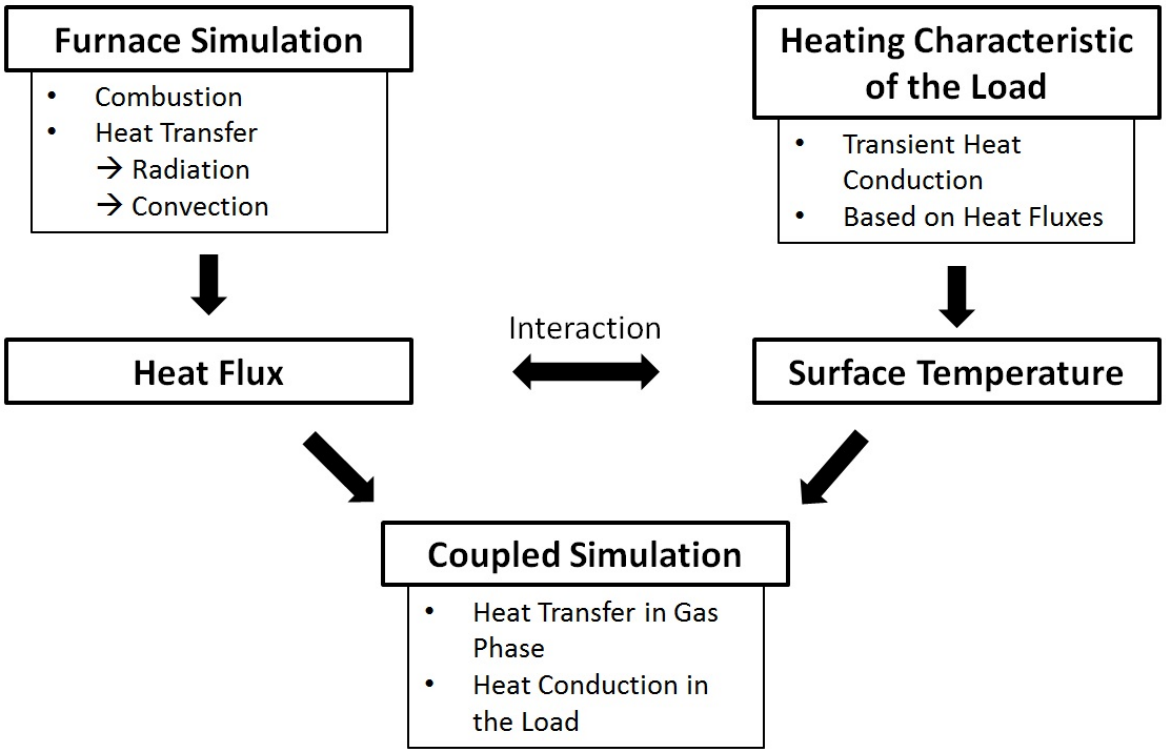

Fig. 3. Coupling of gas phase combustion and transient heating.

A literature review with special emphasis on reheating furnaces in the steel industry found several numerical studies for coupling the transient heating characteristic and furnace operation. The computational methods can mainly be classified as two different approaches.

a) Analysis of the heat transfer by radiation

The majority of the heat flux in high temperature processes is transferred by radiation because of its dependency on the fourth power of the absolute temperature [19]. Thus the modelling of radiation might be sufficient to predict the transient heating with high accuracy. The convective heat transfer is completely neglected (see Han et al. [25] and Kim et al. [26]) or interpreted by empirical correlations/assumptions for the convective heat transfer coefficient (see Emadi et al. [27], Tan et al. [28] and Jang and Huang [29]). Calculation time by considering radiation only is very low and can be implemented in industrial control systems (e.g. [30]). Usually, the zone model, proposed by Hottel and Sarofim [31] is used. With this approach it is possible to calculate the reheating process faster than the real run time [32]. Nevertheless, important information within the furnace like wall and gas temperatures, species concentrations etc. has to be assumed or measured before the calculation. Furthermore, the combustion process (chemical reaction and flame temperature) itself as well as the fluid flow is completely neglected.

b) Solving the Navier-Stokes equations, radiative heat transfer and transient heating simultaneously

This approach considers the fluid flow, combustion and radiation in the furnaces by transient CFD simulations. The transient heating of the solid or molten material in a process is also implemented in the calculation. The interaction between the heat transfer in the furnace (mainly by radiation) and the surface temperature of the load can be taken into account. Solving the governing transport equations for all aspects of the gas phase combustion and the thermal heat conduction within the load leads to an increase of the computational costs compared to the aforementioned method. The main advantage of this method is the fact, that all transport phenomena in the furnace will be calculated. Local temperatures in the furnace and species concentrations are determined by the CFD code, which makes it possible to evaluate the entire process including furnace efficiency and product quality. In literature, several studies dedicated to reheating furnaces in the steel industry were found (for example in Han et al. [33; 34], Gu et al. [35]).

Comparisons and evaluations of solution strategies to predict the transient heating in a reheating furnace have been done by Morgado et al. [36], Singh et al. [37] and Singh and Talukdar [38]. A number of numerical studies on the reheating process revealed the potential for the optimization of the furnace. Changes on the operating conditions such as fuel input, residence time and production rate can be investigated with little effort and without interrupting the manufacturing process (e.g. [25], [28], [34] and [39]). In addition, cross section and distance between the furnace loads can affect the productivity and thermal performance, as found by Jaklic et al. [40] and Chen et al. [41].

1.2 Applications of oxy-fuel combustion

Oxy-fuel combustion or combustion with pure oxygen can be used in power generation as well as in several industries to achieve process intensification and environmental goals like reduction of CO_2 and NO_x emissions. The first application of this method was introduced in the steel industry in the early 1930s, where a cupola blast furnace was operated with additional oxygen in the air [42].

In conventional air-fuel combustion, the nitrogen in the oxidant is ballast during the combustion which absorbs a huge amount of the heat released by the chemical reaction in the flame. Since nitrogen is removed in oxy-fuel combustion, only the reaction products, mainly CO_2 and H_2O, are heated up in the gas phase, resulting in a higher flame temperature as

illustrated in Fig. 4 (see Table 23 in the appendix). Starting at an oxidant mixture of 21 % O_2 and 79 % N_2 (air) the adiabatic flame temperature is approximately 2230 K. Increasing oxygen amount leads to higher adiabatic temperatures until a maximum is reached with pure oxygen.

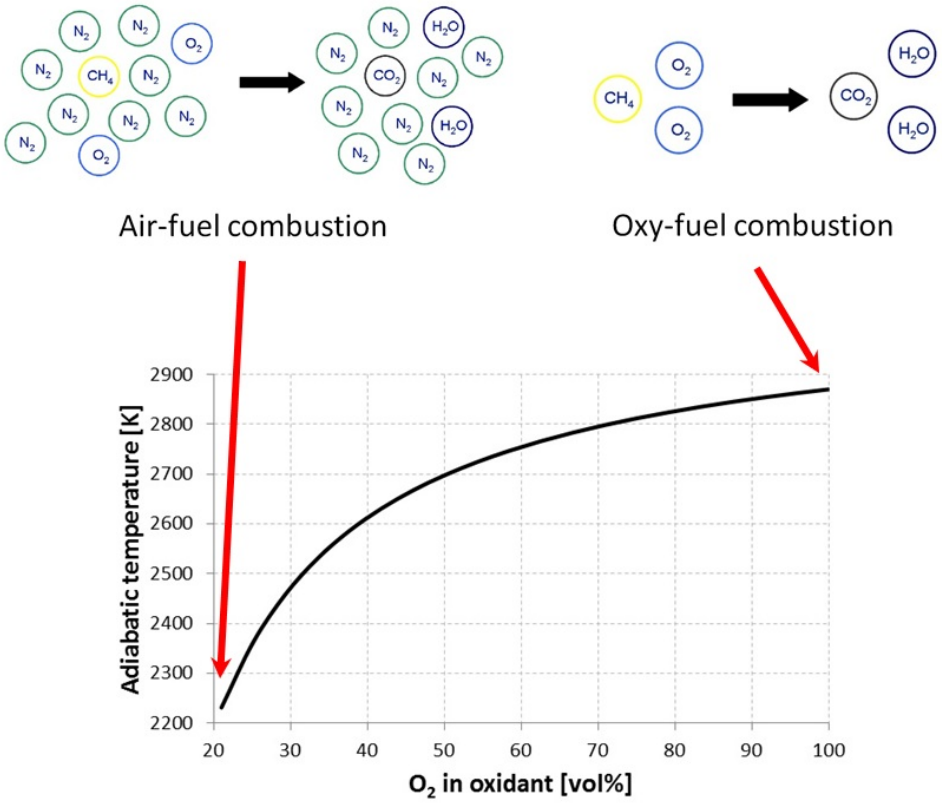

Fig. 4. Adiabatic flame temperature for combustion of methane with different O_2/N_2 mixtures as oxidant [43; 44].

The heat transfer to the load or walls has a huge dependence on the combustion regime. In high temperature processing and power generation, the main heat transfer mode is radiation in furnaces and boilers. The higher flame temperature in oxy-fuel combustion leads to a higher radiation intensity and improved heat transfer. Furthermore, the radiative property of the flue gas is changed by the increased level of H_2O and CO_2. Since a higher radiative heat transfer is achieved in oxy-fuel combustion, more heat from the combustion process can be transferred to the load and membrane walls (power generation). This effect is the basis for the following benefits of using oxy-fuel combustion [19]:

- **Increased productivity:** More heat is available for heating and melting the load and therefore higher production rates are possible.
- **Improved process efficiency:** Heat losses through the flue gas are reduced by lower flue gas flow-rate due to the lack of N_2.

- **Reduced flue gas volume and equipment (capital) costs:** Smaller combustion chambers and recuperators can be used in oxy-fuel combustion due to lower flue gas volume [22].
- **Improved product quality:** Direct flame impingement on the load and refractory can be avoided by shorter oxy-fuel flames compared to air-fuel combustion, which enhances the product quality. In addition, the higher radiation intensity leads to a more homogeneous temperature distribution of the load [43].
- **Higher flexibility:** The amount of oxygen in the oxidant can be adapted for different operating conditions to achieve the desired combustion regime.

Potential problems using oxy-fuel combustion can arise as a result of the increased combustion intensity and flame temperature. The more intense flame and the radiative heat transfer have to be well distributed in the furnace to prevent refractory damage by overheating. Furthermore, the refractory wall is exposed to corrosive species in the flue gas which can be released from the load (e.g. glass bath), radicals formed within the flame and impurities in low quality fuels. Thermal NO_x formed in the high temperature region of flames can be increased in OEC without adapted burner design. This was examined by Bělohradský et al. [44] for different burner configurations. These problems have to be considered, especially for retrofitting existing systems. Furthermore, the production of oxygen is an energy demanding procedure, with related additional costs. Methods of oxygen production and their costs are summarized in Section 1.2.3.

Based on the aforementioned advantages of oxy-fuel or OEC, this technology is appropriate for processes with

- high flue gas temperature,
- limited heat transfer to the load, production rate and thermal efficiency,
- high NO_x emissions and flue gas limitation (CO_2 emission).

Typical industrial applications are metal, glass and cement production as well as incinerators and coal-fired power plants, as summarized in [19].

1.2.1 Oxy-fuel combustion with flue gas recirculation

Oxy-fuel combustion can be applied for power generation, where an air separation unit supplies the pure oxygen for the combustion process (see Fig. 1). Since the combustion intensity and temperatures are much higher in oxy-fuel combustion, wall damages during furnace or boiler operation can arise. The stiffness of materials for gas turbines is also limited to a certain temperature level of approximately 1600 K [45]. To control the flame

temperature, recirculated flue gas is mixed with pure oxygen. This idea was first proposed by Abraham et al. [46] in 1982 for coal-fired power plants to produce CO_2 with high purity, which could be used for enhanced oil recovery [47; 48]. For retrofitted power plants and other industrial applications, it is necessary to keep the combustion temperature and heat transfer rate at a similar level as for air-fired conditions. Similar combustion characteristics as in air-fuel cases can be achieved by increasing the O_2 content in the oxidant up to approximately 25-30 % depending on the operating conditions and the fuel used. The effect of flue gas recirculation on the combustion process is highlighted by Wall [49]. Several experimental and numerical studies for lab-scale conditions have already been carried out to investigate the combustion process with flue gas recirculation (e.g. Al-Abbas et al. [50], Lasek et al. [51]). Other industrial applications also use flue gas recirculation. Granados et al. [18] investigated a rotary kiln for the cement industry. Although the flame temperature with 31 % O_2 in the oxidant was the same as for air combustion, a higher heat transfer to the furnace load was detected due to the enhanced CO_2 and H_2O content in the flue gas. Nevertheless, the main application of oxy-fuel combustion is in the power generation sector, where the reduction of emissions and the importance of energy efficient combustion are receiving much attention due to environmental and economic issues. However, some challenges have to be conquered to be competitive in power generation. The production of oxygen and CO_2 capturing in oxy-fuel combustion mean high energy demands, which result in a penalty on the net efficiency of power generation processes. According to Davison [1], the net efficiency penalties for oxy-coal fired and gas turbine combined power cycles are approximately 8.6 and 10.9 % points, respectively, compared to conventional firing without CO_2 capturing technology. Detailed reviews of the application in oxy-fuel combustion, mainly coal firing with special emphasis on power generation, can be found in Chen at al. [52], Scheffknecht et al. [53], Wall et al. [54] as well as Yin and Yan [55].

1.2.2 Oxygen enhanced combustion for high temperature processes

In many industrial manufacturing processes, high temperature unit operations are applied for annealing, melting and heating purposes. A huge amount of energy, currently covered by the combustion of fossil fuels, is necessary to achieve the desired heat flux to the processed material, whether it is steel, aluminium or glass. Besides the idea of oxy-fuel combustion with flue gas recirculation in 1982, the first use of OEC in metallurgy can be traced back to the 1930s [42]. Nowadays OEC is commonplace in high temperature processing as industries adapt to cope with environmental regulation and rising fuel prices. More than half of the

world production of copper, lead and nickel is done by applying OEC [56]. Oliveira et al. [57] carried out a study of combustion with pure oxygen in metal reheating furnaces at a temperature range of between 1150 to 1250 °C, and determined the viability for large scale furnaces. For melting or annealing, high gas temperatures are necessary to ensure a certain level of heat flux transferred to the load. Due to the lower level of nitrogen in OEC, fuel consumption can be significantly reduced although the same heat flux to the load is reached. This effect is much more evident at high temperatures of the flue gas (see Fig. 5). In this figure, the flue gas temperature (given in °F) is displayed on the right vertical axis. When using pure oxygen instead of air as an oxidant, the fuel savings increase at higher flue gas temperatures. For example, fuel consumption (natural gas) can be reduced by 60 % at 1371 °C (2500 °F) whereas the fuel reduction is only 50 % at 1204 °C (2200 °F). However, major improvements on the fuel reduction can already be detected at low concentrations of O_2 in the oxidant. Therefore, just a small amount of O_2, mixed with the combustion air is needed to optimize the combustion process. Another option is retrofitting existing furnaces for higher production rates through improved heat transfer. Since the costs of oxygen production are a major drawback, further improvements in oxygen production technology will make the use of OEC more attractive in the future.

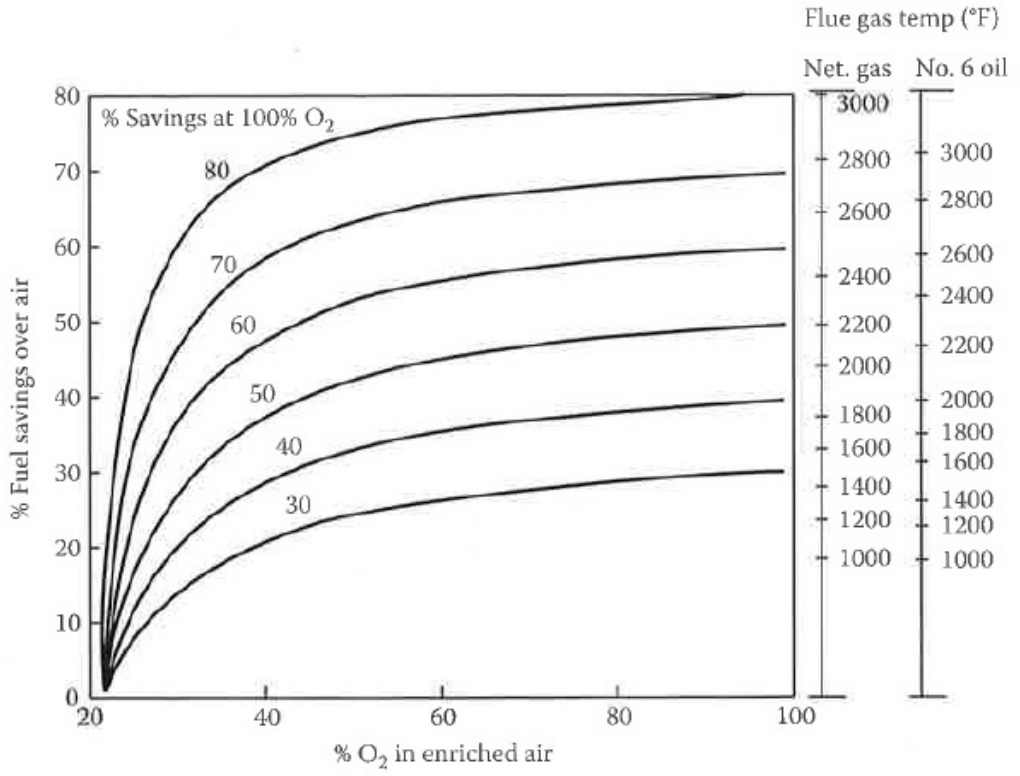

Fig. 5. Fuel saving potential depending on the oxygen enrichment level for natural gas and oil (data from Kobayashi [60]; figure from [19]).

Since low enrichment levels can lead to significant differences to air-fuel combustion, research has been done on oxygen enhanced flames between 21 and 30 % O_2 in the O_2/N_2 mixture. Merlo et al. [58] did experiments on a 25 kW lab-scale burner, investigating flame stability, lift-off and NO_x emissions for different O_2 concentrations. The OH chemiluminescence revealed higher flame stability and lower lift-off with oxygen enhancement. Additional tests on a lab-scale furnace were done by Wu et al. [59] in two steps. First, experiments were done to investigate the time needed to heat up the furnace to 1200 °C with OEC and air-fuel combustion. A significant increase in the heating rate was determined between 700 and 1200 °C for 30 % O_2 compared to air-fuel combustion. Below 700 °C, the difference on the heating rate was low. The second experiments revealed the fuel savings when a steady-state of the furnace is achieved at a fixed temperature level of 1220 °C. There, a 26.1 % reduction of fuel consumed was detected, with 30 % oxygen due to higher heat fluxes to the walls. Similar effects were found by Bělohradský et al. [44; 60] in a 750 kW combustion chamber.

1.2.3 Oxygen production/supply

Separating oxygen from air is an energy demanding process and a huge drawback for the use of oxy-fuel and OEC technology in industrial production. Depending on the amount and purity of the oxygen required, four different methods are common [61]:

- Delivery and storage of liquid oxygen
- Vacuum swing adsorption for on-site supply
- Cryogenic air separation systems for on-site production
- Membrane gas separation

The delivery and storage of liquid oxygen (LOX) is preferred when small quantities are required. LOX is stored in tanks on-site. Before use, it is vaporized and heated up to ambient conditions. The main advantage is that the capital costs for an on-site oxygen production unit can be avoided and high purity oxygen is available (99.5 %). Purchasing LOX is more expensive than on-site production. Oliveira et al. [57] revealed that the cost of LOX was approximately US$ 0.27/Nm³ for the Brazilian market in mid-2012. For comparison, the prices of oxygen extracted from the air by cryogenic separation and adsorption are US$ 0.063/Nm³ and US$ 0.058/Nm³ [57].

Cryogenic air separation has the widest range of oxygen production rate and purity. A flow rate up to 3000 t/d and a purity range from 90 to 99.9 % can be obtained [19]. The components of the air are cooled down and liquefied. Through distillation, oxygen, nitrogen

and other components in the ambient air are separated by their different boiling points and can be stored in tanks separately. A huge amount of energy is necessary to cool down the air.
Adsorption technology has a limited purity of approximately 95 % for oxygen supply because some air components have an equal affinity to the used adsorbents (commonly zeolites). Furthermore the production rate is limited to 100 t/d [19].
For membrane gas separation, MIEC-membranes (Mixed Ionic and Electronic Conductor), for example, with a perovskite or fluorite structure, are commonly used. Reviews of the membrane materials used, and their selectivity and permeation rates on oxygen have been published by Geffroy et al. [62] and Biernatzki [63]. Due to the pressure difference on both sides of the membrane, the air components are dissolved and can diffuse through the membrane. Depending on the selectivity of the membrane, the oxygen permeation rate is much higher and an oxygen enriched gas mixture on the other side of the membrane can be used for further applications, like combustion. For use in industrial scale applications, the energy demand of producing high purity oxygen by means of membrane separation technology is still too high, as a result of the low flow rate through membranes and the high operating temperature. Therefore, membrane technology for use in OEC is as yet restricted to lab-scale applications (e.g. [64]).

1.3 Aim of this study

In the present study, the effect of OEC on industrial applications is investigated by lab-scale experiments. The experiments were done on a lab-scale furnace with and without thermal load. All tests were carried out with oxygen enhanced combustion between 21 (air-fuel) and 100 % O_2 in the oxidant. Experiments were done at a fixed, pre-defined gas temperature in the furnace. To maintain the temperature level in the furnace the fuel consumption was adapted, which allows observing the fuel reduction potential in OEC. The experiments with thermal load were done at two temperature levels of 1000 and 1220 °C. Although several studies were found in literature for small enrichment levels or combustion with pure oxygen, these experiments should summarize the effect of OEC with natural gas in the full range of oxygen enrichment on a lab-scale furnace. The main goals of the lab-scale experiments are:

- Reveal fuel saving potential of OEC in industry for high temperature processes (above 1000 °C) compared to air-fuel combustion (experiments without thermal load)
- Determine heat fluxes, temperatures and furnace efficiencies in the full range of oxygen enrichment (experiments with thermal load)

- Provide measurement data for validation of the numerical models

Since numerical modelling of combustion processes is very sensitive on the chemistry and radiation models used, different approaches were evaluated for use in air-fuel combustion and OEC. In a first step, several detailed reaction mechanisms were numerically studied by the means of 1D simulation with CHEMKIN, to analyse their applicability for different oxygen levels. The investigated mechanisms are further used in 3D simulations with the commercial software package ANSYS Fluent. The goal was, to develop a numerical approach which can predict the transport phenomena in high temperature environments with high accuracy and low computational demand by 3D CFD simulations. Results, obtained with the different combustion and radiation models in conjunction with the investigated reaction mechanisms, are compared with the experimental data from the lab-scale furnace. The validated model should be applicable for small as well as large scale industrial furnaces with a low computational demand and in the full range of OEC. The aim of the numerical studies can be summarized as follows:

- 1D simulations to reveal the applicability of different reaction mechanisms for air-fuel combustion and OEC
- Investigation of turbulence, radiation and turbulence/chemistry interaction models for use in CFD simulations of OEC
- Validation of the CFD results with experimental data
- Development of a time efficient CFD approach applicable in the full range of OEC in large industrial furnaces
- Appraisal of OEC for high temperature processes using numerical and experimental data

The developed time efficient numerical model was used to simulate an industrial walking hearth furnace for reheating steel billets up to approximately 1200 °C. For this purpose, an iterative solution procedure was applied to predict the flow field, species concentrations and temperature in the walking hearth furnace, as well as the transient heating characteristic of the steel billets in the furnace for air-fuel conditions and OEC with 25 % O_2. The targets of this part are:

- Development of an iterative solution procedure to couple gas phase combustion and transient heating of steel billets
- Application of the developed CFD model for air-fuel combustion and OEC in the industrial walking hearth furnace

- Confirm the increase of furnace efficiency due to OEC by experiments and simulations of the walking hearth furnace
- Ensure that the target temperature and the temperature distribution in the billet is equal in both cases

2 Combustion principles

In Section 2, the combustion of gaseous fossil fuels (natural gas) is described briefly and is related to relevant literature from Chung [65], Joos [66], Warnatz et al. [67], Liberman [68], Turns [69] and Baukal [70], as well as basic principles of physical chemistry from Atkins [71]. Small amounts of sulphur and other components in the natural gas were not considered in this dissertation because of their minor influence on the combustion modelling in this work. Section 2.1 comprises basic information of the chemistry in gas phase reactions including chemical equilibrium, adiabatic temperature, etc. In Section 2.2, different flame configurations are summarized and these represent the basis for the numerical modelling of turbulent flames. Heat transfer modes and their importance for high temperature processes are examined in Section 2.3. The main differences between air-fuel combustion and OEC are presented in Section 2.4.

2.1 Gas phase combustion

Technical combustion is the rapid oxidation of fuel and one of the most complex processes involving chemistry, fluid mechanics, heat and mass transfer. To start the combustion of hydrocarbons, the bond between C and H atoms has to be broken, and radicals like CH_3 etc. are formed by overcoming the activation energy. Radicals are highly reactive molecules with unpaired electrons. This process is called ignition. In some cases, a global consideration of the hydrocarbon oxidation can be sufficient, with the assumption of infinite fast chemistry and full immediate conversion to the reaction products. Such consideration only involves the brutto-reaction or global reaction given in reaction (R. 1) for gaseous hydrocarbons. Reactants on the left hand side (hydrocarbon and oxygen) are rearranged by the exothermic chemical reaction to the reaction products.

$$C_xH_y + \left(x + \frac{y}{4}\right) O_2 \rightleftharpoons xCO_2 + \left(\frac{y}{2}\right) H_2O \qquad \text{(R. 1)}$$

In contrast to non-reacting flows, reacting flows contain a number of different species, such as reactants, products and intermediate species. These have to be considered for the modelling of a combustion process. Species in the form of molecules, atoms and radicals are usually counted in terms of the amount of substance n. For each component k in the homogeneous gas mixture, a mole fraction X_k can be defined, as in Eq. (1) and (2).

$$X_k = \frac{n_k}{n_{total}} \tag{1}$$

$$n_{total} = \sum_k n_k \tag{2}$$

Since the mass m_k of a species k is a fundamental physical property, the mass fraction Y_k is defined in Eq. (3) and (4).

$$Y_k = \frac{m_k}{m_{total}} \tag{3}$$

$$m_{total} = \sum_k m_k \tag{4}$$

The relationship between the amount of substance and the mass of a species k is given by the molecular weight in Eq. (5).

$$m_k = M_k * n_k \tag{5}$$

Besides the molecular weight of a component M_k, the molecular weight of the gas mixture $\bar{M}$ is defined in Eq. (6). With the molecular weight of the gas mixture the conversion of mole and mass fraction can be done by Eq. (7).

$$\bar{M} = \frac{1}{\sum_k \frac{Y_k}{M_k}} = \sum_k X_k * M_k \tag{6}$$

$$Y_k = X_k * \frac{M_k}{\bar{M}} \tag{7}$$

During the combustion process, the number of moles or the mass of a species is not constant. Therefore, in addition to the mole and mass fraction of the components, the elemental mass fraction of the chemical element is introduced. Since, the mass of each element i like C, O, H etc. remains unchanged during the entire combustion process, the elemental mass fraction has the same value. The elemental mass fraction of an element i is defined in Eq. (8) where m_i is the total mass of the element in the entire gas mixture and $\mu_{i,k}$ is the mass fraction of the element i in the component k.

$$Z_i = \frac{m_i}{m_{total}} = \sum_k \mu_{i,k} * Y_K \tag{8}$$

The mass of an element i in the gas mixture can be determined by Eq. (9) with the molecular weight of the element M_i and the number of the element i in the component k denoted by a_{ki}.

$$m_i = M_i * \sum_k \frac{a_{ki}}{M_k} * m_k \tag{9}$$

According to their definition, the sum of mole, mass and elemental mass fraction has to be one (see Eq. (10) to (12)).

$$\sum_k X_k = 1 \tag{10}$$

$$\sum_k Y_k = 1 \tag{11}$$

$$\sum_i Z_i = 1 \tag{12}$$

The state of a gas with one component is defined by the pressure p, temperature T, volume $V$and amount of substance n, which are related by the equation of state. If three variables are known, the fourth can be calculated. The general form of the equation of state is given in Eq. (13).

$$p = f(T, V, n) \tag{13}$$

The simplest form of the equation of state is the ideal gas law defined in Eq. (14), where R is the universal gas constant with a value of 8.314 J/mol*K. The ideal gas law is a combination of three empirically founded correlations.

- **Boyle's law:** change of state at constant temperature and amount of substance

$$p * V = constant$$

- **Charles' law:** change of state at constant pressure and amount of substance

$$\frac{V}{T} = constant$$

- **Avogadro's law:** change of state at constant temperature and pressure

$$\frac{V}{n} = constant$$

$$p * V = n * R * T \tag{14}$$

Since the laws of Boyle and Charles are valid at low pressure, the ideal gas law is commonly used for moderate pressure, which is sufficient for most combustion cases in industrial furnaces. The limits of the ideal gas law's ability to predict the state of a gas can be found in [71] and are not further highlighted in this thesis. According to Dalton's law, the total pressure in a gas mixture is the sum of the partial pressures p_k of all components in the gas (see Eq. (15)). As a consequence the ideal gas law can also be applied for gas mixtures.

$$p = \sum_k p_k \tag{15}$$

A rearrangement of the ideal gas law leads to the definition of the molar density or concentration, which is defined as the amount of a substance per volume unit. This is shown in Eq. (16) and (17) for the molar density of the gas mixture and the component k.

$$c = \frac{n}{V} = \frac{p}{R * T} \tag{16}$$

$$c_k = \frac{n_k}{V} = \frac{p_k}{R * T} \tag{17}$$

The density of the gas mixture and the single component k can be calculated using Eq. (18) and (19).

$$\rho = \frac{m}{V} = \frac{p * \bar{M}}{R * T} \tag{18}$$

$$\rho_k = \frac{m_k}{V} = \frac{p_k * M_k}{R * T} \tag{19}$$

Due to the use of the ideal gas law, the mole fraction can also be calculated by the partial pressure of the component k and total pressure in the system. Furthermore, the mole fraction is equal to the volume fraction (see Eq. (20)).

$$X_k = \frac{n_k}{n_{total}} = \frac{p_k}{p} = \frac{V_k}{V} \tag{20}$$

2.1.1 Chemical reactions and equivalence ratio

In real combustion processes, the oxidation of hydrocarbon fuels is not completely represented by only one reaction as given in (R. 1). Instead, the brutto-reaction consists of many intermediate steps of reactions including molecules, atoms and radicals. In order to gain deep insight into the combustion process, it is necessary to consider the intermediate reaction steps. Two kinds of reactions can be distinguished:

- **Elementary reactions:** An elementary reaction considers the reaction progress on a molecular and atomic level, forming new species through the collision of molecules and atoms. The elementary reaction in (R. 2) shows the oxygen radical breaking the bonds of methane to form two new radicals. Such reactions can occur at the beginning of the methane combustion. The oxygen radical, needed for the reaction, can be formed by dissociation of O_2 due to ignition or the hot flue gases.

$$CH_4 + O^{\cdot} \rightleftharpoons OH^{\cdot} + CH_3^{\cdot} \quad \text{(R. 2)}$$

Elementary reactions can be classified by the number of reactants (molecules and atoms) in monomolecular, bimolecular and three-molecular elementary reactions. In monomolecular reactions only one reactant is involved, as can be seen in (R. 3). Such reactions are characterised by the decay of a component.

$$A \rightleftharpoons product \quad \text{(R. 3)}$$

Bimolecular reactions are the most important type of elementary reactions and involve two reactants. According to (R. 4) the reactants can also be identical.

$$\begin{aligned} A + B &\rightleftharpoons product \\ A + A &\rightleftharpoons product \end{aligned} \quad \text{(R. 4)}$$

Three-molecular reactions are usually a recombination process (see (R. 5)). For example, two hydrogen radicals can form a new H_2 molecule. In such cases, a third reactant is sometimes involved to absorb a part of the collision energy. Otherwise, the collision energy would again break the bond of the H_2 molecule. The third reactant is an inert component, unaffected by the reaction, but could also be a hydrogen radical.

$$\begin{aligned} A + B + C &\rightleftharpoons product \\ A + A + B &\rightleftharpoons product \\ A + A + A &\rightleftharpoons product \end{aligned} \quad \text{(R. 5)}$$

Elementary reactions with more than three reactants are irrelevant for technical combustion processes and are not considered in this thesis. More detailed information about the character of elementary reaction and collision theory in chemistry can be found in the studies mentioned at the beginning of Section 2.

- **Global reactions:** This is the overall reaction of a mole of fuel with the oxidizer to form the product. It can be seen as a summary of several elementary reactions where intermediate species are neglected. An example of a global reaction is given in (R. 6), where the products are formed in a single step reaction. The formation of intermediate species is not considered.

$$CH_4 + 2O_2 \rightleftharpoons CO_2 + 2H_2O \quad \text{(R. 6)}$$

For complete combustion of the fuel, a minimal amount of oxidant is necessary, which is called a stoichiometric amount. In this case, only the reaction products occur after the combustion. When the oxidant is air, the stoichiometric air-fuel ratio $(A/F)_{stoich}$ can be defined by Eq. (21).

$$(A/F)_{stoich} = \left(\frac{m_{air}}{m_{fuel}}\right)_{stoich} \tag{21}$$

In fuel-lean combustion, a higher amount of oxidant exists than for the stoichiometric combustion. As a result, a residual amount of oxygen and nitrogen remains in the flue gas, besides the reaction products, after complete combustion. A lower amount of oxidant than the stoichiometric value leads to fuel-rich combustion, where the fuel is not fully converted to the products. Intermediate species such as CO can be detected in the flue gas. For an indication of whether the combustion occurs under stoichiometric, fuel-lean or fuel-rich conditions, the equivalence ratio Φ or fuel-to-air equivalence ratio is introduced by Eq. (22), where F/A is the fuel-to-air ratio given in Eq. (23).

$$\Phi = \frac{(A/F)_{stoich}}{A/F} = \frac{F/A}{(F/A)_{stoich}} \tag{22}$$

$$\mathrm{F/A} = \frac{1}{A/F} \tag{23}$$

From this definition, it can be concluded that:

- Stoichiometric: $\Phi = 1$
- Fuel-lean: $\Phi < 1$
- Fuel-rich: $\Phi > 1$

In addition, the reciprocal value of the fuel-to-air equivalence ratio is defined in Eq. (24). This is called air-to-fuel equivalence ratio.

$$\lambda = \frac{1}{\Phi} \tag{24}$$

2.1.2 Reaction kinetics and reaction mechanisms

In some cases, it is possible that the chemical reaction or combustion can be assumed as an infinitely fast process. Hence, combustion processes are very complex in terms of their fluid mechanics, physics and chemistry, as well as their interactions; for this reason, a detailed description of the time-dependent progress is necessary for accurate predictions of temperature and species concentrations within a flame. The reaction kinetic considers the temporal progress and reaction pathways of a chemical process from the initial condition to the chemical equilibrium. For elementary reactions, the reaction kinetic can be determined by measurements.

A bimolecular elementary reaction with the collision partners A and B is expressed in (R. 7), where ν'_R is the stoichiometric coefficient of reactant R and ν''_P is the stoichiometric

coefficient of the product P. The rate coefficients for forward and backward reactions are k_f and k_b.

$$\nu'_A A + \nu'_B B \underset{k_b}{\overset{k_f}{\rightleftharpoons}} \nu''_C C + \nu''_D D \qquad \text{(R. 7)}$$

The net rate production of a component k in (R. 7), for example A, B etc., can be expressed by Eq. (25).

$$\nu_k = \nu''_k - \nu'_k \qquad (25)$$

The reaction kinetic is directly proportional to the concentration of the reactants involved. Therefore, the temporal change of the concentration of a component, or reaction rate of the forward reaction r_f, can be written as in Eq. (26), where the forward reaction is considered. In this equation, the sum of the stoichiometric coefficients for A and B represents the order of the reaction. In the present case, the reaction order is two. The reaction rate of the other components is given by Eq. (27).

$$-\frac{1}{\nu'_A}\frac{dc_A}{dt} = k_f * c_A^{\nu'_A} * c_B^{\nu'_B} = r_f \qquad (26)$$

$$-\frac{1}{\nu'_A}\frac{dc_A}{dt} = -\frac{1}{\nu'_B}\frac{dc_B}{dt} = \frac{1}{\nu''_C}\frac{dc_C}{dt} = \frac{1}{\nu''_D}\frac{dc_D}{dt} \qquad (27)$$

The reaction rate of backward reaction r_b can be expressed in a similar way, which is given in Eq. (28). A backward reaction can take place when the components C and D are available to form A.

$$\frac{1}{\nu'_A}\frac{dc_A}{dt} = k_b * c_C^{\nu''_C} * c_D^{\nu''_D} = r_b \qquad (28)$$

The overall reaction rate r for the considered bimolecular reaction, including forward and backward reactions, is given by Eq. (29) and (30).

$$\frac{1}{\nu_A}\frac{dc_A}{dt} = r_f - r_b = r \qquad (29)$$

$$r = k_f * c_A^{\nu'_A} * c_B^{\nu'_B} - k_b * c_C^{\nu''_C} * c_D^{\nu''_D} \qquad (30)$$

In general, the reaction rate of a chemical reaction is given in Eq. (31).

$$r = k_f * \prod_k c_k^{\nu'_k} - k_b * \prod_k c_k^{\nu''_k} \qquad (31)$$

The rate coefficients for forward and backward reactions are temperature dependent and have their origins in molecular collision theory, which highlights the frequency of the collisions

between atoms and molecules in a gas mixture. The number of collisions increases at higher temperatures, causing the higher kinetic energy of the particles. Besides the collision of reactants, a characteristic energy level has to be achieved during the collision in order to start the chemical reaction. This energy level is called activation energy E_A and is displayed in Fig. 6. For the exothermic forward reaction the activation energy E_f is necessary to run the reaction. During the process the enthalpy of the reaction and the activation energy E_f are released. Since the backward reaction is endothermic, the activation energy E_b is needed to start the reaction.

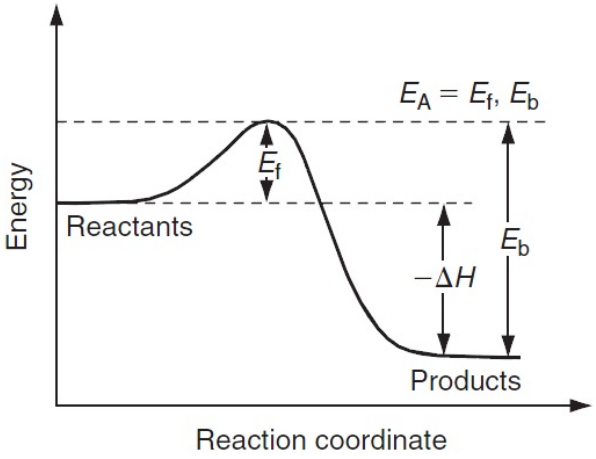

Fig. 6. Activation energy for a chemical reaction **[72]**.

The temperature dependence of the rate coefficient is described by the Arrhenius equation given in Eq. (32), where k_0 is the pre-exponential factor or frequency factor. The pre-exponential factor and activation energy for a reaction can be determined by experiments. The data for $\ln k$ and $1/T$ can be plotted and fitted according to the linear equation in Eq. (33). The slope of the line fit is an expression for $-E_A/R$.

$$k = k_0 * e^{-\frac{E_A}{R*T}} \tag{32}$$

$$\ln k = \ln k_0 - \frac{E_A}{R * T} \tag{33}$$

The frequency factor k_0 is not constant. Based on collision theory, the frequency factor is directly proportional to $T^{1/2}$. In combustion modelling, a more common expression of the Arrhenius equation is given in Eq. (34), which is also applied in the chemical reaction sets in this thesis for the CFD simulation. In this equation, the term T^b represents the temperature dependency of the frequency factor.

$$k = k_0 * T^b * e^{-\frac{E_A}{R*T}} \tag{34}$$

For a detailed consideration of a steady-state combustion process, a number of elementary reactions are required. The collection of the elementary reactions necessary to describe the combustion is called reaction mechanism. For example, the oxidation of hydrogen with oxygen requires approximately 40 elementary reactions for an accurate prediction. Even the combustion of the simplest hydrocarbon CH_4 can be comprised of up to 400 elementary reactions. Depending on the initial thermodynamic condition and the kind of fuel, a suitable reaction mechanism has to be found. Although the interaction between the elementary reactions affects the entire combustion, only a few reactions in the entire set of reactions are important for an accurate prediction. Therefore, a detailed reaction mechanism with several hundred reactions can be reduced by eliminating the redundant reactions and species. These can be determined by an analysis of the reaction set, for example, using sensitivity, reaction flow or eigenvector analysis. After the reduction, the smaller reaction set is called the skeletal reaction mechanism, and it is usually valid for a smaller range of operating conditions than the detailed one [61].

Although skeletal mechanisms comprise a lower number of reactions and species, the calculation time for the numerical investigations of a combustion process can be very high, especially for some combustion models in CFD simulations. Hence, a further reduction of the reaction mechanism is possible, containing just a few global reaction steps. Such mechanisms are called global reaction mechanisms. A typical mechanism was proposed by Westbrook and Dryer [73] with a 2-step reaction mechanism (see (R. 8) and (R. 9)), where CO was also taken into account. In this case, the prediction of intermediate species and radical formation is limited.

$$CH_4 + \frac{3}{2}O_2 \rightarrow CO + 2H_2O \tag{R. 8}$$

$$CO + \frac{1}{2}O_2 \rightleftharpoons CO_2 \tag{R. 9}$$

In contrast to elementary reactions, where the stoichiometric coefficients (reaction order) are integers, the coefficients ν_k' and ν_k'' in Eq. (31) are no longer related to the chemical reaction when global mechanisms are used. Even values below one are possible for the stoichiometric coefficients. Thus, the parameters for the rate coefficient and the stoichiometric coefficients for each global reaction have to be adapted for the investigated combustion case and are validated by experimental data. As an example, Yin et al. [74] adapted global reaction mechanisms from Westbrook and Dryer [73] as well as Jones and Lindstedt [75] for use in

oxy-fuel combustion. Numerical problems using global reaction mechanisms arise due to the fact that the reaction order can be lower than one. As a consequence, negative values for the concentrations can be calculated [76].

The chemical reaction mechanisms used in this thesis are summarized in Section 4.3.4.

2.1.3 Chemical equilibrium

Chemical reactions occur in both forwards and backwards directions according to the reaction equation. Chemical equilibrium is achieved when forward and backward reactions take place at the same reaction rate. Hence, the concentration of the components in the homogeneous gas mixture is constant. The reaction yield is represented by the equilibrium constant which is dependent on the initial and boundary conditions of the reaction, according to the principle of le Chatelier. Although the chemical equilibrium constant of a reaction is known, no conclusion about the reaction kinetic can be made.

To determine the equilibrium constant, the fundamental thermodynamic relation is derived by the first and second law of thermodynamics. The change of the internal energy in a closed system is given Eq. (35) as stated in the first law of thermodynamics.

$$dU = dQ - p * dV \tag{35}$$

The change of the entropy for reversible and irreversible processes is given in Eq. (36) (second law of thermodynamics). For the chemical equilibrium, the entropy reaches a maximum value and as a consequence $dS = 0$.

$$dS = \frac{dQ_{rev}}{T} \qquad\qquad dS > \frac{dQ_{irrev}}{T} \tag{36}$$

The combination of Eq. (35) and (36) leads to the fundamental thermodynamic relation for constant amount of a pure substance. This is expressed in Eq. (37), where the internal energy is $U = U(V, S)$.

$$dU = T * dS - p * dV \tag{37}$$

The free energy G (or Gibbs function) and its total differential are defined in Eq. (38) and (39).

$$G = H - T * S \tag{38}$$

$$dG = dH - S * dT - T * dS \tag{39}$$

Furthermore, the enthalpy H is given in Eq. (40) and in Eq. (41).

$$H = U + p * V \tag{40}$$

$$dH = dU + p * dV + V * dp \tag{41}$$

A combination of Eq. (37), (39) and (41) leads to the fundamental thermodynamic relation of the free energy, expressed in Eq. (42) for a pure component with a constant amount of a substance. Thus, it follows that the free energy is $G = G(p, T)$.

$$dG = V * dp - S * dT \tag{42}$$

In case of a gas mixture with several components, the free energy is a function of temperature, pressure and the amount of substance n_k with $G = G(p, T, n_k)$. Hence, the Eq. (42) is extended by an additional term as given in Eq. (43), where $\bar{\mu}_k$ is the chemical potential of the component k.

$$dG = V * dp - S * dT + \sum_k \bar{\mu}_k * dn_k \tag{43}$$

The total differential of the free energy can also be written as expressed in Eq. (44).

$$dG = \left(\frac{\partial G}{\partial p}\right)_{T, n_{k \neq j}} * dp + \left(\frac{\partial G}{\partial T}\right)_{p, n_{k \neq j}} * dT + \sum_k \left(\frac{\partial G}{\partial n_k}\right)_{p,T} * n_k \tag{44}$$

The chemical potential is defined in Eq. (45).

$$\bar{\mu}_k = \left(\frac{\partial G}{\partial n_k}\right)_{p,T} \tag{45}$$

A system in thermodynamic equilibrium shows the maximum entropy and, as a consequence, the lowest free energy. This leads to the expression of $dG = 0$. The integration of Eq. (44) for constant temperature and amount of substance n_k leads to Eq. (46). The reference conditions (commonly standard conditions) are indicated by ^{0}:

$$G(T, p_k, n_k) = G^0(T, p^0) + \int_{p^0}^{p_k} V * dp \tag{46}$$

Using the ideal gas law in Eq. (46), it follows Eq. (47).

$$G(T, p_k, n_k) = G_k^0(T, p^0) + n * R * T * \ln \frac{p_k}{p^0} \tag{47}$$

Differentiation of Eq. (47), with respect to the amount of substance n_k, leads to the chemical potential in Eq. (48).

$$\bar{\mu}_k = \bar{\mu}_k^0(T) + R * T * \ln \frac{p_k}{p^0} \tag{48}$$

Considering a chemical reaction which reaches equilibrium with constant temperature and pressure, Eq. (49) can be derived.

$$dG = \sum_k \bar{\mu}_k * dn_k = 0 \tag{49}$$

A reaction progress variable η is introduced in Eq. (50).

$$d\eta = \frac{dn_k}{\nu_k} \tag{50}$$

Replacing dn_k in Eq. (49) leads to the following equation valid for chemical equilibrium.

$$\left[\sum_k \nu_k * \bar{\mu}_k\right] * d\eta = 0 \tag{51}$$

Eq. (48) and Eq. (51) result in the following equation.

$$\begin{aligned}\sum_k \nu_k * \bar{\mu}_k^0 + R * T * \sum_k \nu_k * \ln\frac{p_k}{p^0} \\ = \sum_k \nu_k * \bar{\mu}_k^0 + R * T * \sum_k \ln\left(\frac{p_k}{p^0}\right)^{\nu_k} = 0\end{aligned} \tag{52}$$

In Eq. (52) the first term on the left hand side can be expressed as given in Eq. (53), where G_k^0 is the standard free energy of formation for component k, and ΔG_R^0 is the standard free reaction energy.

$$\sum_k \nu_k * \bar{\mu}_k^0 = \sum_k \nu_k * G_k^0 = \Delta G_R^0 \tag{53}$$

Based on Eq. (52) and (53) the equilibrium constant of a reaction is defined in Eq. (54). In addition, using the ideal gas law, the equilibrium constant can also be expressed by the concentrations K_c in Eq. (55).

$$K_p = e^{-\frac{\Delta G_R^0}{R*T}} = \prod_k \left(\frac{p_k}{p^0}\right)^{\nu_k} \tag{54}$$

$$\begin{aligned}K_p = \prod_k \left(\frac{c_k * R * T}{p^0}\right)^{\nu_k} = \prod_k (c_k)^{\nu_k} * \prod_k \left(\frac{R * T}{p^0}\right)^{\nu_k} \\ = K_c * \left(\frac{R * T}{p^0}\right)^{\sum_k \nu_k}\end{aligned} \tag{55}$$

The equilibrium constant for a reaction is dependent on the temperature, which is considered by the Van't Hoff equation given in Eq. (56), where ΔH_R^0 is the standard reaction enthalpy. According to Hess's law, the standard reaction enthalpy can be calculated by the standard enthalpy of formation for the components k.

$$\left(\frac{d(\ln K(T))}{dT}\right)_p = \frac{\Delta H_R^0}{R * T^2} \tag{56}$$

After the integration of Eq. (56), the equilibrium constant for a distinct temperature Tcan be determined by Eq. (57), where T^0 is the reference temperature.

$$\ln K(T) = \ln K\,(T^0) - \frac{\Delta H_R^0}{R} * \left(\frac{1}{T} - \frac{1}{T^0}\right) \tag{57}$$

The chemical equilibrium is also dependent on the pressure. Because all combustion processes in this thesis are considered under atmospheric and isobar conditions, the pressure dependence is not examined.

2.1.4 Adiabatic flame temperature

The adiabatic flame temperature is the temperature of the burnt gases after the combustion process in an adiabatic system ($dQ = 0$). Under the assumption that the combustion occurs at a constant volume, the first law of thermodynamics (see Eq.(35)) yields Eq. (58)).

$$dU = 0 \qquad with \quad V = constant \tag{58}$$

More important is the combustion at constant pressure. In this case, the combination of Eq. (35) and (41) shows that the enthalpies of the burnt and unburnt gases are equal, which is given in Eq. (59) and (60). In Eq. (60) the indices u and b stand for the unburnt and burnt gases, H_{fuel} and H_{ox} are the enthalpies of the fuel and oxidant before combustion, and ΔH_R is the reaction enthalpy or lower heating value H_u. In contrast to the lower heating value, the gross heating value also comprises the enthalpy of the evaporation of the H_2O in the flue gas. Therefore, it has a higher value than the lower heating value. On the right hand side, T_b and T_u are the temperatures of the burnt and unburnt gases and $c_{p,k}$ is the specific heat capacity of the gas component k.

$$dH = 0 \qquad with \quad p = constant \tag{59}$$

$$H^{(u)} = H_{fuel} + H_{ox} + \Delta H_R = H^{(b)} = \sum_k \left(\int_{T_u}^{T_b} c_{p,k} * dT\right) \tag{60}$$

With Eq. (60) the adiabatic gas temperature T_b can be calculated in an iterative solution procedure because of the temperature dependence of the heat capacity of the burnt gases. Considering the combustion of gaseous fuel under fuel-lean or stoichiometric conditions, Eq. (60) can be written as expressed in Eq. (61), where the left hand side represents the enthalpies of the fuel and oxidant as well as the lower heating value, and the right hand side represents the enthalpy of the burnt gases.

$$\dot{m}_{fuel} * \left(c_{p,fuel} * T_{fuel} + H_u\right) + \dot{m}_{ox} * c_{p,ox} * T_{ox} = \left(\dot{m}_{fuel} + \dot{m}_{ox}\right) * c_{p,b} * T_b \quad (61)$$

Since, the combustion products dissociate to radicals and CO at high flame temperatures, the heating value is not completely released during the combustion process. This effect is very important in OEC, as displayed in Fig. 7, where the adiabatic flame temperature for methane combustion is displayed. The calculation with the one–step reaction mechanism (see Table 24 in the appendix), according to (R. 6), showed a huge increase in the adiabatic flame temperature from 2325 K for air-fired combustion to 5143 K for combustion with pure oxygen. At high temperatures, H_2O and CO_2 can dissociate to radicals and CO due to the high amount of energy within the gas mixture, which is capable of breaking the bonds of the molecules H_2O and CO_2. The dissociation of H_2O and CO_2 is a highly endothermic process and absorbs a significant amount of the heat of reaction. These dissociation effects can be covered by detailed reaction mechanisms like the GRI3.0, where a number of intermediate species are considered.

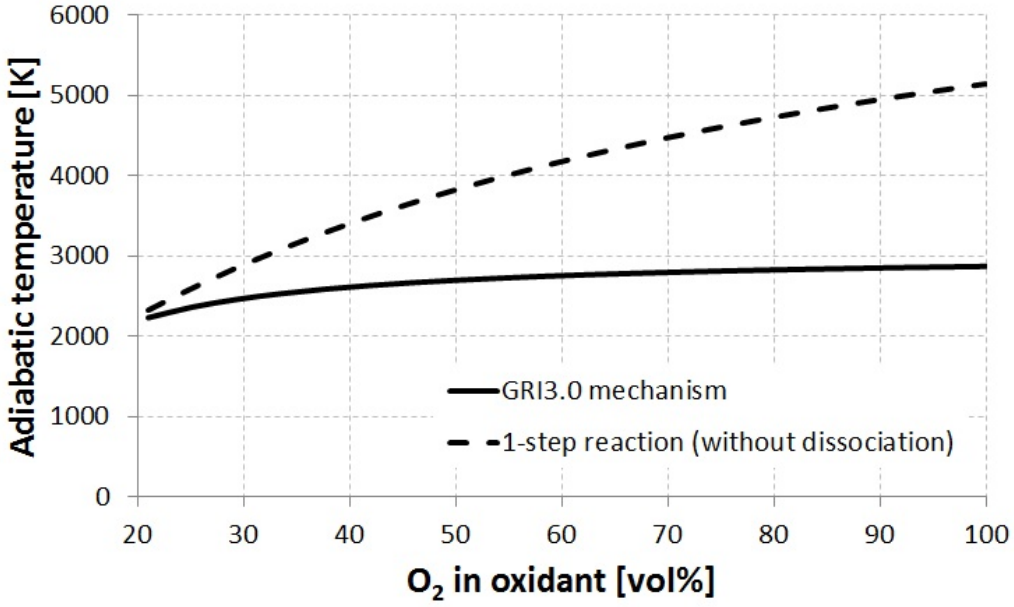

Fig. 7. Adiabatic flame temperature of CH_4 combustion calculated with GRI3.0 mechanism and 1-step global mechanism with full conversion (see Table 23 and Table 24).

2.2 Flame configuration

The mixing of fuel and oxidant in combustion processes is a crucial aspect. Where the mixing takes place is dependent on the application, and is used as a distinction for the flame types in premixed and non-premixed flames. For each flame configuration, the flames are further subdivided by the fluid flow during combustion. An overview of flame configurations is

given in Table 2 according to [67]. Furthermore, a hybrid configuration of both flame types is known as partially premixed flame described in section 2.2.3.

Table 2
Flame types and examples.

Mixing type	Fluid flow	Examples
Premixed flame	Turbulent	Gasoline engine Stationary gas turbine
	Laminar	Flat flame Bunsen flame
Non-premixed flame	Turbulent	Pulverized coal combustion Diesel engine OEC in industrial process
	Laminar	wood fire candle

2.2.1 Premixed combustion

The chemical reaction is strongly related to the flow field and the mixing rate between fuel and oxidant. A simple description of a combustion process can be derived in a homogenous premixed fuel oxidant mixture in a laminar flow field before combustion. In this case, the chemical reaction is not affected by the mixing rate of fuel and oxidizer. Investigations of laminar flame structures can form the basis for modelling turbulent flames. The simplest premixed flames are flat flames or Bunsen flames with a planar or conical flame front, as displayed in Fig. 8 with air as oxidant.

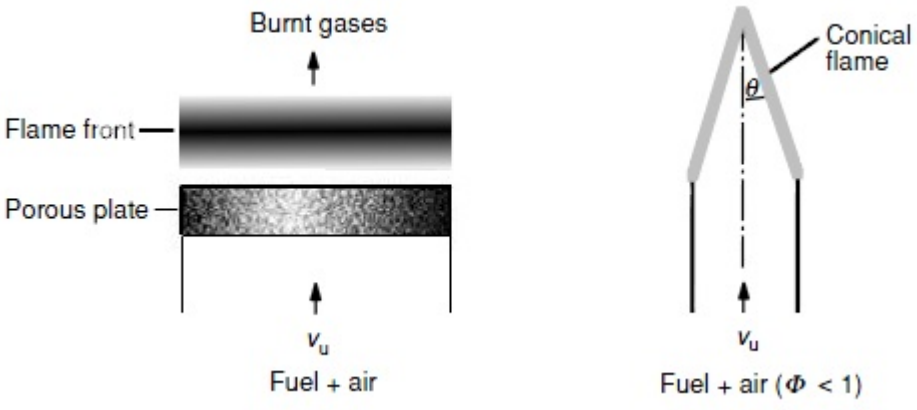

Fig. 8. Laminar flat flame and Bunsen flame [70].

If the combustion of a premixed flame occurs in a turbulent fluid flow, the flame front is distorted by the turbulent eddies. This curved and wavy flame front (see Fig. 9) can be seen as a collection of smaller laminar flames. Turbulent premixed combustion is applied when high combustion intensity takes place in a small space. Due to the greater control of the

combustion process, peak temperatures can be avoided by pre-combustion under fuel-rich conditions. As a consequence, the formation of thermal NO_x can be minimized. The full oxidation of the fuel is completed during a second air supply stage.

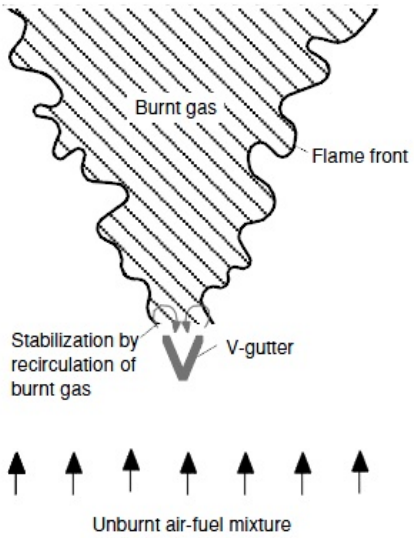

Fig. 9. Flame front of a turbulent premixed flame with V-shaped flame stabilization body [70].

Despite the advantages of premixed flames, they are not used for combustion with high O_2 content in OEC because of their high potential for explosions.

2.2.2 Non-premixed combustion

In non-premixed or diffusion flames, the mixing of fuel and oxidant, as well as the chemical reaction, occurs simultaneously. The equivalence ratio in a non-premixed flame can vary between 0 in the oxidant stream and ∞ in the fuel stream. In Fig. 10, the configuration of a laminar coflow flame is displayed. The inner flame zone consists of a fuel-rich mixture, which is surrounded by the oxidant stream with an equivalence ratio below 1. The flame front is located in the vicinity of the stoichiometric mixture with $\Phi \approx 1$ and also defines the flame length L_f. In this region, the unburnt gases are transported from the fuel-rich and fuel-lean side to the flame front by convection and diffusion. After the mixing process, the mixture is ignited by the hot burnt gases in the flame zone. Due to the mixing and heat losses, the flame temperature of non-premixed flames is lower than those of premixed flames. Furthermore, the soot emission increases, which is formed in the fuel-rich side of the flame zone.

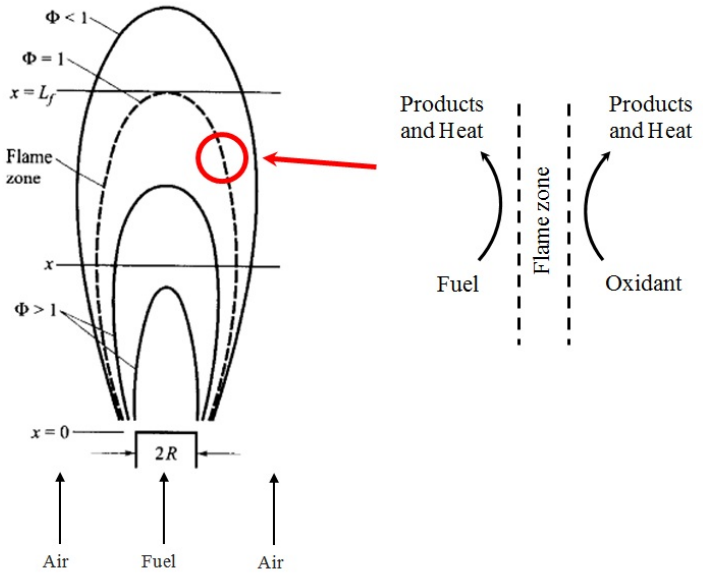

Fig. 10. Configuration of laminar coflow non-premixed flame [68; 72].

For a turbulent non-premixed flame, the smooth surface of the flame front is disturbed by the turbulent fluid flow. Similar to the premixed flame, the flame zone gets curved. Burners using a non-premixed flame configuration are usually used in industrial furnaces because of safety considerations.

They are able to deal with high purity oxygen in a much safer manner than burners with premixed flames. Considering the flame shape, burners can be subdivided into jet flames and flat flame burners. Jet flames have the same configuration as displayed in Fig. 10. The jet has a high momentum in axial direction. Such a burner type was arranged in the lab-scale furnace and is described in Section 3.1. Flat flame burners were designed to maximize the flame coverage over the furnace load. This can be achieved in two ways. First, several small fuel and oxidant injection points are distributed on a surface of the furnace wall. The numerous small flames can cover a larger surface where heat is transferred to the load. Second, a swirl is introduced to the fuel and oxidant jet in the burner. Consequently, the flame shows a higher radial momentum and is directed along the furnace wall. This type of flat flame burner was arranged in the industrial walking hearth furnace investigated in this thesis (see Section 3.2).

2.2.2.1 Mixture fraction

The simplest way to describe the flame zone is the Burke-Schumann model, which assumes an infinitely fast chemistry and the full conversion of fuel and oxidant. The reaction progress at each position between the fuel and oxidant sides is able to be determined by the equivalence ratio. However, using the equivalence ratio is not useful because of the undefined

value on the fuel side. Thus, the mixture fraction is introduced, which represents the mixing of fuel in the overall mass of the gas mixture. The definition of the mixture fraction f is given in Eq. (62), where $\dot{m}_{fuel}$ and $\dot{m}_{ox}$ are the mass-flow rates of fuel and oxidant and Z_i is the elemental mass fraction of the element i, as defined in Eq. (8) in the entire mixture. In addition, $Z_{i,fuel}$ and $Z_{i,ox}$ stand for the elemental mass fraction in the fuel and oxidant.

$$f = \frac{\dot{m}_{fuel}}{\dot{m}_{fuel} + \dot{m}_{ox}} = \frac{Z_i - Z_{i,ox}}{Z_{i,fuel} - Z_{i,ox}} \tag{62}$$

According to the definition of f, on the fuel and oxidant sides, the mixture fractions are 1 and 0, respectively. The advantage of the formulation of the mixture fraction is that the mass fractions have a linear dependence on the mixture fraction. Consequently, the process within the reaction zone is reduced to a single mixing problem by the mixture fraction. Since the assumption of equal diffusivity of the components is sufficient in most combustion cases, the mixture fraction is not affected by the selection of the element i.

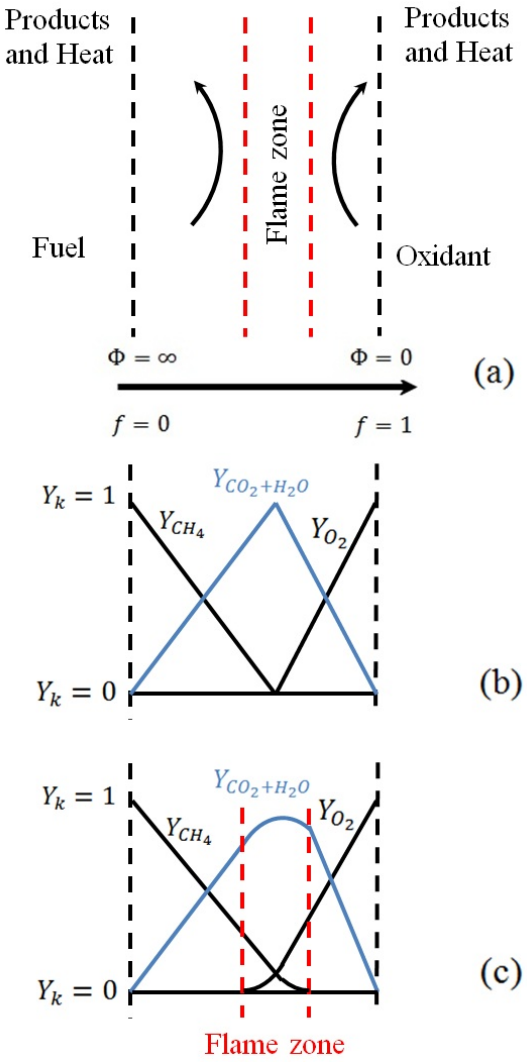

Fig. 11. Scheme of mass transport (a) and mass fractions in the flame zone (a, b) in a non-premixed flame.

In Fig. 11, the mass transfer to the reaction zone and mass fraction of the components are schematically displayed for an oxidation of methane with pure oxygen to the carbon dioxide and water. Fig. 11b shows the linear dependence of the mass fractions on the mixture fraction for an infinitely fast chemistry. The flame zone is reduced to an infinitely small region (reaction sheet).

If finite-rate chemistry, with intermediate species and chemical equilibrium, has to be considered, the linear trend of the mass fractions within the flame zone is no longer valid. The reaction sheet gets wider and the reactants occur simultaneously in the flame zone. Since full conversion and fast chemistry is assumed, this model cannot predict flame extinction and pollutant emissions such as NO_x.

2.2.2.2 Counter-flow diffusion flame

In addition to the configuration of a coflow laminar non-premixed combustion, the laminar opposed-flow diffusion flame is the simplest setup of a laminar non-premixed flame. This type was often used for numerical and experimental investigations in the past. For example, Marinov et al. [77] highlighted the formation path of aromatics and polycyclic aromatics in a diffusion flame with numerical and experimental methods. In Fig. 12, the setup of a laminar opposed-flow diffusion flame is displayed. Fuel and oxidant are transported to the flame zone from opposite directions and react in the flame zone, similar to the coflow configuration in Fig. 10.

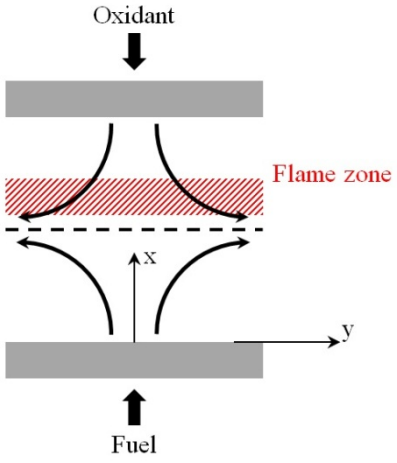

Fig. 12. Configuration of a laminar opposed-flow diffusion flame.

One advantage of such a burner configuration is that the transport phenomena and chemical reactions within the flame zone can be reduced or approximated by a 1D problem. Only the stagnation streamline at $y = 0$ is considered. Several assumptions have to be made for such an approach:

- Diffusion in y-direction is neglected
- Velocity component in x-direction, temperature and species concentrations are only a function of x
- Velocity component in y-direction is proportional to the distance from the x-axis

For a steady-state process, the governing equations for the species concentrations and temperature are given in Eq. (63) and (64), where u is the velocity component in x-direction, λ is the thermal conductivity of the gas, $\tilde{V}_k$ is the diffusion velocity of the component k, and ω_k is the production rate of the component k.

$$\rho u \frac{dY_k}{dx} + \frac{d}{dx}\left(\rho \tilde{V}_k Y_k\right) - \omega_k = 0 \tag{63}$$

$$\rho u \frac{dT}{dx} - \frac{1}{c_p}\frac{d}{dx}\left(\lambda \frac{dT}{dx}\right) + \frac{\rho}{c_p}\left(\sum_k c_{p,k} Y_k \tilde{V}_k\right)\frac{dT}{dx} + \frac{1}{c_p}\sum_k h_k \omega_k = 0 \tag{64}$$

Based on the mixture fraction theory as described in Section 2.2.2.1, temperature and species concentrations in the opposed diffusion flame can also be related on the mixture fraction f instead of the x-coordinate. This leads to the modelling approach that the flame zone (vicinity of the stoichiometric mixture fraction) of a turbulent non-premixed flame consists of a number of small laminar diffusion flamelets, which is known as the steady laminar flamelet model (see Section 4.3.3). With this approach, OEC cases in large scale furnaces can also be simulated with low calculation time.

2.2.3 Partially premixed combustion

In partially premixed combustion systems for industrial burners, the fuel is mixed with a fraction of the total oxidant/air (primary air) before the combustion occur (see Fig. 13). Commonly, the premixed fuel/oxidant mixture is fuel-rich to minimize soot formation, temperatures in the flame and reduce the NO_x formation. The final burnout of the fuel occurs after secondary air is transported to the main reaction zone, leading to an overall equivalence ratio lower than 1. With this flame configuration, the combustion characteristic related to temperature, heat transfer, flame shape etc. is between the premixed and non-premixed flame. This approach is often used to achieve a higher stability of the flame in contrast to a fully premixed case as well as to ensure a lower potential for explosion/flashbacks [70].

Fig. 13. Configuration of a partially premixed flame [73].

2.3 Heat transfer in furnaces

During combustion, the chemical conversion of fuel and oxidant is used as a heat source in industrial furnaces and boilers. Due to the temperature gradients in the furnace, which arise from the high temperature in the main reaction zone of a flame, the heat is transferred by conduction, convection and radiation.

2.3.1 Conduction

This heat transfer mode is characterized by the energy transport from molecule to molecule by collisions within the gas, liquid or solid phase. In metals, the energy transfer also occurs by the free electrons in the metal structure. Basically, energy transport by conduction is driven by the temperature gradient and is proportional to the thermal conductivity λ. Considering a steady-state solution, the specific heat flux by conduction is calculated using the Fourier's law in Eq. (65) [78].

$$\dot{q} = -\lambda * \nabla T \tag{65}$$

In the gas phase of combustion processes, conduction has a minor effect on the overall heat transfer. Conduction in a furnace has to be considered within solids like the furnace refractory walls and the furnace load, e.g. steel, glass etc. For example, the conductive heat flux is significant when a cold body is put into the furnace and laid on the hot hearth [79]. To determine the heat losses through the furnace wall during the combustion process, an accurate prediction of the conduction is necessary. Therefore, knowledge of the thermal conductivity is necessary but difficult to determine in most industrial furnaces. Since the refractory walls are commonly made with several layers in order to minimize heat losses, small gaps between the layers as well as between the refractory elements can be detected. In Fig. 14, the gaps in the refractory walls of the walking hearth furnace described in Section 3.2 are displayed for different zones.

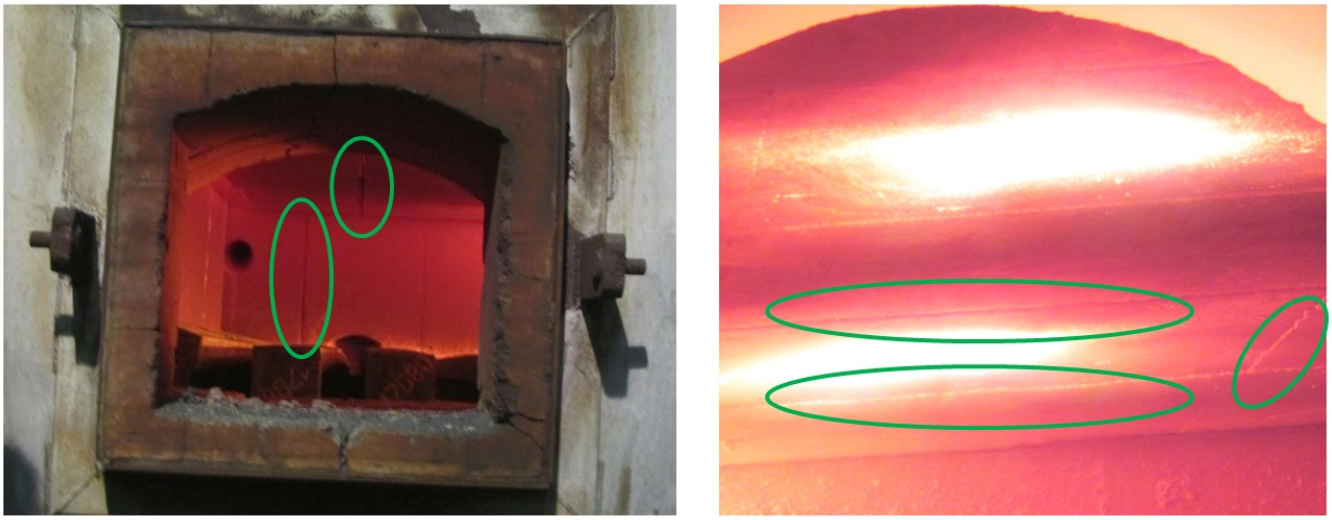

Fig. 14. Gaps in the refractory walls of a walking hearth furnace; left: pre-heating zone; right: soaking zone.

In addition to the gaps between the refractory elements, the transport system and inspection windows as well as the measurement equipment in an industrial furnace represent further sites of potential heat loss.

2.3.2 Convection

Through the fluid flow in a combustion chamber, heat is not only transferred by conduction, but also by convection. In contrast to conduction, convection is the heat transfer by macroscopic fluid motion, with a distinct enthalpy and kinetic energy of the fluid volume, from hotter (colder) to colder (hotter) regions. In general, convection can be divided into forced and natural convection. Natural convection is induced by density differences within the gas or fluid phase due to temperature variation. Forced convection is the heat transfer by fluid motion within an externally driven flow field. Due to the fact that heat transfer by natural convection has a much lower intensity than forced convection, only the latter is considered in this section.

For technical purposes, the convective heat transfer from a fluid to a surface is important and is influenced by the flow conditions in the boundary layer at the surface. With a special emphasis on combustion, the heat is transferred from the hotter gas phase to the colder furnace walls and furnace load through the boundary layer. The specific heat is then proportional to the temperature difference between the gas and the surface (see Eq. (66)). In the following equation, α is the heat transfer coefficient, T_g and T_s are the temperatures of the gas in the bulk and the surface of the wall or load, respectively.

$$\dot{q} = \alpha * (T_g - T_s) \tag{66}$$

The heat transfer coefficient is difficult to determine because of its strong dependence on the flow conditions at the surface, and is thus usually estimated by empirical correlations. Furthermore, the gas temperature T_g in furnaces is not constant. Detailed information about the determination of the heat transfer coefficient can be found in relevant literature on heat transfer (e.g. [78]).

2.3.3 Radiation

Thermal radiation is the exchange of heat to the environment by a spectrum of electromagnetic waves. Related to the wavelength of the electromagnetic waves, radiation can be classified as gamma rays, x-rays, microwaves, etc. For thermal heat transfer, wave lengths between 0.1 µm and 100 µm are of the most importance because the majority of the heat is transferred in this region [80]. This covers the visible wave spectrum, as well as parts of the ultraviolet and infrared region, as indicated in Fig. 15.

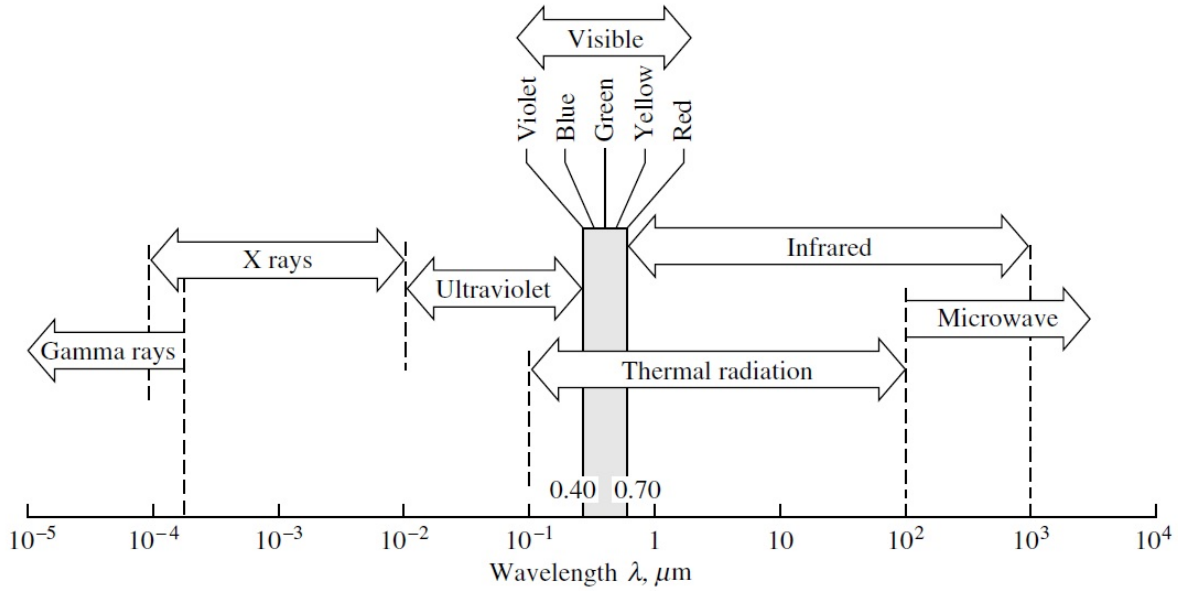

Fig. 15. Electromagnetic wave spectrum in vacuum [83].

Electromagnetic waves interact with molecules and atoms of a gas, liquid or solid phase and can be absorbed, reflected and transmitted. Each phenomenon can be related to the overall irradiation on a surface (see Fig. 17).

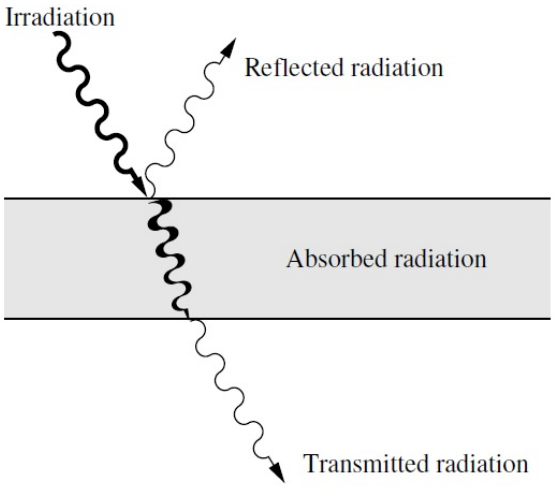

Fig. 16. Absorption, reflection and transmission of irradiation on a solid media [83].

2.3.3.1 Radiation between solids

Each body with a positive thermodynamic temperature emits thermal radiation, depending on the surface temperature [78]. A body with an absorptance of one, which is a so-called "black body", can emit the maximum radiation intensity given in Eq. (67), where σ is the Stefan-Boltzmann constant with a value of $5.67*10^{-8}$ W/m²K^4 and T_s is the surface temperature.

$$\dot{q}_{rad,black} = \sigma * T_s^4 \tag{67}$$

On real surfaces, all three phenomenon occur simultaneously, although transmission in a non-transparent body is limited to a thin surface layer. The emitted radiation of a real surface is lower than that of a black body. Therefore, emissivity is defined as the emitted radiation of the real surface related to the emissivity of the black body surface at the same temperature. Hence, the emitted radiation of a surface can be calculated by Eq. (68), where ε is the emissivity of the surface.

$$\dot{q}_{rad} = \varepsilon * \sigma * T_s^4 \tag{68}$$

It is important to note that the emissivity of a surface is not a constant value, as defined for technical purposes, but also depends on the wave length, the direction of the radiation, and surface condition. To cover all of these impact factors, which are difficult to determine, a huge amount of calculation time would be necessary for numerical applications.

Considering heat exchange between two surfaces with different temperatures, heat is not only transferred from the hotter (e. g. furnace wall) to the cooler body (e.g. furnace load), but also vice versa. The net radiative heat transfer from the hotter to the colder surface can be calculated by the difference of the emitted radiation intensities of both bodies. This is given in Eq. (69) for two surfaces of a black body with an Area A and an absorptance of one.

$$\dot{Q}_{hot\rightarrow cold} = \sigma * A * (T_{hot}^4 - T_{cold}^4) \quad (69)$$

Considering real surfaces, the emissivity is respected by Eq. (70) and (71).

$$C_{hot\rightarrow cold} = \frac{\sigma}{\left(\frac{1}{\varepsilon_{hot}} + \frac{1}{\varepsilon_{cold}} - 1\right)} \quad (70)$$

$$\dot{Q}_{hot\rightarrow cold} = C_{hot\rightarrow cold} * A * (T_{hot}^4 - T_{cold}^4) \quad (71)$$

2.3.3.2 Radiation of gases

In contrast to a black body, gases interact with thermal radiation only in distinct wave bands, which are dependent on the molecule structure. Hence, the total emissivity of a gas mixture has to be determined for the present combustion case. In typical hydrocarbon combustion processes, the main species are CO_2, H_2O and N_2. Intermediate species, radicals and components with minor concentrations have a low contribution to the radiative heat transfer. Furthermore, mono- and diatomic gases like N_2 and O_2 can be seen as diathermic for thermal radiation. In combustion processes, one must distinguish between radiation from clear gases/flames and luminous flames. Luminous flames, for example those used in coal combustion, have an additional radiative heat flux from soot particles. Such particle radiation has a higher radiation intensity, than the radiation from clear gases [66]. Since radiation from particles is emitted within the visible wave length, the flames are luminous.

Radiation emitted by clear gases to the furnace walls and load can be calculated by Eq. (72), where ε_g and ε_s are the emissivities of the gas mixture and furnace walls, and a_g is the absorptance of the gas for radiation.

$$\dot{Q} = \frac{A * \sigma * \varepsilon_s}{1 - (1 - a_g) * (1 - \varepsilon_s)} * \left(\varepsilon_g * T_g^4 - \alpha_g * T_s^4\right) \quad (72)$$

In most combustion process with a high operating temperature within the furnace, the radiative heat transfer is crucial compared to the convective heat flux. This fact is examined in Fig. 17. It is pointed out in [79] that below a temperature of 1100 °F (593 °C) the convective heat flux is dominant. For high temperature processes, the gas temperature is commonly above 1000 °C, where the radiation intensity increases in proportion to T^4. It is also important to note that the convective heat flux can be increased by using a high velocity burner [79] or direct flame impingement (DFI) to the load, which is also applicable for oxy-fuel combustion [81]. The increase of the heat fluxes to a plate using flame impingement can be found in a review published by Chander and Ray [82]. Nevertheless, radiation is the dominant heat transfer mode in combustion processes.

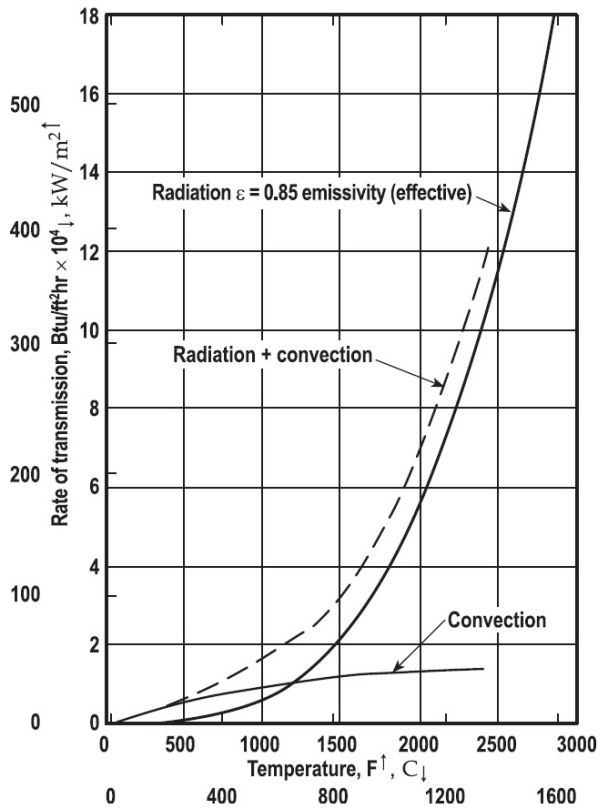

Fig. 17. Radiative and convective heat flux at different temperature ranges for an emissivity of 0.85 [82].

It is assumed in Eq. (72) and Fig. 17, that gas temperature and emissivity are constant in the entire furnace. However, for real furnace operation in high temperature processes, the gas temperature can differ significantly within the furnace. Additionally, the species concentrations in the gas mixture have a huge impact on the gas emissivity, especially in the main reaction zone, where high gradients of the concentrations can occur. Therefore, Eq. (72) and Fig. 17 can only be used for a rough approximation of the radiative heat transfer in a furnace.

2.4 Combustion modelling – Air-fuel vs. oxy-fuel combustion

CFD simulations of combustion processes should be able to predict several transport phenomena as accurately as possible. Besides solving the fluid flow within a furnace, the crucial elements for a numerical analysis of combustion are the chemistry within the main reaction zone and the heat transfer, mainly due to radiation. Several combustion (including reaction mechanisms) and radiation models are already available to predict temperature, species concentrations and the heat transfer in furnaces, but these have to be tested for their applicability in OEC. In the following sections, the differences between air-fuel and oxy-fuel combustion are examined.

2.4.1 Chemistry

Due to the higher flame temperature in OEC, the chemical kinetics is very different from conventional air-fuel combustion. Radical formation by dissociation and intermediate species has to be included in the set of reactions for the proper prediction of the flame temperature and species concentrations. This is the basic information necessary to determine the radiation intensity emitted by the flue gas.

For example, to determine the dissociation effects at high temperature, the reaction (R. 10) is considered. In this reaction, the dissociation of H_2O to OH and H was calculated using EES (engineering equation solver) [83]. The calculation was done according to Section 2.1.3 and the EES-code, and the results can be found in Section 10.2.2.

$$H_2O \rightleftharpoons OH + H \qquad \text{(R. 10)}$$

The chemical equilibrium for the dissociation of H_2O is shown in Fig. 18. It points out that, for moderate temperatures, the chemical equilibrium is on the left hand side of (R. 10). At approximately 2200 K, which is in the range of the adiabatic flame temperature for air-fuel combustion (see Fig. 7), radicals formed by the dissociation of H_2O only occur in very small amounts. In this case, global reaction mechanisms, only considering the main species, can cover the effects within an air-fuel flame quite well. In oxygen enriched combustion, the flame temperature is higher, and subsequently, the chemical equilibrium of (R. 10) starts to shift from the left hand side to the right. It can be seen in Fig. 18 that when the flame temperature increases to approximately 2500 K, the dissociation of H_2O starts. The adiabatic flame temperature for the combustion of natural gas with pure oxygen is approximately 3000 K (see Fig. 7). Therefore, it is necessary to consider intermediate species and radicals within the main reaction zone for the proper prediction of OEC processes.

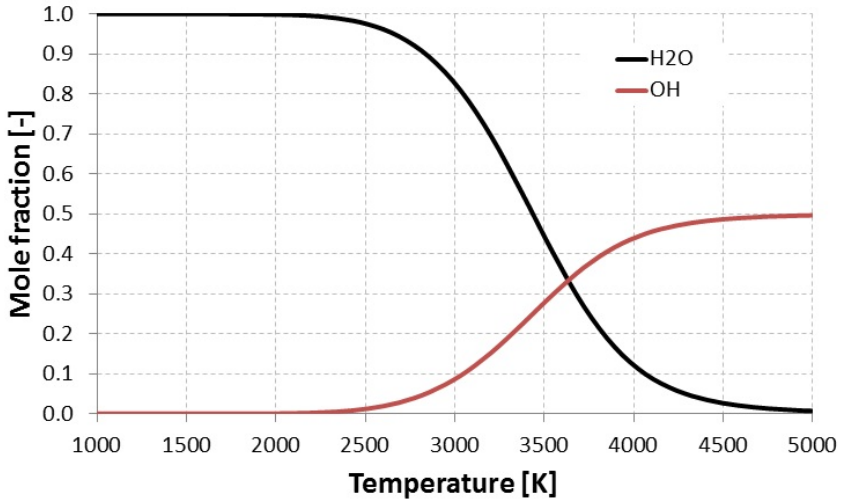

Fig. 18. Chemical equilibrium of (R. 10) dependent on temperature (p = 1 atm = const.).

To observe the formation of radicals and intermediate species in a high temperature flame, the chemical equilibrium for the combustion process of methane with different O_2/N_2 mixtures were calculated. Adiabatic and stoichiometric conditions were assumed for these calculations. The composition of the gas mixture at chemical equilibrium is shown in Fig. 19. The mole fraction is given without the N_2 content, as defined in Eq. (73), for a better comparison of air-fuel and OEC.

$$X_k = \frac{X_k}{1 - X_{N_2}} \tag{73}$$

For the full conversion of CH_4 into combustion products, the flue gas composition should only contain H_2O and CO_2, with mole fractions of 2/3 and 1/3. In air-fuel combustion with 21% O_2, the mole fractions of H_2O and CO_2 were calculated with values of 0.63 and 0.30. As a consequence of the high mole fractions of CO_2 and H_2O, only small concentrations of intermediate species arise during the chemical reaction. For example, the OH and CO mole fractions are 0.011 and 0.030. By increasing the O_2 content in the oxidant, the chemical equilibrium differs significantly from air-fuel combustion as a result of the higher flame temperature. The mole fractions of CO_2 and H_2O decrease to values 0.159 and 0.459 due to the dissociation. In contrast to the main species, the concentrations of OH and CO increase up to 0.073 and 0133. Considering the chemical equilibrium only, it can be seen that proper consideration of the chemistry within a high temperature flame is necessary for accurate prediction of the flame temperatures, which also affect radiative heat transfer.

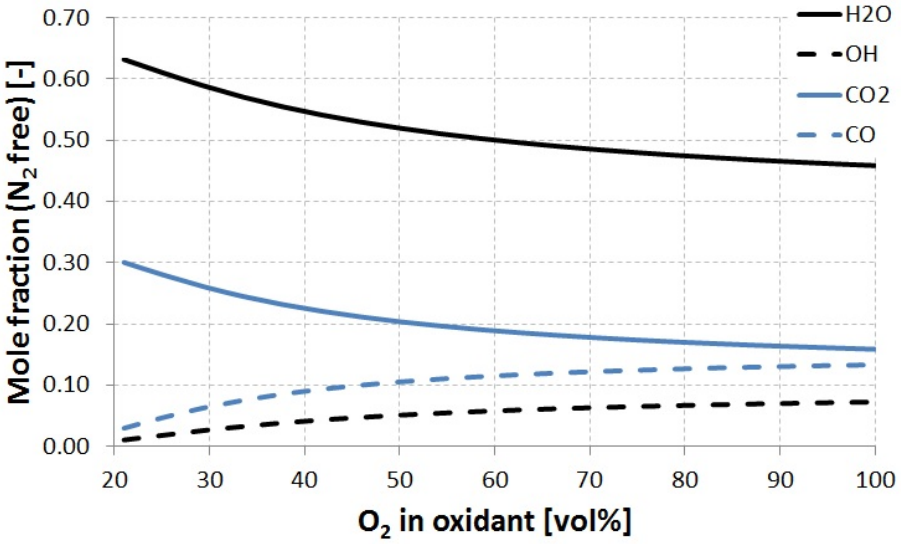

Fig. 19. Composition of the gas mixture at chemical equilibrium for stoichiometric and adiabatic CH_4 combustion calculated with CHEMKIN-PRO (see Table 23).

2.4.2 Radiation

Modelling of the radiative heat transfer in combustion is closely related to the H_2O and CO_2 concentrations in the gas phase. In OEC cases, the H_2O and CO_2 content can differ from lower amounts in air-fuel combustion up to volume fractions of 0.66 and 0.33 for atmospheric oxy-fuel combustion. Therefore, the numerical model must be able to calculate the radiative properties of the gas mixture in a wide range of temperature and flue gas concentrations. Since the emissivity and absorptance of a gas is not homogeneous across the entire spectrum, the discretization of the spectrum is crucial for their prediction. Basically, the models can be subdivided into tree methods:

- Line-by-line model (LBL)
- Band model
- Global method

The three methods were summarized by Becher et al. [84] in Fig. 20. The LBL is the most accurate model and considers the spectral dependence of the participating molecules based on databases. Nevertheless, it is not suitable for CFD simulation due to the high computational demand and the number of radiative transport equations (RTEs) which have to be solved. The band models, such as the statistical narrow band model (SNB) [85] and exponential-wide-band model (EWB) [86], reduce the numerical effort by summarizing the section between distinct wave lengths to a number of bands. For CFD simulations, only grey gas models are suitable for calculating the radiative heat transfer in a furnace with reasonable calculation time. This model assumes that the flue gas is a single grey gas or a mixture of several grey gases. The overall emissivity is determined by weighting factors for the absorptance and emissivity of each grey gas. Such a global method is the weighted-sum-of-grey-gases model (WSGGM) proposed by Hottel and Sarofim [31] (see Section 4.4.3.1). A disadvantage of this approach is that the spectral dependencies of some species in the flue gas cannot be considered. This is examined in Fig. 20, where the peaks at approximately 2.8 and 4.3 µm are not covered by the WSGGM.

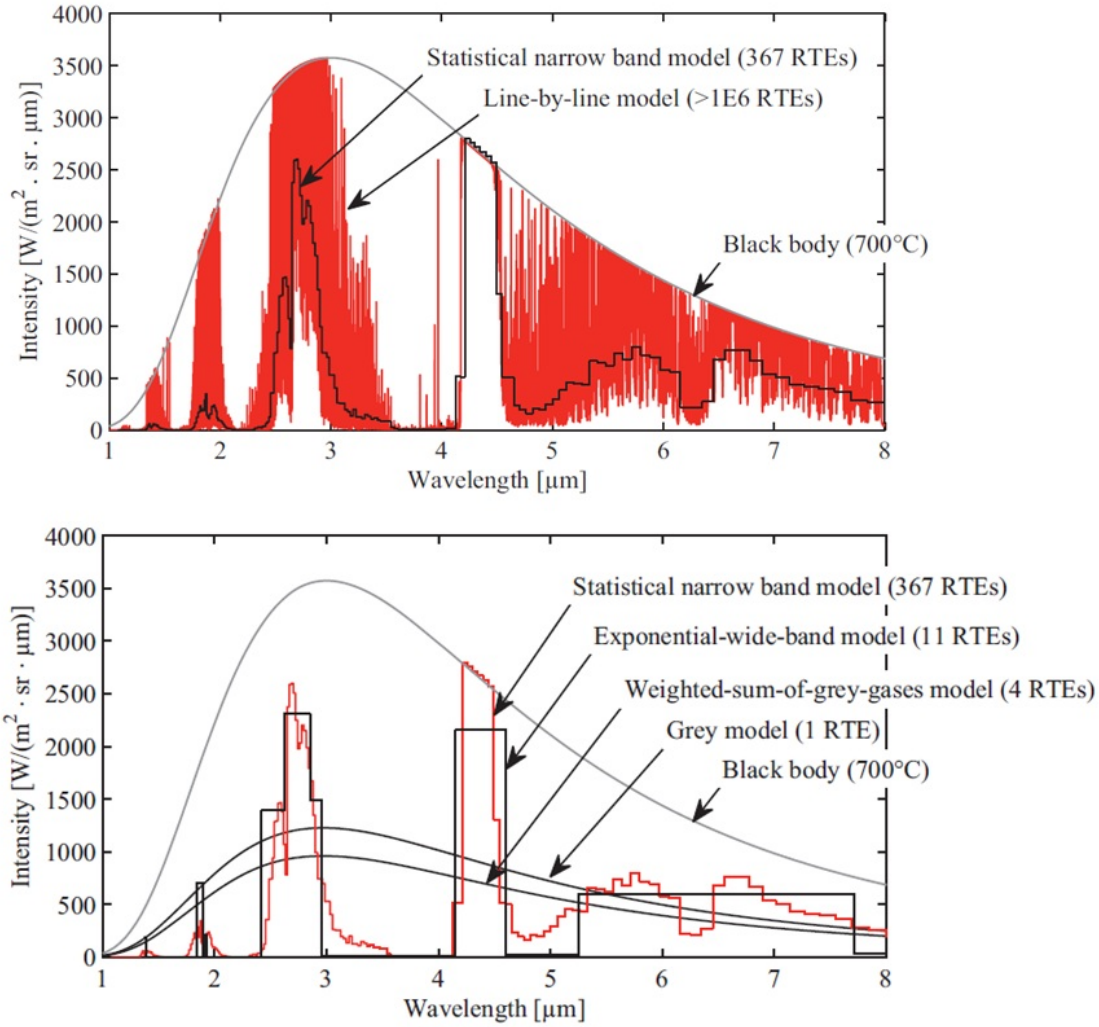

Fig. 20. Methods for spectral discretization as an example for natural-gas combustion with air (temperature of 700 °C and beam length of 0.7 m [87].

Becher et al. [84; 87] validated the LBL model with several databases (HITEMP2010 [88], HITEMP1995 [89], HITRAN2008 [90] and HITRAN2004 [91]) and band models (RADCAL [92], EM2C [93] and EWB) against the gas cell experiments carried out for oxy-fuel conditions. The highest accuracy was found with the database HITEMP2010, and was used for a comparison with the WSGG model with the coefficients published by Smith et al. [94], which are widely used for combustion simulations. A maximum deviation of 59 % was found between the HITEMP2010 and the WSGG model for oxy-fuel combustion. On that account, it is recommended to treat the flue gas as a non-grey gas, especially at high H_2O and CO_2 concentrations. Therefore, in recent years, many authors have published adapted coefficients, which are more suitable for modelling the gas emissivity in conjunction with the WSGG model under air-fuel and oxy-fuel conditions. Such WSGG parameters for oxy-fuel combustion have been published by Bordbar et al. [95], Johansson et al. [96; 97], Kangwanpongpan et al. [98], Krishnamoorthy [99], Rehfeldt et al. [100] and Yin et al. [101].

Some of the proposed model coefficients were tested and validated against more accurate models or databases.

The gas emissivity for different WSGG parameters is shown in Fig. 21 as a function of the beam length. Only combustion with pure oxygen as oxidant is considered. Since the lab-scale furnace investigated in this thesis has small dimensions, and as a consequence, a smaller beam length, a more detailed look at gas emissivity between 0 and 3 m is shown on the right hand side in Fig. 21. From this figure, it is evident that the effect of WSGG parameters on gas emissivity is quite high for large scale furnaces like boilers. In lab-scale experiments up to 0.5 m, the calculated gas emissivity is in a close accordance, and therefore, the modelling of the radiative properties in lab-scale dimensions is of less significance.

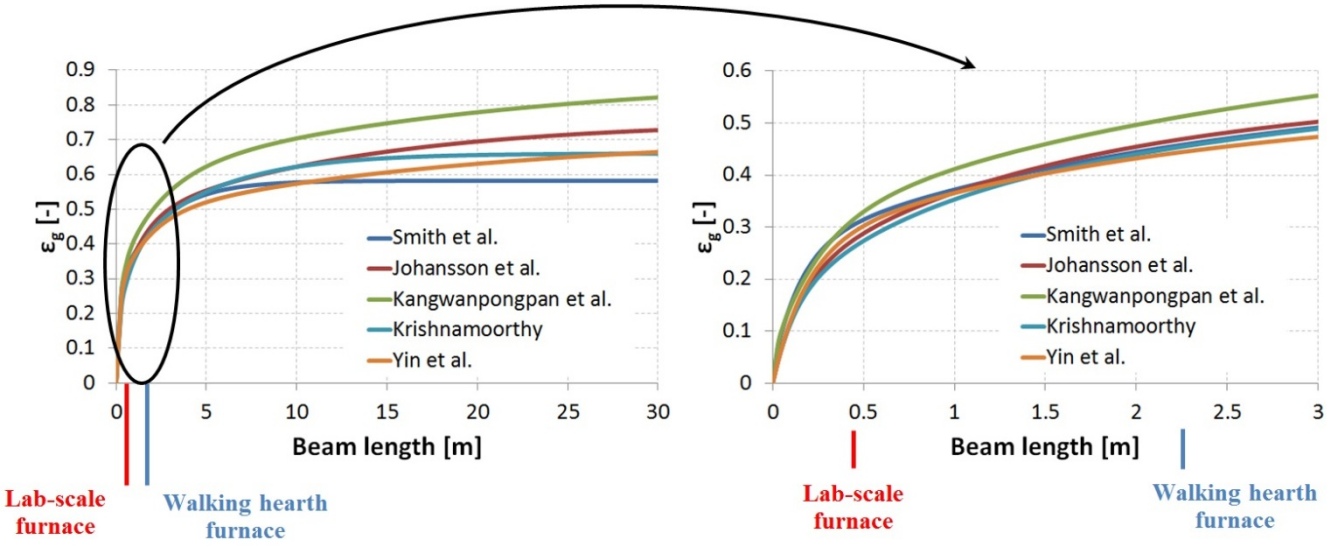

Fig. 21. Gas emissivity for OEC with pure oxygen calculated with WSGG model using parameters from different references (T_g = 1500 K and p = 1 atm); Smith et al. [97], Johansson et al. [99; 100], Kangwanpongpan et al. [101], Krishnamoorthy [102], Yin et al. [104].

Although the WSGG model neglects the spectral dependence of H_2O and CO_2, it is mainly used for the simulation of OEC. The fast simulation run time of this model is a huge advantage and the enhancement of the WSGG parameters for a non-grey consideration leads to its applicability in a wide range of combustion cases (also OEC with various O_2 contents in the oxidant).

3 Experimental setup

Two furnaces were used to gain experimental data for comparison with different numerical models. Both furnaces can be operated under both air-fuel and OEC conditions. The lab-scale furnace is described in Section 3.1 and the industrial walking hearth furnace in Section 3.2.

3.1 Lab-scale furnace

The lab-scale furnace, which is displayed in Fig. 22 (with open front door), was operated for different OEC cases from 21 % to 100 % O_2 in the oxidant and a positive pressure of between 0.3 and 0.4 mbar to prevent the leakage of ambient air into the furnace. A pressure measurement was arranged at the rear end of the furnace. The dimensions of the main combustion chamber are 0.99 x 0.77 x 0.75 m. The flue gas exit can be seen at the rear end of the chamber (see Fig. 22). The flue gas exit duct has a semi-circle cross section of 0.33 m (see Fig. 24). Considering radiative heat transfer, the mean beam length for radiation in the main chamber is 0.494 m, according to Eq. (74) (see [102]), where s is the mean beam length, V and A are the chamber volume and inner surface area of the chamber.

$$s_{gl} = 0.9 * \frac{4 * V}{A} \tag{74}$$

The furnace is surrounded by ceramic insulation with a thickness of 0.2 m. At the bottom, the ceramic insulation is replaced by bricks on which the thermal load can be placed (see Section 3.1.2).

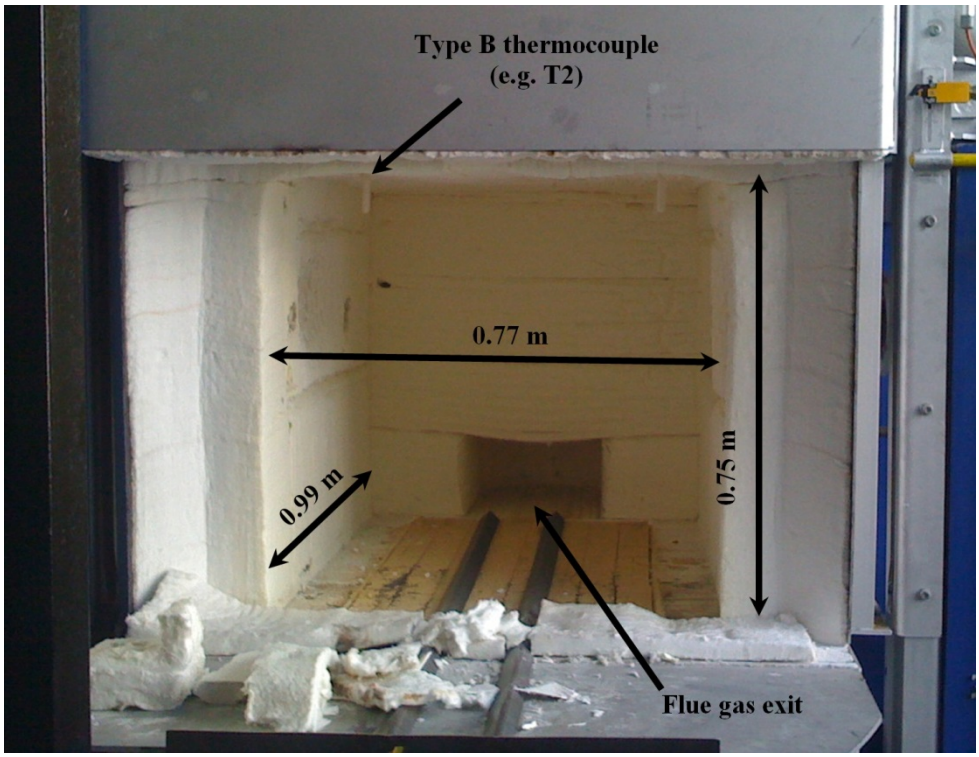

Fig. 22. Dimensions of the lab-scale furnace.

The furnace is equipped with three “Messer Oxipyr®-Flex” (see Fig. 23) burners for natural gas combustion with a maximum fuel input of 33 kW per burner. The resulting flame is a non-premixed diffusion jet flame with a turbulent fluid flow. Natural gas is supplied by a central tube with a diameter of 3.5 mm and the oxidant is supplied by an annulus with an inner and outer diameter of 10.5 and 15 mm, respectively. Two burners are positioned on the left wall and one on the right wall. All burners are lowered 70 mm into the ceramic insulation (see Fig. 24 and Fig. 25). The burners are 0.5 m from the bottom of the furnace. According to the axis displayed in Fig. 24 and Fig. 25, burner 2 is at $z = 0\,m$. Burner 1 and 3 are at $z = 0.25\,m$ and $z = -0.25\,m$. The N_2/O_2 mixture was prepared by mixing air and pure oxygen before entering the burner.

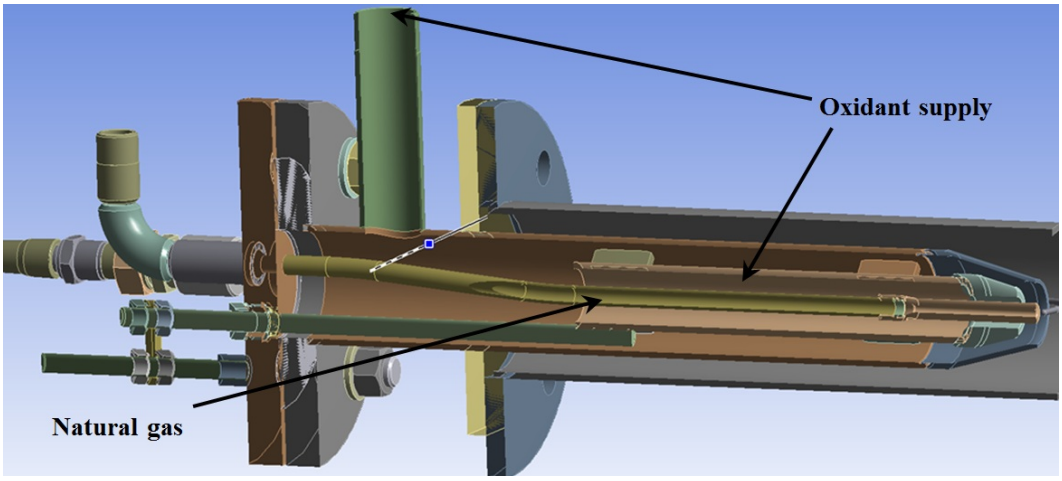

Fig. 23. CAD model of the burner in the lab-scale furnace.

Seven thermocouples were arranged for temperature measurement inside the furnace (see Fig. 24 and Fig. 25). The red coloured thermocouples are inserted into the furnace through the insulation of the top wall (e.g. T2 in Fig. 22). Thermocouples T4 and T7 are inserted through the right and left walls and are coloured in green. Thermocouple T5 is inserted through the front door. The positions of all thermocouples, related to the coordinate system in Fig. 24 and Fig. 25, are given in Table 3. The coordinate system is placed in the centre of the combustion chamber. All thermocouples (except T5) are encapsulated by a ceramic material.

Table 3
Position and types of thermocouples in the lab-scale furnace.

	T1	T2	T3	T4	T5	T6	T7
x-coordinate [m]	0.290	-0.290	0.290	0.315	-0.285	0.290	-0.375
y-coordinate [m]	0.325	0.305	0.310	-0.135	-0.325	0.220	0.125
z-coordinate [m]	-0.250	0.000	0.250	-0.250	0.445	0.000	0
Thermocouple Type	B	B	B	B	K	B	B

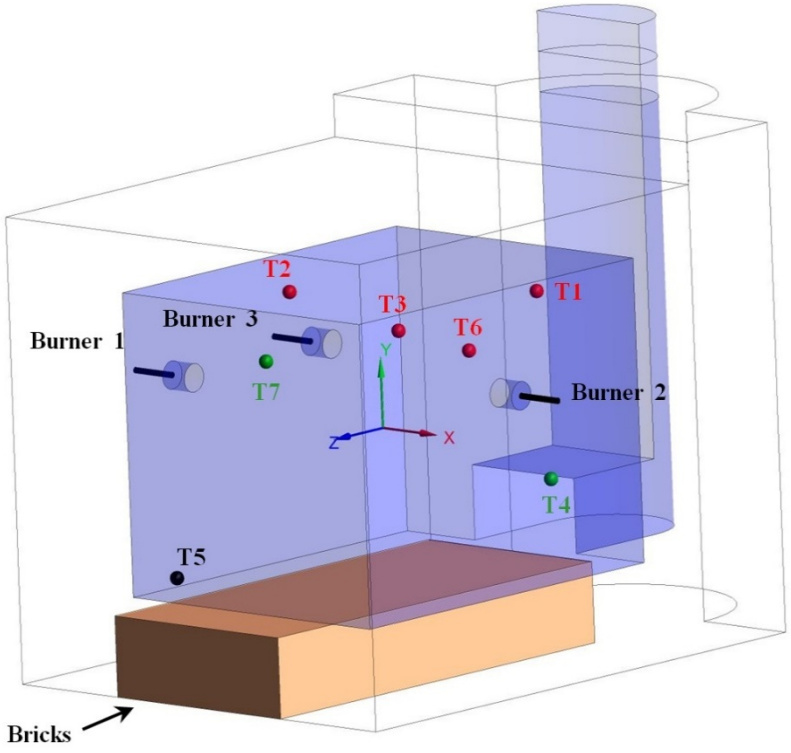

Fig. 24. 3D model lab-scale furnace.

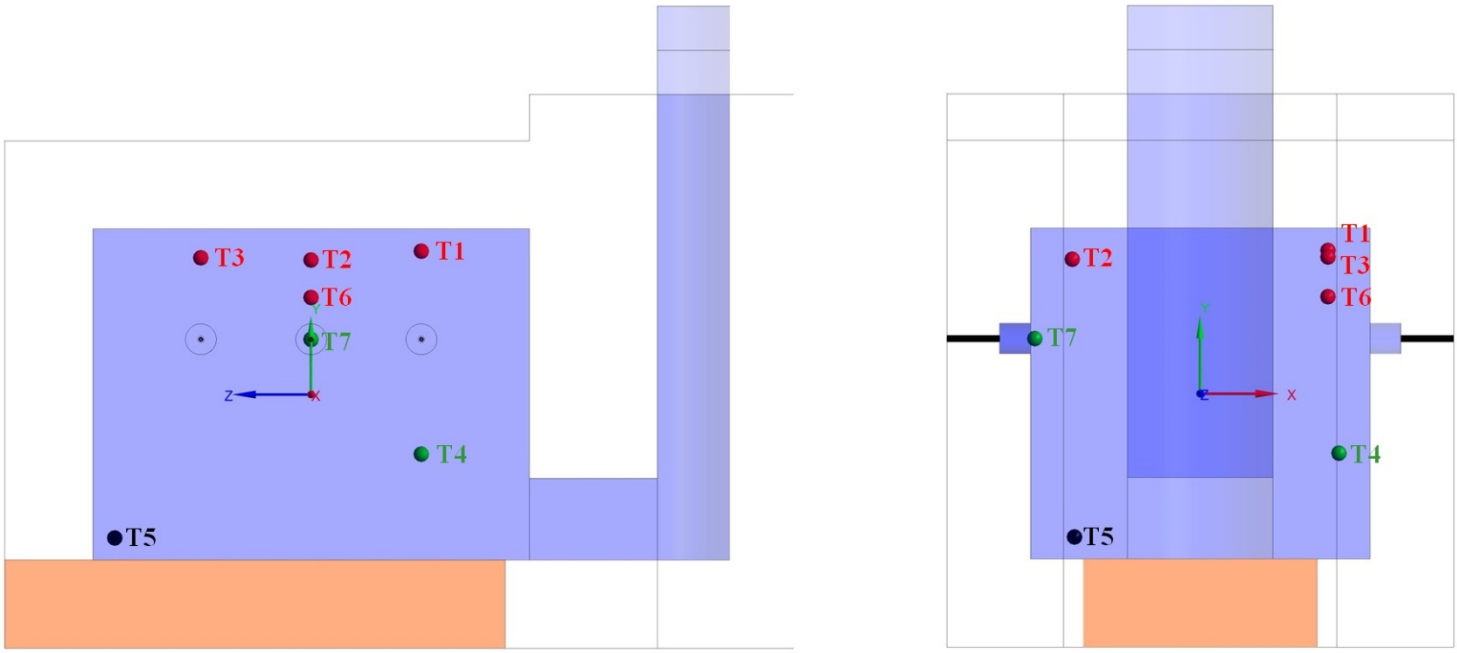

Fig. 25. Side (left) and front (right) view of the lab-scale furnace.

3.1.1 Experiments without thermal load

Experiments without a thermal load were done to investigate the effect of different numerical models for OEC. The furnace was operated with only burner 2 activated (see Fig. 22). To prevent damage, burners 1 and 3 were removed from the furnace during these tests. The experiments are summarized in Table 4. One test run was carried out with a fuel input of 11.5 kW and pure oxygen, so-called “1-OXY”. A second test run was done for 5 different OEC cases with varying O_2 concentrations in the oxidant from 21 to 100% O_2 (called “2-OEC”). The goal was to keep the furnace at a fixed temperature level indicated by thermocouple T5 with a value of approximately 1090 °C.

Table 4
Operating conditions for the experiments without load.

	Fuel input [kW]	**O_2 in the oxidant [%]**	**Equivalence ratio Φ [-]**	**O_2 in the dry flue gas [%]**
1-OXY				
1-OXY_100	11.5	100	1.075	1 ... 4
2-OEC				
2-OEC_100	16.0	100	1.17	5.76
2-OEC_45	16.0	45	1.0	3.74
2-OEC_30	16.0	30	1.0	2.38
2-OEC_25	16.5	25	1.0	1.99
2-OEC_21	18.0	21	1.0	2.00

Although the experiments were done under a positive pressure inside the furnace, air leaking could not be avoided completely (which is also true for experiments with thermal load). Since the positive pressure was measured at one position at the rear end of the furnace, it cannot be guaranteed that a positive pressure was also achieved at the front door. Air leakage was determined by measuring the O_2 concentration in the dry flue gas. Due to the stoichiometric and fuel-rich conditions, no O_2 should be detected in the flue gas. The highest amount of air leakage was detected for combustion with pure oxygen ("2-OEC_100"), with an O_2 concentration of 5.76 % in the dry flue gas. Due to the lack of nitrogen, a lower amount of flue gas is available, which hampers the effort to keep positive pressure in the entire furnace. For OEC between 21 and 30 % O_2 in the oxidant it was possible to keep the air leakage at a moderate level, indicated by an O_2 concentration of approximately 2 % in the flue gas.

One experiment was carried out to identify possible regions of air leakage (not listed in Table 4). During this experiment air leakage was examined with thermal images of the furnace while it was being operated under a much higher positive pressure than 0.4 mbar. Such high pressure was achieved by closing the flue gas duct with a porous material. As a consequence, the hot flue gas exits the furnace through small gaps and can reveal possible air leakage by thermal images, as displayed in Fig. 26. The images indicated that small gaps between the front door and the furnace, as well as the installation of burner 1, are mainly responsible for the air leakage.

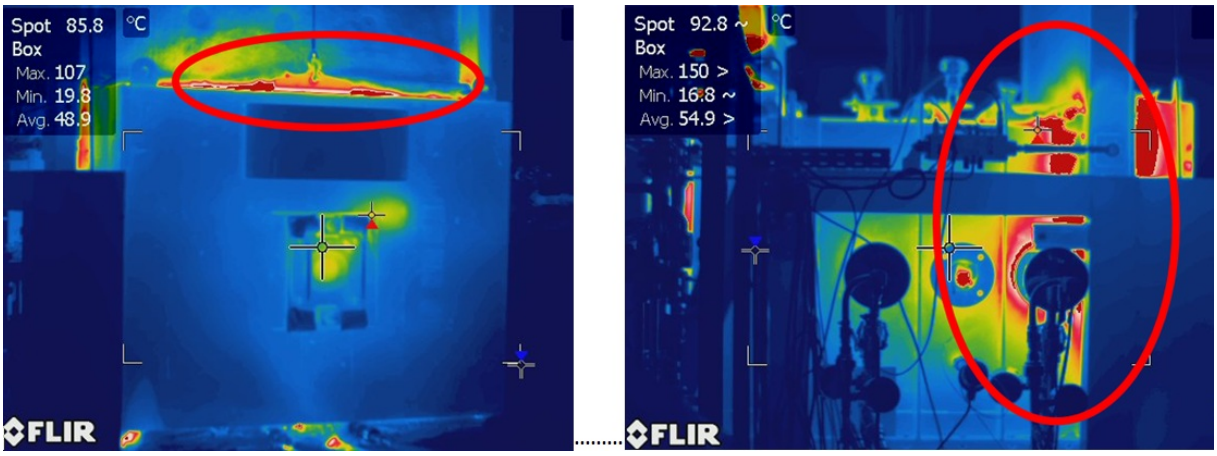

Fig. 26. Thermal images of the lab-scale furnace; left: front view; right: view from the left side.

The operating conditions already reveal the potential of OEC for fuel savings. With a detailed look at the cases "2-OEC_21", "2-OEC_25" and "2-OEC_30", where the air leakage is almost constant (2% O_2 in the flue gas), fuel consumption can be reduced from 18 kW to 16 kW with 30 % O_2 in the oxidant to achieve 1090 °C at T5. Further fuel savings at higher O_2 concentrations were not achieved due to increased air leakage.

3.1.2 Experiments with thermal load

The thermal load inside the furnace was simulated by a water-cooled copper plate with dimensions of 0.4 x 0.4 x 0.05 m. It was arranged in the middle of the furnace with a distance of approximately 0.8 m from the front door (see Fig. 27). All three burners were activated for the experiments with load.

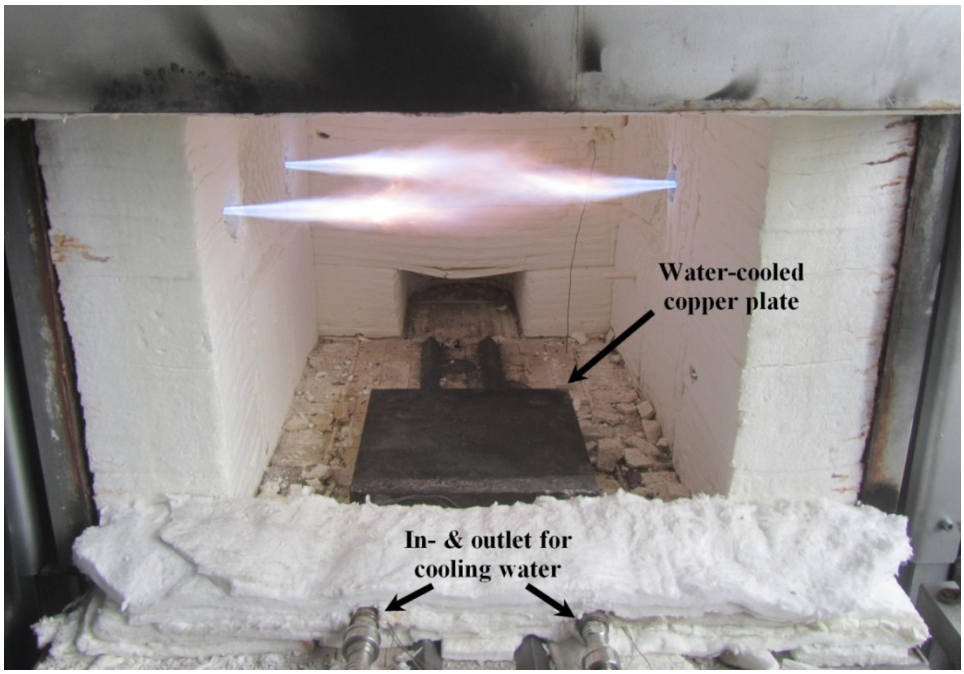

Fig. 27. Lab-scale furnace with thermal load.

The surface of the plate was coated with soot from a fuel-rich natural gas flame to achieve maximum emissivity. Water supply was maintained by tubes below the front door. The copper plate was equipped with measuring instruments for the temperature of the cooling water before and after the plate as well as the volume flow-rate to determine the overall heat fluxes. During the experiments four Type K thermocouples were placed 10 mm below the upper surface of the copper plate. Two test runs with thermal load were done at temperature levels of 1000 and 1220 °C indicated by T4. Similar to the experiments without load, the fuel input was adapted to achieve the desired temperature levels of 1000 and 1220 °C, respectively. The operating conditions are summarized in Table 5. It can be seen that all experiments (except 1220-OEC_30) were carried out with an equivalence ratio of 1 or higher, which determines stoichiometric or fuel-lean conditions. Hence, O_2 concentration in the flue gas should be zero. However, air leakage led to higher O_2 concentrations in the flue gas than expected.

Table 5
Operating conditions for the experiments with thermal load.

	Fuel input [kW]	**O_2 in the oxidant [%]**	**Equivalence ratio Φ [-]**	**O_2 in the dry flue gas [%]**
1000-OEC				
1000-OEC_100	42.5	100	1.020	8.12
1000-OEC_45	41.7	45	1.0	2.34
1000-OEC_30	43.0	30	1.0	2.45
1000-OEC_25	46.8	25	1.0	2.7
1000-OEC_21	51.0	21	1.0	2.29
1220-OEC				
1220-OEC_100	74.8	100	1.042	4.24
1220-OEC_45	87.6	45	1.020	3.31
1220-OEC_30	97.0	30	0.980	2.04
1220-OEC_25	---	---	---	---
1220-OEC_21	---	---	---	---

At a temperature of 1220 °C, it was not possible to operate the furnace with an oxygen concentration below 30 % in the oxidant because a fuel input higher than 99 kW would be needed to achieve 1220 °C. Such a fuel input would exceed the burner limit of 33 kW.

3.2 Industrial walking hearth furnace

This furnace is used for reheating steel billets for the further deformation process on a rolling mill in the steel industry. In this kind of furnace, the billets are placed on stationary refractory blocks (hearths). In Fig. 28, the steel billets can be observed through an inspection window before they are discharged from the furnace. In the background of Fig. 28, the discharge door of the furnace can be seen. The movement of the load is done by moving or walking hearths, which raise the billets and transport them towards discharging with a distinct step size. After this movement, the billets are placed on the stationary hearths again. The residence time of the load in the furnace can be adapted by the distance between the two positions at the stationary hearths (step size) and the time between the billet movements. A detailed overview of continuous industrial furnace designs and equipment is given in [79; 103].

Fig. 28. Steel billets on the stationary hearths right before discharging (discharging door in the background).

A 3D model of the furnace and burner and a schematic description of the walking hearth furnace are given in Fig. 29 and Fig. 30, respectively. Because the furnace is symmetrical, only one half of the furnace is displayed in Fig. 29. The furnace has dimensions of approximately 17 x 13 x 1.6 m and is divided into two parts by a water-cooled plate, which passes through the entire width of the furnace. According to Eq. (74), the mean beam length for each half of the furnace is 2.2 m. Eight burners (yellow) are placed in the first half of the furnace, which represents the pre-heating zone. The second half is further subdivided into a heating zone (red) and soaking zone (orange) with 24 and 16 burners, respectively, resulting in a total number of 48 burners. All of the burners are placed on the ceiling and have a non-premixed fuel and oxidant supply. Natural gas enters the burner through the central tube with an ambient temperature of 25 °C, whereas the oxidant is injected into the fuel stream with a

tangential velocity component, in order to obtain a swirl and assure the better mixing of fuel and oxidant. The oxidant is pre-heated to 310 °C by a recuperator system. For the test runs, the furnace was operated with 25 % O_2 in the oxidant and air-fuel combustion. The average operating conditions for both cases are given in Table 6, and were observed over a one hour period. After the reheating process, a target temperature of between 1150 and 1200 °C has to be achieved at the surface.

Table 6
Operating conditions of the walking hearth furnace.

	Air-fuel	**OEC (25% O_2)**
Fuel (natural gas)		
Pre-heating [MW]	3.99 (21.9 %)	4.11 (22.4 %)
Heating [MW]	10.80 (59.4 %)	11.10 (60.5 %)
Soaking [MW]	3.40 (18.7 %)	3.15 (17.1 %)
Total [MW]	**18.19 (100 %)**	**18.36 (100 %)**
Equivalence ratio Φ [-]	0.97	0.97
O_2 in the dry flue gas [%]	0.7	0.8
Production rate [t/h]	47.428	52.668
Specific fuel consumption [Nm^3/t]	38.35	34.85

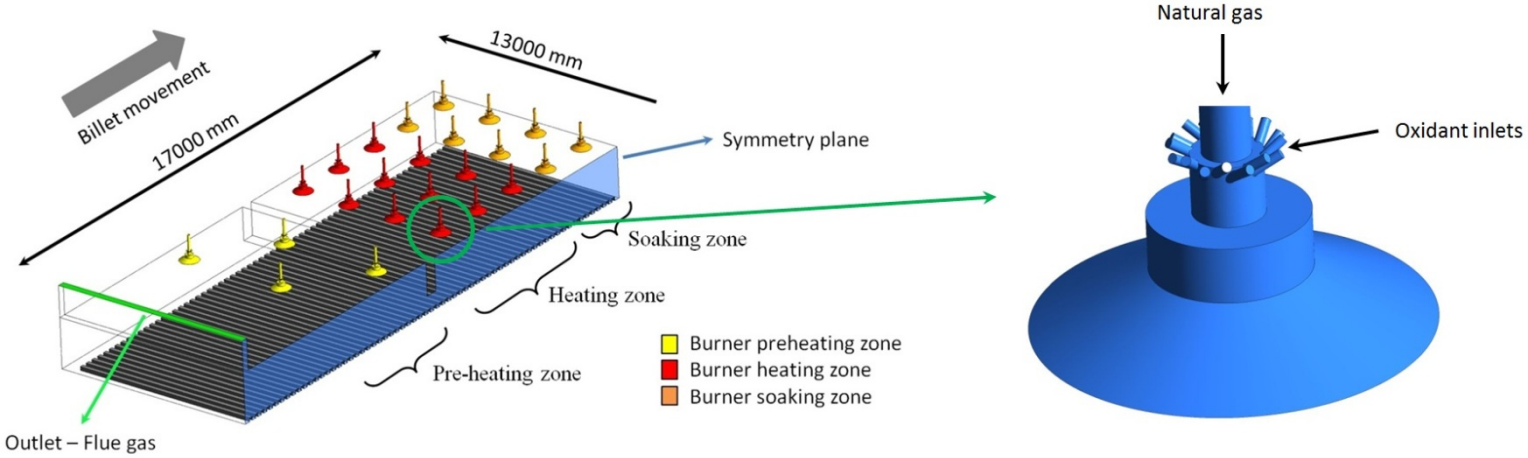

Fig. 29. Left: 3D model of the walking hearth furnace; Right: Detailed view of the burner [107].

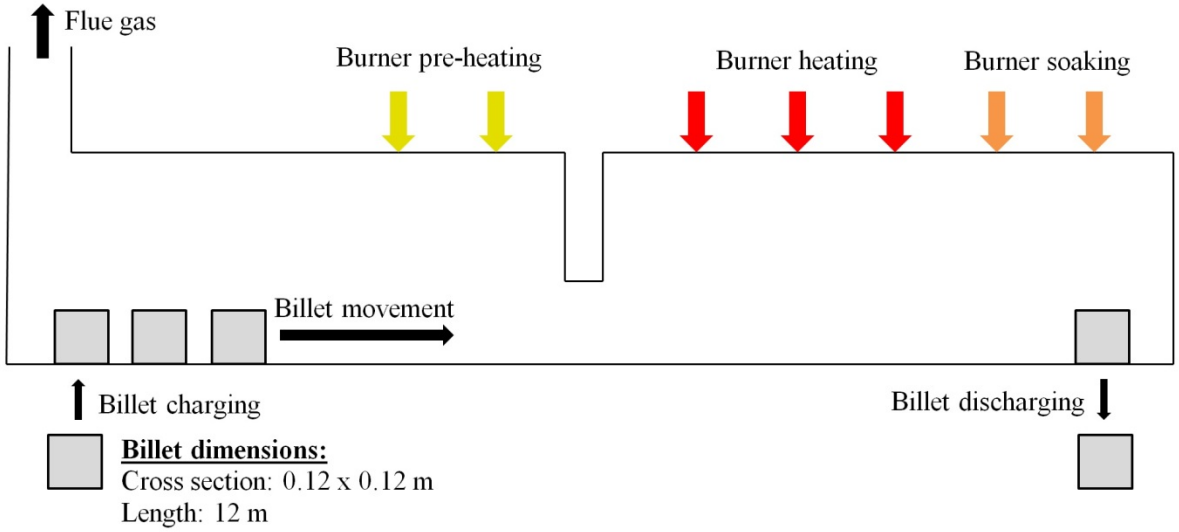

Fig. 30. Schematic overview about the furnace operation [108].

The low-alloy steel billets, with dimensions of 0.12 x 0.12 x 12 m, are loaded into the furnace with a temperature of 20 °C and moved in counter-current to the flue gas. During furnace operation, 64 billets were charged. Upon discharging, the target surface temperature of the billet should be within the range of 1150 and 1200 °C, with a homogenous temperature distribution within the billets. The density of the low-alloy steel was 7800 kg/h before charging. The thermal conductivity and specific heat of the steel were determined with JMatPro [104] and are displayed in Fig. 31.

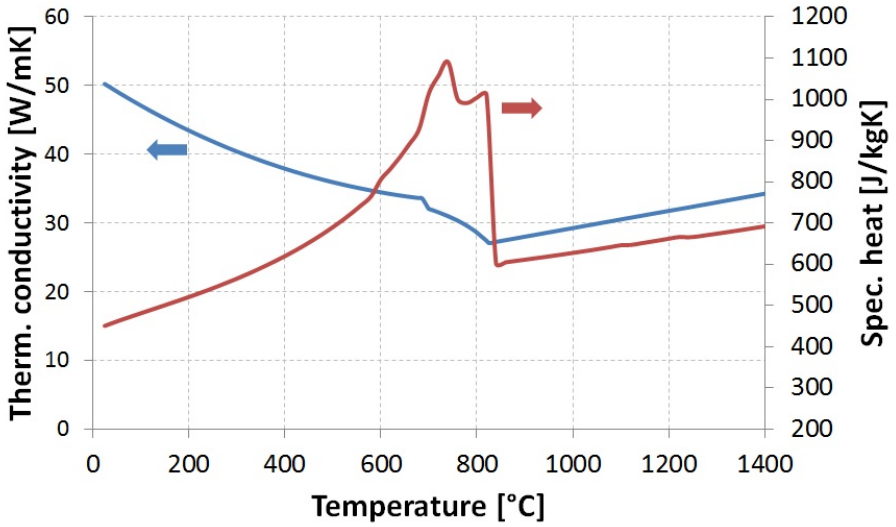

Fig. 31. Thermal conductivity and specific heat of the low-alloy steel.

For the furnace control, four thermocouples are arranged inside the furnace. In the pre-heating and heating zone, one thermocouple is placed in the middle of each zone. The soaking zone is equipped with two thermocouples. During furnace operation, the temperatures of the side walls and of the burner walls are measured for air-fired and oxygen enriched conditions.

4 Numerical simulation

This section provides an overview of the governing transport equation and the basic theory of modelling turbulent flows (see Section 4.1 and 4.2). More detailed information about numerical methods in fluid dynamics can be found in the relevant literature, for example, Ferziger and Peric [105], Poinsot [106] and Moukalled [107]. In Section 4.3, the combustion models and reaction mechanisms used in this thesis are explained. Turbulence/chemistry interaction models are described and the different ways of calculating the source terms of chemical reactions are examined. The radiation models, including the modelling of the radiative properties of the flue gas, are given in Section 4.4. Finally, the numerical grids of the lab-scale furnace and the walking hearth furnace are displayed in Section 4.5.

4.1 Flow modelling

The basic idea of the finite volume method (FVM) for use in computational fluid dynamics (CFD) is that the domain considered is subdivided into a finite number of control volumes (CV), as displayed in Fig. 32. According to continuum mechanics, for each control volume, conservation equations for mass, momentum, energy and other scalars, such as species concentrations, can be solved by numerical methods.

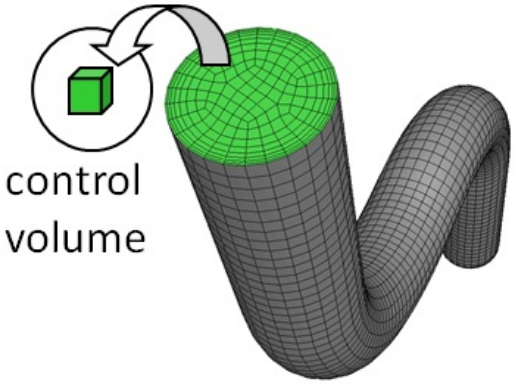

Fig. 32. Discretization of the simulation domain in control volumes [113; 114].

In general, the conservation equation for transport property ϕ can be written as expressed in Eq. (75) (integral form) and Eq. (76) (differential form), where $\vec{v}$ is the vector of the velocity, Γ is the diffusion coefficient, $\vec{n}$ a unit vector normal to the surface of the CV and ω_ϕ is the source or sink for ϕ. In these equations, the terms on the left hand side represent the time

dependent variation within the CV, and the convective flux of ϕ through the surface of the CV. On the right hand side, the first term represents the diffusive flux through the boundaries of the CV and the last term is the generation/destruction of ϕ (including body forces).

$$\frac{\partial}{\partial t}\int_{V_{CV}} \rho\phi dV_{CV} + \int_{S_{CV}} \rho\phi\vec{v}\cdot\vec{n}dS_{CV} = \int_{S_{CV}} \Gamma\nabla\phi\cdot\vec{n}dS_{CV} + \int_{V_{CV}} \omega_\phi V_{CV} \tag{75}$$

$$\frac{\partial(\rho\phi)}{\partial t} + \nabla\cdot(\rho\phi\vec{v}) = \nabla\cdot(\Gamma\nabla\phi) + \omega_\phi \tag{76}$$

4.1.1.1 Conservation of mass

The differential form of the conservation equation for the mass, which is the so-called continuity equation, is given in Eq. (77). In this case, the fluid variable ϕ becomes one. Since the continuity equation has to be solved for each phase in a multi-phase flow, the mass exchange between the phases can lead to source or sink terms for a phase on the right hand side.

$$\frac{\partial\rho}{\partial t} + \nabla\cdot(\rho\vec{v}) = 0 \tag{77}$$

4.1.1.2 Conservation of momentum

The conservation equation for momentum is given in Eq. (78), where τ is the stress tensor and $\vec{g}$ is the gravitational vector. Again, the terms on the left hand side are the transient and convective terms of the conservation equation. On the right hand side, the terms represent the forces on the CV resulting in normal and shear stresses as well as the gravitational force.

$$\frac{\partial(\rho\vec{v})}{\partial t} + \nabla\cdot(\rho\vec{v}\vec{v}) = -\nabla p + \nabla\cdot\tau + \rho\vec{g} \tag{78}$$

For a three-dimensional Cartesian coordinate system, the stress tensor is a 3 x 3 matrix given in Eq. (79), where the normal e.g., τ_{ii} (excluding pressure) and shear stresses e.g., τ_{ij} on the surface of the CV are listed.

$$\tau = \begin{pmatrix} \tau_{xx} & \tau_{xy} & \tau_{xz} \\ \tau_{yx} & \tau_{yy} & \tau_{yz} \\ \tau_{zx} & \tau_{zy} & \tau_{zz} \end{pmatrix} \tag{79}$$

The stresses in a Newtonian fluid are a linear function of the strain rate and can be expressed as in Eq. (80), where μ is the dynamic viscosity and I is the identity matrix (3 x 3).

$$\tau = \mu\left[(\nabla\vec{v} + (\nabla\vec{v})^T) - \frac{2}{3}(\nabla\cdot\vec{v})I\right] \tag{80}$$

Furthermore, it should be assumed that the flow is incompressible and that the material properties (density, viscosity) are constant. This leads to the conservation equation for the momentum also known as Navier-Stokes equation (see Eq. (81)).

$$\frac{\partial(\rho\vec{v})}{\partial t} + \nabla \cdot (\rho\vec{v}\vec{v}) = -\nabla p + \mu\nabla^2\vec{v} + \rho\vec{g} \tag{81}$$

4.1.1.3 Conservation of energy

The conservation equation for the energy is given in Eq. (82), where e is the energy, λ is the thermal conductivity, h_k and $\vec{J}_k$ are the enthalpy of the component k and the diffusive flux of the component through the boundaries of the CV (see Eq. (83) and (84)). The diffusive flux $\vec{J}_k$ comprises mass diffusion and diffusion according to the Soret effect as written in Eq. (84). In this equation D_k and $D_{k,T}$ are the diffusion coefficients for the component k and Sc_t is the turbulent Schmidt number with a default value of 0.7. The turbulent viscosity is denoted by μ_t and is further defined in Eq. (92). The source term for the energy is represented by ω_e, which has to be determined by the combustion and radiation model in the CFD simulation. Here, the terms on the right hand side stand for the energy as a result of the pressure and stresses on the CV, the heat flux to the CV by thermal conductivity, and the enthalpy by diffusive flux of a component k.

$$\frac{\partial(\rho e)}{\partial t} + \nabla \cdot (\rho\vec{v}e) = -\nabla \cdot (p\vec{v}) + \nabla \cdot (\tau \cdot \vec{v}) - \nabla \cdot (\lambda\nabla\mathrm{T}) - \nabla \cdot \sum_k h_k\vec{J}_k + \omega_e \tag{82}$$

The energy equation can also be written in terms of enthalpy, internal energy or temperature using Eq. (83) and Eq. (85).

$$h_k = \int_{T^0}^{T} c_p * dT \tag{83}$$

$$\vec{J}_k = -\underbrace{\left(\rho * D_k + \frac{\mu_t}{Sc_t}\right) * \nabla Y_k}_{laminar\ and\ turbulent\ mass\ diffusion} - \underbrace{D_{k,T} * \frac{\nabla T}{T}}_{thermophoresis\ (Soret\ effect)} \tag{84}$$

$$e = h - \frac{p}{\rho} + \frac{\vec{v}}{2} \tag{85}$$

4.1.1.4 Conservation equation for species

In the conservation equation for the species or component k in a gas mixture, the transient, convective, diffusive and source terms are used. The source term for the component has to be modelled by the combustion model (chemistry).

$$\frac{\partial(\rho Y_k)}{\partial t} + \nabla \cdot (\rho Y_k \vec{v}) = -\nabla \cdot \vec{J}_k + \omega_{Y_k} \tag{86}$$

4.2 Turbulence modelling

The turbulent flow in industrial furnaces, especially in the vicinity of the burner, is determined by fluctuations of the velocity components, which affect mass, momentum and energy transfer as well as the mixing process in a multi-component system. These fluctuations arise from eddies in the turbulent flow, which are formed by shear stress in the fluid and between the fluid and wall. Generally, the instantaneous value of a variable ϕ is calculated by the mean value $\bar{\phi}$ and the fluctuating value ϕ' as given in Eq. (87). Furthermore, the mean value for a statistical steady-state fluid flow is defined in Eq. (88).

$$\phi = \bar{\phi} + \phi' \tag{87}$$

$$\bar{\phi} = \lim_{t\to\infty} \frac{1}{t} \int_0^t \phi * dt \tag{88}$$

A turbulent fluid flow can occur at different length scales depending on the energy transported by the eddies. Larger eddies can interact and break-up into smaller ones due to absorbed energy. At the smallest length scale, the absorbed energy dissipates. The flux of energy from larger eddies to the smallest turbulent structure and the final dissipation is called energy cascade.

Solving of the transport equations for a turbulent flow can be computationally demanding depending on the desired resolution of the smallest turbulent structures (eddies). Direct numerical simulations (DNS) resolve the smallest eddies within a flow field, where the full instantaneous Navier-Stokes equations are solved. Only errors can arise from the discretization of the domain, which can be controlled by a fine grid. Because larger eddies have more energy and a more significant influence on the fluid flow, these are the most worthy of consideration (see Fig. 33). This approach is called large eddy simulation (LES). With LES, smaller structures are modelled and the computational grid is coarser than for the DNS. The application of DNS and LES is limited to small scale furnaces and flames, which results in long calculation times.

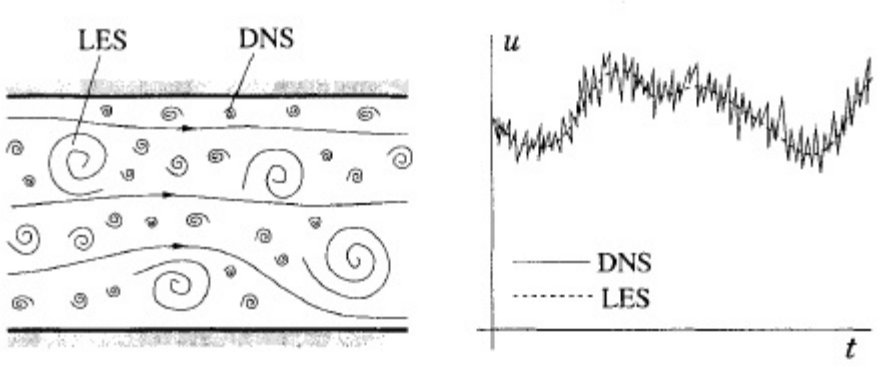

Fig. 33. Turbulent motion and eddies in a flow field (left) and the fluctuating velocity component [110].

In this thesis, the turbulence modelling was done using the Reynolds–averaged Navier-Stokes (RANS) equations to simulate the turbulent fluid flow. This approach models the turbulent eddies, and time dependent fluctuations in the fluid flow are not considered. In Fig. 34, the length scales of the eddies, which can be resolved by the approaches mentioned, are displayed schematically.

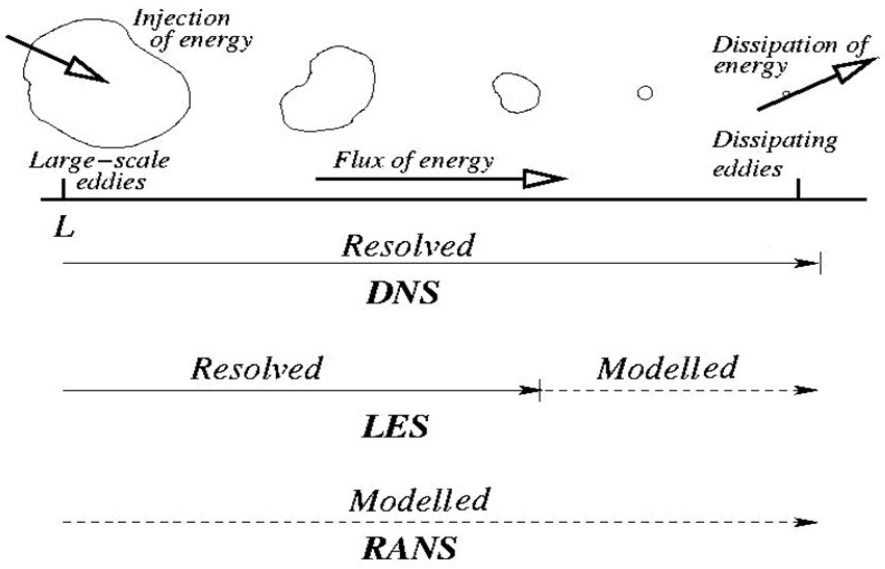

Fig. 34. Length scales ***L*** of resolved eddies for different numerical approaches to solve the conservation equations [114; 115].

The Reynolds averaging is done according to Eq. (87), leading to the Reynolds-averaged Navier-Stokes equations. The RANS equations for mass and momentum is given in Eq. (89) and (90) for an incompressible. This can be extended to the conservation equations for energy and species, but is not discussed in detail here. As a consequence of the averaging procedure, unclosed terms (Reynolds stresses) emerge in the momentum equation, which must be modelled.

$$\frac{\partial \rho}{\partial t} + \nabla \cdot \left(\rho \vec{\bar{v}}\right) = 0 \tag{89}$$

$$\frac{\partial \left(\rho \vec{\bar{v}}\right)}{\partial t} + \nabla \cdot \left(\rho \vec{\bar{v}} \vec{\bar{v}}\right) = -\nabla \bar{p} + \nabla \cdot \tau - \nabla \cdot \left(\underbrace{\rho \overline{\overrightarrow{v'}\,\overrightarrow{v'}}}_{Reynolds\ sresses} \right) + \rho \vec{g} \tag{90}$$

In turbulent applications, the fluctuation of flow variables such as pressure and temperature result in a variation of the density. Therefore, the mass may be not conserved by means of Reynolds averaging method. To handle this difficulty, mass-weighted averages of the variables (scalars) in the flow field are introduced (Favre average). The conservation equations are solved for the Favre-averaged values of velocity, temperature, etc.

Strategies for modelling the Reynolds stresses are subdivided into:

- Boussinesq approaches (zero-, one- and two-equation models)
- Reynolds stress model (RSM; Modelling of the components of the stress tensor)

The CFD simulations were carried out with two different two-equation models and the RSM for turbulence modelling, which are described briefly in the following sections.

4.2.1 Standard k-epsilon model

The standard k-epsilon model [108] is a two-equation model for the approximation of the Reynolds stresses. Since the robustness of the standard k-epsilon model means it is used in a wide range of applications, it was selected for the simulations in this thesis. It is assumed that the Reynolds stresses can be calculated according to the Boussinesq hypothesis in Eq. (91), where μ_t is the turbulent (eddy) viscosity, k is the turbulent kinetic energy, and δ_{ij} is the Kronecker delta.

$$-\rho \overline{\overrightarrow{v'}\,\overrightarrow{v'}} = \mu_t \left(\nabla \vec{\bar{v}}\right) - \rho \frac{2}{3} k \delta_{ij} \tag{91}$$

The turbulent viscosity is modelled by Eq. (92), where C_μ is a model constant and ε is the dissipation rate.

$$\mu_t = \rho C_\mu \frac{k^2}{\varepsilon} \tag{92}$$

In addition to the conservation equations for mass, momentum, energy and species, transport equations for the turbulent kinetic energy k and the dissipation rate ε have to be solved. The equations are given in Eq. (93) and Eq. (94), written with the Einstein notation. In these equations, G_k and G_b represent the generation of the turbulent kinetic energy due to velocity

gradients (see Eq. (95)) and buoyancy effects (see Eq. (96)), where Pr_t is the turbulent Prandtl number. In Eq. (97) the thermal expansion coefficient is defined.

$$\frac{\partial}{\partial x_i}(\rho k u_i) = \frac{\partial}{\partial x_j}\left[\left(\mu + \frac{\mu_t}{Pr_k}\right)\frac{\partial k}{\partial x_j}\right] + G_k + G_b - \rho\varepsilon \tag{93}$$

$$\frac{\partial}{\partial x_i}(\rho \varepsilon u_i) = \frac{\partial}{\partial x_j}\left[\left(\mu + \frac{\mu_t}{Pr_\varepsilon}\right)\frac{\partial \varepsilon}{\partial x_j}\right] + C_{1\varepsilon}\frac{\varepsilon}{k}(G_k + C_{3\varepsilon}G_b) - C_{2\varepsilon}\rho\frac{\varepsilon^2}{k} \tag{94}$$

$$G_k = -\rho\overline{u_i' u_j'}\frac{\partial u_j}{\partial x_i} \tag{95}$$

$$G_b = \beta g_i \frac{\mu_t}{Pr_t}\frac{\partial T}{\partial x_i} \tag{96}$$

$$\beta = -\frac{1}{\rho}\left(\frac{\partial \rho}{\partial T}\right)_p \tag{97}$$

The model constants have default values defined in [108; 109], which are summarized in Table 7.

Table 7
Values for the model constants used in the standard k-epsilon model.

Model constant	Value
C_μ	0.09
Pr_k	1.0
Pr_ε	1.3
$C_{1\varepsilon}$	1.44
$C_{2\varepsilon}$	1.92

In equation (94), the variable $C_{3\varepsilon}$ is calculated according to Eq. (98), where v and u are the velocity components parallel and perpendicular to the gravitational vector [110].

$$C_{3\varepsilon} = \tanh\left|\frac{v}{u}\right| \tag{98}$$

4.2.2 Realizable k-epsilon model

The realizable k-epsilon model, proposed by Shih et al. [111], is similar to the standard k-epsilon model, with the main differences being the modelling of the turbulent viscosity, the turbulent Prandtl number and a modified transport equation for the dissipation rate ε (see (99)). Modelled parameters in Eq. (99) are given in Eqs. (100) to (102).

$$\frac{\partial}{\partial x_i}(\rho\varepsilon u_i) = \frac{\partial}{\partial x_j}\left[\left(\mu + \frac{\mu_t}{\sigma_\varepsilon}\right)\frac{\partial \varepsilon}{\partial x_j}\right] + \rho C_1 S\varepsilon - \rho C_2 \frac{\varepsilon^2}{k + \sqrt{\nu\varepsilon}} + C_{1\varepsilon}\frac{\varepsilon}{k}C_{3\varepsilon}G_b \quad (99)$$

$$C_1 = max\left[0.43, \frac{\eta}{\eta + 5}\right] \quad (100)$$

$$\eta = S\frac{k}{\varepsilon}, \qquad S = \sqrt{2S_{ij}S_{ij}} \quad (101)$$

$$S_{ij} = \frac{1}{2}\left(\frac{\partial u_j}{\partial x_i} + \frac{\partial u_i}{\partial x_j}\right) \quad (102)$$

The realizable k-epsilon model has already been tested for a wide range of applications given in Kim et al. [112]. It is an improved k-epsilon model compared to the standard k-epsilon model with regard to high streamline curvatures and spreading rates in an axisymmetric jet [109]. This is a result of the different formulation of the transport equation for the dissipation and the turbulent viscosity, where C_μ is not a constant compared to the standard k-epsilon model. This model parameter is now calculated based on an eddy viscosity formulation from Reynolds [113] and can be found in [109]. All model constants used in the realizable k-epsilon model are summarized in Table 8.

Table 8
Values for the model constants used in the realizable k-epsilon model.

Model constant	Value
Pr_k	1.0
Pr_ε	1.2
C_2	1.9
$C_{1\varepsilon}$	1.44

4.2.3 Reynolds stress model (RSM)

The Reynolds stress model is the most sophisticated approach to solving the RANS equations. The Reynolds stresses are determined by solving a transport equation for each component of the stress tensor. Therefore, a large amount of both computational time and memory size are needed to achieve a converged solution of the turbulent fluid flow. In contrast to the eddy-viscosity approach in the k-epsilon model, the RSM considers anisotropic behaviour of complex flows with high streamline curvature (swirls), rapid changes of the strain rate, etc. [105; 114; 115; 116]. The Transport equation for the Reynolds stress is given in Eq. (103), where $\tau_{ij} = \rho\overline{u_i' u_j'}$ is the Reynolds stress tensor. In this equation, the terms for the dissipation tensor, turbulent diffusion and the pressure-strain have to be modelled, which is done using

the dissipation rate. As a consequence, seven transport equations are used (six stresses, one dissipation rate) for the turbulence modelling with the RSM [105].

$$\underbrace{\frac{\partial \tau_{ij}}{\partial t}}_{time\ derivative} + \underbrace{\frac{\partial\left(\bar{u}_k \tau_{ij}\right)}{\partial x_k}}_{convective\ term} = \underbrace{-\left(\tau_{ik}\frac{\partial \bar{u}_j}{\partial x_k} + \tau_{jk}\frac{\partial \bar{u}_i}{\partial x_k}\right)}_{stress\ production\ term} + \underbrace{\frac{\partial}{\partial x_k}\left(\frac{\mu}{\rho}\frac{\partial \tau_{ij}}{\partial x_k}\right)}_{molecular\ diffusion} + \underbrace{2\mu\overline{\frac{\partial u_i'}{\partial x_k}\frac{\partial u_j'}{\partial x_k}}}_{dissipation\ tensor} + \frac{\partial}{\partial x_k}\left(\underbrace{\rho\overline{u_i' u_j' u_k'} + \overline{p' u_i'}\delta_{jk} + \overline{p' u_j'}\delta_{ik}}_{turbulent\ diffusion}\right) - \underbrace{\overline{p'\left(\frac{\partial u_i'}{\partial x_j} + \frac{\partial u_j'}{\partial x_i}\right)}}_{pressure-strain} \tag{103}$$

4.3 Gas phase combustion

4.3.1 Eddy dissipation model (EDM)

Based on the assumption that the chemistry is infinitely fast compared to the mixing time scale, the combustion process can be reduced to a simple mixing problem. Proposed by Magnussen and Hjertager [117], the EDM predicts the net rate production of a species k for a mixing-limited combustion problem. The characteristic value for the production rate is the large eddy mixing time scale (see Spalding [118]). To predict the net rate production of the component k, the minimum of Eq. (104), reactant mixing rate, and Eq. (105), the product mixing rate, is defined as the species source term.

$$\omega_{k,r} = \nu'_{k,r} M_k A \rho \underbrace{\frac{\varepsilon}{k}}_{\substack{mixing \\ time \\ scale}} min_R\left(\frac{Y_R}{\nu'_{R,r} M_R}\right) \tag{104}$$

$$\omega_{k,r} = \nu'_{k,r} M_k A B \rho \frac{\varepsilon}{k}\frac{\sum_P Y_P}{\sum_j^N \nu''_{j,r} M_j} \tag{105}$$

In these equations, the subscripts r, R and P denote the reaction, reactant and product species, respectively. The model parameters A and B are 4.0 and 0.5, which are default values for conventional combustion problems, have to be adapted for different applications. This was also determined by Edge et al. [119] and Chui et al. [120] for volatile combustion under oxy-

fuel conditions with flue gas recirculation. Due to the high concentration of product species at the burner outlet, the reactant mixing rate was overestimated. Hence, adapted model parameters for oxy-fuel combustion were suggested by Chen et al. [52]. Karimi and Saidi [121] used the EDM for CFD simulations of a reheating furnace with an oxygen enrichment of 60 % and found that the parameter B had to be changed to a value of 2.0. Nevertheless, in this work, the default values were applied because of the different levels of oxygen enrichment, which would require optimized values for each operating condition.

What is remarkable about the EDM is its restriction of the number of reactions. A maximum of two reactions are recommended for consideration because the reaction rates for the reactions can be significantly different due to the Arrhenius rate. For this project, the following reactions were used.

$$CH_4 + 1.5O_2 \rightleftharpoons CO + 2H_2O \quad \text{(R. 11)}$$

$$CO + 0.5O_2 \rightleftharpoons CO_2 \quad \text{(R. 12)}$$

4.3.2 Eddy dissipation concept (EDC)

Due to the high temperature in an OEC flame, the consideration of radical formation requires a multi-step reaction mechanism. The EDC approach is based on the work of Magnussen [122] and has already been used for oxy-coal combustion by many researchers (e.g. [123; 74; 124; 125]). The reaction is assumed to occur in fine scales, where the full chemical reaction mechanism is solved for each iteration step. The length fraction and time scale is defined according to Eq. (106) and (107) [126], with values for the volume fraction constant C_ξ and time scale constant C_t of 2.1377 and 0.4082, respectively.

$$\xi^* = C_\xi \left(\frac{\mu\varepsilon}{\rho k^2}\right)^{1/4} \quad (106)$$

$$t^* = C_t \left(\frac{\mu}{\rho\varepsilon}\right)^{1/2} \quad (107)$$

The source term for a component k is predicted by Eq. (108), where Y_i^* is the fine scale mass fraction.

$$\omega_k = \frac{\rho(\xi^*)^2}{t^*[1-(\xi^*)^3]}(Y_i^* - Y_i) \quad (108)$$

A limitation for the application of the EDC model is the high calculation time needed to integrate the chemistry for each iteration step. The calculation time can be reduced by using

Pope's [127] in-situ adaptive tabulation (ISAT) method. Galletti et al. [124] suggest an ISAT error tolerance of at least 10^{-5}.

4.3.3 Steady laminar flamelet model (SFM)

Another model to simulate the non-premixed combustion process is based on the laminar diffusion flamelet theory, described in Section 2.2.2. The idea of this model, the so-called steady laminar flamelet model (SFM), is that a turbulent flame front can be modelled by a number of laminar counter-flow diffusion flames as shown in Section 2.2.2 [128; 129]. Therefore, the chemistry and the turbulent fluid flow can be handled separately.

In a first step, the small laminar flamelets are simulated with a detailed reaction mechanism. To apply this approach in the CFD simulation, the flamelet equations given in Eq. (63) and (64), are transformed from physical space into the mixture fraction space [130]. Since the mixture fraction shows a monotonic decrease from the fuel side to the oxidant side, it can be used as a quantity to describe the thermochemical state at each point in the flamelet. The simplified flamelet equations in the mixture fraction space, which are used in this work, are given in Eq. (109) and (110) [131]. Here, χ is the scalar dissipation rate that can be seen as the inverse of the diffusion time or the residence time of the fluid, and ρ_∞ is the density at the inlets. When the scalar dissipation is equal to zero, chemical equilibrium has been reached. At higher dissipation rates, the difference to the chemical equilibrium increases. The scalar dissipation varies with the mixture fraction space, and has to be modelled according to Eq. (111), where a_s is the strain rate [132]. A detailed description of the model theory can be found in [109], but it is important to mention that the flamelet assumption is valid for fast chemistry compared to the mixing time scale.

$$\rho \frac{\partial Y_k}{\partial t} = \frac{1}{2}\rho\chi \frac{\partial^2 Y_k}{\partial f^2} + \omega_k \tag{109}$$

$$\rho \frac{\partial T}{\partial t} = \frac{1}{2}\rho\chi \frac{\partial^2 T}{\partial f^2} - \frac{1}{c_p}\sum_k H_k\omega_k + \frac{1}{2c_p}\rho\chi\left[\frac{\partial c_p}{\partial f} + \sum_k c_{p,k}\frac{\partial Y_k}{\partial f}\right]\frac{\partial T}{\partial f} \tag{110}$$

$$\chi = \frac{a_s}{4\pi}\frac{\left(\sqrt{\frac{\rho_\infty}{\rho}}+1\right)^2}{2\sqrt{\frac{\rho_\infty}{\rho}}+1} exp\{-2[erfc^{-1}(2f)]^2\} \tag{111}$$

With the flamelet equations, the temperature and species concentrations in the small flamelet can be predicted quickly, although a detailed reaction mechanism is used. Hence, the integration of the full reaction mechanism during the CFD simulation can be avoided and the

thermochemical state in the flamelet (temperature, species concentrations, density) is defined by the mixture fraction f and the scalar dissipation χ. The calculated results are, dependent on f and χ, are stored in look-up tables (see Section 5.2). In a non-adiabatic case, the instantaneous values for temperature, species concentrations and density are also related on the enthalpy H (see Eq. (112)).

$$\phi = \phi(f, H) \tag{112}$$

In a second step, the instantaneous values for the mixture fraction from the flamelet equations have to be coupled with the turbulent fluid flow using a turbulence/chemistry interaction model. For this purpose, a presumed probability density function (PDF) was applied in this thesis. The PDF represents the relationship between the instantaneous value of a fluctuating scalar and the averaged value as shown in Eq. (113) for a non-adiabatic case. In this equation, $p(f)$ is the presumed PDF, which can be seen as the fraction of time the fluid is in state f in the fluctuating fluid flow. In non-adiabatic cases the PDF should be considered as a joint PDF dependent on the mixture fraction and the enthalpy like $p(f, H)$. Presumed PDF's provide good results when only one parameter is considered (e.g. mixture fraction). In cases with more variables, the generation of multi-dimensional PDF's (e.g. $p(f, H)$) becomes complicated. Therefore it is assumed that the variables are statistically independent, which leads to Eq. (114), where the joint PDF is split to single variable PDF's [106]. Additionally, the enthalpy fluctuations and enthalpy level can be treated as independent [109]. In Eq. (114), δ is the single Dirac PDF, which means that $\overline{H} = H(f)$ and as a consequence only the PDF for the mixture fraction is required.

$$\bar{\phi} = \int_0^1 p(f)\phi(f, \overline{H})\, df \tag{113}$$

$$p(f, H) \approx p(f) * \delta(H - \overline{H}) \tag{114}$$

For the presumed PDF, a so-called β-function was used and was observed in experiments [109]. The shape of the PDF is then defined by the mean mixture fraction $\bar{f}$ and its variance $\overline{f'^2}$ [133], as given in Eq. (115) to (118).

$$f' = f - \bar{f} \tag{115}$$

$$p(f) = \frac{f^{\alpha-1}(1-f)^{\beta-1}}{\int_0^1 f^{\alpha-1}(1-f)^{\beta-1}df} \tag{116}$$

$$\alpha = \bar{f}\left(\frac{\bar{f}(1-\bar{f})}{\overline{f'^2}} - 1\right) \tag{117}$$

$$\beta = (1-\bar{f})\left(\frac{\bar{f}(1-\bar{f})}{\overline{f'^2}} - 1\right) \tag{118}$$

To take the heat losses by radiation etc. into account, several PDF layers, depending on the heat loss/gain, are created. In such a PDF layer, the averaged scalars of temperature, species concentrations and density are only related on the mean value of the mixture fraction and the mixture fraction variance. The PDF's layers for the temperature, calculated with different reaction mechanisms, are displayed in Section 5.4.

The main advantage of this approach is that the entire chemistry can be reduced to a simple mixing problem solved by two additional transport equations, which provide the mean mixture fraction and its variance, given in Eq. (119) and (120), where C_g and C_d are model constants with values of 2.86 and 2.0, respectively. The energy equation for the SFM is displayed in Eq. (121), where λ_t is the turbulent thermal conductivity and $\omega_{\bar{H}}$ is the source term for the enthalpy (e.g. due to radiation). In addition to the predicted values of $\bar{f}$ and $\overline{f'^2}$, the temperature and species concentrations, as well as the density can be found in the look-up tables (see Section 5.4) Thus, the computational expensive integration of the set of chemical reactions can be avoided.

$$\frac{\partial}{\partial t}\left(\rho\overline{f}\right) + \nabla\cdot\left(\rho\vec{v}\overline{f}\right) = \nabla\cdot\left(\frac{\mu_t}{Pr_t}\nabla\overline{f}\right) \tag{119}$$

$$\frac{\partial}{\partial t}\left(\rho\overline{f'^2}\right) + \nabla\cdot\left(\rho\vec{v}\overline{f'^2}\right) = \nabla\cdot\left(\frac{\mu_t}{Pr_t}\nabla\overline{f'^2}\right) + C_g\mu_t\left(\nabla\overline{f}\right)^2 - C_d\rho\frac{\varepsilon}{k}\overline{f'^2} \tag{120}$$

$$\frac{\partial}{\partial t}(\rho\bar{H}) + \nabla\cdot(\rho\vec{v}\bar{H}) = \nabla\cdot\left(\frac{\lambda_t}{c_p}\nabla\bar{H}\right) + \omega_{\bar{H}} \tag{121}$$

4.3.3.1 Limitation of the SFM for OEC

Despite the fast calculation time, the SFM is limited to fast chemistry compared to the mixing time scale. Another limit, related to the burner configuration, was examined by Mayr et al. [134]. These researchers investigated natural gas combustion with pure oxygen in different furnaces with jet flames. One furnace was the lab-scale furnace described in Section 3.1 and

the second was an IFRF furnace with 0.8 MW fuel input, numerically investigated by Yin et al. [74; 135]. These studies noted that the outlet velocities of fuel and oxidant at the burner are crucial for the prediction of an accurate flame with the SFM. The burner configuration of the IFRF furnace leads to a small relative velocity of fuel and oxidant (see Fig. 35), and, as a consequence, small shear rates occur between the streams. Predicted flames in the lab-scale furnace, with higher shear rates, showed a comprehensible flame shape and closely resembled the measurements. This will be examined further in Section 6. At small strain rates, the SFM failed to predict the correct flame shape. In the IFRF furnace, the SFM showed lower temperatures in the vicinity of the burner, whereas the EDC model simulated a temperature profile with significant differences in the near burner region (see Fig. 36).

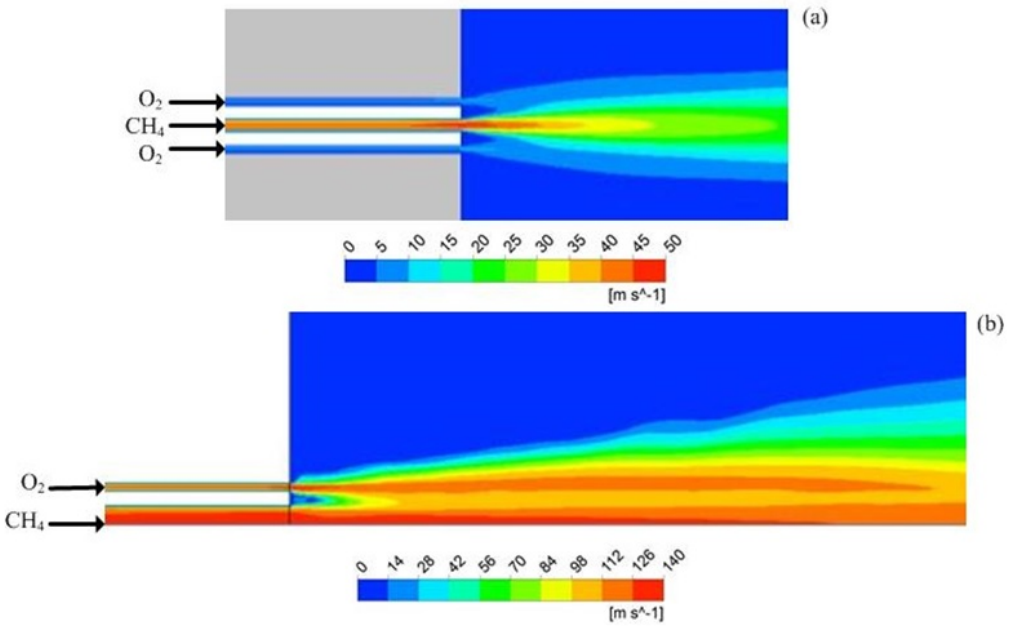

Fig. 35. Velocities at the burner; (a) Lab-scale furnace, (b) IFRF furnace [142].

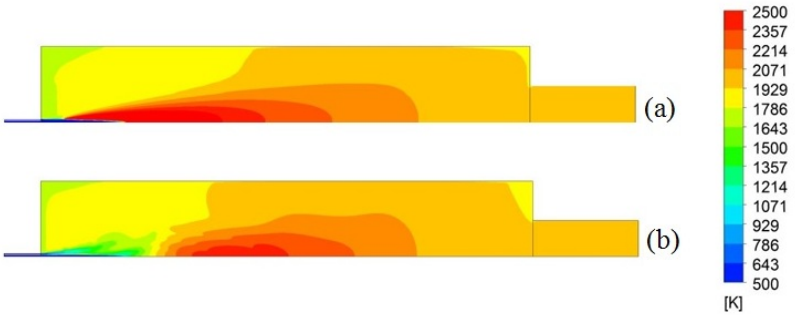

Fig. 36. Calculated temperatures of the IFRF furnace; (a) EDC, (b) SFM [142].

Another way to avoid the obstacles of the SFM is the flamelet generated manifold (FGM) approach, proposed by van Oijen and de Goey [136]. It is similar to the SFM, with the

introduction of a second transport variable beside the mixture fraction to describe the chemistry in a flame. This transport variable is called the progress variable and can be defined with the mass fraction(s) of specie(s). Generally, the chosen species should represent the reaction progress from unburnt to burnt gases by their concentrations. For example, H_2O or CO_2, which have their minimum concentrations in the unburnt gases and maximum concentrations in the burnt gases. Two additional transport equations for the progress variable and its variance have to be solved. This approach should be able to predict OEC cases as well as flame extinction and ignition delay. Since this model was not investigated in detail in the course of this work, it is addressed further in the outlook of this thesis (see Section 8).

4.3.4 Reaction mechanisms

Many reaction mechanisms can be found in literature for the combustion of hydrocarbons with air. Since the natural gas in the simulation is treated as pure methane, no higher hydrocarbons (e.g. aromatic compounds) are necessary in the reaction mechanism.
To model flames, skeletal reaction mechanisms are widely used instead of full or detailed reaction mechanisms, in order to avoid computationally demanding procedures. Such skeletal mechanisms are usually derived from a detailed mechanism for a certain condition (e.g. fuel-lean, kind of fuel, etc.) and their applicability is restricted. In this work, the main focus was the analysis of different reaction mechanisms for use in OEC combined with the combustion models mentioned in Section 4.3. The goal was to find a reaction mechanism, which could predict an oxygen enhanced flame in the full range from 21 to 100 % oxygen in the oxidant. For this purpose one detailed, three skeletal, and one 3-step global mechanisms were tested (see Table 9).

Table 9
Overview of the used reaction mechanisms.

Reaction mechanism	Number of species	Number of reactions
GRI3.0	53	325
DRM19	19	84
smooke46	17	46
skeletal25	17	25
3-step	5	3

The GRI3.0 mechanism is a detailed mechanism developed by Smith et al. [137] for the combustion of hydrocarbons. It also includes the formation of NO_x and was extensively validated against data from literature. Because of the high number of reactions and species, this mechanism was only used for the simulation with the SFM.

The DRM19 [138] mechanism was derived from the GRI mechanism (v1.2) for the combustion of methane with air under a wide range of pressures, equivalence ratios and initial temperatures. It was tested against the GRI mechanism with consideration given to the flame speed and ignition delay.

The smooke46 mechanism was proposed by Smooke et al. [139]. In their study, experiments with a counter-flow diffusion flame were used to test the mechanism. However, diluted air was used as an oxidant.

The skeletal25 mechanism was published by Peeters [140] in a PhD thesis. This mechanism is a modification of the mechanism from Smooke and Giovangigli [141], where the pressure dependent reaction (R. 13) was adapted for atmospheric conditions.

$$CH_4 + (M) \rightleftharpoons CH_3 + H + (M) \qquad \text{(R. 13)}$$

The global 3-step mechanism was proposed by Yin et al. [74] for use in oxy-fuel combustion of natural gas and is based on a global mechanism from Westbrook and Dryer [73]. Only the major species are involved in this mechanism. The global reactions and kinetic parameters are given in Table 10.

Table 10
Kinetic parameters of the 3-step global reaction mechanism with the units m, kmol, s, K, J [74].

Reaction no.	Reaction	k_0	b	E_A
1	$CH_4 + 1.5\ O_2 \rightarrow 2\ H_2O + CO$	$5.03*10^{11}$	0	$2.00*10^{8}$
2	$CO + 0.5\ O_2 \rightarrow CO_2$	$2.24*10^{6}$	0	$4.18*10^{7}$
3	$CO_2 \rightarrow CO + 0.5\ O_2$	$1.10*10^{13}$	-0.97	$3.28*10^{8}$

All skeletal reaction mechanisms can be found in the appendix and the GRI3.0 can be downloaded [137].

4.4 Radiation models

As examined in Section 2.3, the majority of the heat transfer in industrial furnaces occurs via radiation. To predict radiation intensity the radiative transfer equation (RTE) in Eq. (122) has to be solved. The first term stands for the change of radiation intensity dependent on the path length.

$$\frac{I(\vec{x},\vec{s})}{ds} + (a+\sigma_s)I(\vec{x},\vec{s}) = an^2\frac{\sigma T^4}{\pi} + \frac{\sigma_s}{4\pi}\int_0^{4\pi} I(\vec{x},\vec{s}')\Phi(\vec{s}\cdot\vec{s}')d\Omega \qquad (122)$$

In Eq. (122) $I(\vec{x},\vec{s})$ is the radiation intensity dependent on the position and the direction vector, a is the absorption coefficient, σ_s is the scattering coefficient, n is the refractive index,

$\vec{s}'$ is the direction of scattered radiation, Φ is the phase function and Ω the solid angle. The second term represents optical thickness, and calculates the loss of radiation intensity due to scattering and absorption in the gas phase. Since radiative heat transfer is only considered in the gas phase without any particles, the refractive index and scattering coefficient were set to values of 1 and 0 s^{-1}. The RTE was solved using the P1 model [142; 143] and the discrete ordinates model (DOM) [144; 145], which are described briefly in the next sections. More detailed information can be found in [109]. The dependence of the wave length on the radiative heat transfer is neglected in this work because of its higher computational demand as stated in Section 2.4.2

4.4.1 P1 model

This model assumes that the propagation of the radiation is not dependent on the direction. The radiation intensity is integrated over all directions leading to a diffusion equation for the RTE as given in Eq. (123), where $\nabla \cdot q_{rad}$ is the radiative heat flux and G_r is the incident radiation. Results for the radiative heat flux in this equation are used in the energy equation as source/sink term.

$$-\nabla \cdot q_{rad} = aG_r - 4an^2\sigma T^4 \tag{123}$$

The RTE is easy to solve and computational demand is reasonable. However, the best predictions were found to be achieved in cases with a high optical thickness (high beam length). Generally, the radiative heat flux is over-predicted in many cases [109].

4.4.2 Discrete ordinates model (DOM)

In this model, the propagation of the radiative heat transfer is calculated for a number of solid angles. For each direction $\vec{s}$ (angle), an RTE as shown in Eq. (122) is solved. The discretization of the angles (number of angles) has a distinct effect on the calculation time. In this work, each octant was discretized with 4 x 4 solid angles leading to an overall number of 128 directions for the radiative heat transfer. Habibi et al. [16] tested the P1 model and DOM for a gas fired steam cracking furnace. They found a similar prediction of the heat flux, but suggested the use of DOM because of the wider range of applications.

4.4.3 Radiative properties of the flue gas

The interaction of the flue gas components is strongly related to the wave length of the thermal radiation, and should thus be modelled with special consideration of the wave length

(non-grey approach). This is also recommendable when the concentrations of the participating gas components (H_2O and CO_2), as well as the beam length, are high. Although the H_2O and CO_2 concentrations increase with higher oxygen enrichment, a grey gas approach was used here. Since the furnaces investigated have mean beam lengths of 0.494 and 2.2 m, the differences of the gas emissivity provided in Fig. 21 are very low, despite having been calculated with WSGG parameters adapted for non-grey consideration.

4.4.3.1 Weighted sum of grey gases model (WSGGM)

The WSSGM considers the flue gas mixture as a mixture of fictional grey gases. For the gas mixture, the total emissivity can be calculated according to Eq. (124), where $a_{\varepsilon,i}$ is the emissivity weighting factor for the gas i, a_i is the absorption coefficient for the gas i, p is the partial pressure of all absorbing components, and s is the beam length

$$\varepsilon = \sum_{i=0}^{I} a_{\varepsilon,i}(T)(1 - e^{-a_i p s}) \tag{124}$$

The emissivity weighting factors are calculated by Eq. (125), where $b_{\varepsilon,i,j}$ is the emissivity gas temperature polynomial coefficient. For the coefficient $i = 0$, Eq. (126) is valid, to account for spectral windows in regions of high absorption [109].

$$a_{\varepsilon,i} = \sum_{j=1}^{J} b_{\varepsilon,i,j} T^{j-1} \tag{125}$$

$$a_{\varepsilon,0} = 1 - \sum_{i=1}^{I} a_{\varepsilon,i} \tag{126}$$

In this thesis, the values from Smith et al. [94] were used for a_i and $b_{\varepsilon,i,j}$ and can be found in the Appendix.

4.5 Numerical grids

A crucial part of CFD modelling is the generation of the numerical grid with small control volumes, which affects the calculated results significantly. The cell type and size have to be selected carefully, especially in regions of high velocity, species and temperature gradients. In combustion modelling, the main focus is on species and temperature distribution in the near burner area, where the highest gradients in furnaces occur.

4.5.1 Lab-scale furnace

Two numerical grids were created for the lab-scale furnace to simulate the experiments with and without thermal load. The strategy for the mesh generation was the same in both cases and was derived from a detailed grid independency test with four different meshes. This test was based on the Richardson extrapolation [146], to determine the deviation of the numerical result from the exact value. A detailed analysis of the grid independency test is given in Section 6.1. Besides the flue gas exit duct, all volume regions (main combustion chamber and walls) were modelled with hexahedrons and wedges, whereas the flue gas exit duct was created with tetrahedrons. The main focus was on the main reaction zone. In this region a fine grid of hexahedrons and wedges was created. In Fig. 37 and Fig. 38, the numerical grids for the lab-scale furnace are displayed. At the outlet, a porous zone was arranged to achieve flow resistance in the simulation and maintain a positive pressure between 0.3 and 0.4 mbar according to the experiments.

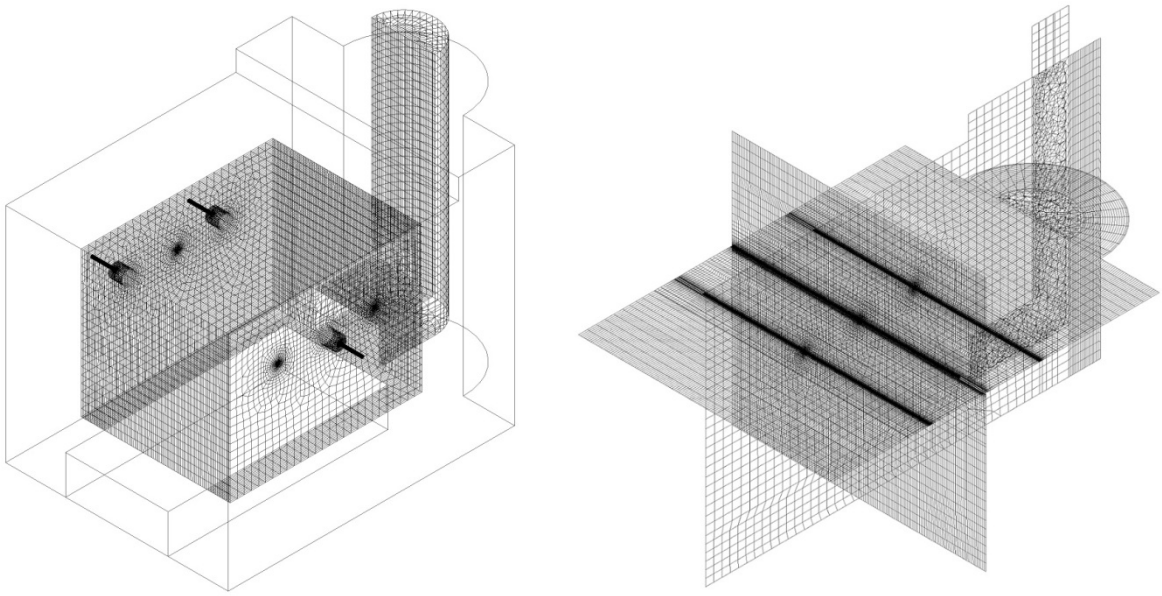

Fig. 37. Computational grid of the lab-scale furnace without thermal load [155].

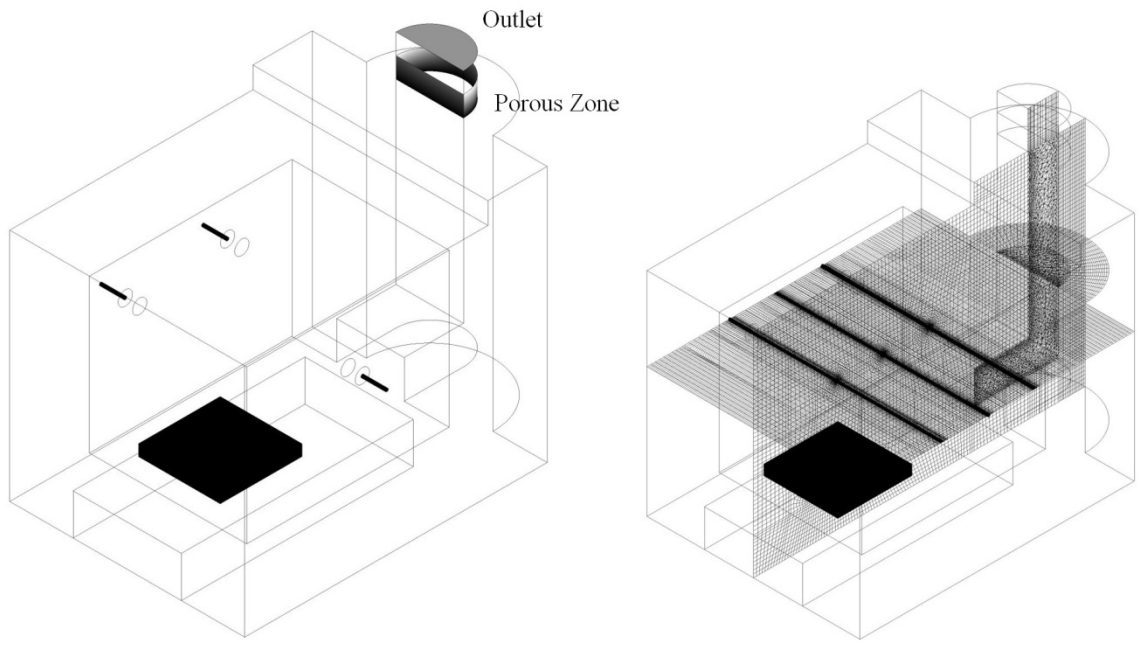

Fig. 38. Computational grid of the lab-scale furnace with thermal load [156].

The number of cells and quality of the grid are summarized in Table 11. For the grid with thermal load, the number of cells has been doubled because the vicinity of the thermal load was resolved with a fine grid for an accurate prediction of the heat transfer to the load.

Table 11
Mesh size and quality.

	Number of cells	**Skewness (max./average)**	**Aspect ratio (max./average)**
without load	630,413	0.89/0.16	40.0/5.95
with load	1,431,339	0.89/0.15	34.5/3.67

4.5.2 Walking hearth furnace

The numerical grid of the walking hearth furnace was created only for one half of the furnace because of the symmetry reasons described in Section 3.2. It was created with an overall number of cells of 5,797,749 (tetrahedrons and hexahedrons/wedges) including the combustion chamber and furnace walls. In Fig. 39a, only the combustion chamber (without walls) is displayed, which was made of 4,830,514 cells. Similar to the lab-scale furnace, the near burner region was modelled with a fine grid, as can be seen in Fig. 39b. Because of the complex swirl geometry at the oxidant inlets, tetrahedrons were used instead of hexahedrons. Although the burner's dimensions are small compared to the whole furnace, the burners were created with approximately 1.9 million. The maximum skewness of the mesh was 0.8 with an average value of 0.22. For the aspect ratio, maximum and average values of 19.8 and 2 were

detected. The numerical grid and boundary conditions for the CFD simulation of the walking hearth furnace are given in Prieler et al. [147].

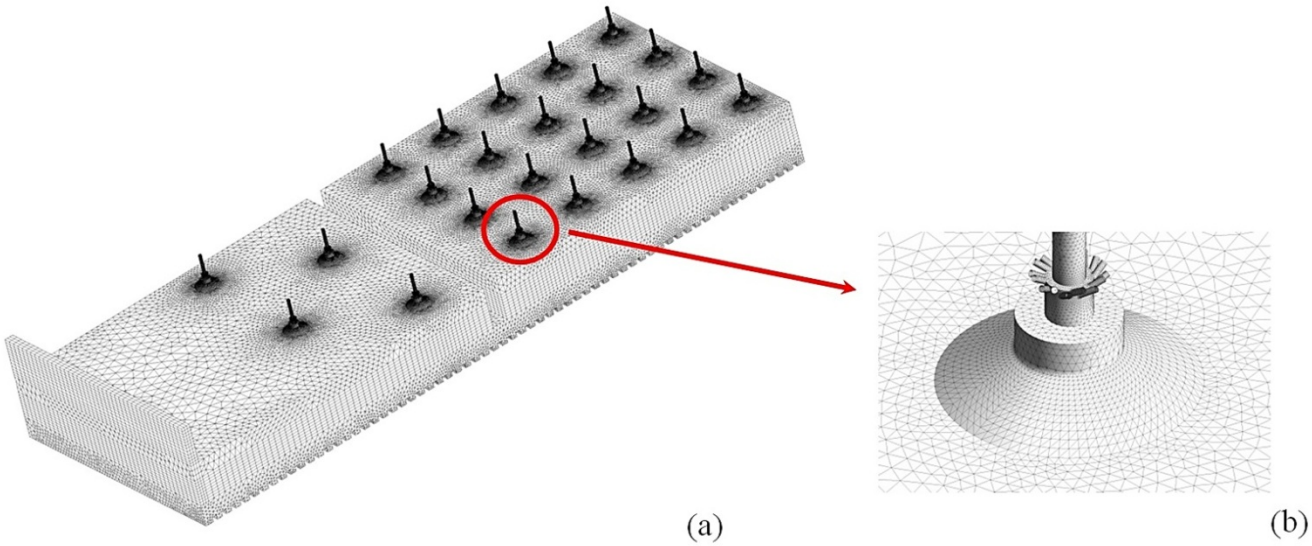

Fig. 39. Computational grid of the walking hearth furnace without walls.

5 Analysis of the reaction mechanisms

5.1 Chemical equilibrium

The chemical equilibrium was determined for the reaction mechanisms mentioned in Section 4.3.4 based on the minimization of the free energy described in Section 2.1.3. For this purpose, the element-potential method (see Stanford software STANJAN [113]) was implemented in CHEMKIN-PRO [148]. The air-fuel and oxy-fuel (100 % O_2) cases were considered in this section. The calculations were carried out with pure methane as fuel, which is the main component in natural gas.

The temperature in case of chemical equilibrium for air-fuel and oxy-fuel combustion is displayed in Fig. 40, as a function of the equivalence ratio. Besides the global reaction mechanism (3-step), the GRI3.0 and DRM19 mechanisms were also considered in this section to calculate the chemical equilibrium. For the calculation, only the thermodynamic data of the species was used. The chemical kinetic of each reaction was not considered for the chemical equilibrium. Additionally, the calculations were done for an adiabatic system. Due to the fact that all detailed mechanisms (skeletal25, smooke46, etc.) produce very similar results, and would be barely distinguishable in the charts, only these mechanisms are displayed in Fig. 40. In air-fuel combustion, the calculated temperatures are in close agreement with detailed and global mechanisms with a maximum temperature detected for an equivalence ratio of 1.05. Since radical formation has a lower importance below 2500 K (for example, see Fig. 18), the 3-step mechanism also works quite well for air-fuel combustion. With a higher distance to the stoichiometric equivalence ratio, the flame temperature decreases significantly. Because higher amounts of nitrogen are available under fuel-lean conditions ($\Phi < 1$), a huge amount of the heat of reaction is absorbed by the nitrogen. In contrast, the decrease of the flame temperature at a higher equivalence ratio is caused by the missing oxygen in the combustion system, which means that not all of the fuel can be conversed to the reaction products. This is further examined by the predicted CO concentration at chemical equilibrium, which increases under fuel-rich conditions (see Fig. 41). In oxy-fuel combustion, the flame temperature, calculated by the global mechanism, is much higher than with the GRI3.0 and DRM19. This statement is valid for the full range of the equivalence ratios considered. The peak temperature was above 4000 K with the global 3-step mechanism. Including radical formation

within the GRI3.0 and DRM19 mechanism, a temperature of approximately 3000 K was predicted for all investigated equivalence ratios.

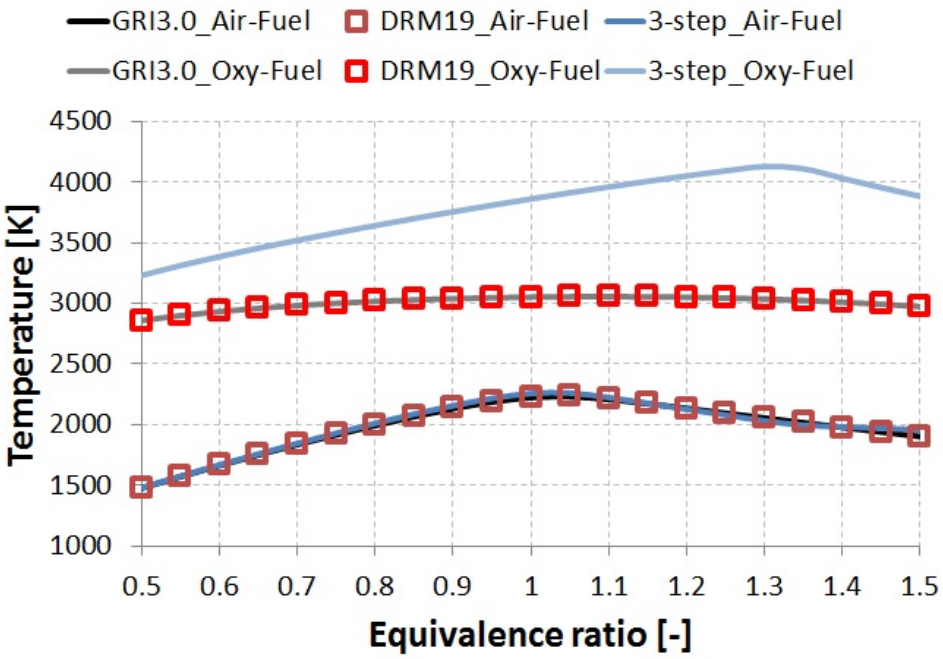

Fig. 40. Flame temperature at chemical equilibrium calculated with the species involved in the GRI3.0, DRM19 and 3-step mechanisms.

The CO concentration at chemical equilibrium is given in Fig. 41. In air-fuel combustion, a significant increase of the CO concentration can be seen under fuel-rich conditions, which is caused by the lack of oxygen necessary to complete the fuel conversion. The detailed mechanisms showed a linear increase of the CO concentrations under fuel-rich conditions. Furthermore, the predicted CO concentration is higher for oxy-fuel combustion, which was also detected under fuel-lean conditions. The linear trend of air-fuel and oxy-fuel combustion between an equivalence ratio of 1 and 1.5 is very similar except for an offset of approximately 0.15.

As an example for radicals formed by the chemical reaction, the OH concentrations are displayed in Fig. 42. Only the GRI3.0 and DRM19 mechanisms are considered because the radicals are not included in the 3-step mechanism. The predicted results showed that the peak OH concentration occurs under slightly fuel-lean conditions, which contradicts the aforementioned statement that radical formation is improved at higher temperature. The dissociation of the combustion products and the formation of radicals is related to an endothermic process, and energy is consumed in this reaction. Therefore, the temperature at the peak OH concentration is slightly lower than the maximum temperature at an equivalence ratio of 1.05.

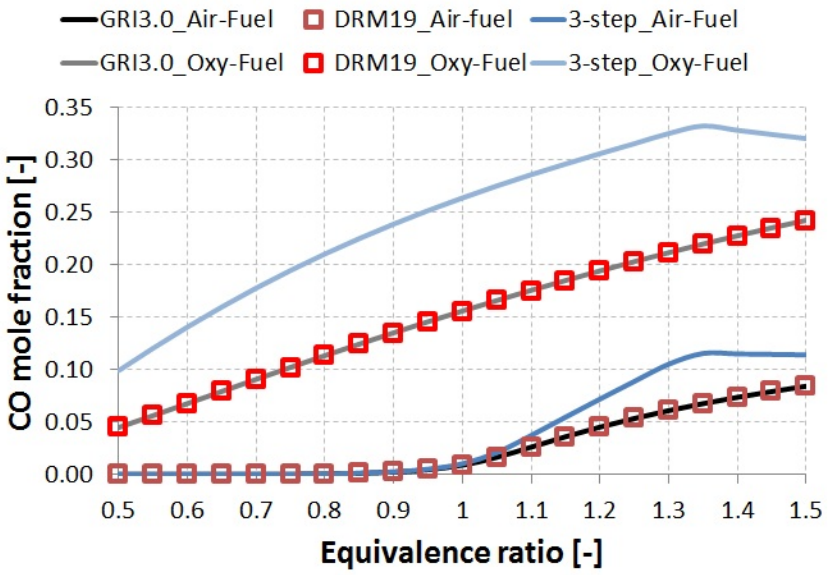

Fig. 41. CO concentration at chemical equilibrium calculated with the species involved in the GRI3.0, DRM19 and 3-step mechanisms.

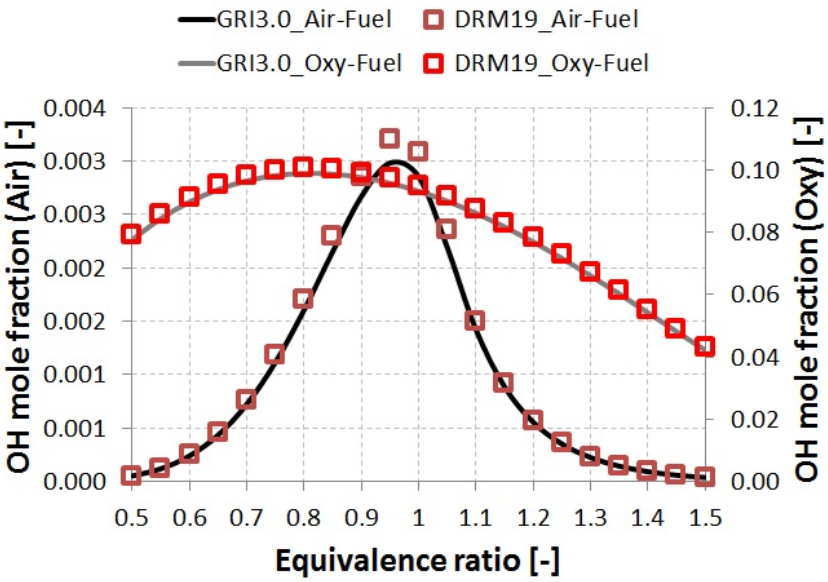

Fig. 42. OH concentration at chemical equilibrium calculated with the species involved in the GRI3.0, DRM19 and 3-step mechanisms.

5.2 Flamelet libraries

As described in Section 4.3.3, laminar flamelets were calculated for the stoichiometric combustion of methane with air (21 % O_2) and pure oxygen. The calculations were done for the GRI3.0, DRM19, smooke46 and skeletal25 mechanisms. Since the 3-step mechanism was only used for the EDC model, it was not applied for the flamelet calculations presented in this section. The thermochemical state (temperature, species concentrations and density) is only related to the mean mixture fraction and the scalar dissipation. These flamelet libraries are the

basis for the generation of the presumed PDF. It is important to note that the flamelets addressed in this section were calculated without heat losses due to radiation. The heat losses are considered within the probability density functions in Section 5.4.

The calculated temperatures under air-fuel conditions are displayed in Fig. 43. The temperature of the fuel and oxidant was set to a value of 298 K, which can be seen at mixture fractions of 1 and 0, respectively. It is obvious from Fig. 43 that all four investigated mechanisms have a similar temperature trend in the full range of the mean mixture fraction and the scalar dissipation. From the fuel ($f = 1$) and oxidant side ($f = 0$), the temperature trend shows an increase until the peak is reached at the stoichiometric mixture fraction $f \approx 0.055$. Near chemical equilibrium ($\chi \approx 0$), the global maximum for the temperature with each mechanism was detected. For example, the GRI3.0 mechanisms calculated a maximum temperature of 2195 K. The other mechanisms were in the same temperature range with a deviation of 5 to 9 K. Flame extinction was observed at strain rates (scalar dissipation) between 26 and 31 s^{-1}.

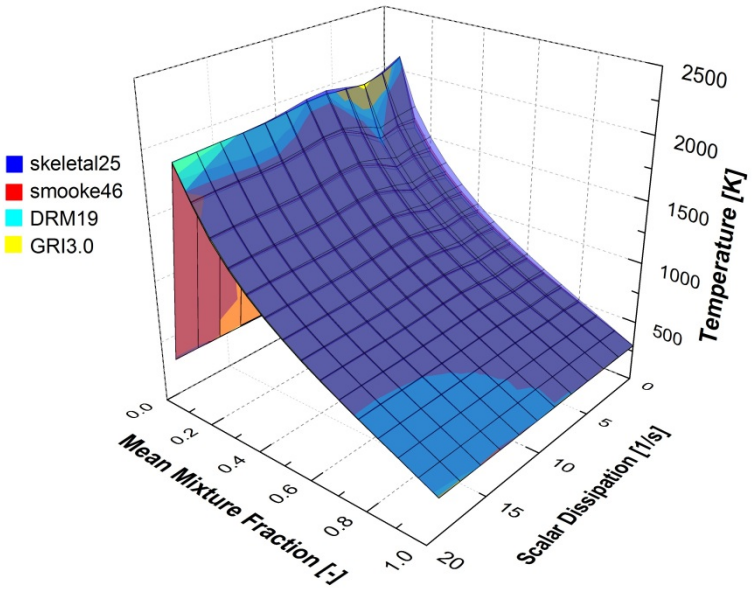

Fig. 43. Results of the flamelet calculation (adiabatic) for air-fuel combustion with different combustion mechanisms.

In Fig. 44, the results for the combustion with pure oxygen are shown. In that case, only the GR3.0, DRM19 and smooke46 mechanisms showed a close accordance with one another. Furthermore, the shape of the surface plot is quite similar to that of the air-fuel combustion. The peak temperatures are approximately 3000 K and were calculated at the stoichiometric mixture fraction, which has a value of $f \approx 0.2$ for combustion with pure oxygen. In contrast to the air-fuel case, the region of the maximum temperature is in a wider range of the mean mixture fraction. In contrast, this peak occurs only at the mixture fraction of $f \approx 0.055$ for

the air-fuel combustion (see Fig. 43). The skeletal25 mechanism shows a significantly different temperature trend in Fig. 44. At a distance from the stoichiometric mixture fraction, skeletal25 is very similar to the other mechanisms. However, in the vicinity of the stoichiometric mixture fraction the skeletal25 mechanism predicts higher temperatures. This is more obvious at low scalar dissipation rates, where the global maximum is reached with 4878 K.

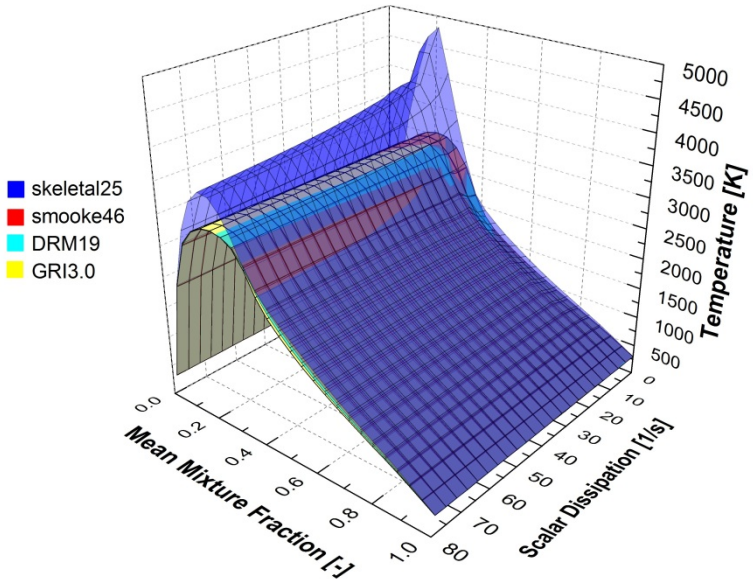

Fig. 44. Results of the flamelet calculation (adiabatic) for combustion with pure oxygen and different combustion mechanisms.

When the oxygen concentration in the oxidant is 30 %, the temperature trend calculated with the skeletal25 mechanism is in close agreement to the other mechanisms (smooke46, DRM19 and GRI3.0). This is shown for a comparison of the skeletal25 and smooke46 mechanism in Fig. 45. Only the small temperature peak at $\chi \approx 0$ was over-predicted by the skeletal25 mechanism.

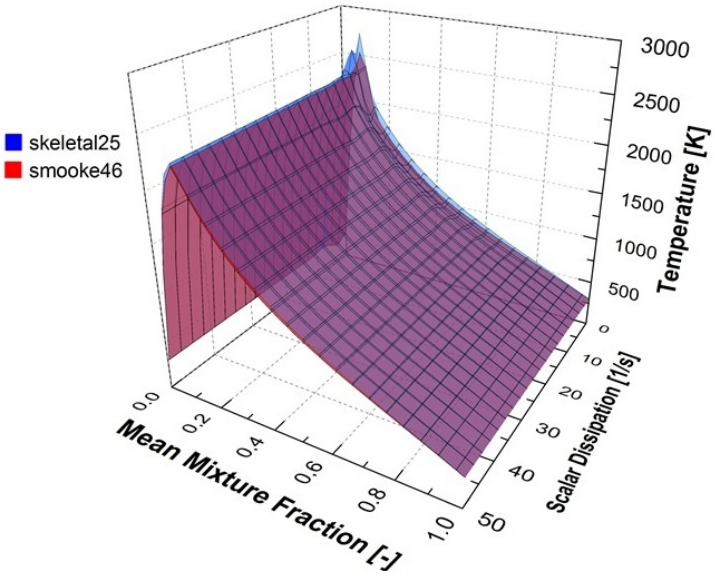

Fig. 45. Flamelet calculation (adiabatic) for combustion with 30 % O_2 [43; 156].

Thus, it is possible to conclude that all reaction mechanisms should predict the same temperatures and species concentrations in the CFD simulation with the SFM, up to an oxygen enrichment of 30 %. Although the calculations were done for adiabatic conditions, it is expected that the results for a "real" case will be similar, between the smooke46, DRM19 and GRI3.0 mechanisms. For higher oxygen concentrations, there might be considerable differences in flame shape as well as temperature and species concentrations with the skeletal25 mechanism.

5.3 Counter-flow diffusion flames

In this section, the reaction mechanisms are investigated in detail at small scalar dissipation rates, where the highest temperature deviations were detected in the previous section. For this purpose, single counter-flow diffusion flames were calculated with all four reaction mechanisms for air-fired conditions and OEC. The distance between the fuel and oxidant inlet was chosen to be 10 cm to achieve a low strain rate ($\chi_{max} \approx \pm 10\ s^{-1}$), especially at the peak temperature. Due to sensitivity analysis, the most important reactions for the prediction of the temperature should be found and reveal the differences between skeletal25 and the other mechanisms.

5.3.1 Temperature and species concentrations

The results for the temperature, strain rate and species concentrations for the stoichiometric combustion of methane (fuel) and air (oxidant) are presented in Fig. 46 and Fig. 47 for adiabatic conditions. Fuel and oxidant enter the simulation domain at 0 and 10 cm, respectively. As it was seen in Fig. 43, the temperature trends are very similar for the air-fuel combustion case. In all cases, the flame zone with the maximum temperature is on the fuel side at approximately 2 cm. This is because of the higher mass-flow rate of the oxidant for stoichiometric combustion of methane. Here, the mass-flow rate of air is 17.2 times higher than for methane. Therefore, the flame zone is shifted to the fuel side by the higher momentum of the air flow. Starting from the fuel side, the temperature shows a linear increase until the peak temperature is reached. Peak temperatures between 2118 K (DRM19) and 2167 K (skeletal25) were observed. On the oxidant side, the temperature increase occurs much faster than on the fuel side. Whereas the temperature peak is reached after 2 cm on the fuel side, on the oxidant side, the temperature increase from 298 K to the peak temperature takes place within 1 cm (between 2 and 3 cm). From the temperature trend, it is possible to conclude that the main reactions occur within the first 3 to 4 cm of the counter-flow diffusion flame.

This is further determined by the species concentrations in the flame. According to the position of the maximum temperature, the highest concentrations of main reaction products, like CO_2 and H_2O, can be observed at the same position. All reactions mechanisms predict nearly the maximum possible H_2O concentration of about 18 to 19 % in the gas mixture. Only small amounts of dissociation products of H_2O, such as OH and H radicals, were formed. Larger differences were found for the predicted CO_2 and CO concentrations. With the skeletal25 mechanism, higher CO_2 concentrations were predicted in the region of the maximum temperature. As a consequence, the oxidation of CO is the main reason for the slightly higher temperature of 2167 K, calculated with the skeletal25 mechanism. Although the maximum CO concentrations are 0.035 (skeletal25) and 0.06 (DRM19), the difference between the maximum temperatures of the mechanisms is only 49 K, because nitrogen absorbs the majority of the heat of formation from the CO oxidation.

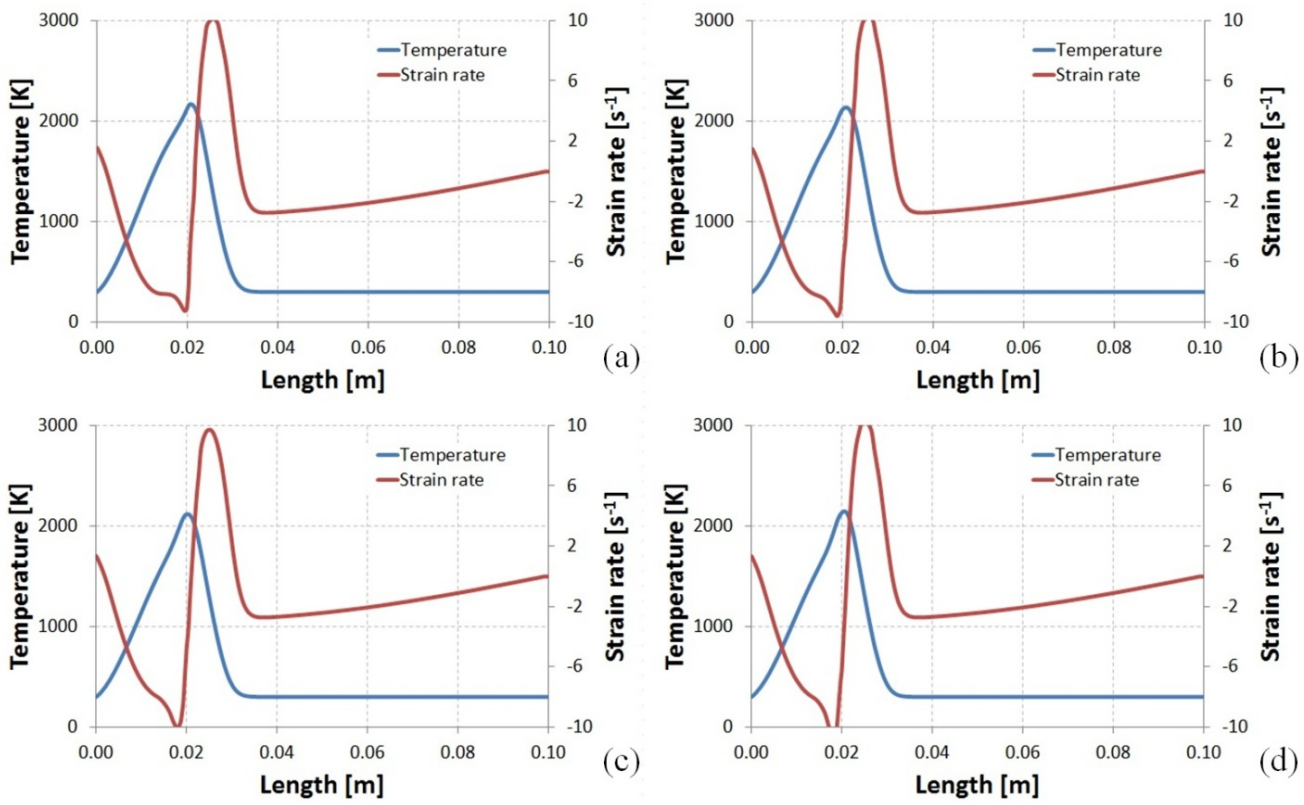

Fig. 46. Temperature and strain rate in the counter-flow diffusion flame (adiabatic) under air-fuel conditions: (a) skeletal25, (b) smooke46, (c) DRM19, (d) GRI3.0.

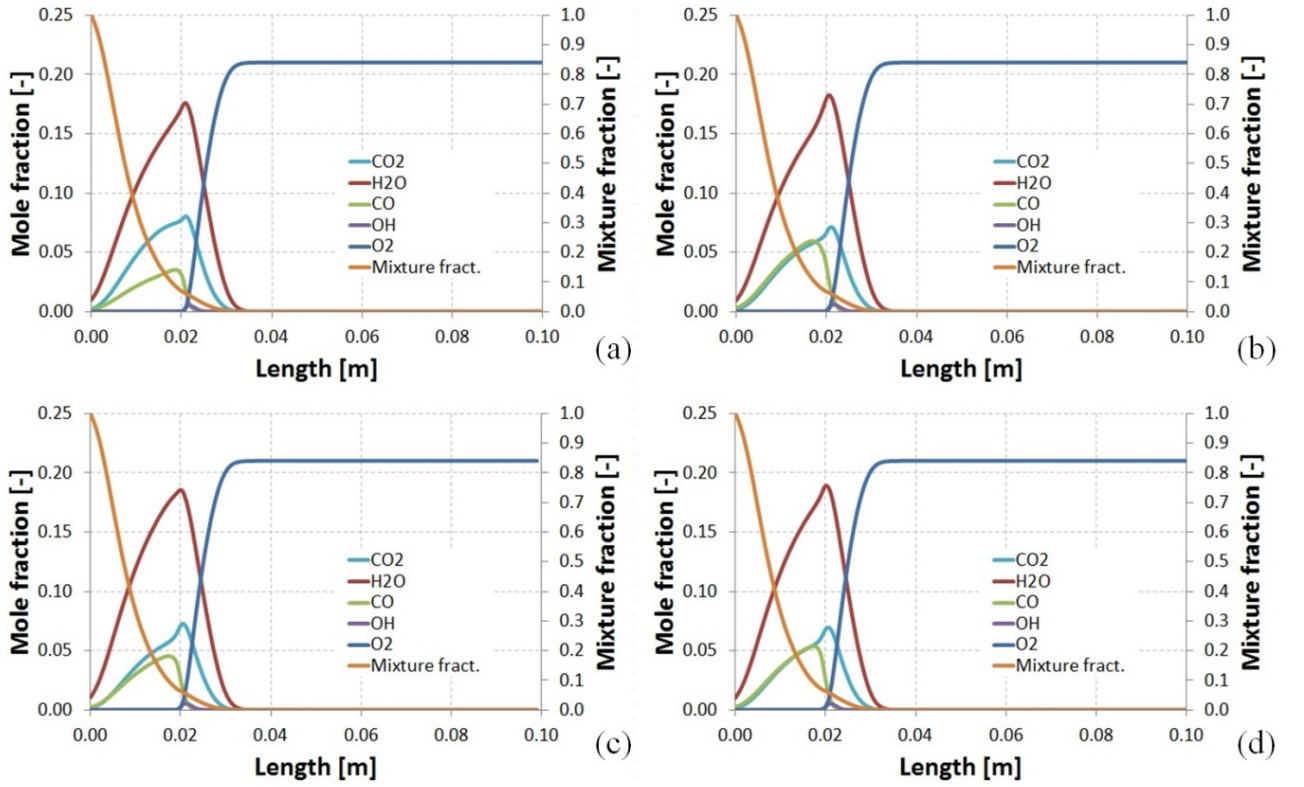

Fig. 47. Species concentrations and mixture fraction in the counter-flow diffusion flame (adiabatic) under air-fuel conditions: (a) skeletal25, (b) smooke46, (c) DRM19, (d) GRI3.0.

The results for the stoichiometric and adiabatic combustion of methane (fuel) and pure oxygen (oxidant) are presented in Fig. 48 and Fig. 49. In Fig. 48, it is possible to see that the chemical reactions take place in a wider range of the diffusion flame. In contrast to the small reaction zone in air-fired conditions (from 0 to 4 cm), the oxy-fuel case shows, that the reactions occur within the range of 0 to 7.5 cm. As discussed in Section 5.2, the skeletal25 mechanism showed a significant difference related to the maximum temperature for oxy-fuel conditions (see Fig. 48). Besides this difference in the region of stoichiometric conditions, all mechanisms showed the same trend. From 0 to approximately 2.7 cm, all mechanisms are similar regarding the temperature increase. At 2.7 cm, a higher rate of the temperature increase is detected for all mechanisms. The temperature peaks were found at 4 cm with values between 2977 and 2981 K (DRM19/GRI3.0 and smooke46), as well as 4671 K for the skeletal25 mechanism.

Fig. 49 displays the species concentrations in the flamelet. Based on the species concentrations, it is obvious that the skeletal25 mechanism predicts higher concentrations of combustion products like H_2O and CO_2. The maximum CO_2 concentration with the skeletal25 mechanisms was 0.23, whereas the other mechanisms predicted values of 0.13. All mechanisms predicted the maximum CO_2 concentrations at approximately 4 cm. Furthermore, the same effect can be seen with the concentration of H_2O. While all mechanisms calculated similar concentrations of H_2O in the flame for air-fired conditions, in oxy-fuel combustion, the H_2O concentration was much higher with the skeletal25 mechanism. The trend of the H_2O concentration also explains the higher rate of the temperature increase at 2.7 cm. In this region, the formation of H_2O increases and higher amounts of the heat of formation are released.

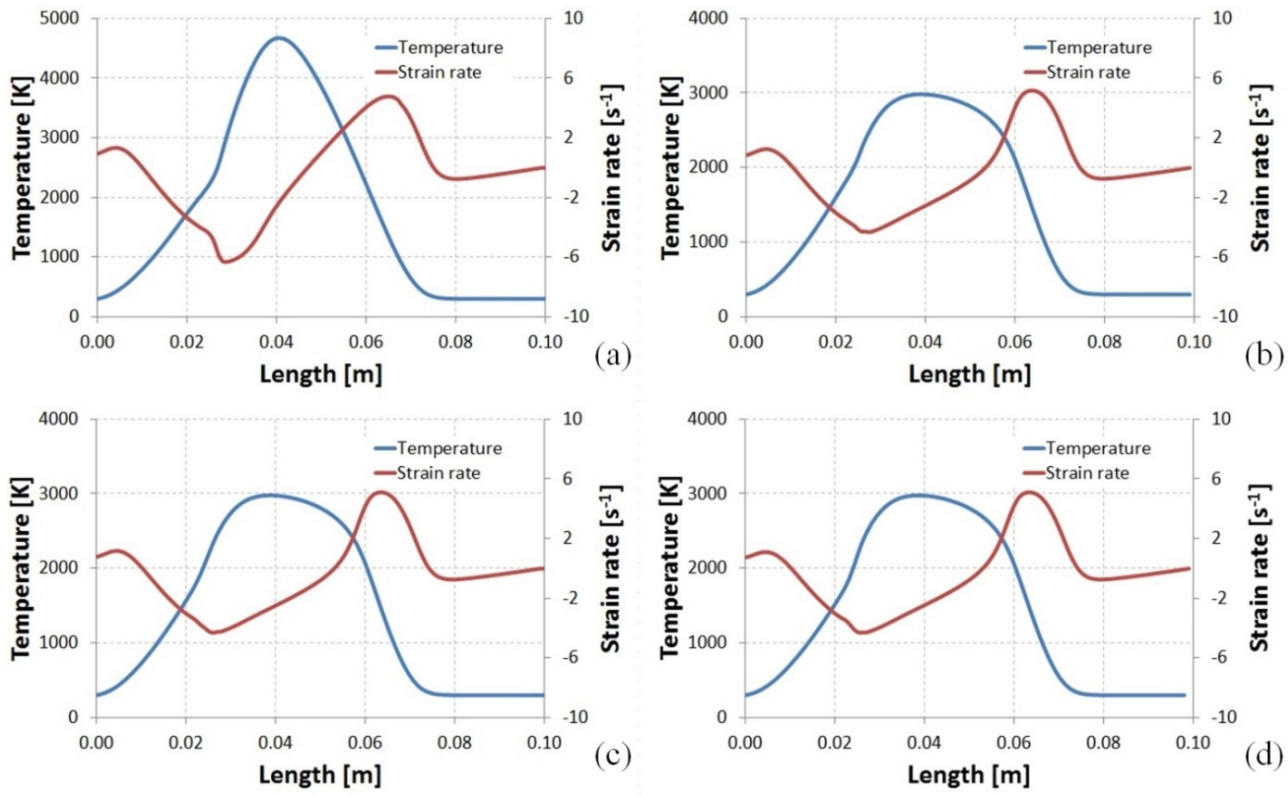

Fig. 48. Temperature and strain rate in the counter-flow diffusion flame (adiabatic) under oxy-fuel conditions: (a) skeletal25, (b) smooke46, (c) DRM19, (d) GRI3.0.

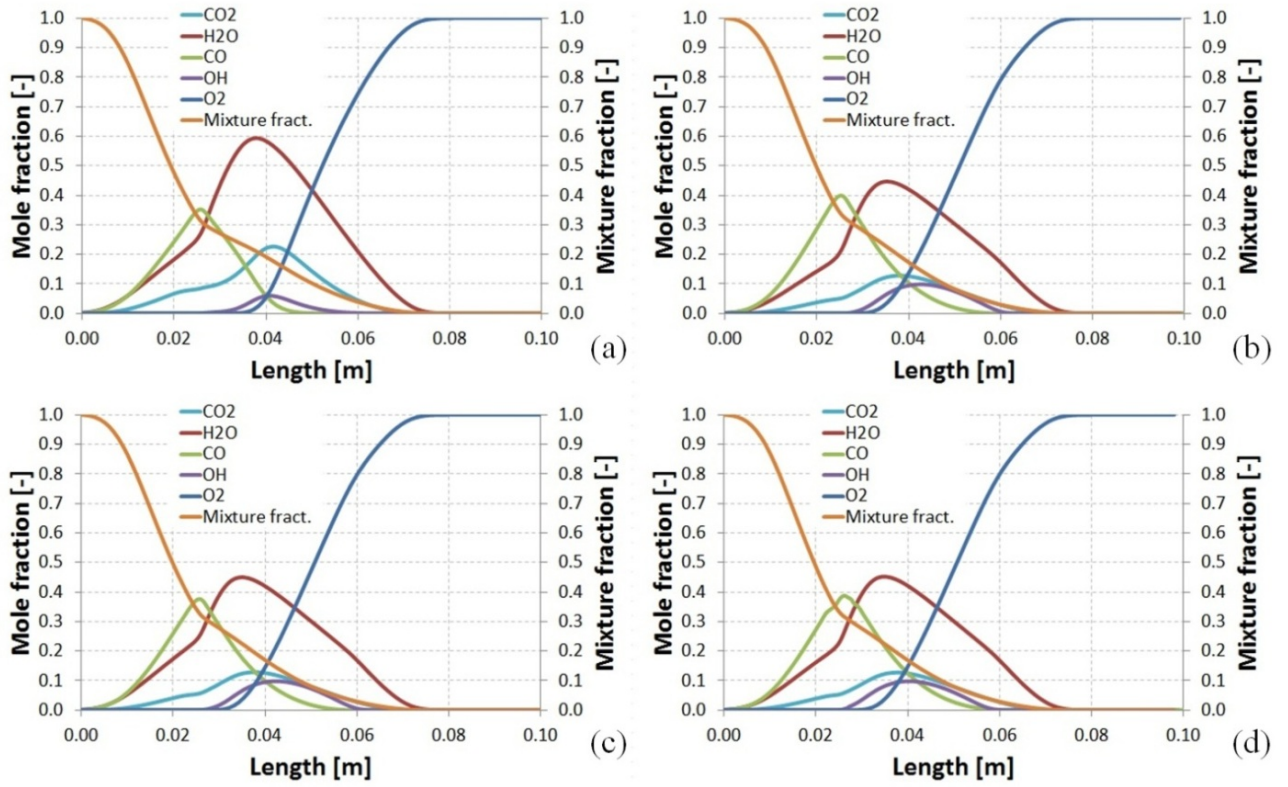

Fig. 49. Species concentrations and mixture fraction in the counter-flow diffusion flame (adiabatic) under oxy-fuel conditions: (a) skeletal25, (b) smooke46, (c) DRM19, (d) GRI3.0.

The temperature trends and species concentrations indicated that the smooke46, DRM19 and GRI3.0 mechanisms will predict very similar results with the SFM in the CFD simulations for air-fired conditions and OEC. Only the skeletal25 mechanism is assumed to calculate different temperatures and species concentrations compared to the other mechanisms. The skeletal25 mechanism is expected to predict higher concentrations of the reaction products H_2O and CO_2, as well as higher temperatures in OEC, compared to the other mechanisms.

5.3.2 Sensitivity analysis

The previous section established, that in contrast to the other mechanisms, the skeletal25 mechanisms will predict higher temperatures in the region of the stoichiometric mixture as well as higher concentrations of the reaction product. In this section, an analysis of the most important reactions within the mechanisms should be given. This was done by means of sensitivity analysis. For example, the relative sensitivity coefficient $E_{i,rel}^{sens}$ for the concentration of the component k related to a parameter α_i (e.g. reaction rate) is given in Eq. (127). More detailed information about the sensitivity analysis can be found in [65; 66; 148].

$$E_{i,rel}^{sens} = \frac{\alpha_i}{c_k}\frac{\partial c_k}{\partial \alpha_i} = \frac{\partial \ln(c_k)}{\partial \ln(\alpha_i)} \tag{127}$$

In Fig. 50, the sensitivity coefficients for the temperature due to the heat of formation of the selected species are shown for the skeletal25 and GRI3.0 mechanisms. For oxy-fuel combustion, the skeletal25 mechanism shows the highest temperature sensitivity by the formation of H_2O, at approximately 2.93 cm (see Fig. 50a). This explains the high temperature calculated with the skeletal25 mechanism due to the peak concentration of H_2O (see Fig. 49). A lower effect was detected by the formation of CO and CO_2. Negative sensitivity coefficients were calculated for CH_4 and H, which means that the temperature decreases when these species are formed. In contrast to the skeletal25 mechanism, this temperature increase is mainly affected by the formation of CO_2 at 2.42 cm and 6.26 cm with the GRI3.0 mechanism (see Fig. 50b). The formation of H_2O is only important at approximately 3.5 cm, but the highest overall sensitivity is found by the heat of formation of CO_2. Whereas the formation of H_2O is most important for the temperature with the skeletal25 mechanism, CO_2 has the highest significance for the temperature when the GRI3.0 mechanism is used.

In the air-fuel case, the skeletal25 mechanism calculates the peak level of the sensitivity coefficient for H_2O and CO_2 at 2.53 cm (see Fig. 50c). Although the heat of formation of

H_2O still has the biggest effect on the temperature, the CO_2 formation becomes more important in the case of air-fuel combustion. This was also seen in Fig. 47, where the higher concentration of CO_2 leads to an increase in the maximum temperature compared to the other mechanisms. The GRI3.0 mechanism revealed that CO_2 is the most sensitive to the temperature (Fig. 50d). The effect of the formation of H_2O is minor.

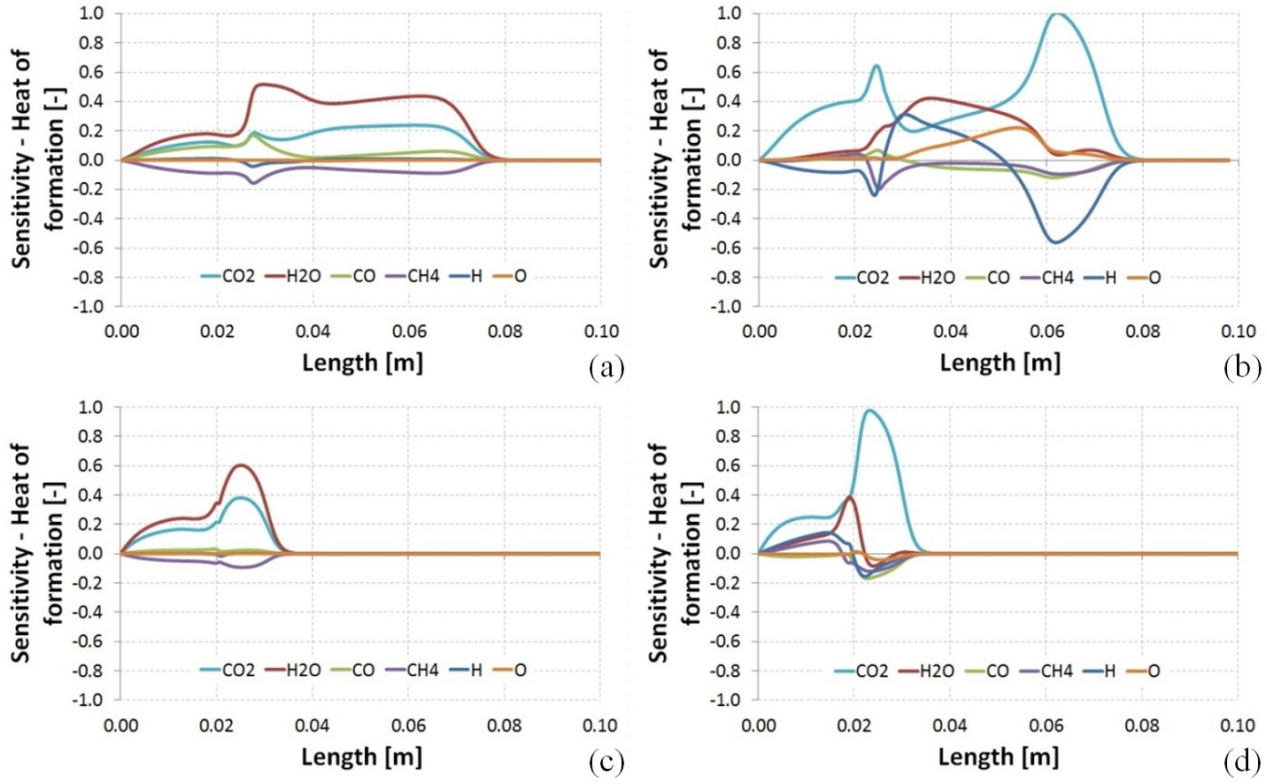

Fig. 50. Sensitivity coefficients for the species with the largest temperature sensitivity for the heats of formation: (a) skeletakl25; oxy-fuel, (b) GRI3.0; oxy-fuel, (c) skeletal25; air-fuel, (d) GRI3.0; air-fuel.

Fig. 51 presents the normalized sensitivity coefficients for the most important reactions in the skeletal25 mechanism related to the production/destruction of H_2O and CO_2. In the case of oxy-fuel, only two reversible reactions are mainly responsible for the high production rate of H_2O and the high temperature peak of above 4000 K. The reversible reaction #5/6 (according to the reaction number in the appendix) is directly involved in the formation of H_2O, whereas the reversible reaction #13/14 has a positive coefficient and prefers the formation of H_2O due to the production of OH, which is a reactant in reaction #6. A higher OH concentration leads to an improved production rate of H_2O in reaction #6. Although these reactions also show the highest sensitivity for the formation of CO_2, its effect on the predicted temperature is less important (see Fig. 50a).

In addition to the aforementioned reactions, the destruction of CH_4 into radicals and the interaction of CH_4 and H_2O (reaction #19/20) also show an increased impact on the H_2O

production rate. Since the destruction of CH_4 is an endothermic reaction, the sensitivity coefficient of these reactions is higher because in air-fuel combustion less energy (temperature) is available to ignite (destruct) the CH_4. The reason for this is that a part of the energy needed to destruct (ignite) the CH_4 is absorbed by the nitrogen in air-fuel combustion, which is not the case under oxy-fuel conditions. Therefore, these reactions can limit the formation of H_2O in air-fuel combustion.

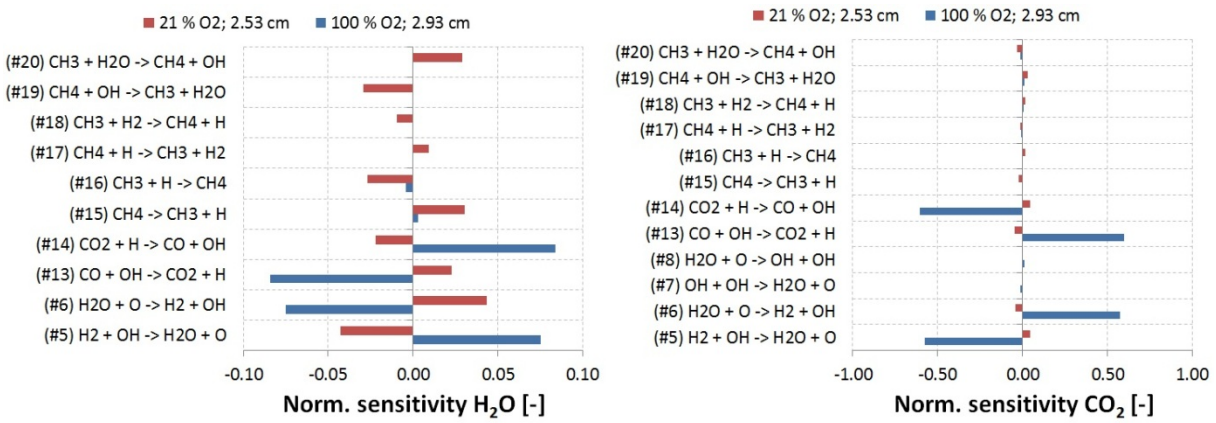

Fig. 51. Sensitivity of CO_2 and H_2O production in relation to the rate of reaction calculated with the skeletal25 mechanism for air-fuel and oxy-fuel conditions.

As the most complex mechanism and representing the other mechanisms, the sensitivity coefficients for the GRI3.0 mechanism are displayed in Fig. 52. In this figure, only the oxy-fuel condition is displayed. As was found in Section 5.3.1, the peak concentrations of H_2O and CO_2 are higher with the skeletal25 mechanism. The sensitivity analysis of the GRI3.0 (as well as other mechanisms) showed that more reactions are involved in the destruction of H_2O and CO_2 than in their formation. This is especially obvious in the case of oxy-fuel combustion at 2.42 cm. Here, the highest values for the sensitivity coefficient are negative, which means that the destruction of the species is preferred. As a consequence, the formation of CO_2 and H_2O is handicapped, and the concentration of radicals and CO increases.

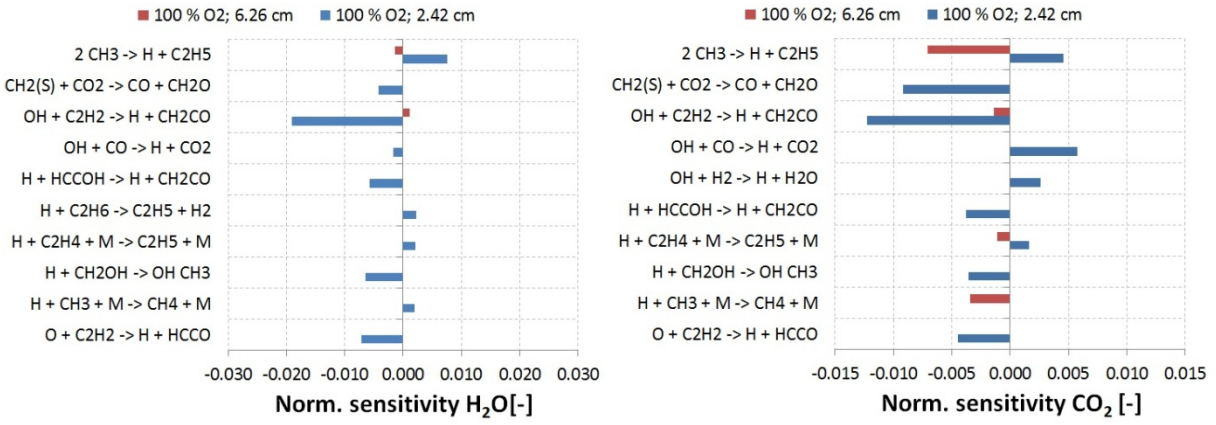

Fig. 52. Sensitivity of CO_2 and H_2O in relation to the rate of reaction calculated with the GRI3.0 mechanism.

The sensitivity analysis revealed the main difference between the air-fuel and oxy-fuel cases, especially for the skeletal25 mechanism, where the predicted temperatures are higher under stoichiometric conditions compared to the other reaction mechanisms. Two reversible reactions were found to be responsible for the increase in temperature due to the higher formation rate of H_2O and CO_2.

5.4 Probability density function (PDF)

This section presents the PDF look-up table for the skeletal25 and smooke46 mechanisms only, because of the negligible differences between the smooke46, DRM19 and GRI3.0 mechanisms. With these look-up tables, only the mean mixture fraction, mixture fraction variance and the enthalpy have to be calculated by solving the transport equations to determine the temperature, species concentrations and density of the flue gas. In this section, only the calculated temperatures are displayed.

5.4.1 PDF – Air-fuel combustion

Fig. 53 displays the look-up table for the temperature at different scalar dissipation levels for air-fuel combustion. The PDF tables were calculated for the adiabatic case. As stated in Section 5.2, the results using different reaction mechanisms are very similar for conventional natural gas (methane) combustion with air. The maximum temperature was detected at $\chi = 0\ s^{-1}$ with approximately 2240 K for both mechanisms (skeletal25 and smooke46). In accordance with Fig. 43, the maximum temperature decreases slightly at higher scalar dissipation rates.

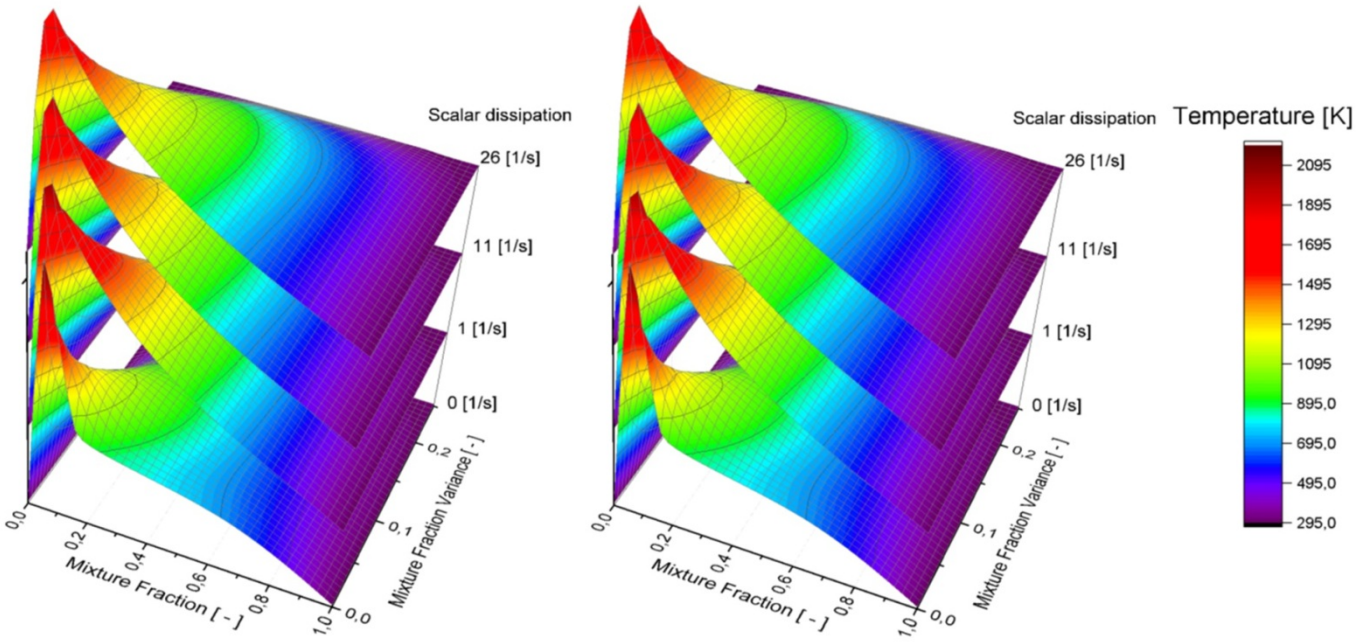

Fig. 53. PDF look-up table for air-fuel conditions and different scalar dissipation rates (adiabatic): skeletal25 (left), smooke46 (right).

Since the heat losses due to radiation have to be considered in combustion, the PDF look-up tables were created for different enthalpy levels to respect the radiation heat loss. For non-adiabatic combustion systems, the enthalpy not only depends on the mixture fraction, but also on the wall heat transfer and radiation. As a consequence, a PDF look-up table would be necessary for each enthalpy value. This leads to the calculation of several PDF layers, each corresponding to a normalized heat loss or gain. The first layer corresponds to the maximum heat loss (e.g. radiation). Detailed information about this can be found in [109].

Fig. 54 presents the PDF table for the calculated temperature at different enthalpy levels and a scalar dissipation rate of $\chi = 1\ s^{-1}$. In this figure, the adiabatic case is displayed by "Layer 31". Layers 1 to 30 represent the temperatures in case of heat losses by radiation with the maximum heat loss at layer 1. In the full range of the enthalpy layers, both mechanisms showed the same results.

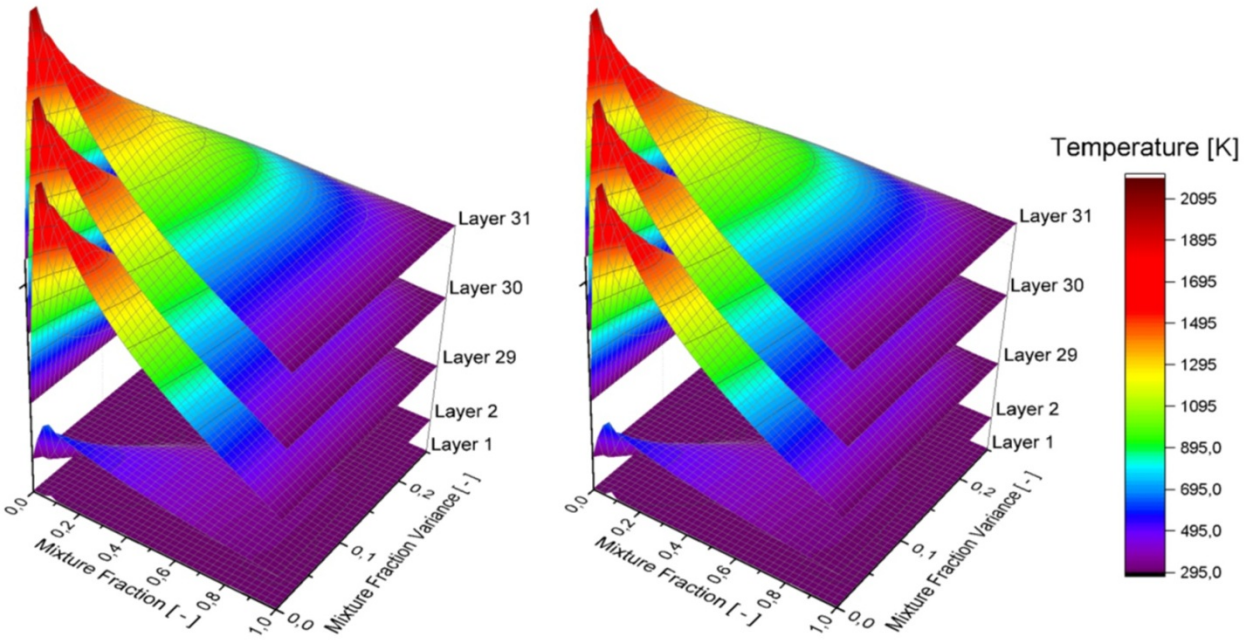

Fig. 54. PDF look-up table for air-fuel conditions and different enthalpy levels: skeletal25 (left), smooke46 (right).

For the simulation of air-fired cases or low oxygen enrichments, the results in this section show that all mechanisms will lead to the same results for the temperature and species concentrations using the SFM.

5.4.2 PDF – Oxy-fuel combustion

The same PDF tables were also created for the oxy-fuel combustion case. Fig. 55 presents the PDF for different scalar dissipation rates at adiabatic conditions and examines the big difference in the predicted temperature with the skeletal25 mechanism. Near the chemical equilibrium at $\chi = 1\ s^{-1}$, a maximum temperature of 4486 K was observed. At higher dissipation rates, the temperature decreases according to the flamelet library in Fig. 44. Although the maximum temperature with the smooke46 mechanism was also reached at $\chi = 1\ s^{-1}$ with 3087 K, an increase in the scalar dissipation had no significant effect on the calculated temperature.

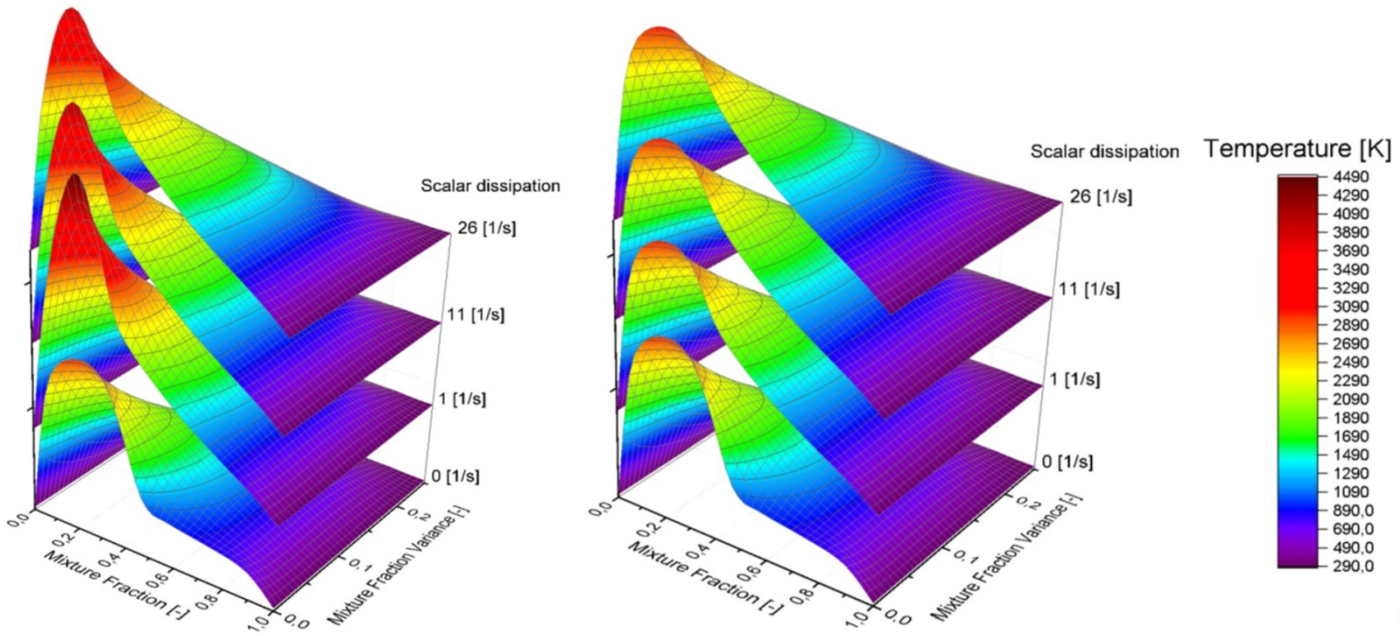

Fig. 55. PDF look-up table for oxy-fuel conditions and different scalar dissipation rates (adiabatic): skeletal25 (left), smooke46 (right).

Fig. 56 displays the PDF table for the different enthalpy levels at $\chi = 1\ s^{-1}$. The skeletal25 mechanism shows significantly higher temperatures for all enthalpy levels compared to the smooke46 mechanism. At the maximum heat loss level (layer 1), the peak temperature is also much higher. This effect is more obvious at low values for the mixture fraction variance.

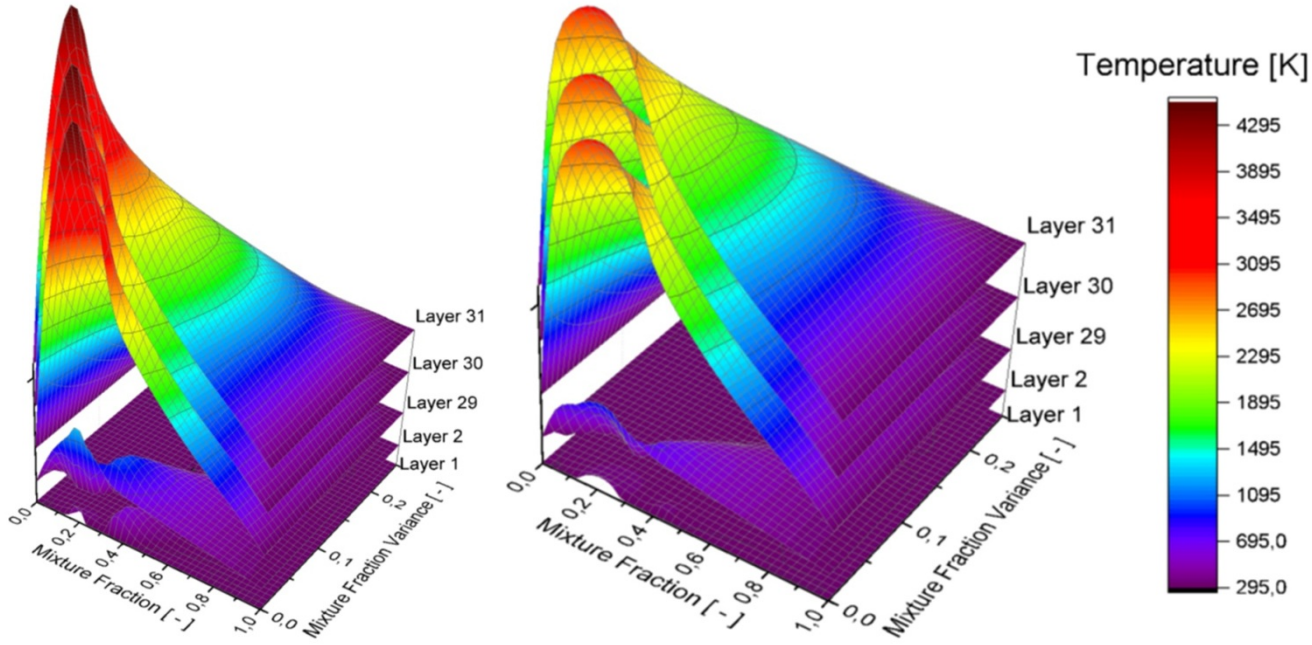

Fig. 56. PDF look-up table for oxy-fuel conditions and different enthalpy levels: skeletal25 (left), smooke46 (right).

From the results of the flamelet calculation and the PDF table generation for oxy-fuel combustion, the skeletal25 mechanism predicts higher temperatures as well as higher H_2O and CO_2 concentrations, especially in the vicinity of the stoichiometric mixture fraction. This effect was observed at all enthalpy levels investigated during the PDF table generation. It is important to note that at higher values of the mixture fraction variance, the difference in the results of the skeletal25 and smooke46 mechanisms is rather distinct. For air-fuel combustion, the results presented in this section showed that the predicted temperature in the CFD simulation would be very similar for all mechanisms.

6 Results – Lab-scale furnace

In this section, the results of the CFD simulations are compared with the temperatures measured in the lab-scale furnace. First, a grid independency test was done with a fuel input of 27.3 kW for four different meshes, which is presented in Section 6.1. A Richardson extrapolation was carried out to determine the grid independency. Furthermore, the results of two different k-epsilon models and the RSM were compared in Section 6.2. The effects of different models on solving the RTEs are briefly examined in Section 6.3 and then compared to the measured data of the "1-OXY_100" test case. Different combustion models and reaction mechanisms were tested for the test cases without load ("2-OEC_21" to "2-OEC_100") in Section 6.4. Finally, the effect of OEC on the process efficiency is examined in Section 6.5. The main focus in this section was the validation of the most efficient CFD model for use in OEC and air-fuel conditions without changing the model parameters. An overview about the CFD simulations carried out in the sections 6.2 to 6.5 are given in Table 12. The results presented in this section 6 have already been published by Prieler et al. [149; 150; 151; 152]. The figures and data used in this section will not be cited further.

Table 12
Overview of the CFD simulations carried out in the Sections 6.2 to 6.5.

Experiment	Turbulence model	Radiation model	Turbulence/chemistry interaction	Reaction mechanism	Used in section(s)
1-OXY_100	Realizable k-epsilon	DOM	SFM	skeletal25	6.3, 6.4.3
			EDM	2-step	6.4.3
			EDC	smooke46	6.4.3
		P1 model	SFM	skeletal25	6.3
2-OEC_21, 2-OEC_25, 2-OEC_30, 2-OEC_45, 2-OEC_100	Realizable k-epsilon	DOM	SFM	skeletal25	6.4.1, 6.5.1
				smooke46	6.4.1
				DRM19	6.4.1
2-OEC_21, 2-OEC_100	Realizable k-epsilon	DOM	EDC	3-step	6.4.2
2-OEC_100	Realizable k-epsilon	DOM	EDC	3-step	6.4.2
1000-OEC_21, 1000-OEC_25, 1000-OEC_30, 1000-OEC_45, 1000-OEC_100	Realizable k-epsilon	DOM	SFM	skeletal25	6.5.2
1220-OEC_30, 1220-OEC_45, 1220-OEC_100	Realizable k-epsilon	DOM	SFM	skeletal25	6.2 (except OEC_45), 6.5.1
1220-OEC_30, 1220-OEC_100	standard k-epsilon	DOM	SFM	skeletal25	6.2
	RSM				
1220-OEC_100	Realizable k-epsilon	DOM	SFM	smooke46	6.4.1

6.1 Grid independency tests

For the grid independency tests without thermal load, four different meshes were created with different sizes and cell types. The main emphasis was to carefully adapt the mesh in the regions of high gradients for the temperature and species concentrations (main reaction zone). First, a tetrahedron grid (Tet) was created with small cells around the burner inlet (see Fig. 57, left). The cell growth is uniform in all directions with the largest cells in the middle of the furnace. Based on this grid, a polyhedron grid (Poly) was formed by merging the tetrahedrons.

Through this procedure, the number of cells was decreased to a quarter of the tetrahedron grid. The polyhedron grid is shown in Fig. 57 (right). Furthermore, two meshes mainly consisting of hexahedrons and wedges were used (Hex1 and Hex2). The only difference between these meshes is the number of cells along the burner axis. In Table 13, the number of cells and the quality of each computational grid are summarized.

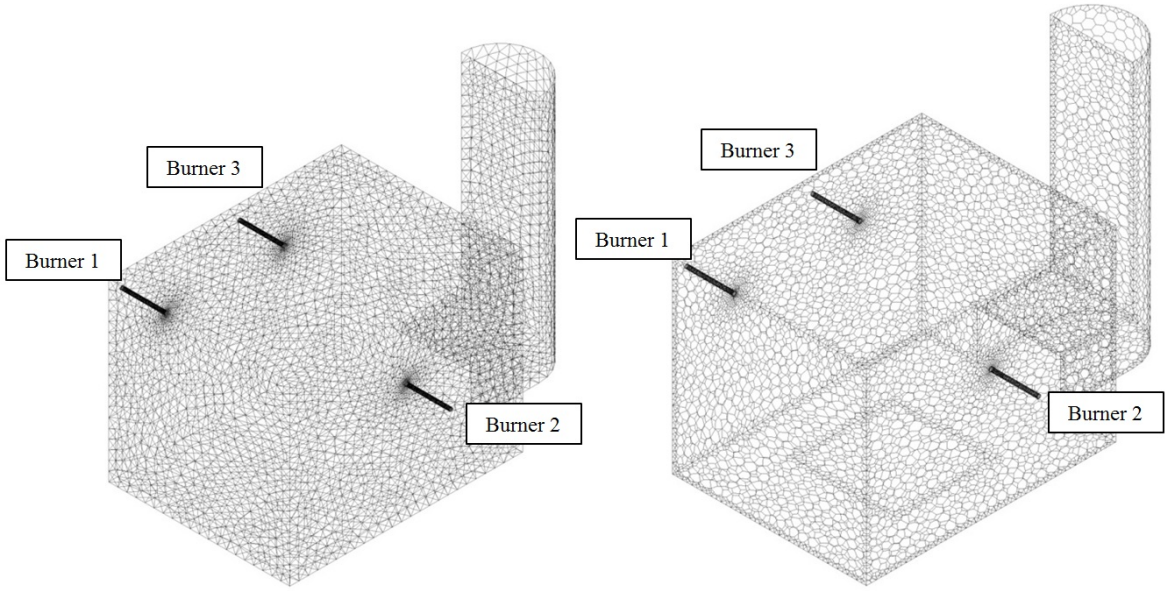

Fig. 57. Computational grids of the lab-scale furnace without walls: tetrahedrons (left), polyhedrons (right).

Table 13
Grids for the independency tests.

Name	Cell types	Number of cells	Max. skewness	Max. aspect ratio
Tet	Tetrahedrons	588,759	0.894	22.3
Poly	Polyhedrons	131,173	0.752	13
Hex1	Hexahedrons + Wedges + Tetrahedrons	476,822	0.899	136
Hex2	Hexahedrons + Wedges + Tetrahedrons	426,563	0.899	51

For the grid independency tests, fuel input of 27.3 kW was chosen with an equivalence ratio of 0.97. Pure oxygen was used as the oxidant. Burner 2 was activated in the CFD simulation. For combustion and radiation modelling, the SFM with the skeletal25 mechanism and the DOM were used. The SFM was applied for these tests because it has the lowest computational demand. Additionally, the DOM was used because of its wide range of applicability in combustion modelling. For the spatial discretization of all scalars, the second order upwind scheme was used.

The temperatures calculated with the different meshes are presented in Fig. 58. Simulations with the Tet and Poly grids predict shorter flames with a slight deflection upwards although the buoyancy effects were disabled in the CFD model. The hexahedron grids predicted a similar flame shape along the burner axis, although Hex2 has a finer grid structure in the flame zone.

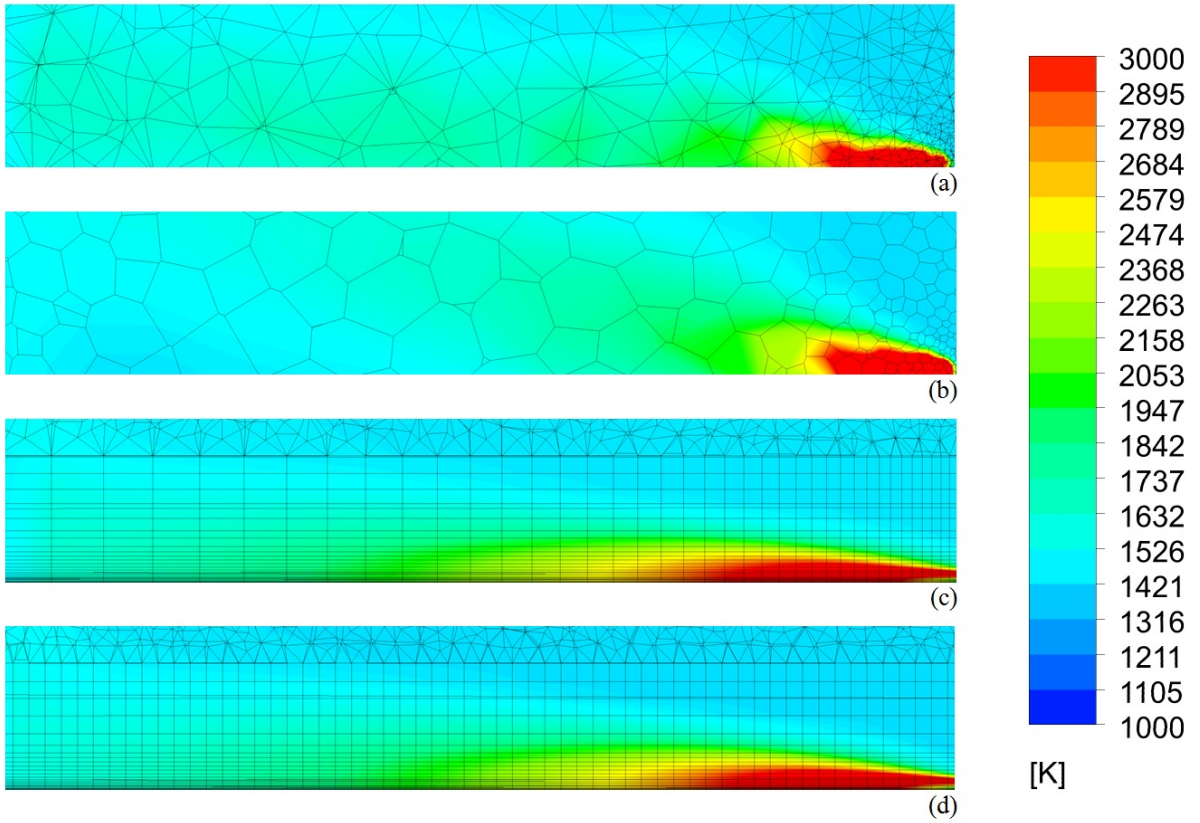

Fig. 58. Contour plots of the temperature for the different grids along the axis of burner 2: (a) Tet, (b) Poly, (c) Hex1, (d) Hex2.

Since the hexahedron grids simulated a reasonable flame shape compared to literature (e.g. Yin et al. [74]), a Richardson extrapolation [146] was carried out for the Hex2 mesh to determine the grid independency. The discrete solution can be assumed by a series given in Eq. (128), where ϕ is the numerical solution (e.g. temperature etc.), ϕ_{exact} is the exact result, and h is the typical grid cell size [153].

$$\phi = \phi_{exact} + a_1 * h + a_2 * h^2 + a_3 * h^3 + \cdots \quad (128)$$

For second order methods the term with h^2 is the most dominant term in Eq. (128). With the Richardson extrapolation, the results of a systematically refined grid can be the basis for the approximation of the exact solution given in Eq. (129). In this equation, r is the refinement factor, p is the formal order of the algorithm accuracy ($p = 2$) and the indices 1 and 2 represent the fine and coarse grids, respectively.

$$\phi_{exact} \approx \phi_1 + \frac{\phi_1 - \phi_2}{r^p - 1} \quad with \quad r = \frac{h_1}{h_2} \tag{129}$$

The Hex2 mesh was defined as the coarse mesh for the Richardson extrapolation. A second mesh based on the Hex2 mesh was created, with a refinement factor of 2, resulting in a fine grid with 3,420,684 cells. To determine the discretization errors of the two meshes compared to the exact solution Eq. (130) and (131) were used.

$$E_1^{fine} = \frac{\phi_2 - \phi_1}{1 - r^p} \tag{130}$$

$$E_2^{coarse} = \frac{r^p * (\phi_2 - \phi_1)}{1 - r^p} \tag{131}$$

The discretization errors were calculated for only four points in the domain. These points are the measurement positions in the lab-scale furnace T1 to T4 and are summarized in Table 14. The results show that the maximum error for the coarse mesh is 1.87 K, which is a relative error of 0.12 %. A maximum deviation of 2 K is sufficient for the CFD simulation in this thesis, especially when the error of the measurement equipment is in the same range for such high temperatures. For the fine grid the deviation from the exact solution was between 0.24 and 0.47 K. From these results, it can be concluded that a mesh with approximately 400,000 cells should be able to predict the combustion process sufficiently, especially when the main reaction zone is resolved by small cells and a moderate cell growth rate.

Table 14
Discretization errors on the Hex2 mesh and the refined version.

Measurement position	E_1^{fine} [K]	E_2^{coarse} [K]	E_2^{coarse}/ϕ_2 [%]
T1	0.39	1.58	0.11
T2	0.47	1.87	0.12
T3	0.24	0.96	0.06
T4	0.31	1.24	0.08

Based on the results of the Richardson extrapolation, the numerical grids for the lab-scale furnace with and without load were created according to Section 4.5.1. For both meshes, the number of cells was significantly higher than the tested Hex2 mesh.

The same procedure was carried out for the computational grid with thermal load. For this extrapolation, the grid described in Section 4.5.1 was used as the coarse one, with 1,431,339 cells. The refined version has an overall number of 11,465,154 cells. CFD simulations were done for the experiment 1220-OEC_100. The other settings were the same as for the grid without thermal load, mentioned above. Due to the fact that the mesh with

thermal load contains more than one million cells, the maximum discretization error is lower than for the Hex2 mesh (approximately 1 %). The discretization errors are displayed in Table 15.

Table 15
Discretization errors for the mesh with thermal load.

Measurement position	T_{coarse} [K]	E_1^{fine}/f_2 [%]	E_2^{coarse}/f_2 [%]
T1	1540	-0.19	-0.77
T2	1535	-0.26	-1.04
T3	1512	-0.15	-0.61
T4	1488	-0.27	-1.10

6.2 Turbulence models

As described in Section 4.2, three turbulence models were investigated for their applicability to the prediction of jet flames. Combustion and radiation models were chosen according to the grid independency test in Section 6.1. Although the turbulence models were applied for almost every combustion case carried out in these experiments, only experiments 1220-OEC_30 and 1220-OEC_100 are considered in this section.

In Fig. 59, the calculated temperatures along burner 2 are displayed. It is possible to see that the realizable k-epsilon model and the RSM predict a similar flame length and shape. Besides the same flame shape, the maximum flame temperature was predicted to be about 2000 K with the RSM, whereas the results of the realizable k-epsilon model showed a lower temperature of 200 K. The flame length, simulated with the standard k-epsilon model, was in close accordance to the other turbulence models; however, the flame shape was significantly different. For the axisymmetric jet, the spreading rate was over-predicted by the standard k-epsilon model, and therefore the temperature in the vicinity of the burner outlet was very high, with values above 1400 K. Such high temperatures would cause damage to the tips of the burner during furnace operation, which was not determined after the experiments. In contrast, the cold jets of the natural gas and oxidant stream are well defined downstream (blue contour at the burner outlet). These streams cool the burner tips and prevent burner damage caused by overheating.

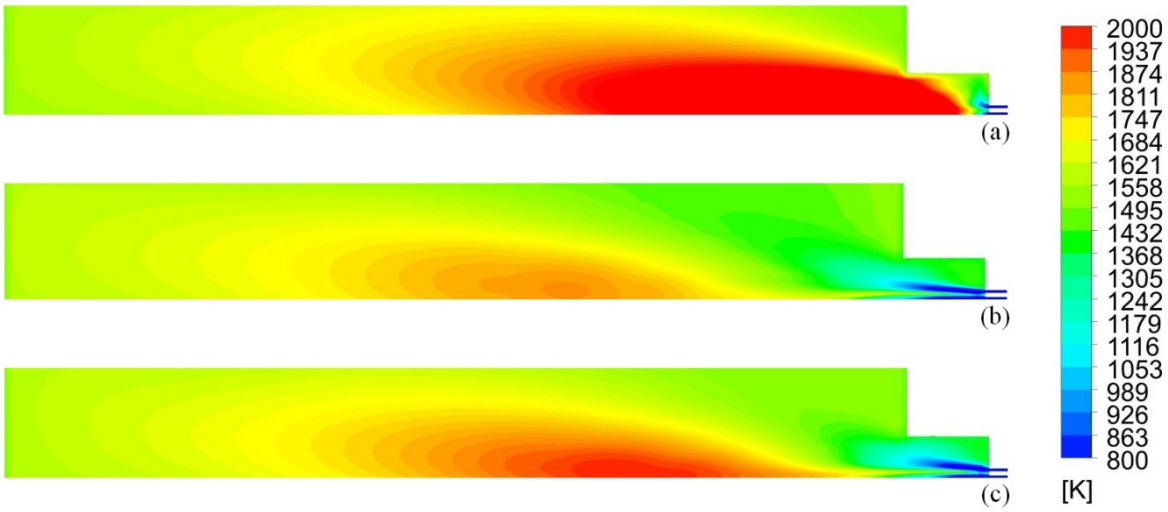

Fig. 59. Contour plots of the temperature at 30 % O_2: (a) standard k-epsilon, (b) realizable k-epsilon, (c) RSM.

The same investigation was carried out for combustion with pure oxygen (1220-OEC_100), as can be seen in the temperature profiles of burner 2 in Fig. 60. In contrast to the case with 30 % O_2, a small difference can be detected in the flame length between the realizable k-epsilon model and the RSM. The RSM predicts a slightly higher spreading rate of the jet right after the burner exit. This can be determined by the shorter jet of the oxidant (blue region at the burner outlet) compared to the realizable k-epsilon model. This effect leads to a shorter flame with the RSM. Nevertheless, both models are in close accordance with one another. For the standard k-epsilon model, the spreading rate is much higher than in the combustion case with 30 % O_2. Again, the gas temperature is too high in the vicinity of the burner, where values above 2000 K were found.

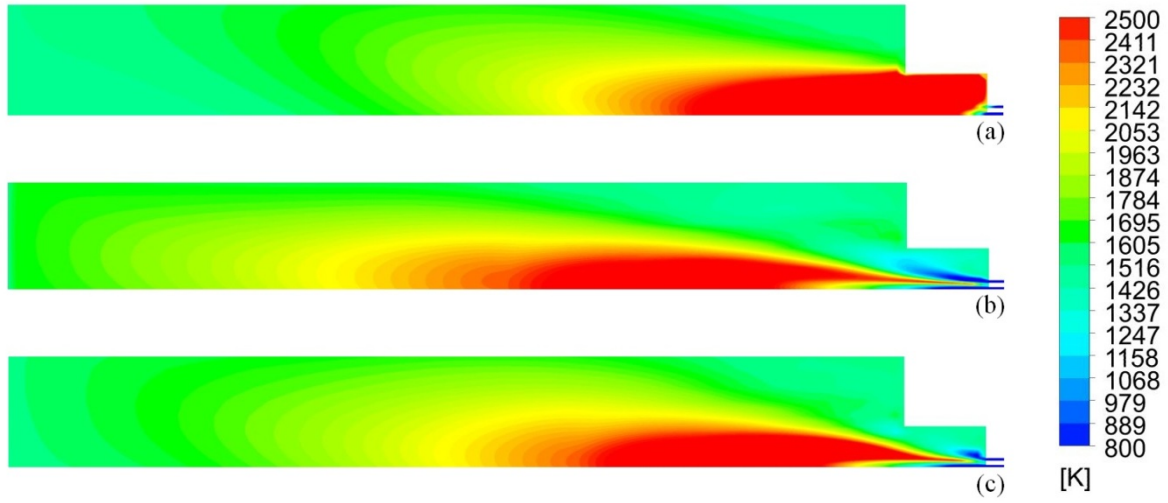

Fig. 60. Contour plots of the temperature at 100 % O_2: (a) standard k-epsilon, (b) realizable k-epsilon, (c) RSM.

A comparison between the measured and calculated temperatures is given in Fig. 61. In the case of 30 % O_2 (see Fig. 61a), it can be seen that all turbulence models lead to the same

over-prediction of the temperature at T1 and T2 of about 20 to 40 K, which can be explained by more air leakage in the back of the furnace during the test run. The measurements at T3 and T4 are in good agreement with all turbulence models. The experimental data for the combustion with pure oxygen showed that not only T3 and T4 are well predicted by CFD, but also T1 and T2. Only marginal differences between the turbulence models were found when the results were compared with the measured temperatures.

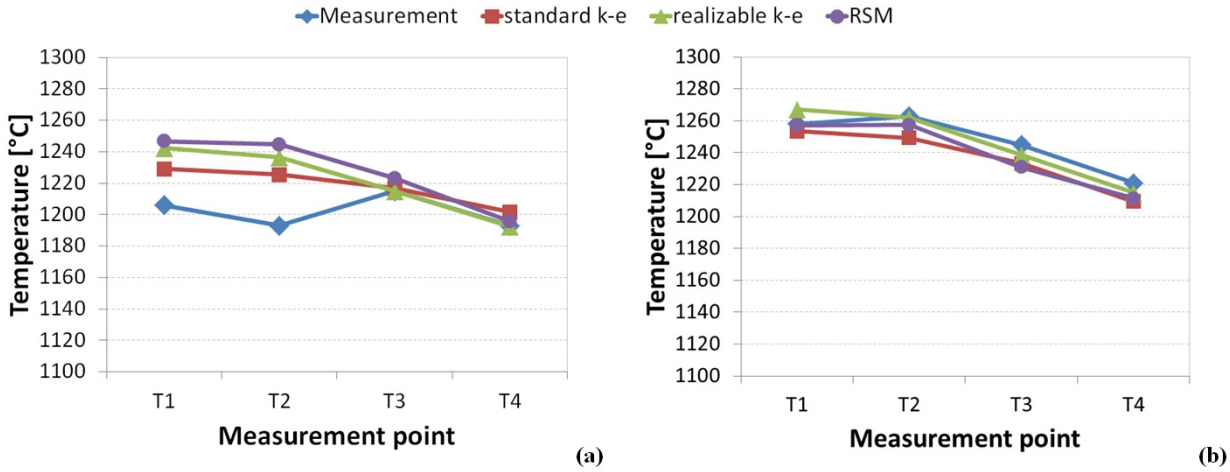

Fig. 61. Measured and calculated temperatures with different turbulence models: (a) 30 % O_2, (b) 100 % O_2.

The analysis showed that the realizable k-epsilon model as well as the RSM predicts the flame shape of the jet flame with a similar spreading rate for 100 % O_2. However, a small deviation was found at 30 % O_2, where the flame is a bit longer with the realizable k-epsilon model. Although the predicted temperatures from the standard k-epsilon model were quite accurate in relation to the measurement, this turbulence model was not able to predict the spreading rate of the jet flame. As a consequence, the standard k-epsilon model calculated too high temperatures at the burner and is therefore not suitable for further simulations in this thesis. Since, the realizable k-epsilon model can be applied in the CFD simulation by solving only two additional transport equations, it is a time saving alternative to the RSM. Thus, it was used for the subsequent simulations in this section.

6.3 Radiation models

In this section, the differences between the DOM and P1 model in CFD simulation of oxy-fuel combustion will be examined. These simulations were carried out with boundary conditions from 1-OXY_100.

In Fig. 62, the calculated temperatures of burner 2 are shown for the DOM and P1 model. From the contour plot, it can be seen that the maximum temperature predicted by the DOM

was slightly higher than that of the P1 model. The DOM produces a flame which is deflected upwards due to buoyancy effects. However, this was not observed with the P1 model. Although the flame temperature is not significantly lower with the P1 model, this could explain the flame's lack of uplift. In the present test case, the P1 model tends to over-predict the radiation intensity and lower the gas temperature. This leads to a more homogeneous temperature distribution in the furnace, which is barely detectable in the contour plot.

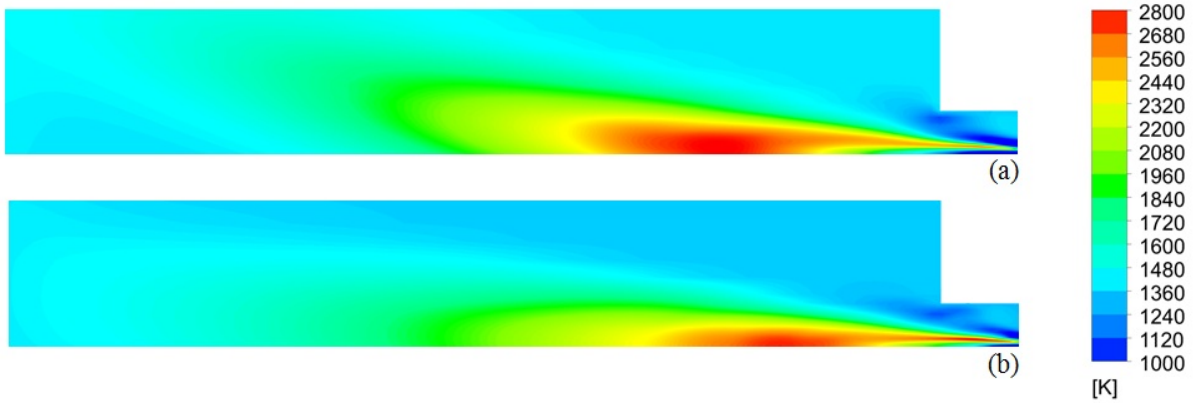

Fig. 62. Temperature plot of burner 2 for 1-OXY_100: (a) DOM, (b) P1 model.

A better view of the more homogeneous temperature distribution using the P1 model is given by the comparison with the measured temperatures in Fig. 63. Due to the overestimated radiative heat flux, the predicted temperatures at T1 to T4 show small differences. Furthermore, the simulated temperature level is 40 to 70 K lower than the measured temperatures. In contrast, the measured temperatures are in close accordance to the results with the DOM. Even the temperature peak at T2 (above the flame of burner 2) was well predicted using the DOM. For example, the difference between the temperature peak (T2) and T1 was simulated with a value of 40 K compared to 43 K from the measurement. This difference was not covered by the P1 model with a value of 14 K, and is therefore not suitable for operating conditions in OEC. The basic theory is that the DOM requires higher computational costs (depending on the spatial discretization) to solve the RTE compared to the P1 model. However, during these CFD simulations, this theory was not observed to be true. In the cases presented, simulation with the DOM was finished after 4 days whereas, with the P1 model, convergence was only reached after 7 days. The reason for this was a larger number of iterations necessary to reach convergence with the P1 model.

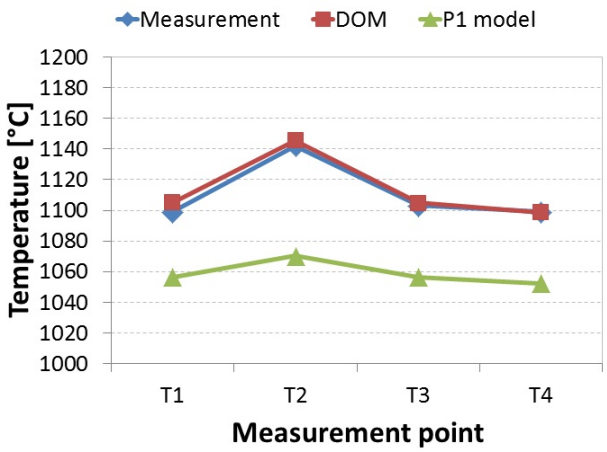

Fig. 63. Comparison of temperatures calculated with different radiation models and measured temperatures.

The present results of the DOM and P1 model are in contrast to Habibi et al. [16], which found that both models calculated the same radiative heat flux. This is in conjunction with the larger dimensions (6.796 x 1.2 x 3.0 m) and higher optical thickness of the furnace investigated by the authors. Since the P1 model is suitable for a high optical thickness, the results for the P1 model and DOM published by Habibi et al. [16] are similar. The optically thin atmosphere of the lab-scale furnace can be seen as the origin of the inaccuracy of the P1 model.

6.4 Combustion models and reaction mechanisms

The applicability of different combustion models and reaction mechanisms for air-fuel and oxy-fuel combustion is investigated in this section, with the main aim of finding a time efficient CFD model. For this purpose, different reaction mechanisms were tested with the SFM and EDC models. The most suitable mechanisms are then applied to compare the predicted results and calculation times between EDM, EDC and SFM.

6.4.1 SFM with different reaction mechanisms

The skeletal25, smooke46, DRM19 and GRI3.0 mechanisms were applied in combination with the SFM. From the information presented in Sections 5.2 and 5.3, it is to be expected that the GRI3.0 mechanisms will simulate similar results to the smooke46 and DRM19; thus, the GRI3.0 is not considered in this section. Simulation results with the GRI3.0 mechanism for oxy-fuel combustion have already been presented in Prieler et al. [151]. The simulations presented here were done according to the experiments 2-OEC_21 to 2-OEC_100, without thermal load.

6.4.1.1 Temperature

In the following five figures (Fig. 64 to Fig. 68) the contour plots of the temperature along burner 2 are displayed for 21 to 100 % O_2. For conventional natural gas combustion with air, the temperature profiles of the flames are in close agreement for all investigated reaction mechanisms. The maximum flame temperature of approximately 1400 °C was also calculated in the same range. An increase of the oxygen enrichment level up to 25 (Fig. 65) and 30 % O_2 (Fig. 66) leads to minor differences in the flame predicted with the skeletal25 mechanism. The smooke46 and DRM19 mechanisms predict a flame which is split in two regions of the maximum temperature (more obvious in Fig. 66), which was not detected with the skeletal25 mechanism. At this enrichment level, the first small differences in the pre-calculated flamelet library occur in the range of the stoichiometric mixture and small scalar dissipations (see Fig. 45). A further increase in the oxygen enrichment to 45 and 100 % O_2 intensifies this effect. In Fig. 67 and Fig. 68, it can be observed that the region of flame ignition is very similar between the reaction mechanisms. Nonetheless, after ignition, the smooke46 and DRM19 mechanisms calculate a cooler region enveloping the vicinity of the burner outlet. Especially for the case of 100 % O_2, the cooler region shows temperatures below 300 °C which is obviously false. In contrast, the skeletal25 mechanism was able to simulate a reasonable flame shape and temperature profile in the full range of oxygen enrichment as well as air-fuel combustion.

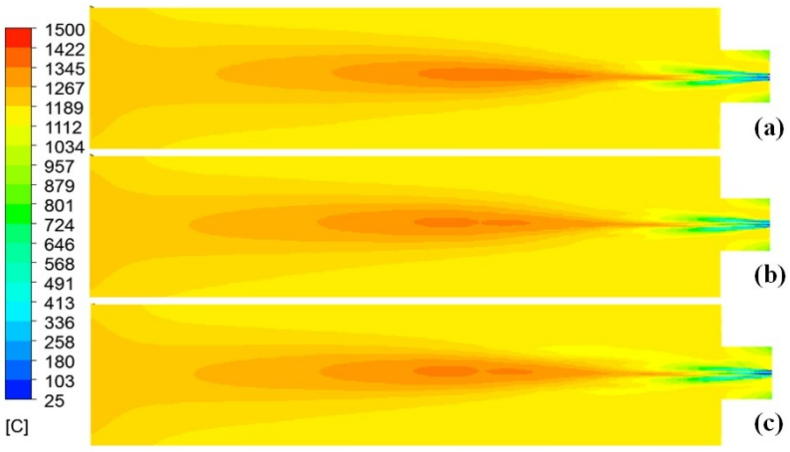

Fig. 64. Contour plots of the temperature along burner 2 for 21 % O_2 calculated with SFM: (a) skeletal25, (b) smooke46, (c) DRM19.

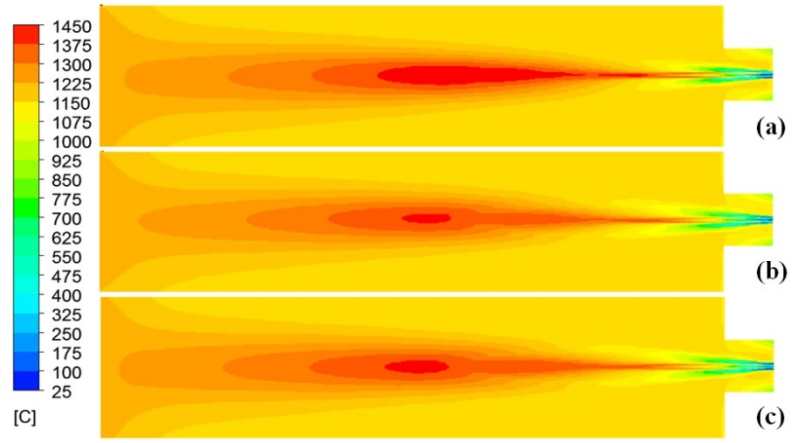

Fig. 65. Contour plots of the temperature along burner 2 for 25 % O_2 calculated with SFM: (a) skeletal25, (b) smooke46, (c) DRM19.

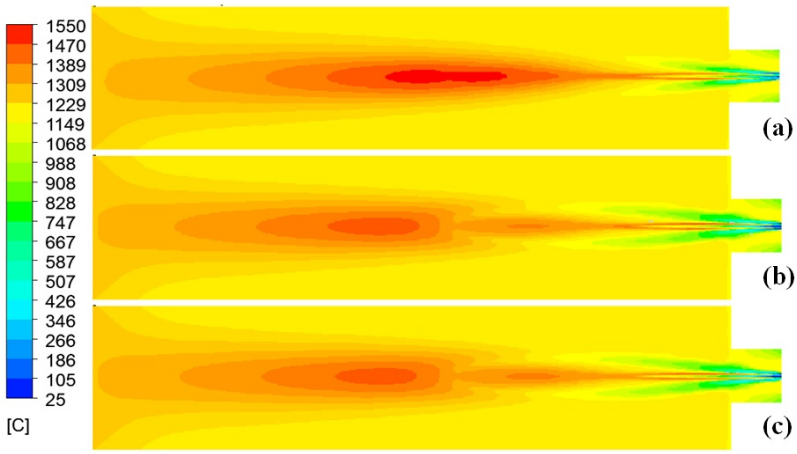

Fig. 66. Contour plots of the temperature along burner 2 for 30 % O_2 calculated with SFM: (a) skeletal25, (b) smooke46, (c) DRM19.

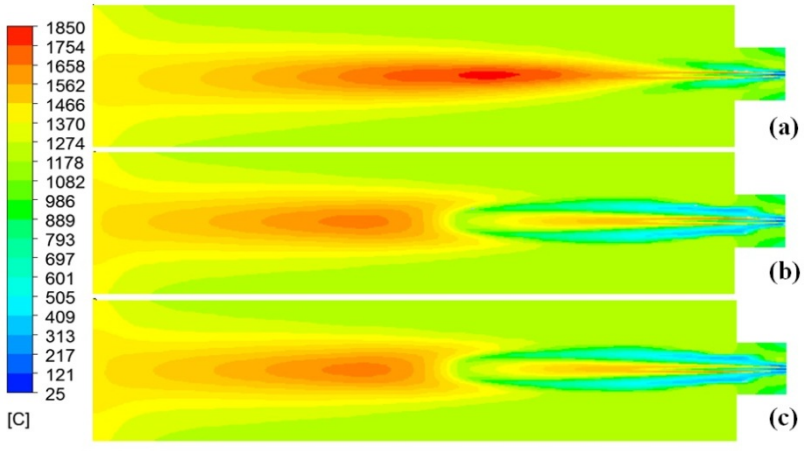

Fig. 67. Contour plots of the temperature along burner 2 for 45 % O_2 calculated with SFM: (a) skeletal25, (b) smooke46, (c) DRM19.

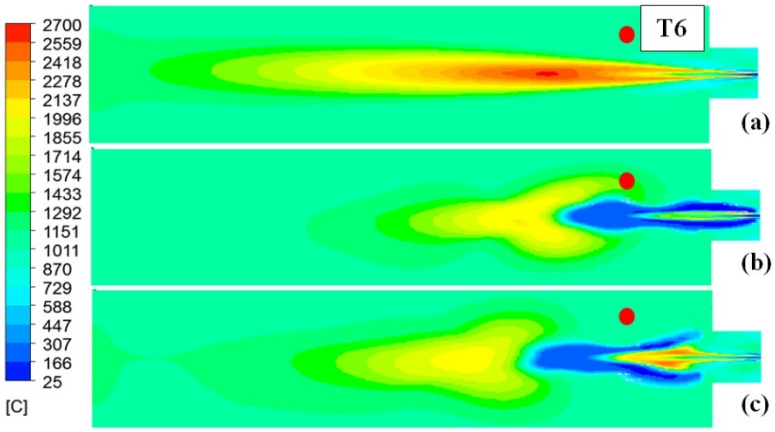

Fig. 68. Contour plots of the temperature along burner 2 for 100 % O_2 calculated with SFM: (a) skeletal25, (b) smooke46, (c) DRM19.

In Fig. 69, the reason for the cooler region in the vicinity of the burner using the smooke46 and DRM19 mechanisms is examined. Although this figure represents the CFD results for the 1220-OEC_100 case, the same conclusion can be made for the experiments at lower temperature levels (1000-OEC_100). The black line shows the position where the flame temperature starts to decrease. In the contour plots below, the values for the scalar dissipation and mean mixture fraction are approximately 1 s^{-1} and 0.2, respectively. Furthermore, the mixture fraction variance was very low. A comparison with the flamelet library shows that the position of the temperature decrease in the CFD simulation fits with the marked part of the flamelet library. Although the skeletal25 mechanism calculates much higher temperatures in the flamelet, the CFD simulation showed a maximum temperature of approximately 2700 °C for 100 % O_2 due to heat loss via radiation (see Fig. 68). This heat loss was not considered during the flamelet calculation, but was taken into consideration in the PDF generation procedure. Section 5.4 presented the calculated temperatures in the PDF with heat loss and showed the same trend as the flamelet. This trend is that the predicted temperature in the region of the stoichiometric mixture is higher when the skeletal25 mechanism is used. In contrast, the heat loss significantly affects the results with the smooke46 and DRM19 mechanisms, resulting in a temperature decrease.

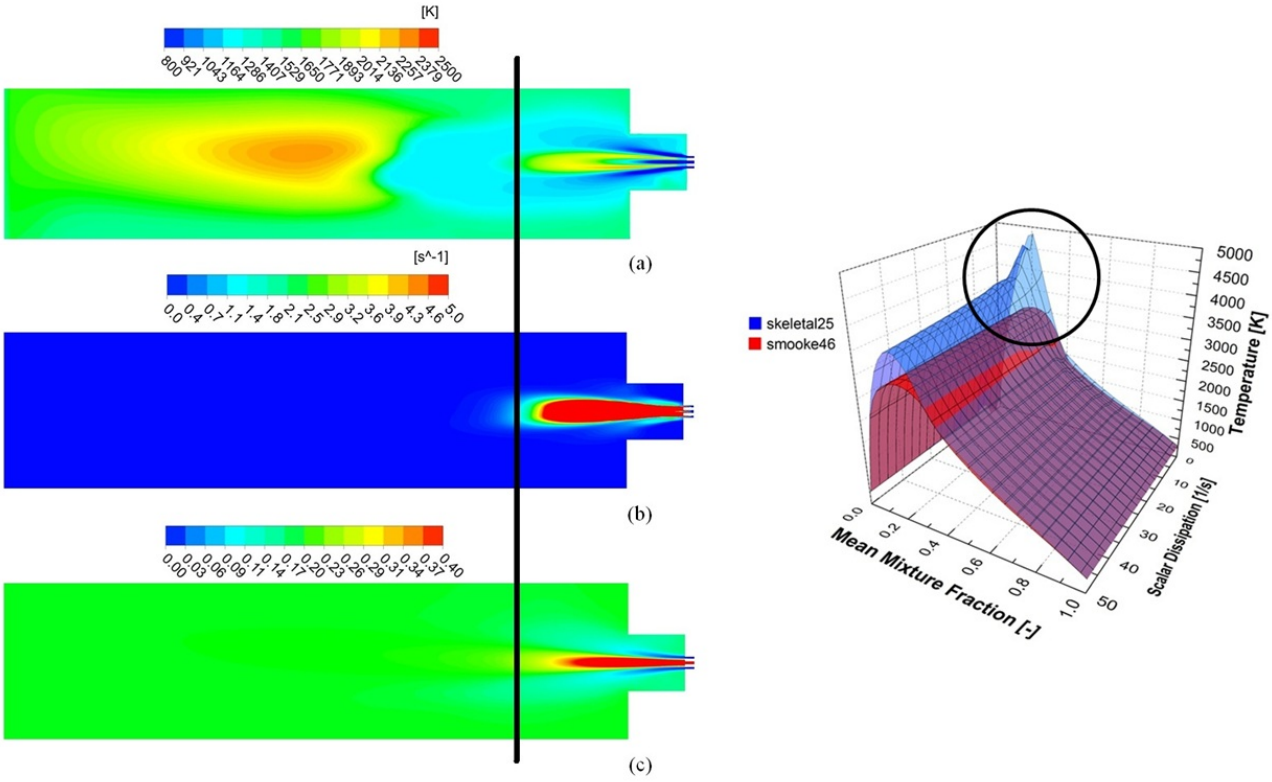

Fig. 69. Simulated values for the temperature (a), mean mixture fraction (b) and the scalar dissipation (c) with the smooke46 mechanism and 100 % O_2 in the oxidant.

A comparison between the simulated temperatures with the three reaction mechanisms and the measured data in the lab-scale furnace can be found in Fig. 70. Starting with air-fuel combustion, all of the reaction mechanisms were able to predict the measured values in the furnace with the SFM. Since T2 is arranged above the flame of burner 2, the measured temperature is higher, which can be said of all CFD simulations. Furthermore, T7 on the opposite wall of burner 2, is an indicator of the flame length. The measurement at T7 shows higher temperatures for longer flames. For 21 % O_2, the temperature at T7 was well predicted, and as a consequence, the flame length was as well. For the measurement positions T1 to T6, a close accordance to all reaction mechanisms was also found for oxygen enrichment up to 45 % with a maximum deviation of 27 K (T2 at 30 % O_2).

The measured oxygen concentration in the flue gas, reported in Section 3.1, shows that the air leakage increases with higher oxygen enrichment. To achieve the same concentration of O_2 in the flue gas, the equivalence ratio in the CFD simulation was slightly decreased, causing a higher mass-flow rate of oxidant. This higher momentum in the axial direction caused a longer flame and higher temperatures at position T7 (opposite of burner 2). The deviation between measurement and CFD increases with the oxygen enrichment, and, as a consequence, with the level of air leakage (compare O_2 concentrations in Table 4).

For the combustion of natural gas with pure oxygen in the lab-scale furnace, the reaction mechanisms vary significantly. The best agreement to the measured data can be found with the skeletal25 mechanism, as expected based on the temperature profiles above. It shows a similar temperature at T2, located above the flame of burner 2. The measurement points T1 as well as T3 to T6 are over-predicted by about 40 K by the skeletal25 mechanism. Although the temperature distribution in the furnace was expected to be very homogeneous, the measured values show a higher difference between the peak temperatures (T2 and T7) and the others. It was found that the measured temperatures T1 and T3 to T6 were affected by the air leakage, which has the highest intensity with 100 % O_2 (see O_2 concentration in the flue gas - Table 4). This additional ambient air cools down the flue gas in the furnace. Since T2 and T7 were arranged in the vicinity of the flame, which is in the middle of the furnace, these positions were hardly affected by the air leakage, which is why these temperatures are higher. The simulated temperature distribution with the skeletal25 mechanism is quite homogeneous in the entire furnace, but predicted a slightly longer flame (see T7). Nevertheless the skeletal25 mechanism with the SFM was also able to predict the entire range of OEC. All simulations using the SFM were finished after approximately 3 days (Hardware: 8 core-CPU, 32 GB RAM; Grid: approximately 630 000 cells).

The anomaly at T6 for 100 % O_2, which was predicted by the smooke46 mechanism, is displayed in Fig. 68b. In this figure, the measurement position of T6 is marked with a red dot. It can be seen that the smooke46 mechanism predicts higher temperatures at T6, which is caused by the anomaly in the flame shape as predicted by the smooke46 and DRM19 mechanisms (see Fig. 68).

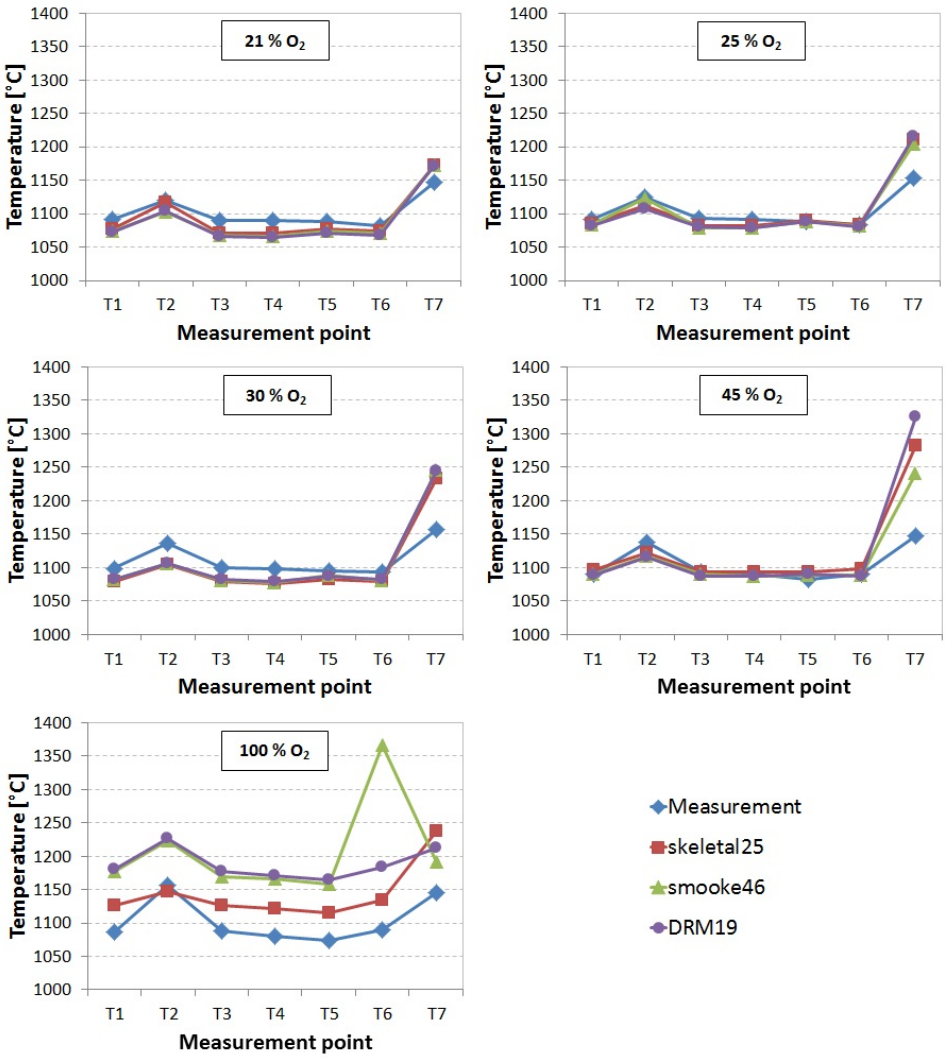

Fig. 70. Measured and calculated temperatures for the 2-OEC experiments.

6.4.1.2 Mole fractions of CO and OH

As stated in Section 5.3, the skeletal25 mechanism was expected to predict lower concentrations of CO and radicals in the flame compared to the smooke46, DRM19 and GRI3.0 mechanisms. This statement is validated by the results in the present section.

Fig. 71 to Fig. 73 display the mole fractions of CO in the flame of burner 2 for 21, 45 and 100 % O_2. For air-fuel combustion, the difference between the reaction mechanisms is quite minor for the CO concentrations (see Fig. 71). OEC cases of 45 and 100 % O_2 (see Fig. 72 and Fig. 73), simulated with the smooke46 and DRM19, show a significant difference for the CO concentrations compared to the skeletal25 mechanism. Here, the CO concentration is higher in the region near the burner (see red circle). Additionally, the jet formed by the CO concentrations has a different shape with the smooke46 and DRM19 at 100 % O_2 compared to the simulation with the skeletal25 mechanism. Despite the different shape of the jet formed

by the CO plots, the difference in the predicted values for the maximum CO mole fraction in the flame between the reaction mechanisms is minor.

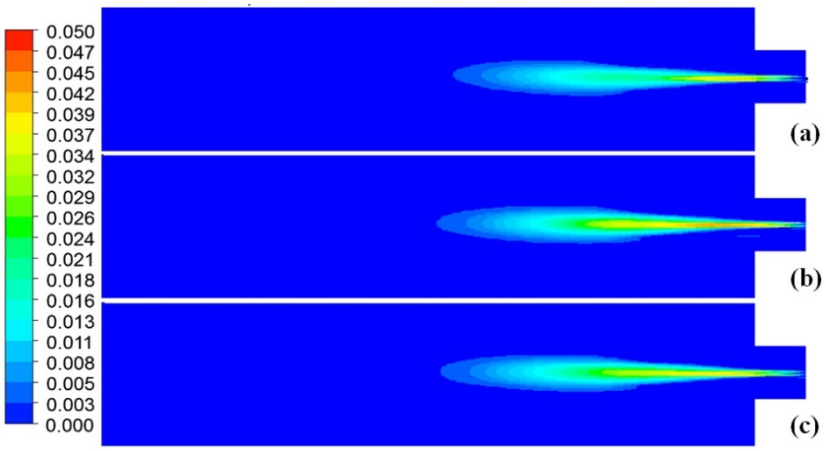

Fig. 71. Contour plots of the CO mole fraction along burner 2 for 21 % O_2 calculated with SFM: (a) skeletal25, (b) smooke46, (c) DRM19.

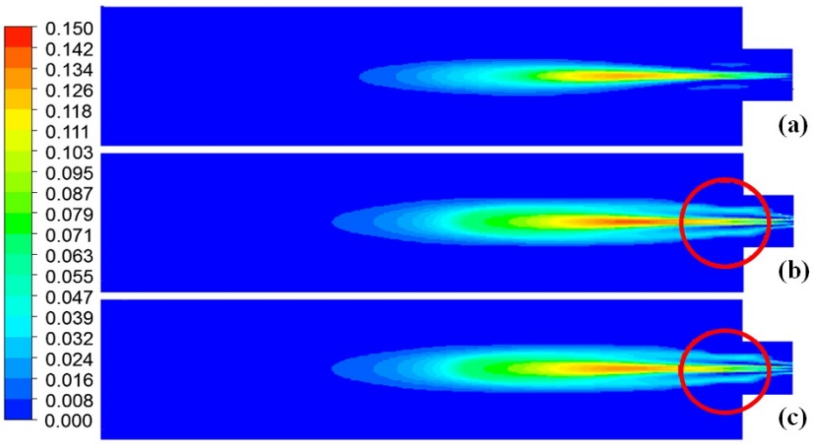

Fig. 72. Contour plots of the CO mole fraction along burner 2 for 45 % O_2 calculated with SFM: (a) skeletal25, (b) smooke46, (c) DRM19.

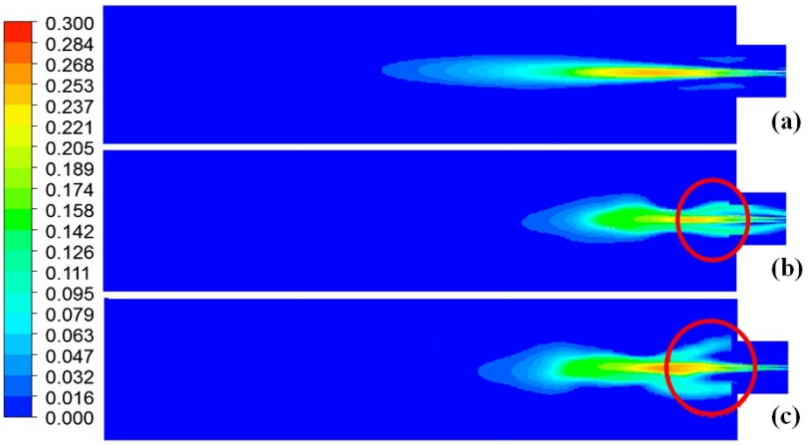

Fig. 73. Contour plots of the CO mole fraction along burner 2 for 100 % O_2 calculated with SFM: (a) skeletal25, (b) smooke46, (c) DRM19.

During the sensitivity analysis in Section 5.3.2, the highest sensitivity was found in the production/destruction of H_2O with the skeletal25 mechanism. Thus, the difference in the OH radical, mainly involved in the reactions for the production/destruction of H_2O, should be higher when the reaction mechanisms are compared.

In Fig. 74 and Fig. 75, the OH mole fractions in the flame are presented for 21 and 100 % O_2. Similar to the predicted CO concentrations, the contour plots for the OH radicals show no differences between the reaction mechanisms for air-fuel combustion. However, the combustion with pure oxygen leads to wrong concentrations of the OH radicals with the smooke46 and DRM19 mechanisms. Whereas the skeletal25 mechanism predicts values of approximately 1 to 3 % in the main reaction zone, the other mechanisms obviously over-predict the formation of OH radicals. It is not just that the maximum concentration with 10 % is too high, but also that the highest concentration occurs in the cooler region enveloping the vicinity of the burner. Based on the chemical equilibrium for the dissociation of water in Fig. 18, temperatures above 2500 K are necessary. Since the smooke46 and DRM19 show the highest OH concentration in cooler regions, it was concluded that these mechanisms are not able to cover the dissociation effects in the oxy-fuel flame.

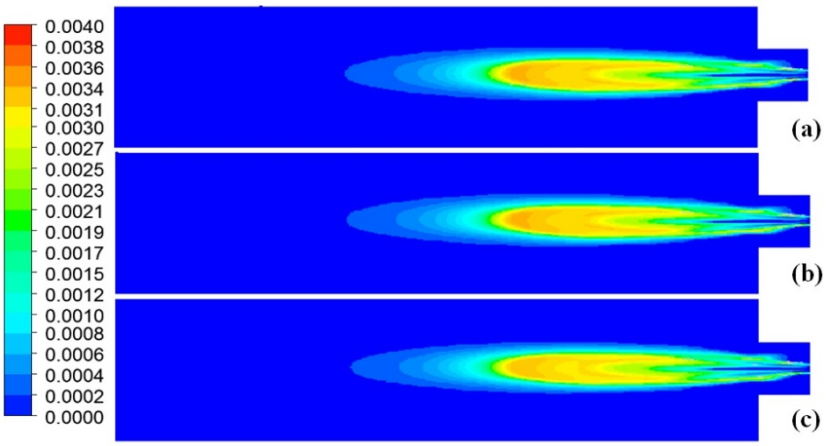

Fig. 74. Contour plots of the OH mole fraction along burner 2 for 21 % O_2 calculated with SFM: (a) skeletal25, (b) smooke46, (c) DRM19.

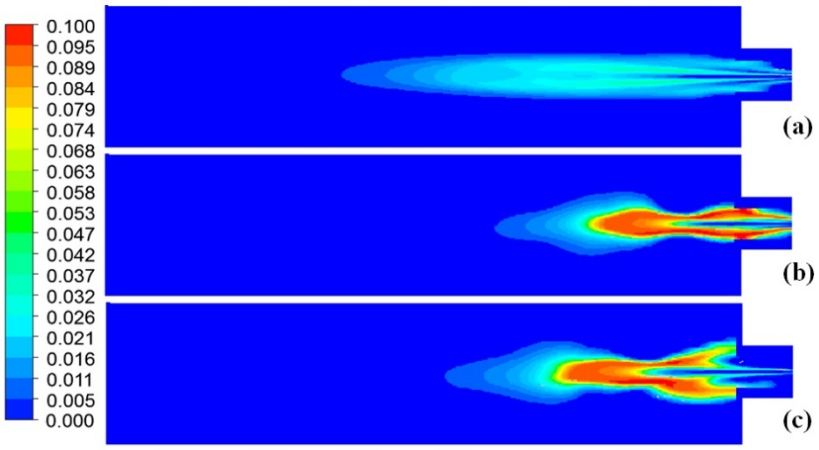

Fig. 75. Contour plots of the OH mole fraction along burner 2 for 100 % O_2 calculated with SFM: (a) skeletal25, (b) smooke46, (c) DRM19.

6.4.2 EDC with different reaction mechanisms

With the EDC model, only two mechanisms were investigated due to the high computational costs of this method.

6.4.2.1 3-step global mechanism

Global mechanisms have successfully applied to air-fuel combustion in the past (e.g. Westbrook and Dryer [73], Jones and Lindstedt [75]). In the case of oxy-fuel combustion, these mechanisms tend to over-predict the reaction rate, which leads to higher maximum flame temperatures. Therefore, the reaction parameters for the global reactions have to be adapted for natural gas combustion with pure oxygen, which was done, for example, by Yin et al. [74]. This adapted 3-step mechanism is tested in this section.

In Fig. 76, the contour plots of the temperature along burner 2 are displayed for 21 and 100 % O_2. Since the model parameters were adapted for oxy-fuel combustion, the CFD simulation for 21 % O_2 does not show a regular flame. Instead, the combustion takes place in the entire combustion chamber. In the oxy-fuel case, the 3-step mechanism with the EDC model shows a reasonable flame shape with a small ignition delay at the burner compared to the results of the skeletal25/SFM in the previous section. The maximum temperature was detected with a value of 2940 °C, which is approximately 200 K higher than the skeletal25/SFM.

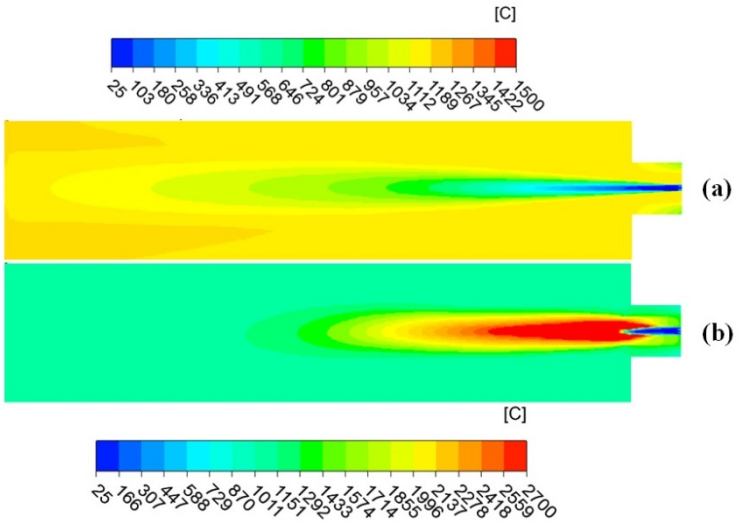

Fig. 76. Contour plots of the temperature calculated with the EDC model and the 3-step mechanism: (a) 21 % O_2, (b) 100 % O_2.

A comparison to the measured data revealed higher temperatures for all measurement points except T7 (see Fig. 77). Compared to the skeletal25/SFM, only the peak temperature T2 above the flame was over-predicted, which is a result of the higher maximum flame temperature further determined by T6 in the vicinity of the burner. Although the flame temperature is too high, T7 is in close accordance with the measurement. This can be explained by the shorter flame predicted with the 3-step mechanism. A comparison of the measurement and the CFD results for the air-fuel case reveals a significant difference in temperature from T1 to T5 with a peak level at T6 of more than 1350 °C.

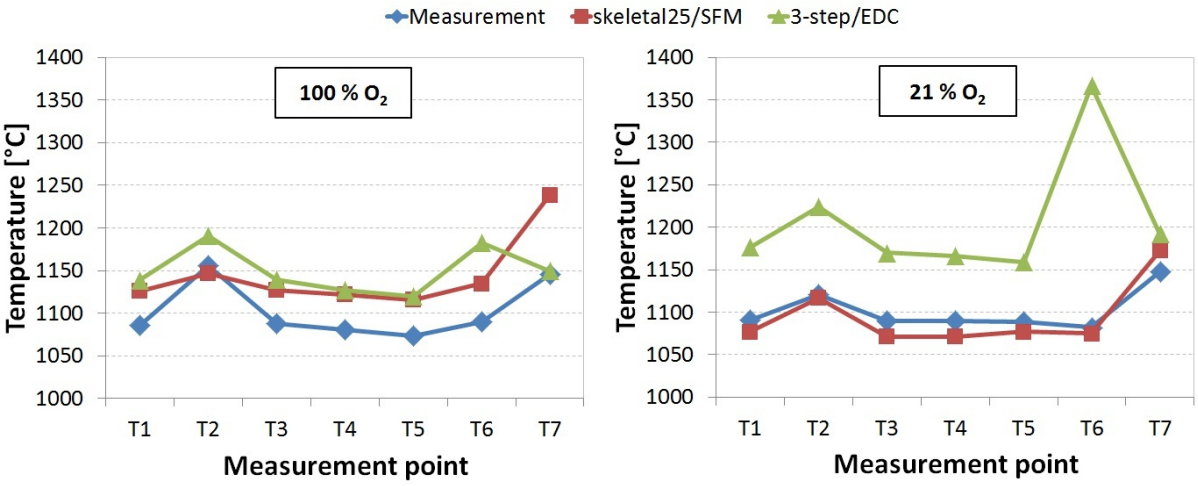

Fig. 77. Comparison of measured and calculated temperatures for the 3-step/EDC and skeletal25/SFM (left: oxy-fuel, right: air-fuel).

6.4.2.2 Smooke46 mechanism

Based on the Master's thesis of Stallinger [11], which found that the smooke46 mechanism can predict the oxy-fuel flame with the EDC model, this mechanism was used in this section.

In Fig. 78, the contour plots of the temperature along the burner are shown for the simulations with the skeletal25/SFM and smooke46/EDC. Both the predicted flame shape and the temperature level in the flame are very similar. The comparison with the measured data also showed very good accordance for this reaction mechanism combined with the EDC model. Although the EDC simulation with the smooke46 mechanism predicted good results, the calculation time of approximately 3 weeks was dramatically longer than for the SFM.

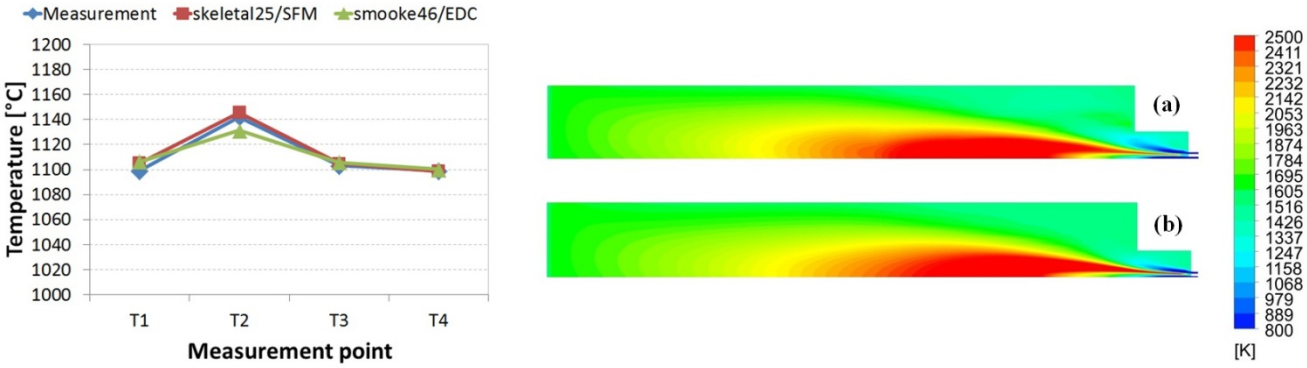

Fig. 78. Comparison of measured and calculated temperatures for smooke46 mechanism with the EDC model (left); Contour plot of the temperature with skeletal25/SFM (a) and smooke46/EDC (b).

6.4.3 Effect of turbulence/chemistry interaction models (EDM vs. EDC vs. SFM)

In this section, the SFM and EDC model are compared to the EDM with a 2-step approach. The EDM, as a so-called “mixed is burnt” approach, does not consider a set of chemical reactions with their Arrhenius parameters. Since the reaction kinetics, based on the Arrhenius approach is strongly related to the temperature, the reaction rate is calculated by two parameters. These parameters only consider the mixing rate in order to predict the reaction progress. Therefore, only 2 global reactions, with CO as intermediate species, are used with the EDM.

In Fig. 79, the simulations with the EDM, EDC model and the SFM are considered with regard to their temperature and species concentrations of CO_2, CO and OH along the centre line of the burner 2. For this purpose, the simulation for the experiment 1-OXY_100 was used. The EDM predicted a temperature peak that is 400 – 500 K higher than the results with the SFM and EDC model. Furthermore, the fuel conversion occurs at a faster rate with the EDM, indicated by the position of the temperature peak at 0.17 m. In contrast, in the other models, the peak is further downstream. Thus, it can be concluded that fuel conversion with the EDM is much faster due to the lack of a reaction kinetic and radical formation. This is further confirmed by the CO_2 and CO concentrations: the maximum CO_2 level is almost

reached at 0.17 m, where the highest temperature can be detected. Using the EDC model or SFM, the CO_2 concentration increases much more slowly and in conjunction with the higher CO level of about 25 %. The EDM predicts that the fuel conversion occurs too fast, and in addition, predicts higher flame temperatures along the burner axis. In contrast, the EDC and SFM calculations showed a good agreement with regard to the temperature and species concentrations along the burner axis. The simulated temperatures with the EDM, EDC model and SFM are compared to the measurement of 1-OXY_100 in Fig. 80. Despite the over-predicted flame temperature with the EDM, the temperature at T2 is 26 K lower than the measured value. This is due to the much shorter flame simulated by the EDM, which cannot reach T2 on the ceiling. The other temperature positions are in good agreement with the EDM. Although the EDM can predict the temperature in the furnace quite well, it is not suitable for calculating cases of oxy-fuel combustion. This is because this model is not able to predict the flame length nor, of particular importance, the flame temperature. Thus, the radiation emitted by the flame, which is related to the flame temperature, is not predictable with the EDM. For this reason, the use of the EDM for oxy-fuel combustion in high temperature processes is not recommended. The results of the EDC model and SFM fit well with the measurements and were described in Sections 6.4.1 and 6.4.2.

A higher number of iterations was also necessary to achieve convergence with the EDM, which leads to an increased total calculation time. This could be a result of the neglected reaction kinetic, but given the unsuitability of the EDM, this effect was not further considered.

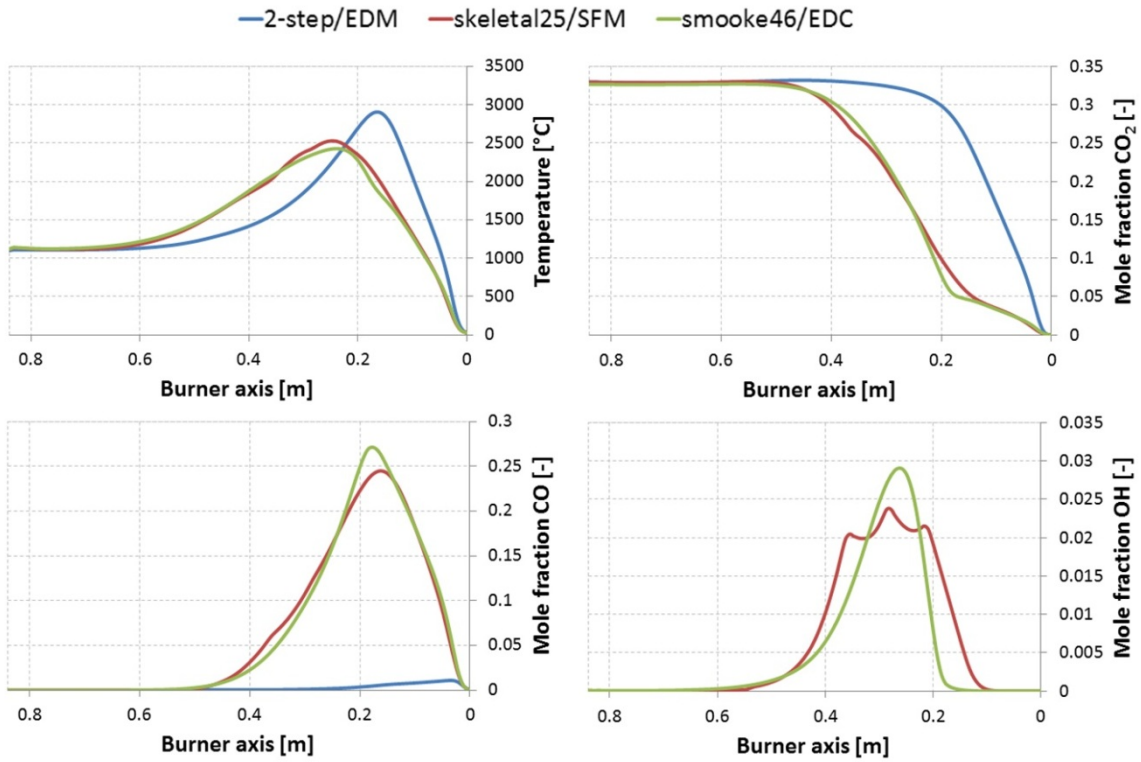

Fig. 79. Temperatures and mole fractions along the axis of burner 2 with different combustion models for the 1-OXY_100 case.

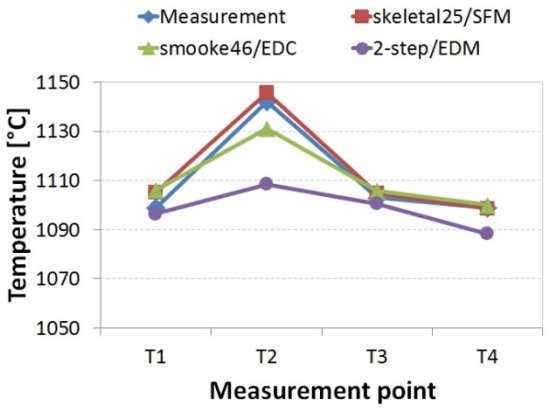

Fig. 80. Calculated temperatures with different combustion models and comparison with measurement.

6.4.4 Conclusion – Combustion models and reaction mechanisms for OEC

In this section, the investigations of the combustion models and reaction mechanisms for use in OEC will be summarized. Starting with the SFM, the skeletal25 mechanism was found to cover the entire OEC range, as well as the air-fuel combustion. The other reaction mechanisms showed only good agreement for air-fuel combustion or very low oxygen enrichments up to 30 % O_2. The main advantage of the SFM was the low computational demand. Using this model, all calculations were done within 3 days (Hardware: 8 core-CPU, 32 GB RAM; Grid: approximately 630 000 cells). The smooke46 mechanism with EDC also

showed good results and was in close accordance to the skeletal25/SFM; however, the calculation time was approximately 3 weeks. The EDM model was not found to be suitable for oxy-fuel applications because of the missing reaction kinetic. The “Mixed is burnt” approach leads to an over-prediction of the flame temperature, which would affect the calculation of the heat transfer in furnaces.

Due to both the accuracy of the predicted results and the time efficiency, the skeletal25 mechanism in conjunction with the SFM was found to be the best option for predicting OEC and air-fuel combustion cases. Thus, it was used for all CFD simulations presented in the following sections.

In Table 16, the models used for all further investigations in this thesis are summarized. This combination of chemistry and radiation models provided the best agreement with the measured data as well as the lowest computational costs.

Table 16
Most efficient combination of models to predict air-fuel and OEC.

Turbulence modelling:	Realizable k-epsilon
Turbulence/chemistry interaction:	SFM
Reaction mechanism:	skeletal25
Radiation modelling:	DOM

6.5 Efficiency analysis of OEC in the lab-scale furnace

An increase in process efficiency is an important step for future fuel savings and for the reduction of CO_2 emissions, especially for energy demanding high temperature processes in the steel, glass, cement and chemical industries. OEC provides one way of achieving this goal. In this section, the effect of OEC on fuel consumption and heat transfer in the lab-scale furnace is investigated at two temperature levels.

First, the fuel input was adapted for each OEC case in order to achieve the desired temperature levels of 1000 and 1220 °C. Thus, the fuel savings at higher oxygen enrichment levels can be determined. For this purpose, the furnace was operated without thermal load.

In the second part, experiments were carried out with the water cooled copper plate, which represents a thermal load in annealing and melting processes. In these experiments, the available heat transferred to the load was measured under different operating conditions (oxygen enrichment). From the available heat and fuel input, the efficiency of the heating process was derived, dependent on the oxygen level in the oxidant.

CFD simulations with the most efficient models, found in the last section, were carried out for all operating conditions. The ability of the developed CFD model to accurately predict the

temperature was examined in the previous section; however, for high temperature processing, the heat transfer in the furnace is also important. Therefore, the correct calculation of the heat transfer with the CFD model is tested in this section against the measured heat flux to the thermal load.

6.5.1 Lab-scale furnace without thermal load

The experiments without thermal load have already been described in Section 3.1.1 and were carried out for a target temperature of 1090 °C, indicated by measurement position T4 (called 2-OEC). Fig. 81 shows the fuel input, which is necessary to achieve the temperature level and the O_2 concentration in the dry flue gas. Since the experiments were done for the stoichiometric combustion of natural gas, oxygen was still present in the flue gas. This is an indication of air leaking into the furnace during the experiments. The lowest O_2 concentrations were found for air-fuel combustion and 25 % O_2 with a value of approximately 2 %. Air leakage also had a minor influence on the experiments when 30 % O_2 was used in the oxidant. In contrast, an increase up to 45 and 100 % O_2 reveals much higher oxygen concentrations of 3.74 and 5.76 % in the dry flue gas. This indicates even more air leakage. The reason for the higher air leakage in oxy-fuel combustion is the lower volume-flow rate of the flue gas due to the missing (reduced) nitrogen content. With the reduced flow rate, the operating pressure in the furnace is lower and ambient air can be drawn into the furnace. Considering the fuel input during the experiments (see Fig. 81), a significant decrease from 18 kW to 16 kW was achieved using pure oxygen instead of air as an oxidant. The use of oxygen enriched air showed a high fuel reduction even for small oxygen concentrations in the oxidant. From the experimental data, fuel savings of 1.5 kW with 25 % O_2 and 2 kW with 30 % O_2 was found. This corresponds to a reduction in the fuel consumption of 8.3 % and 11.1 % for 25 % O_2 and 30 % O_2, respectively, when compared to the air-fuel case. However, further fuel savings were not detected for higher oxygen enrichment levels of 45 and 100 % O_2. As mentioned before, the vast increase in air leakage with 45 and 100 % O_2 compensates for the effect of OEC. Therefore, fuel consumption was not further decreased. Nevertheless, the positive effects of OEC on the fuel consumption were highlighted for OEC up to 30 % O_2. Even with small additional amounts of oxygen in the oxidant, a reasonable improvement on the fuel consumption can be achieved.

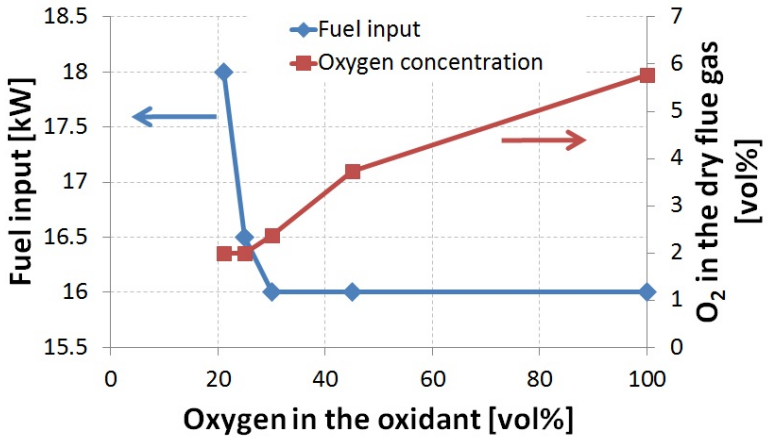

Fig. 81. Fuel input and O_2 concentration in the flue gas for the 2-OEC experiments.

Fig. 82 shows the heat losses through the outlet and the outlet temperatures of the flue gas, calculated by CFD simulations. The air-fired experiment revealed a heat loss through the outlet of 8 kW and a flue gas temperature of about 950 °C. Compared to the fuel input of 18 kW, approximately 45 % of the heat of formation exits the furnace through the outlet. The use of oxygen enriched air for the combustion in the lab-scale furnace leads to a higher radiative heat flux to the walls, caused by the increased flame temperature and concentrations of H_2O and CO_2. Hence, the outlet temperature of the flue gas decreases with the oxygen concentration in the oxidant. As a consequence, heat loss through the flue gas exit was significantly reduced. Considering the combustion with pure oxygen, the resulting outlet temperature was reduced to 761 °C. Only 11.5 % (1.84 kW) of the fuel input exits the furnace through the flue gas when pure oxygen is used for the combustion process. For air-fired conditions, the heat loss through the outlet was significantly higher, with a value of 45 %.

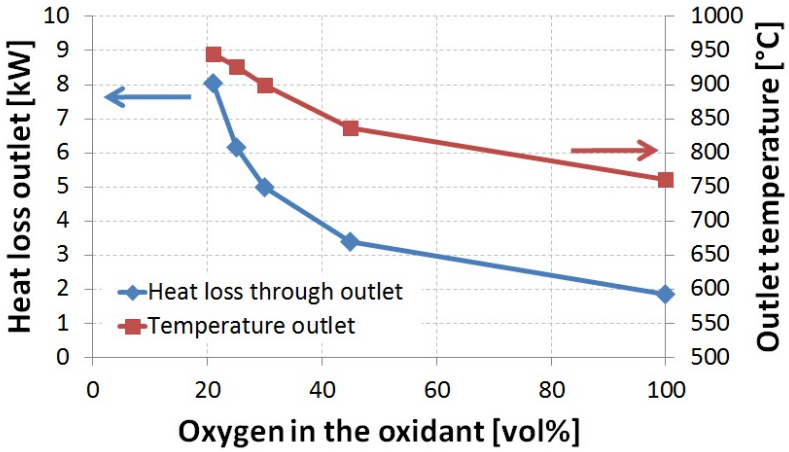

Fig. 82. Simulated heat losses and flue gas temperatures at the outlet for the experiments without thermal load.

6.5.2 Lab-scale furnace with thermal load

In this section, air-fuel combustion and OEC cases were investigated with the water cooled copper plate inside the furnace. These experiments will reveal how much of the fuel input is available in OEC to carry out thermal processes in industry, such as heating, melting, etc. The boundary conditions for the experiments have already been described in Section 3.1.2. Two different temperature levels of 1000 and 1220 °C, which were indicated at position T4 in the furnace, were investigated (labelled with 1000-OEC and 1220-OEC).

The necessary fuel input to achieve the desired temperature levels is displayed in Fig. 83. At a temperature level of 1000 °C, the same trend with regard to the needed fuel input can be seen as for the experiments without load. The O_2 concentration in the dry flue gas was very similar, with a value of 2 % for all cases, except for combustion with pure oxygen (approx. 8 %). For air-fired conditions, 51 kW was needed to achieve a temperature of 1000 °C. When the oxygen concentration in the oxidant was increased to 45 % only 41.7 kW was necessary. Even for small oxygen enrichment levels in the oxidant, considerable fuel savings were identified by the experimental data. With 25 % O_2, the fuel input was reduced to 46.8 kW, which is 8.2 % lower than for the air-fuel combustion. This is extended with 30 % O_2 in the oxidant, where the fuel consumption is further reduced to 43 kW (15.7 % compared to air-fuel). The experiments with and without load revealed a similar trend for the fuel savings, especially at low enrichment levels. For the combustion with pure oxygen, no increase in fuel savings was detected compared to 45 % O_2, because of excessive air leakage. Since the furnace equipment is restricted to a maximum fuel input, the experiments at 1220 °C were only carried out for 30, 45 and 100 % O_2. Here, the fuel input for 100 % O_2 was 74.8 kW. For the OEC cases with 30 % and 45 O_2, the fuel input had to be increased to 98 and 87.6 kW, respectively. Considering the OEC cases with 30 and 45 % O_2, it can be seen that the potential for fuel reduction increases with higher temperature levels. To determine this, the reduction in fuel consumption at 1000 and 1220 °C was 1.3 (30 % O_2) and 9.4 kW (45 % O_2), respectively. This corresponds to fuel savings of 3 and 9.7 %.

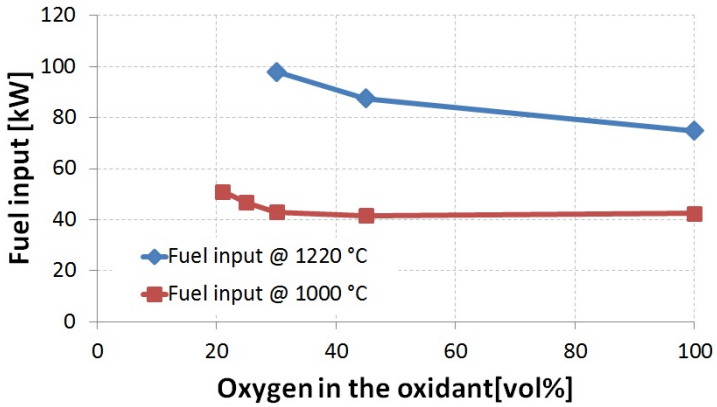

Fig. 83. Fuel input for the experiments with thermal load for 1000 and 1220 °C.

Since CFD simulation were used in this thesis to predict the heat transfer for air-fuel and OEC cases, the calculated results are compared to the measured temperatures (see Fig. 84). At 1000 °C, the CFD simulations showed a very good agreement to the measurements for all investigated cases. Only for oxy-fuel combustion did the measurements show lower temperatures for all measurement points, which can be explained by the higher rates of air leakage described above. Hence, the gas temperature decreases in the furnace. Since the CFD simulation calculates a slightly longer flame, the temperature at T7 was over-predicted for all cases. This fact was already examined in detail in Section 6.4.1 (see Fig. 68 and Fig. 70). A close accordance to the measured temperatures was also found at a temperature level of 1220 °C. Due to the good agreement between the measurement and CFD results, the SFM, in conjunction with the skeletal25 mechanism, was found to be suitable for the prediction of the heat fluxes and temperatures in natural gas combustion with air and oxygen enrichment. The model can be applied for the full range of oxygen enrichment and can predict the heat transfer in furnaces at different temperature levels.

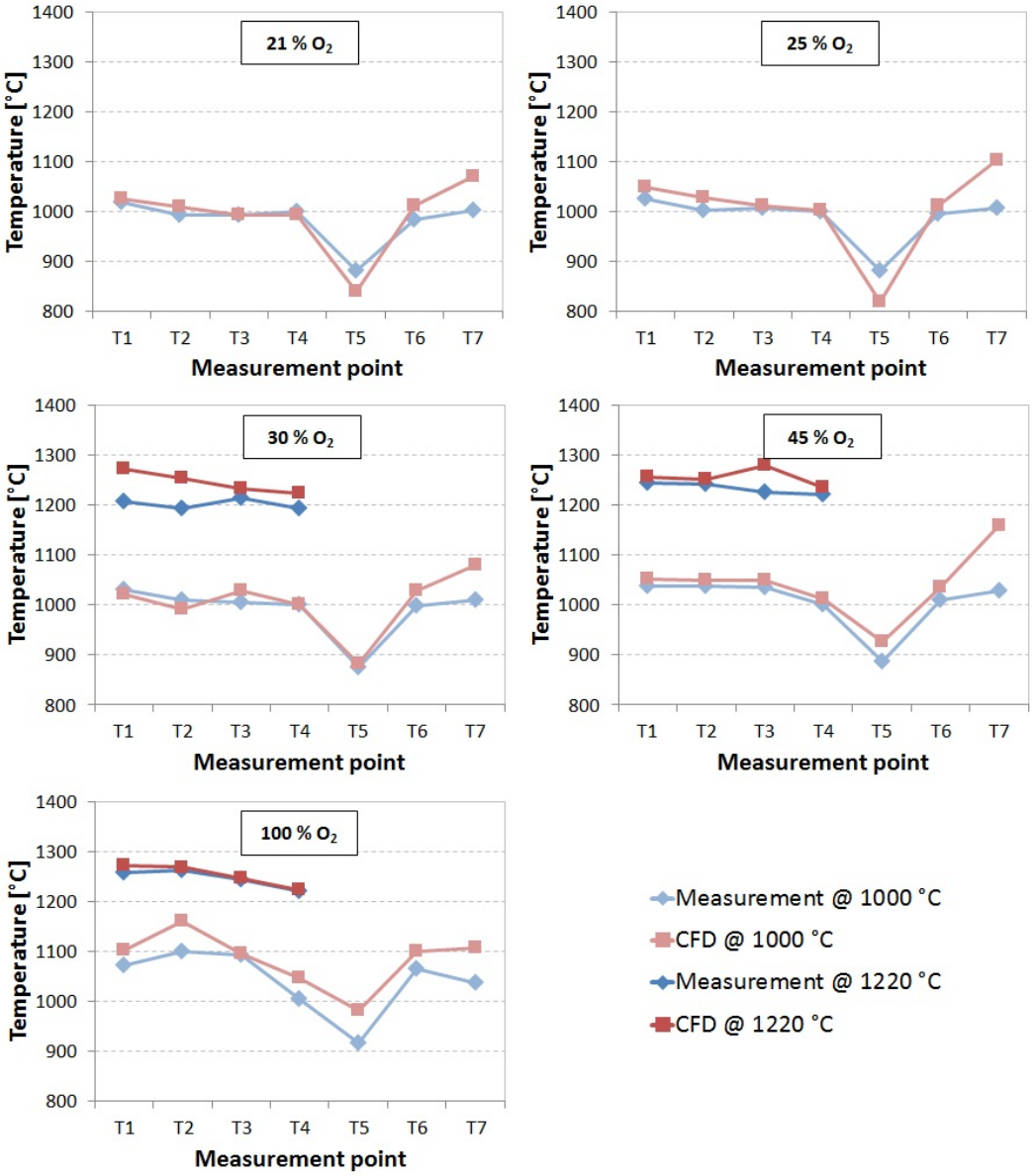

Fig. 84. Comparison of measured and calculated temperatures with thermal load at 1000 °C (1000-OEC) and 1220 °C (1220-OEC).

In Fig. 85, the measured and simulated heat fluxes to the thermal load are displayed for 1000 and 1220 °C. Both the experiments and the CFD simulation showed an increase in the heat flux of approximately 25 kW between all OEC cases for 1000 and 1220 °C. At 1000 °C heat fluxes in the range of 20.4 – 22.8 kW were measured, as well as 40.5 – 43 kW at 1220 °C. Although the temperature level was the same, for example 1000 °C, a slight increase in the heat flux from air-fuel to oxy-fuel conditions was observed in the experiments. This effect is caused by the higher CO_2 and H_2O concentrations in the flue gas, which improves the radiative heat flux to the furnace walls and load. The experiments showed that the heat flux to the load was very similar for the OEC and air-fuel cases despite the fact that the fuel input was reduced, as mentioned above.

In industrial scale furnaces, experiments to determine the heat fluxes to the load are very demanding. Thus, CFD simulations provide an opportunity to determine the local heat fluxes and temperature distribution, as well as species concentrations, without expensive experiments. From the results in Fig. 84 and Fig. 85, it is possible to conclude that the CFD model is not only capable of predicting the temperatures in the furnace, but also the heat fluxes to the load. For the experiments at 1000 °C, the simulated heat fluxes showed an average deviation of 0.47 kW, which is a relative error of 1.7 %. At 1220 °C, higher deviations were detected, caused by increased air leakage during the experiments, which was determined by the oxygen concentrations in the dry flue gas (see Table 5). For the experiments 1220-OEC, an average deviation of 4 kW (9.5 % relative error) between the measured and predicted heat fluxes was found.

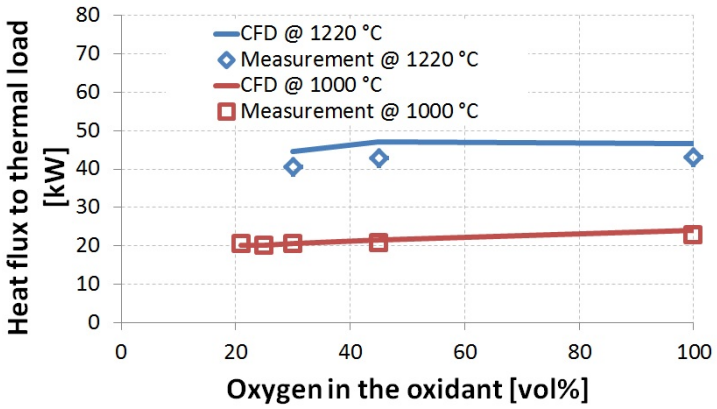

Fig. 85. Measured and calculated heat fluxes to the thermal load at 1000 and 1220 °C.

Fig. 86 presents the contour plots of the specific heat fluxes on the copper plate at a temperature level of 1000 °C. From the results in Fig. 85, it was already possible to see that the heat flux increases with the oxygen enrichment level, which is confirmed by the contour plots of the heat fluxes. The specific heat flux on the thermal load increases at higher oxygen concentrations in the oxidant. In all cases, the peak heat flux was detected at the corner on the right hand side. This is explained by the higher convective heat flux in this region.

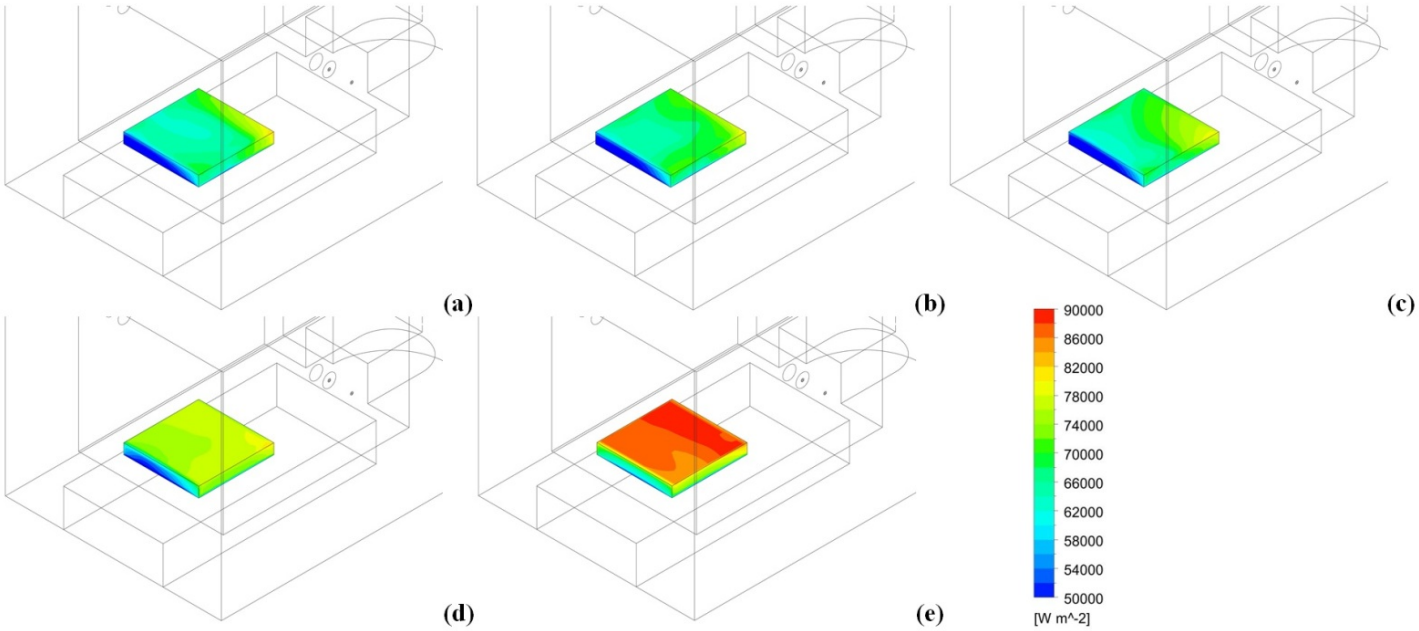

Fig. 86. Contour plots of the specific heat flux to the load at 1000 °C (1000-OEC): (a) 21 % O_2, (b) 25 % O_2, (c) 30 % O_2, (d) 45 % O_2, (e) 100 % O_2.

The measured and predicted furnace efficiency, which is defined by Eq. (132), is given in Fig. 87 for 1000 and 1220 °C. In this equation, $\dot{Q}_{load}$ is the heat flux to the thermal load and $\dot{Q}_{fuel}$ is the fuel input. The heat flux to the thermal load represents the heat flux necessary in an industrial application to achieve the desired heating or melting process. At 1000 °C the measurement and CFD simulation are in close accordance with regard to the furnace efficiency. An increase of the furnace efficiency from 40 to 53.6 % was measured compared to the simulation with values between 39.5 and 56.7 %. The results revealed that an oxygen enrichment level of 30 % O_2 would already improve the furnace efficiency by about 10 %, representing a reasonable opportunity for fuel savings and a reduction of CO_2 emissions in industry. A mere 4 – 7 % higher furnace efficiency can be achieved using pure oxygen instead of 30 % O_2 in the oxidant. The maximum efficiency was observed at 1220 °C and 100 % O_2 with values of 57.5 % (measured) and 62.5 % (CFD). Although higher values can be reached at 1220 °C, the efficiency dropped faster at lower oxygen enrichment levels. When the oxygen enrichment was decreased to 45 % in the experiments, the efficiency at 1220 °C (49 %) was already lower than the efficiency at 1000 °C (49.9 %). The CFD simulations showed that the efficiency at 1220 °C dropped below the efficiency at 1000 °C when using an oxygen enrichment level of 30 % O_2.

$$\eta_{eff} = \frac{\dot{Q}_{load}}{\dot{Q}_{fuel}} \tag{132}$$

Based on the results, small oxygen enrichment levels are more effective for higher temperature levels, but can also improve the furnace efficiency significantly at 1000 °C. For use in industry, primarily due to the adaptation of existing systems, the lower oxygen enrichment levels have to be preferred. Thus, the effort to adapt the existing furnace/burner can be kept to a minimum.

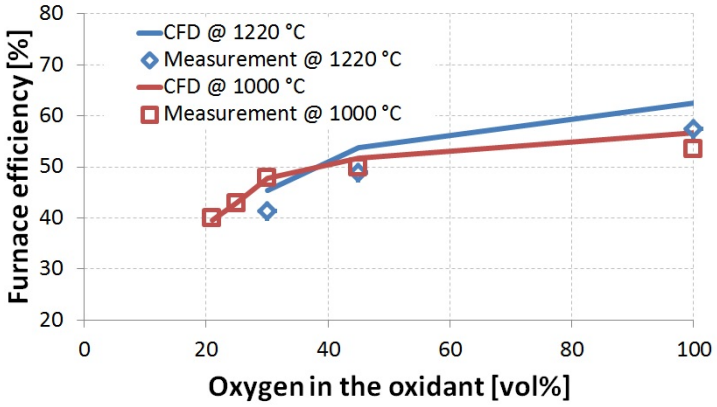

Fig. 87. Measured and calculated furnace efficiency at a temperature level of 1000 and 1220 °C.

6.6 Conclusion

In Section 6, two main goals were set forth. The first was to figure out the best available CFD approach, consisting of turbulence model, reaction mechanism, turbulence/chemistry interaction and radiation model, and to predict air-fuel combustion as well as OEC in the full range of O_2 concentration in the oxidant. Only detailed reaction mechanisms with the EDC model and SFM were able to predict the oxy-fuel flame. Global reaction mechanisms might be applicable for air-fuel or oxy-fuel combustion, but the model parameters would have to be adapted for each case. With respect to the calculation time, the SFM with the skeletal25 mechanism was the most time efficient method. In the lab-sale furnace, simulations with the SFM and EDC were finished after 3 days and 3 weeks, respectively (Hardware: 8 core-CPU, 32 GB RAM; Grid: approximately 630 000 cells). Furthermore, the SFM showed the best agreement with the measured temperatures in the furnace. For the radiative heat transfer, only the DOM was usable for the investigated furnace. The P1 model over-predicted the radiation intensity in the furnace, determined by a more homogeneous temperature distribution, which was in contrast to the measurement. For turbulence modelling, the RSM and realizable k-epsilon model were able to predict the jet flame. With the standard k-epsilon model, the

spreading rate of the flame was too high, leading to an over-predicted temperature in the vicinity of the burner.

The second aim of this section was to investigate, by means of experiments, the potential of OEC to provide fuel savings and to increase process efficiency in industrial furnaces. These experiments showed that furnace efficiency can be significantly improved, also with low oxygen enrichment levels, though this improvement is more obvious at higher temperatures in the furnace. As a consequence, more heat from the fuel input is available in OEC compared to air-fuel combustion to maintain industrial processes for steel, cement or glass production.

All experiments were compared to the CFD simulations with the skelatl25/SFM and DOM. The measured temperatures and heat fluxes in the furnace were in close accordance to the simulated results, although air leakage could not be completely avoided in the experiments. The results discussed in this section have shown that OEC can be used for industrial processes in order to improve efficiency. Additionally, a CFD model was found, which can predict air-fuel combustion and OEC. Thus, CFD simulations can be used to predict the temperatures and heat fluxes in furnaces without expensive test runs. In Section 7, the CFD model is used to investigate an industrial walking hearth furnace used to reheat steel billets, which can be operated under air-fuel conditions or OEC. The CFD simulation will reveal the heat fluxes to the steel billets and simulate the transient heating process for both combustion cases.

6.7 Further validation of the CFD model in cooperation with Brno University of Technology (BUT)

In the course of the literature review carried out for this thesis, another test facility for air-fuel combustion and OEC was found at Brno University of Technology (BUT). Courtesy of Dr. Petr Bělohradský, it was possible to obtain all of the measured data for this furnace. Thus, this furnace was simulated with the aforementioned CFD model and the results were compared to the measurements. This provides a valuable opportunity to further validate the CFD model.

The experimental setup will be described here only in brief because the experiments were carried out entirely by the BUT, and have already been presented in [44; 60]. From the entire set of experiments, only three cases were simulated (air-fuel and 2 OEC) and will be presented in this thesis. The models used for the three CFD simulations are summarized in Table 17. The results were published at the Australian Combustion Symposium [154] and will be not further.

Table 17
Used numerical models for the CFD simulation in this section.

Oxygen in the oxidant [%]	Turbulence model	Radiation model	Turbulence/chemistry interaction	Reaction mechanism
21 25.4 30.8	Realizable k-epsilon	DOM	SFM	skeletal25

In Fig. 88, the test facility at BUT is shown. The furnace consists of a horizontal combustion chamber with a length of 4 m and an inner diameter of 1 m. In contrast to the lab-scale furnace described in Section 3.1, which has insulated walls, the walls of the combustion chamber are water cooled and divided into seven cooling zones. Six sections are 0.5 m long, while the seventh section (the end of the chamber) is 1 m long. In each zone, the absorbed heat flux can be determined by measuring the water mass flux and the in- and outlet temperatures. Additionally, the temperature was measured at distances of 0.75, 1.25, 1.75, 2.25, 2.75, 3.25, and 3.75 m from the burner and different radial positions. The flue gas temperature was measured using thermocouples of type R. The furnace was investigated under oxygen concentrations of 21, 25.4 and 30.8 % O_2 in the oxidant. The operating conditions of the three combustion cases are summarized in Table 18.

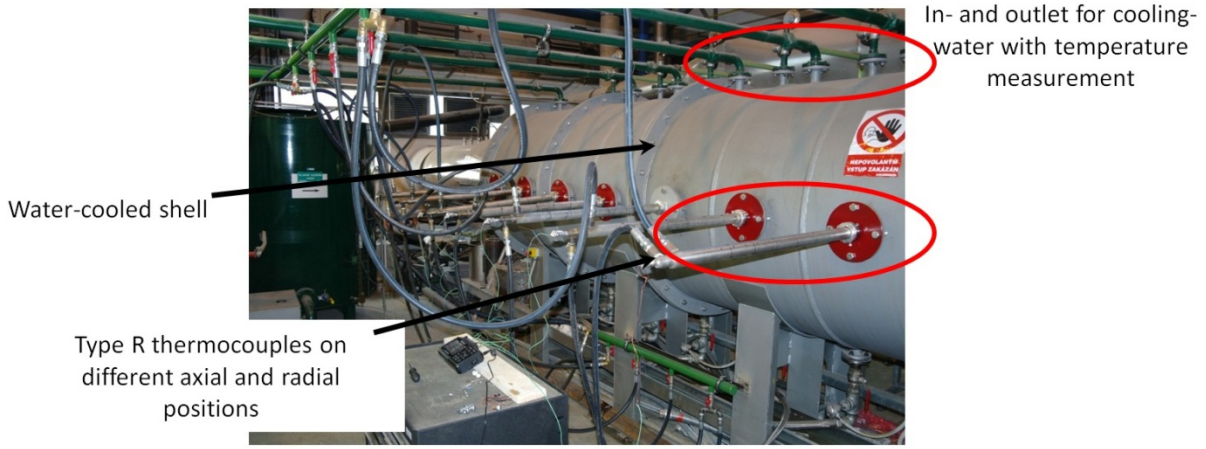

Fig. 88. Experimental setup of the lab-scale furnace at Brno University of Technology.

Fig. 89 shows the CAD model of the combustion chamber, including the air/oxygen duct to the burner. This model is the basis for the generation of the numerical grid, which was made of 1.6 million cells. The natural gas was supplied through the central pipe which has 12 small drillings with diameters of 3 and 2.6 mm. A swirl generator with an outer diameter of 240 mm is arranged in the oxidant stream. This swirl generator has 8 blades with a pitch angle of 35 °.

Premixing of the air and pure oxygen was carried out before they entered the burner in order to achieve the desired OEC level.

Table 18
Operating conditions for the experiments at BUT.

Fuel input [Nm³/h]	O_2 in the oxidant [%]	O_2 in the dry flue gas [vol%]
75.4	21	3.2
75.2	25.4	3.1
75.4	30.8	4.5

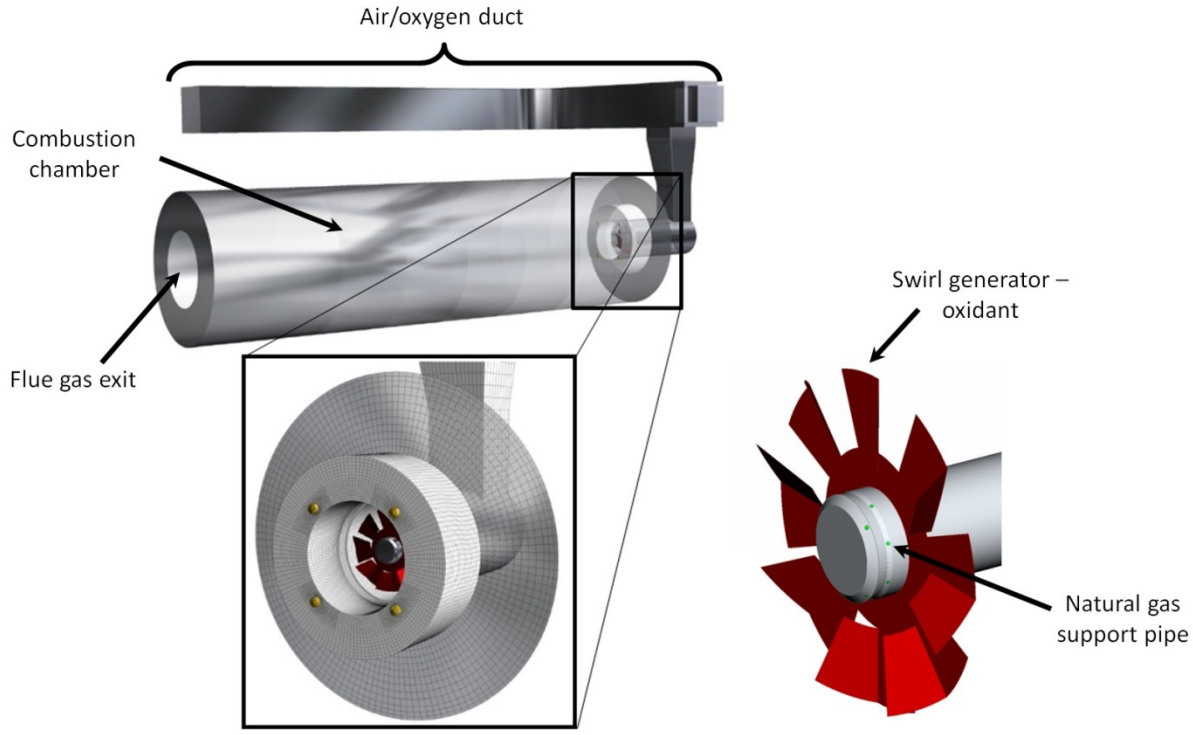

Fig. 89. CAD model of the combustion chamber and the burner.

In Fig. 90, the calculated contour plots of the temperature for the three combustion cases are displayed in the horizontal plane. With increasing oxygen concentration in the oxidant, the flame becomes shorter, as a result of the lower volume-flow rate of the oxidant. The flame temperature increases at higher oxygen enrichment, which was established in Section 6. In the contour plots, a deflection of the flame can be seen for all combustion cases marked with the red circle. Air-fuel combustion and 25.4 % O_2 show a deflection to the left hand side. Analysis of the stream lines revealed the inhomogeneous inflow of the oxidant to the swirl generator, which resulted in the deflection of the flame to the chamber walls.

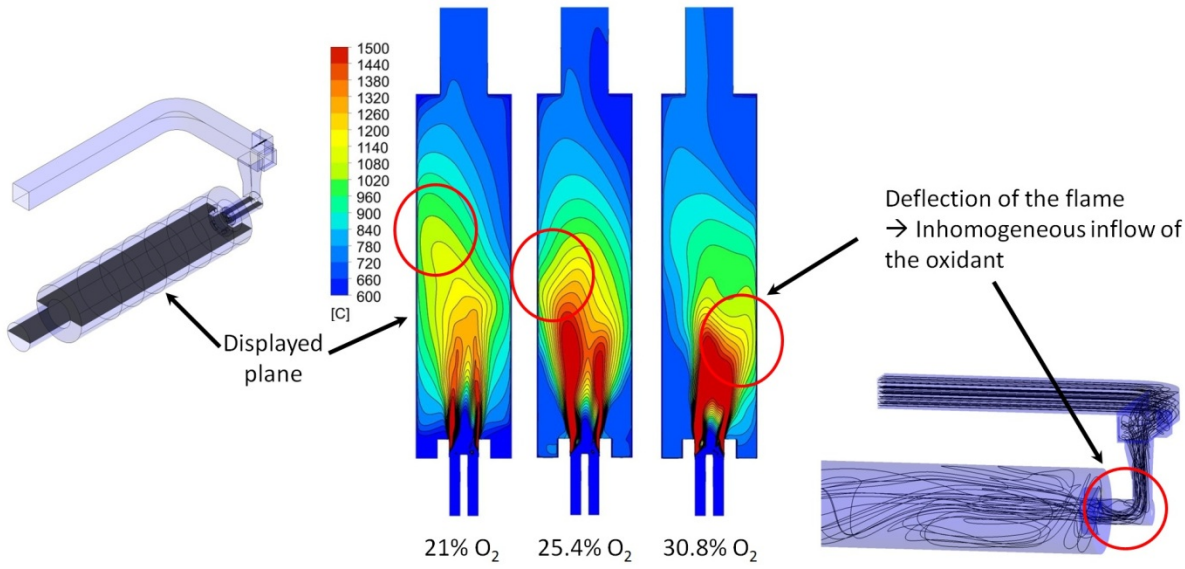

Fig. 90. Results of the CFD simulation for 21, 25.4 and 30.8 % O_2.

The measured temperatures in the furnace were used to generate contour plots of the temperature in the horizontal plane. Fig. 91 provides the contour plots of the temperature for the measured and simulated data. The CFD simulation of the air-fired case and the OEC case with 25.4 % O_2 both revealed the deflection of the flame to the left hand side (according to Fig. 91). The deflection of the flame to the left wall decreases at higher oxygen enrichment levels, which is caused by the lower volume-flow rate of the oxidant. This lower volume-flow rate reduces the radial momentum induced by the swirl burner. The flame length predicted by CFD is longer than the measured flame length for all investigated cases, which had already been observed in the lab-scale furnace. Hence, it is possible to conclude that the CFD model used predicts a longer flame, not only for jet flames, but also for flames with swirl. Nevertheless, CFD simulation with the SFM is also suitable for flames with a swirl induced fluid flow, because the measured temperatures in the furnace and flame are in close accordance to the predicted values.

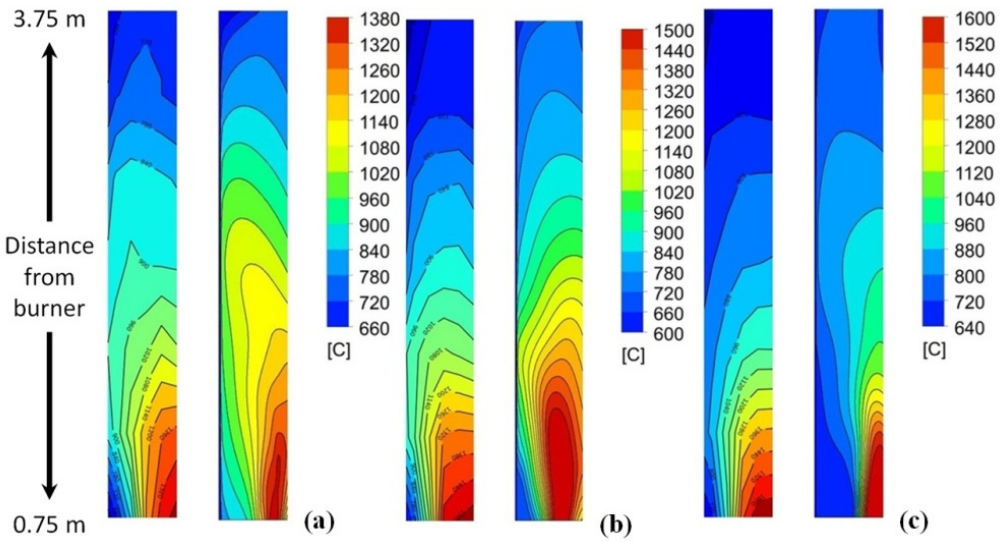

Fig. 91. Comparison between measured and calculated in-flame temperatures for 21 (a), 25.4 (b) and 30.8 % O_2 (c).

Similar to the measured heat flux to the copper plate in the lab-scale furnace, the heat fluxes to the chamber wall were measured in this furnace. The calculated and measured heat fluxes to the furnace walls (sections) are displayed in Fig. 92. Sections 1 to 3, which are near the burner, showed an increase in the heat flux for both measurement and simulation. It was also seen that the heat flux in these sections increased with the OEC level. From section 3 to section 4, the heat flux for 30.8 % O_2 enrichment decreased in the CFD simulation because of the shorter flame. For 21 and 25.4 % O_2, the simulated heat flux began to decrease between sections 4 and 5. The measurement of the heat fluxes showed the maximum specific heat flux in section 3 instead of 4 or 5 as had been predicted in the simulation. This is as a result of the shorter flame during the experiments.

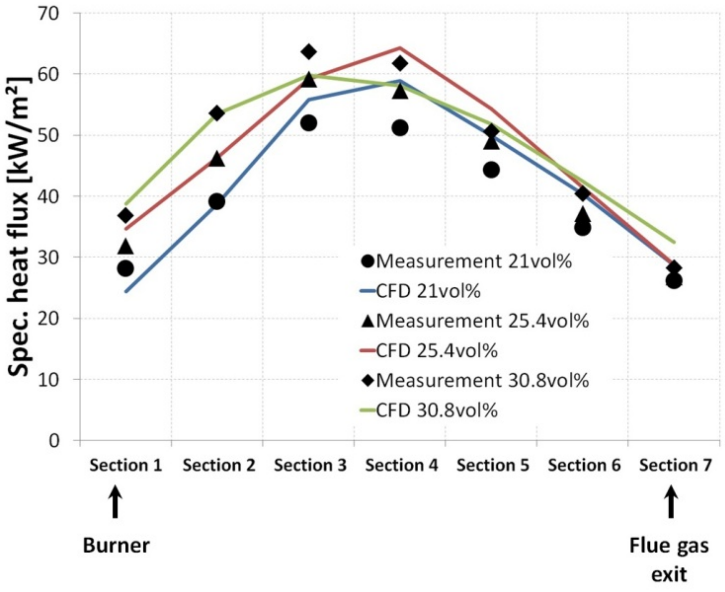

Fig. 92. Specific heat fluxes to the chamber wall.

In Fig. 93, the furnace efficiency, which was defined in Eq. (132), is displayed for both the measurements and CFD simulation. To calculate the efficiency with Eq. (132), $\dot{Q}_{load}$ is represented by the heat flux to the water cooled chamber wall. An increase in the efficiency can clearly be identified for the predicted and measured values, similar to the lab-scale furnace investigated in Section 6.5. The measurement showed an increase from 61 % (air-fuel) to 73.4 % for 30.8 % O_2, which is a difference of 12.4 %. Approximately the same trend was observed in the simulation with values of 66 % (air-fuel) and 74.4 % (OEC for 30.8 % O_2). Deviations between the measured efficiencies (heat fluxes) and the simulated results can be explained by heat losses at the water cooled shell and the air leakage.

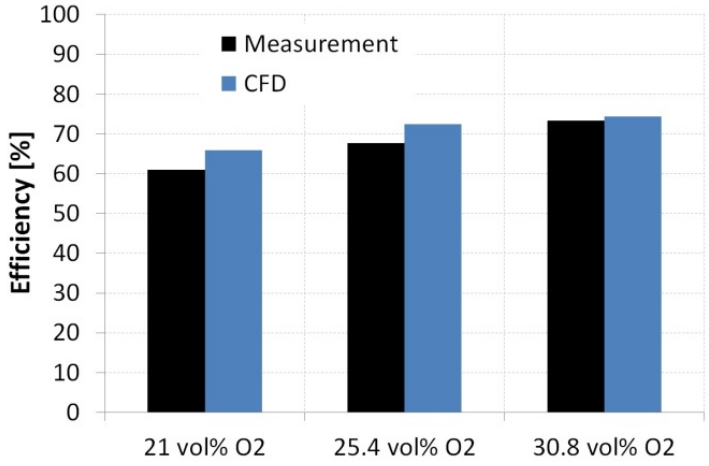

Fig. 93. Furnace efficiency for the air-fuel and the OEC cases.

The experiments at BUT provided confirmation of the results of the lab-scale furnace presented in Section 6, with regard to the flame length and temperature, as well as the furnace efficiencies. The CFD simulations showed good agreement to the temperatures measured in the flame, although the flame length was slightly over-predicted. This had already been found during the work done on the lab-scale furnace. Nevertheless, the SFM with the skeletal25 mechanism is not only suitable for simple jet flames, but also for flames with streamline curvatures.

7 Results – Walking hearth furnace

The best available CFD model for air-fuel combustion and OEC, described in the previous section, will now be used to investigate an industrial walking hearth furnace for reheating steel billets from an ambient temperature to approximately 1200 °C. Further deformation processing on the rolling mill requires a uniform temperature distribution and the desired target temperature of the billet. The experiments described in this section have already been published in Prieler et al. [147; 155]. Thus, the figures and data presented in this section will not be referenced to these papers subsequently.

In this investigation, not only the gas phase combustion will be considered, but also the transient heating process of the steel billets within the furnace. The furnace was operated under air-fired and OEC conditions with an enrichment level of 25 % O_2 in the oxidant. For this purpose, an iterative solution procedure was developed to couple the heat transfer in the gas phase and the transient heating process of the solid material. The solution procedure is explained in detail in Section 7.1.

Since the walking hearth furnace was retrofitted for OEC, an analysis of the expected wall temperatures at the burner was carried out to avoid overheating and damage to the burner or the refractory walls. The simulations of the gas phase combustion at the swirl burners were carried out with two turbulence models to predict the wall temperatures, and the results were compared to measurements (see Section 7.2). Three simulations of the gas phase combustion in the walking hearth furnace were carried out with the numerical models summarized in Table 19.

After the iterative solution procedure for both operating conditions has been described, the effect of air-fuel combustion and OEC on the furnace's efficiency as well as the temperature trends and distribution within the steel billets will be presented in Sections 7.3 and 7.4.

Table 19
Numerical models for the simulation of the gas phase combustion in the walking hearth furnace.

Oxygen in the oxidant [%]	Turbulence model	Radiation model	Turbulence/chemistry interaction	Reaction mechanism
21	Realizable k-epsilon			
21	RSM	DOM	SFM	skeletal25
25	Realizable k-epsilon			

7.1 Iterative solution procedure for the transient heating of steel billets

Since the radiative heat transfer is highly dependent on the surface temperature of the billets, the interaction between the heat transfer to the billets and the emitted radiation from the billet surface has to be considered. Thus, simulations with an assumed temperature profile would lead to an unreliable billet temperature, especially at the corners and edges, where the radiation hits two or more sides of the billet simultaneously. The transport phenomena in the furnace and billets are periodically transient, due to the transport mechanism of the walking hearth furnace. Based on the transport system, the billet remains in a position for 100 seconds and is then transported to the next position, thus, a full transient simulation of the entire heating process of 6400 seconds must be performed (e.g. [33]). For industrial furnaces, the large dimensions, in conjunction with complicated burner geometries, would lead to fine grids and high calculation times. Since the developed CFD model for the gas phase combustion of OEC and air-fuel combustion represents a time saving method, an iterative approach to couple gas phase combustion and transient heating was developed in the present work (see Fig. 94). The main advantage of this method is that the complex transport phenomena in the gas phase can be calculated by a steady-state CFD simulation instead of a transient approach. This reduces the computational time significantly.

The solution procedure is carried out through two different kinds of simulations:

- Steady-state gas phase combustion with the CFD model found in Section 6.
- Transient simulation of the transient heat conduction inside the billet

First, as shown in Fig. 94, the procedure starts with a steady-state CFD simulation of the gas phase combustion in the furnace (called furnace simulation in Fig. 94). The first simulation is referred to as the “Basic” simulation in the following figures. In this initial simulation, the temperature boundary condition at the billet surface is assumed with a linear trend along the

furnace, starting with 34 °C for the first billet and 1186 °C for the last billet (see Fig. 95). After this iteration was finished, the local specific heat fluxes to the billets (radiation and convection through the gas; conduction through hearths) were determined and stored with profile files.

Secondly, the stored specific heat fluxes were used for a transient simulation of a solid billet. For this simulation, only one billet was considered. The model settings for the transient simulation of the steel billet are given in Section 7.1.1. Depending on the time in the furnace, the position and, therefore, the specific heat fluxes to the billets are known. After 100 seconds were simulated, the actual surface temperature at the billet was stored in profile files.

With this calculated temperature and the initial linear temperature trend, a new temperature boundary condition for the furnace simulation can be created by averaging, which can be considered as an under relaxation factor of 0.5. The new temperatures are calculated for each surface area of the billet in the furnace simulation, which leads to a spatial distribution of the temperature boundary condition on the billet surface. Now, a new furnace simulation can be started, which is called the “First” iteration.

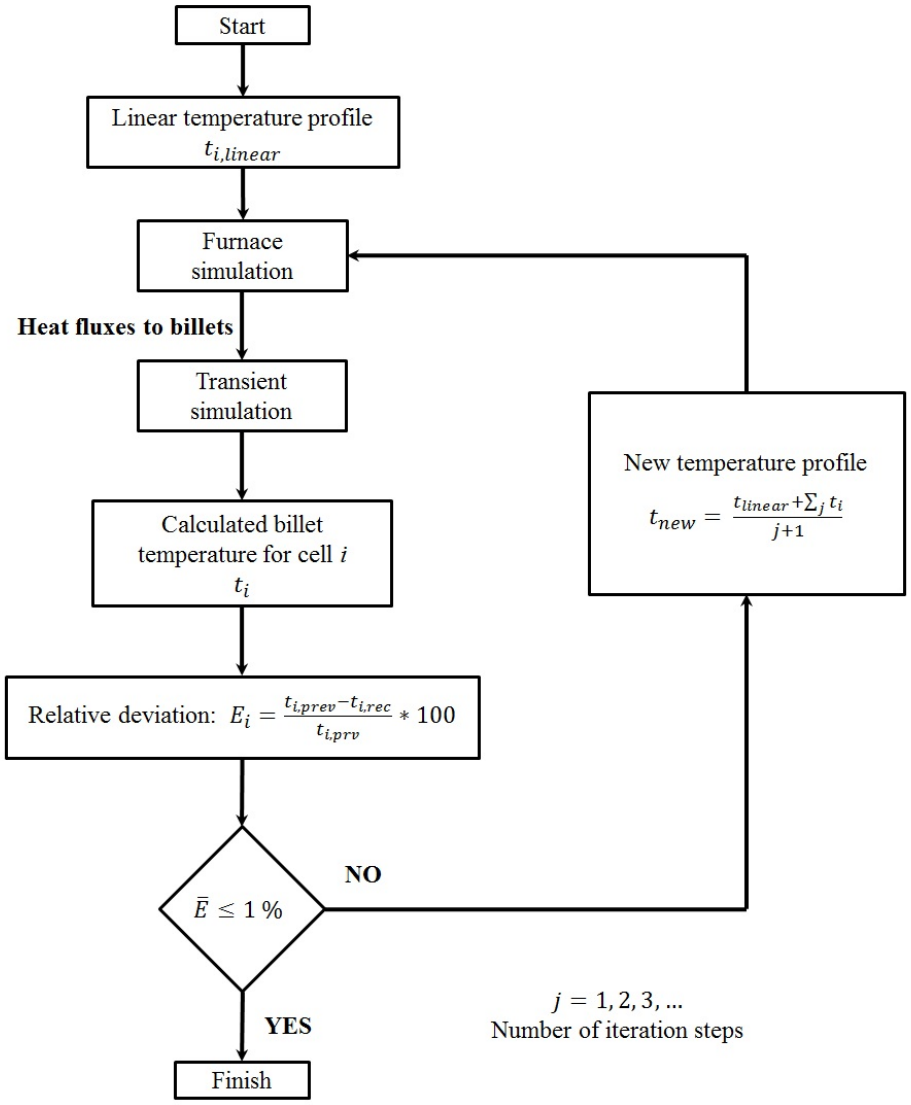

Fig. 94. Scheme of the iterative solution procedure for coupling gas phase combustion and transient heating.

This loop is repeated until convergence is reached, which is determined by the average relative deviation $\bar{E}$ on the temperature for all cells in the solid domain of the billet. After each iteration step, the calculated temperature in each cell i is compared to the previous transient simulation and the relative deviation E_i is calculated according to Eq. (133). In this equation, $t_{i,rec}$ and $t_{i,prev}$ are the temperature in cell i, calculated by the most recent transient simulation and the previous iteration step.

$$E_i = \frac{\left| t_{i,rec} - t_{i,prev} \right|}{t_{i,prev}} \tag{133}$$

The procedure was stopped when the average deviation of all cells was below 1 %. For comparison, the standard tolerance of a type B thermocouple in this temperature range is 0.5 % of the measured value. Therefore, it was found to be sufficient to set the convergence criterion to 1 %.

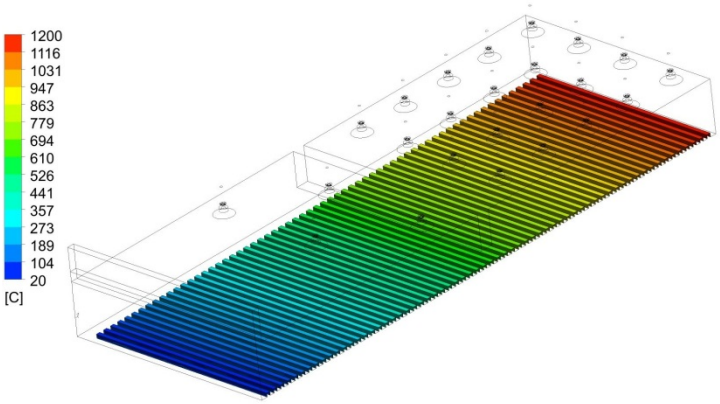

Fig. 95. Assumed surface temperature at the billet for the first iteration step.

The iterative solution procedure was also applied without the averaging of the temperatures after each iteration step. The temperatures calculated from the transient simulation were transported directly into the furnace simulation. With these temperatures as boundary condition, implausibly high temperatures (above the melting point of steel) were calculated in the transient simulation for the second iteration step. These temperatures were detected at the corners and edges of the billet.

Due to the solution procedure used, combined with the CFD model to predict the combustion process, the calculation time was kept at a minimum, although all transport phenomena inside the gas phase as well as the transient heating of the billets were covered by the model. The overall calculation time was 9 to 10 days (CPU: 8 cores; 32 GB RAM; Number of cells: 5,797,749 and 86,400). The Basic furnace simulation showed the highest calculation time of 4 to 5 days. The other furnace simulations were finished after one day because the result of the basic simulation was used as the initial condition. Transient calculations of the billet were finished after 2 hours and have a minor influence on the overall calculation time. The approach used presents a reasonable method of predicting temperature and species concentrations in the gas phase, as well as heat conduction in the billets, with low computational demand.

7.1.1 Transient simulation of the steel billet

The transient heat conduction within the billets was simulated with a structured grid with 86,400 hexahedrons (not shown in this thesis). Temperature dependent material properties of the low-alloy steel were implemented by polynomial functions according to Fig. 31 and the density was fixed with a value of 7800 kg/m³. The initial temperature was set to 20 °C and the heat flux profiles were updated after 100 seconds, according to the transportation system. To update the heat fluxes after 100 seconds, a user-defined function (UDF) was created. A fixed

time step size of 1 second was applied to simulate the entire heating process of 6400 seconds. The convergence criterion for each time step was a residual value of 10^{-11} for the energy equation (see Eq. (134)). In addition, both a second order spatial discretization and second order implicit formulation were used for the energy equation.

$$\frac{\partial}{\partial t}(\rho h) = \nabla \cdot (\lambda \nabla T) \tag{134}$$

7.1.2 Fuel consumption for air-fuel and OEC in CFD

For the numerical investigation of the air-fuel and OEC cases in this section, the reference production rate for both cases was set to a value of 47.428 t/h. Based on the specific fuel consumption determined in the experiments (see Section 3.2), the required total fuel input was calculated. As a result, the fuel input for the simulations was 18.19 MW (air-fuel) and 16.53 MW (OEC) in the CFD simulation. The total heat flux was distributed to the different zones according to the experimental data. The same production rate was chosen for both cases because the time for the transient simulation of 6400 seconds should be the same. With the same residence time inside the furnace, the temperature distribution of the billets can be better compared between the cases. Furthermore, the same heat flux to the billets is required to achieve the same temperature level.

Table 20
Operating conditions used in the CFD simulations.

	Air-fuel	**OEC (25% O_2)**
Specific fuel consumption [Nm³/t]	38.35	34.85
Production rate [t/h]	47.428	47.428
Total fuel input	**18.19 (100 %)**	**16.53 (100 %)**
Pre-heating [MW]	3.99 (21.9 %	3.70 (22.4 %)
Heating [MW]	10.80 (59.4 %)	10.00 (50.5 %)
Soaking [MW]	3.40 (18.7 %)	2.83 (17.1 %)

7.1.3 Determination of the convergence criterion for air-fuel combustion

This section presents the simulation progress of the iterative solution procedure after each iteration for air-fuel combustion. As a reminder, convergence was assumed when the average temperature deviation in all cells was below 1 % from one iteration step to the next.

The contour plots of the calculated temperatures of the billet before discharging from the furnace are shown in Fig. 96 (left) for air-fuel combustion. The temperature trend along the centre line of the top surface is displayed in Fig. 96 (right). Because of the symmetry, only

one half of the billet is shown. After the basic transient simulation, very high temperatures in the billet corners can be seen in the contour plots in Fig. 96. Because the corners of the billet were irradiated from three sides/surfaces (top surface and two side surfaces), the calculated temperatures were much higher. Along the centre line and the corner of the billet, maximum values of 1363 and 1365 °C were detected.

In contrast to the basic transient simulation, the temperatures in the corners of the billet were too low after the first iteration step. Due to the fact that the surface temperature from the basic simulation was used to create the new temperature boundary condition, heat fluxes at the corners were under-predicted for the first iteration step. Thus, the transient simulation of the first iteration step calculates too low temperatures at the edges and corners. This is determined by the minimum temperature at the centre line with a value of 913 °C (see Fig. 96, right).

After the second iteration step, the temperature profile at the billet surface becomes more homogeneous, with the maximum temperature difference inside the billet of 81 K. This is more obvious with the further progress of the solution procedure (third and fourth iterations). The contour plots for the third and fourth iterations show small regions around the corners of the billets with slightly higher temperatures, caused by the irradiation from three sides/surfaces. This is confirmed by the temperatures along the centre line at the top surface, where the temperature trends of the third and fourth iteration are hardly distinguishable and the solution procedure was stopped.

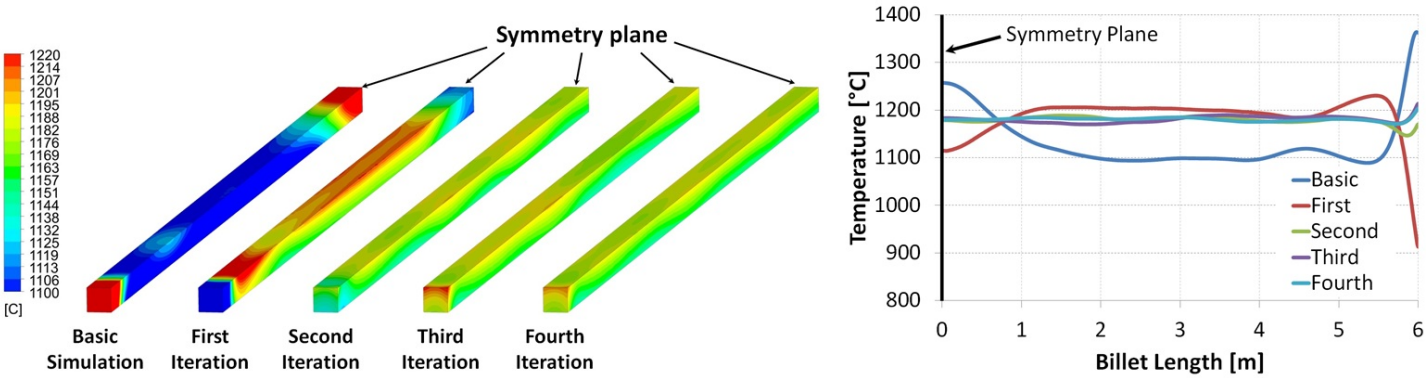

Fig. 96. Surface temperature of the last billet in the furnace after each iteration step for air-fuel combustion (left) and temperature along the centre line of the top surface (right).

To confirm that the convergence was reached after the fourth iteration step, the contour plots of the relative deviations are given in Fig. 97 (left). As it follows from the temperature contour plots, the deviation between the basic simulation and the first iteration step is above 5 % for almost the whole surface. Along the centre line of the top surface, a maximum deviation of 27 % was found. Between the second and third iteration steps, higher deviations of the temperature are only detected at the end of the billet, with a value of 3.1 %. After the

fourth iteration, an average change of the temperature compared to the previous iteration step of 0.39 % was found, with a maximum value of 0.87 %. Therefore, the convergence criterion was fulfilled.

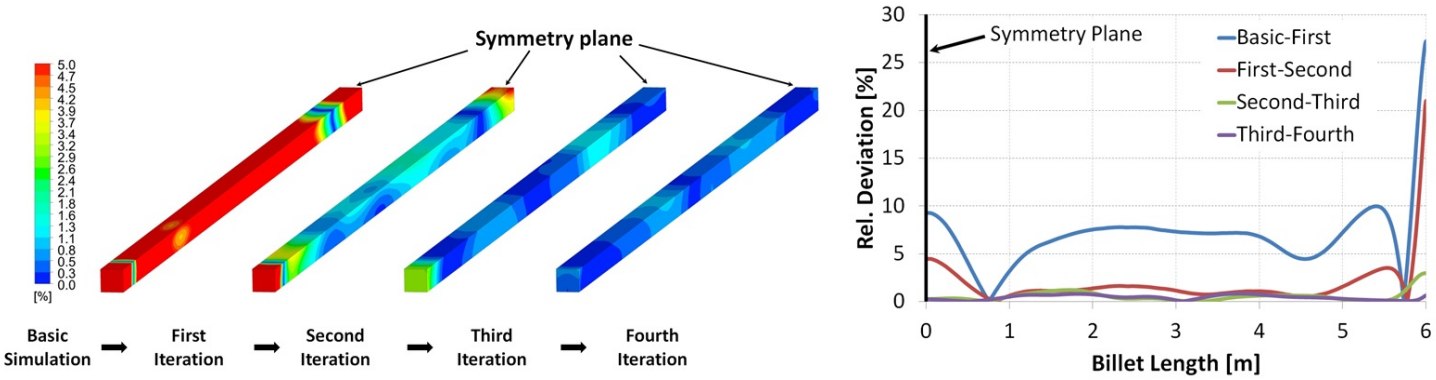

Fig. 97. Calculated relative deviations between the iteration steps with respect to the temperature for air-fuel combustion (left) and deviation along the centre line of the top surface (right).

7.1.4 Determination of the convergence criterion for OEC

The OEC case showed a very similar trend for the progress of the solution procedure compared to air-fuel combustion in Section 7.1.3. The temperatures in the billet corners were significantly over-predicted in the basic simulation, with maximum values in the corners and along the centre line of 1390 and 1387 °C, respectively. After the first iteration, the temperature in the corners of the billet is obviously too low. Considering the temperature of the first iteration along the centre line, a significant decrease of the temperature below 900 °C can be observed.

Similar to the results of the air-fuel combustion, for the OEC case, a more homogeneous temperature distribution was observed after the second iteration step. In the air-fuel case, a maximum temperature difference inside the billet was determined with 81 K. The maximum temperature difference inside the billet is slightly higher for the OEC case. Here, after the second iteration step, temperature was determined with 109 K. The predicted temperatures of the third and fourth iteration steps were quite similar, and showed a very homogeneous temperature distribution at the billet surface.

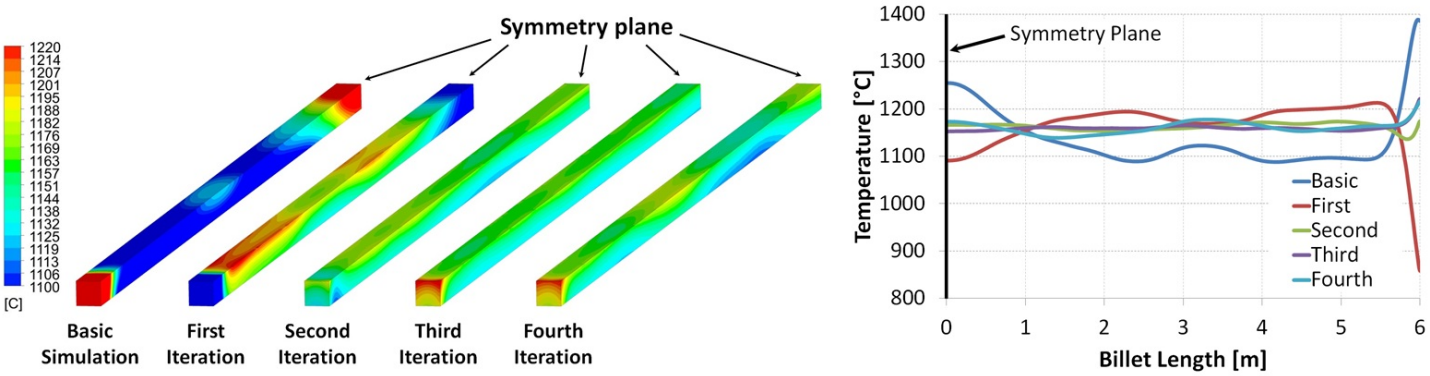

Fig. 98. Surface temperature of the last billet in the furnace after each iteration step for OEC (left) and temperature along the centre line of the top surface (right).

The calculated relative deviations of the temperature after 6400 seconds are displayed in Fig. 99. Since the temperatures for air-fired and OEC conditions were quite similar, the relative deviations at the billet surface were also in close accordance. Only the values of the relative deviations predicted in the OEC case, are slightly higher than in the air-fuel case. Between the second and third iteration steps, the billet showed convergence in almost every region. However, in the corner of the billet, the relative deviation was still too high with 3.8 %. After the fourth iteration step, the average temperature deviation was below 1 % with a value of 0.65 %.

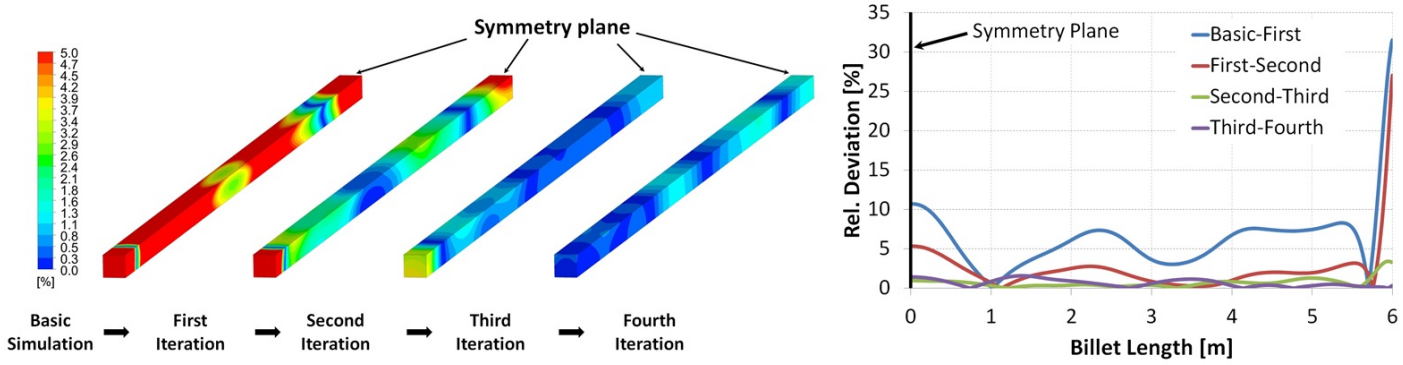

Fig. 99. Calculated relative deviations between the iteration steps with respect to the temperature for OEC (left) and deviation along the centre line of the top surface (right).

7.2 Turbulence models

Although minor differences between the realizable k-epsilon model and the RSM were found for a jet flame in Section 6.2, these turbulence models were tested and compared for the burners in the walking hearth furnace. Since these burners are related to high streamline curvatures and swirl, the use of the RSM is recommended [109]. The basic furnace simulation (according to the solution procedure), with a linear temperature profile at the billets, was used to test both models because the effect of the turbulence model on the flame shape and fluid

flow has to be investigated, instead of the accurate prediction of the temperature value. Pre-heating of the oxidant to 310 °C was not considered in the simulations of the present section. The air-fuel combustion case was investigated because the main focus of this section is the investigation of the turbulence models.

In Fig. 100 and Fig. 101, the contour plots of the temperature and OH mole fractions in the vicinity of the burner are displayed for the realizable k-epsilon model and the RSM. The figures show a burner in the heating zone, which is marked and displayed in detail in Fig. 29. Since the displayed cross-section represents a view from the side wall of the furnace, the flow direction of the flue gas is from the left hand side to right (flue gas exit). The temperature in the flame starts to rise above 1600 °C at the beginning of the conical part of the burner. This was predicted by both turbulence models. The flame, calculated by CFD, is in permanent contact with the burner walls and the ceiling, which indicates a good swirl. Additionally, the maximum temperatures in the displayed flames were in close accordance with 1826 (realizable k-epsilon) and 1831 °C (RSM). From the temperature plots, it is possible to see that the flame is longer when the RSM is used. Furthermore, the flame length can be indicated by the OH mole fraction. Because radical formation is only possible in the main reaction zone, the region of higher radical concentration can also be used to represent the flame length. In Fig. 101, the OH mole fractions showed that the main reaction zone is longer, but also not as voluminous as with the RSM. The RSM led to a more intense swirl in the burner, resulting in a higher radial momentum. This effect is responsible for the longer flame.

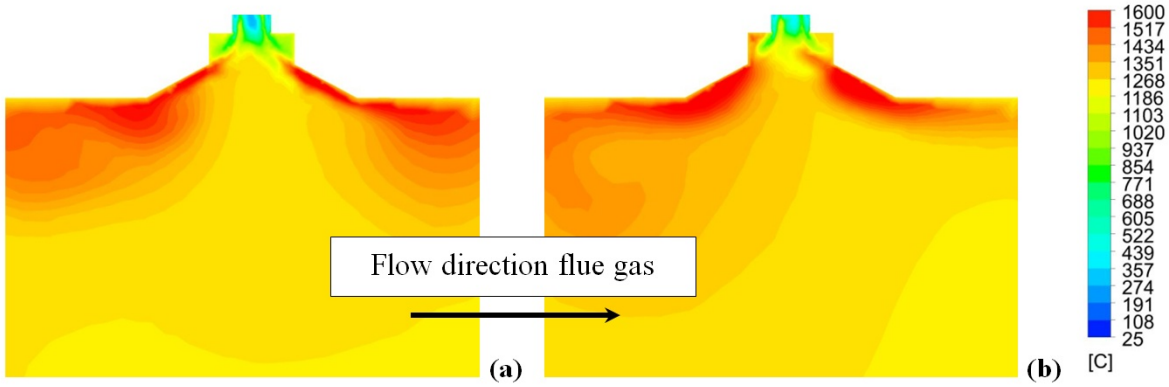

Fig. 100. Contour plots of the temperature in the vicinity of the burner for air-fuel combustion: (a) RSM, (b) Realizable k-epsilon model.

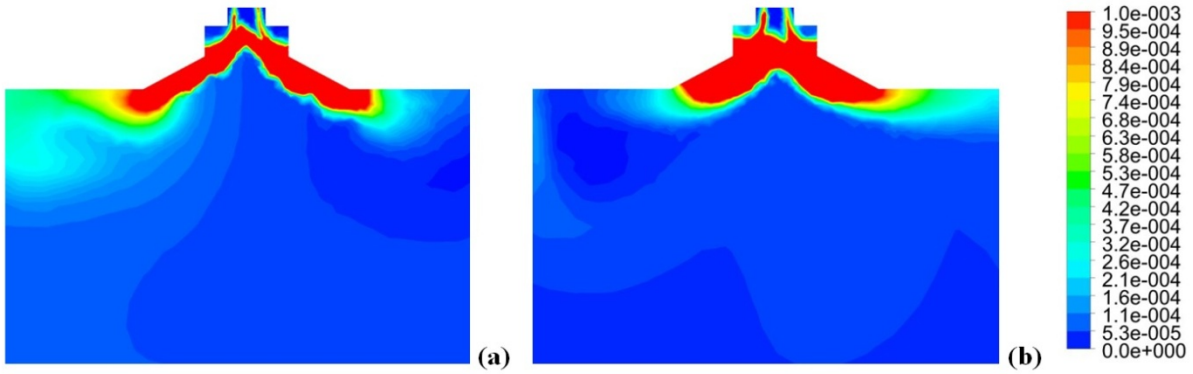

Fig. 101. Contour plots of the OH mole fraction in the vicinity of the burner for air-fuel combustion: (a) RSM, (b) Realizable k-epsilon model.

A slightly asymmetric flame shape can be observed in the contour plots determined by the OH mole fractions. The asymmetric shape is induced by the flue gas stream from the left hand side to the right (indicated in Fig. 100). The temperature field, predicted with the realizable k-epsilon model, is more affected by the flue gas stream due to the lower swirl intensity and radial momentum of the burnt gas.

For the numerical investigation of the walking hearth furnace, not only the predicted flames are important, but also the heat fluxes to the load and furnace walls. To predict the heating characteristics of the billets and the furnace efficiency, the accurate determination of the heat fluxes to the billets and walls is necessary. Therefore, the heat fluxes calculated with the realizable k-epsilon model and the RSM were compared. For this purpose, the simulated heat fluxes to the billets and walls, as well as the flue gas exit, were considered. The comparison takes place according to Eq. (135), where E_q is the relative deviation or error of the heat fluxes between the results with the realizable k-epsilon model and RSM. In Eq. (135), the $\dot{Q}_{RSM}$ and $\dot{Q}_{RKE}$ are the heat fluxes calculated with the RSM and realizable k-epsilon model. The relative deviations (errors) between the heat fluxes from the realizable k-epsilon model and the RSM are displayed in Fig. 102 for the air-fuel case (left) and the OEC case (right).

$$E_q = \left| \frac{\dot{Q}_{RSM} - \dot{Q}_{RKE}}{\dot{Q}_{RSM}} \right| * 100 \qquad (135)$$

Overall, the maximum deviation of the heat fluxes was below 1 % for both operating conditions. A maximum of 0.82 % for the heat fluxes to the walls was found in the air-fuel case. This is equal to a deviation of approximately 40 kW between the realizable k-epsilon model and the RSM. Compared to a total fuel input of 18.19 MW, the deviation of 40 kW has a minor effect on the heating characteristics and furnace efficiency. The OEC case showed a maximum of 0.97 %, which is approximately 95 kW. This value was determined for the heat

flux to the steel billets. An average deviation for all three heat fluxes (billets, walls and flue gas) was found with values of 0.41 % (air-fuel) and 0.43 % (OEC). Compared to a fuel input of 18.19 (air-fuel) and 16.53 MW (OEC), respectively, the difference between the predicted heat fluxes with the two turbulence models is negligible.

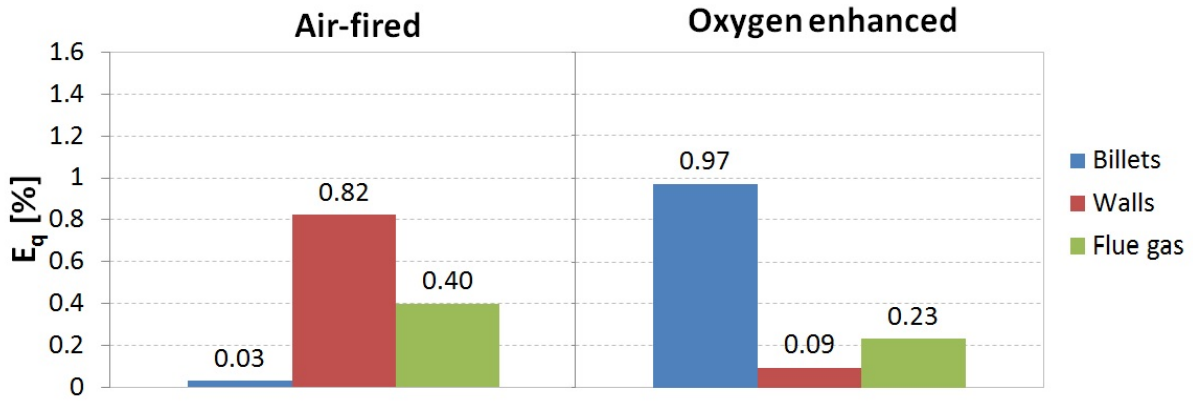

Fig. 102. Relative errors or deviation of the heat fluxes between the realizable k-epsilon model and RSM: Air-fired (left), OEC (right).

The displayed temperature and species concentrations, as well as the heat fluxes in the furnace, have proven that the effect of the turbulence models on the heating characteristic and furnace efficiency is low. There is a slight difference on the predicted flame shape, which does not significantly affect the heat fluxes. As long as the predicted values of the temperature are in close accordance, the heat fluxes to the walls and billets are quite similar due to radiation and convection. Since the prediction of the heat fluxes is the most important part of the furnace simulation, both models can be used for accurate predictions of the furnace efficiency and transient heating of the steel billets.

Since the realizable k-epsilon model uses only two additional transport equations for turbulence modelling, it was used for all further CFD simulations in this section.

7.3 Furnace simulation for air-fuel and OEC

In this section, the results of the furnace simulation from the fourth iteration step are presented. Both combustion cases are considered (air-fuel and OEC). First, a comparison between the measured wall and gas temperatures and the CFD results is given in Section 7.3.1. This represents the validation of the CFD model for the simulation of the walking hearth furnace. Secondly, with the validated model, the spatial distribution of the heat fluxes in the different zones is examined (see Section 7.3.2). Furthermore, the heat flux is subdivided into radiative and convective parts.

7.3.1 Comparison with measured data

The temperatures of the side walls and the burner walls were measured with a quotient pyrometer (Keller Optix Q PT70) during furnace operation. At the burner wall, the temperature was measured at different radial positions, shown in Fig. 103. The temperature was observed at several points on the conical and cylindrical part of the burner, with approximately the same radial distance. Since higher flame temperatures are achieved with oxygen enrichment, the temperature measurements at the burner walls confirm that overheating was avoided. Too high temperatures would lead to burner damage, and must be avoided for reliable furnace operation.

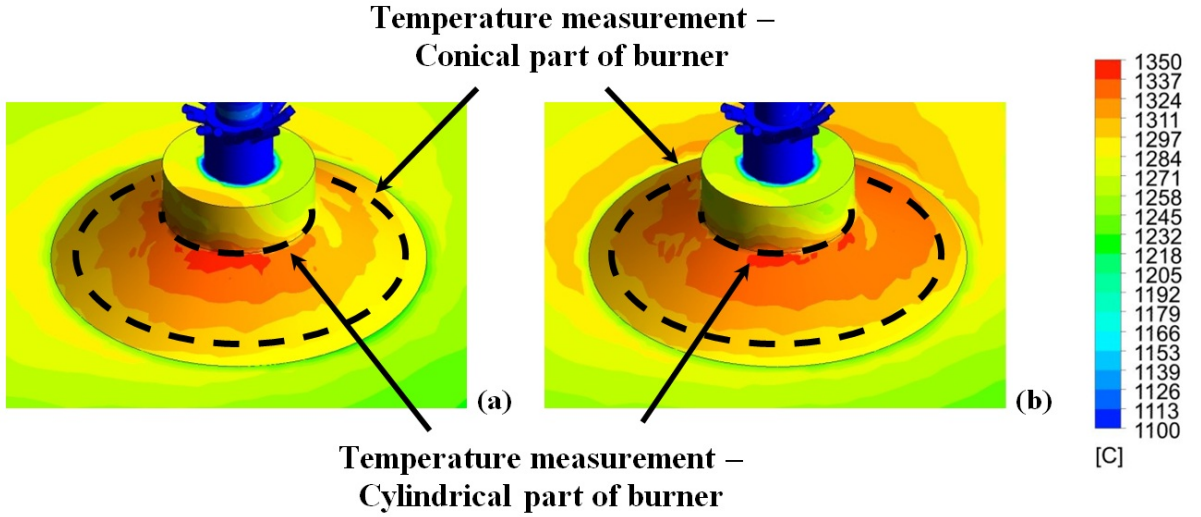

Fig. 103. Wall temperatures at the burner: (a) Air-fuel combustion, (b) OEC.

The measured temperatures at the conical and cylindrical parts of the burner, as shown in Fig. 103, are presented in Table 21. Due to the turbulent fluctuations of the fluid flow, the temperature was measured in a range of 1150 – 1200 °C (air-fuel) and 1250 – 1360 °C (OEC). During the measurement, it was found that the temperature fluctuations had a lower intensity at the cylindrical part of the burner. Therefore, the measurement of the temperature was in a small range of +/-20 – 30 K.

The simulated wall temperatures for the air-fuel (see case Fig. 103a) showed temperatures between 1284 – 1311 °C at the conical part, which is approximately 100 K higher than the measured values. In contrast to the over-prediction in the air-fuel case, the OEC case shows good agreement. The contour plots in Fig. 103b revealed temperatures between 1284 and 1337 °C (conical). At the cylindrical position, the CFD simulations predicted temperatures slightly below 1350 °C for both combustion cases, whereas the measurement showed a difference of approximately 100 K. Considering the temperature fluctuations of 20 – 30 K, the

predicted temperatures at the cylindrical part of the burner are in close agreement with the measurement for both combustion cases. Although the temperature at the conical part of the burner was over-predicted for air-fuel combustion, the CFD simulation calculated temperatures in the same range of the measured data. It was found that with both measurement and CFD simulation, the use of OEC (25 % O_2) does not dramatically exceed the wall temperatures at the burner (approximately 100 K). Thus, the use of OEC is approved for this type of burner.

Table 21
Measured temperatures at the burner walls.

	Conical	**Cylindrical**
Air-fuel	1150 – 1200 °C	≈ 1300 °C
OEC	1250 – 1360 °C	≈ 1400 °C

In Fig. 104, the measured wall temperatures are presented for air-fuel combustion and OEC. The measurements were taken at several positions at the side walls, except for the two temperatures at approximately 8.65 m. In this position, the temperature was measured at the intersection of the side wall and the water cooled wall, which subdivide the pre-heating and soaking zones. In the heating and soaking zones, the temperature determined by measurement and CFD simulations fit well for air-fuel and OEC. Only at the water cooled wall were higher deviations of the temperature found. In the pre-heating zone, the measured values revealed a lower wall temperature for OEC than for air-fuel combustion. Because of the lower volume-flow rate of the flue gas in OEC, the convective heat transfer is lower, and therefore the measured and calculated wall temperatures for air-firing are higher. A comparison of the measured and calculated values in the entire pre-heating zone shows that the CFD simulations predict lower temperatures, which is because of the thermal conductivity, chosen for the walls in the CFD simulations. Although the thermal conductivity is temperature dependent, it was fixed with a certain value for the whole furnace, valid for temperatures of 1200 °C. Since the thermal conductivity decreases with lower temperatures, it is too high in the pre-heating zone, with its lower gas temperatures of 600 – 800 °C (see Fig. 105). For real furnace operation, the lower thermal conductivity, compared to the CFD model, leads to higher wall temperatures. This is obvious for the first two measurement positions with approximately 650 – 700 °C. At 5.9 m, where the temperature is above 800 °C, better agreement between measurement and CFD simulation is detected. Furthermore, the model neglects air-leakage, for example, due to the charging and discharging procedures, leading to an additional air flow rate. Additional air increases the convective heat flux to the furnace and improves the convective heat flux to the

walls in the pre-heating zone, which also increases the wall temperature. Nevertheless, the CFD results showed a close accordance to the measured wall temperatures for the entire furnace length.

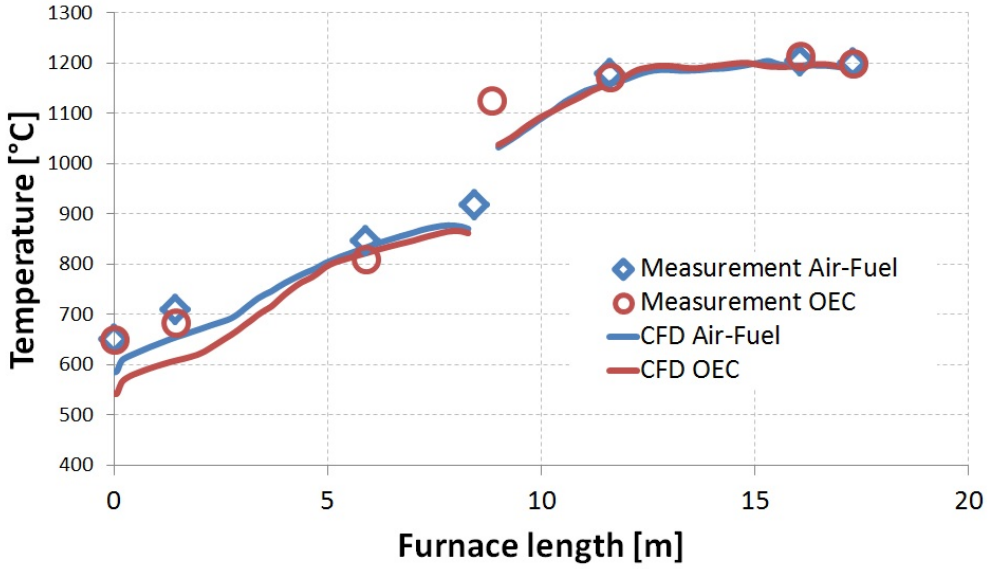

Fig. 104. Measured and calculated wall temperatures in the furnace for air-fuel and OEC.

For the furnace control system, four thermocouples were arranged in the furnace. In Fig. 105, only three positions of the thermocouples are displayed because of the symmetry of the model. The pre-heating and heating zones are equipped with one thermocouple in the centre of each zone. Two thermocouples are used in the soaking zone. All thermocouples were inserted in the furnace through the insulation at the ceiling.

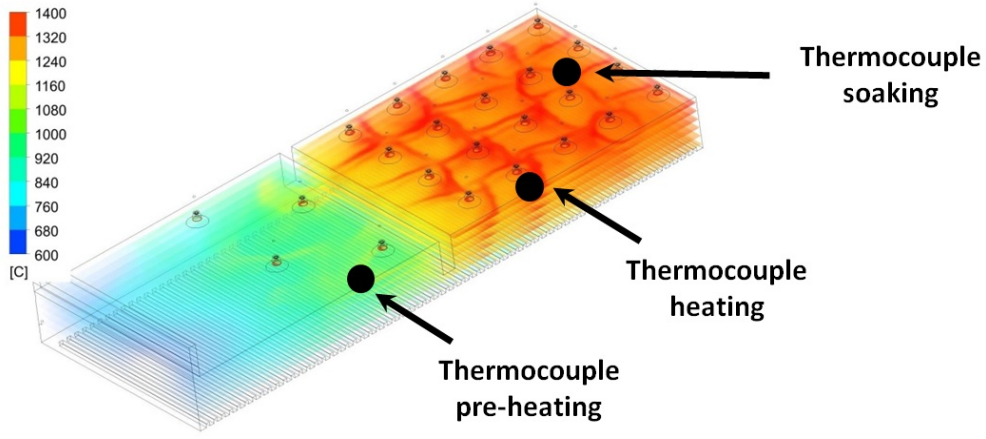

Fig. 105. Position of the thermocouples in the walking hearth furnace (temperature for air-fuel combustion).

The observed temperatures in the zones are summarized in Table 22. Similar to the results of the wall temperatures in the zones, the measured and simulated values in the heating and soaking zones are in close agreement. The temperatures are in the same range, not only for the air-fuel case, but also under OEC conditions. The best agreement was found in the soaking

zone, with a deviation of approximately 20 K. The difference between measurement and simulation is slightly higher in the heating zone with 53 (air-fuel) and 58 K (OEC). The highest deviations were found in the pre-heating zone, with a maximum of 104 K between measurement and CFD. This can be explained by the higher air leakage in this zone, due to the charging process: the additional amount of cooler ambient air reduces the measured temperature. In the CFD model, the air leakage was not considered, and therefore the simulated temperature was higher.

Table 22
Measured and calculated temperatures in the zones of the furnace.

		Measurement [°C]	CFD [°C]
Pre-heating	**Air**	730	834
	OEC	727	799
Heating	**Air**	1036	1094
	OEC	1030	1083
Soaking	**Air**	1131	1109
	OEC	1132	1107

Two conclusions can be drawn from the comparison of the measured and simulated temperatures. First, both CFD and measurement of the burner wall temperature revealed that the use of OEC is reliable in this furnace. Damage to the walls is not expected during furnace operation. Second, the measured wall and gas temperatures were used to validate the CFD model, which is for further applied to predict the heat fluxes and transient heating of the steel billets. In the heating and soaking zones in particular, the temperatures were in close accordance. Since the highest heat fluxes are expected in these zones, it was crucial to simulate the wall and gas temperatures precisely. In the heating zone, minor deviations were found, caused by the simplifications of the CFD model, including neglected air leakage and the over-/under-predicted thermal conductivity of the furnace walls.

7.3.2 Heat fluxes

In the following figures, the heat fluxes to the steel billets are examined in the pre-heating, heating and soaking zones. They are also subdivided into convection and radiation. The total heat flux for each zone is given in Fig. 106. Both operating conditions are considered. As

expected, the highest heat flux to the billets occurs in the heating zone, where the highest fuel input occurs. In the heating zone, approximately 60 % of the total fuel input is transported into the furnace. It is possible to see that the heat flux in the heating zone is slightly higher in OEC (4.88 MW) compared to air-fuel combustion (4.79 MW), caused by the higher radiative heat transfer. Since both the flame temperature and the H_2O and CO_2 concentrations in the flue gas are higher in the OEC case, the heat transfer is enhanced. The same effect was found in the soaking zone, where the heat flux in OEC was 0.11 MW higher than in air-fuel combustion. As opposed to this, the pre-heating zone showed the opposite result. In the pre-heating zone, the convective heat flux increases due to the higher volume-flow rate of flue gas (additional N_2) in the air-fuel case. The radiation intensity also has a lower effect as a consequence of the lower gas and wall temperatures in the pre-heating zone.

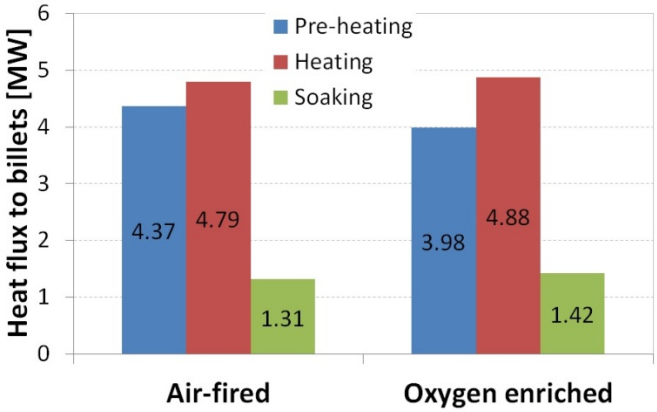

Fig. 106. Calculated heat fluxes to the billets in the pre-heating heating and soaking zones.

The fractions of convection and radiation on the total heat flux in the different zones are examined in Fig. 107. The radiative heat transfer was improved under OEC conditions in all zones of the furnace. Compared to the air-fired case, the radiative heat flux was increased with 0.5 (soaking) and 1.2 (pre-heating) percentage points. In the heating and soaking zones, it was found that convection had a minor effect on the total heat transfer. For both zones, the radiative heat transfer was considerably higher than 95 %. In contrast, the billets in the pre-heating zone are more exposed to the convective heat flux with a fraction of 10.9 (air-fuel) and 9.7 % (OEC). As already mentioned, this is a result of the higher volume-flow rate of the flue gas and an increase in the gas velocities around the billets.

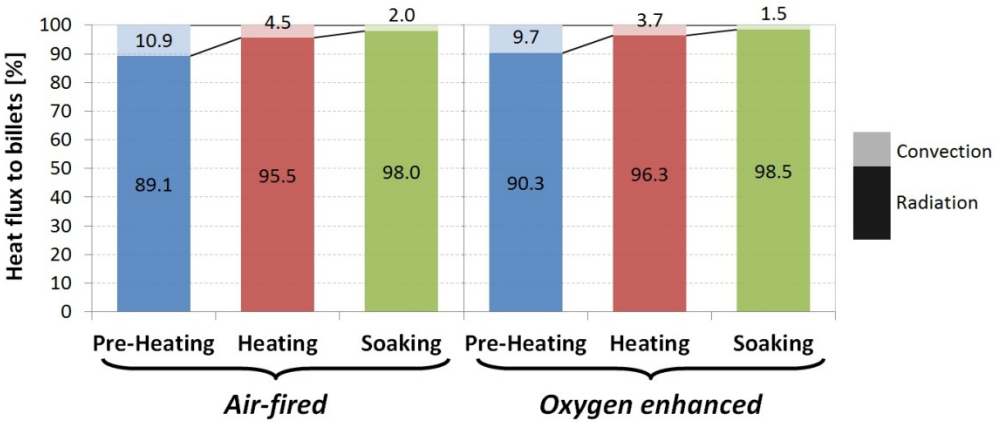

Fig. 107. Calculated radiative and convective heat fluxes to the billets in the different zones.

To further determine the higher convective heat fluxes in the pre-heating zone, the velocity magnitude of the flue gas is displayed in Fig. 108, where air-fuel (a) and OEC (b) case are compared. In this figure, the highest differences in the gas velocity magnitude are marked. The water cooled wall, segregating the pre-heating zone from the second part of the furnace, reduces the cross-section for the flue gas. Therefore, the gas velocity around the billets reaches a maximum in the marked region and makes the differences between air-fuel and OEC more obvious. Due to these higher velocities, the convective heat flux increases.

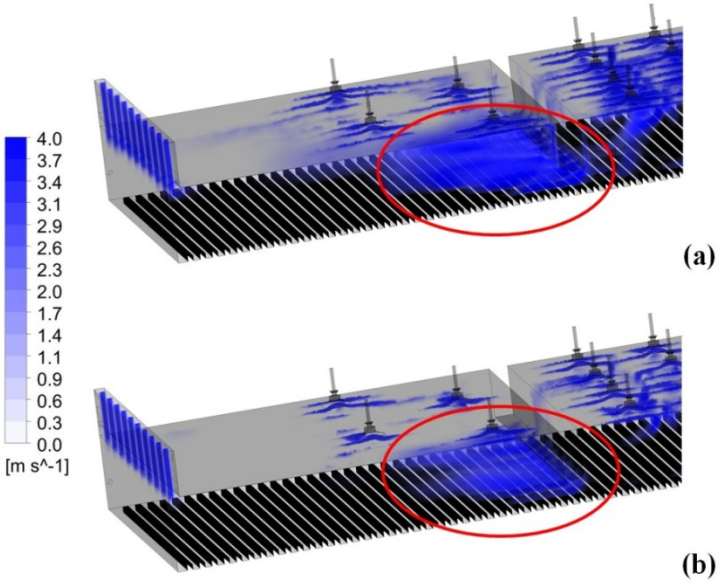

Fig. 108. Velocity magnitude in the pre-heating zone for air-fuel combustion (a) and OEC (b).

In Fig. 109, the heat fluxes (convection and radiation) related to the position in the furnace are displayed for OEC. The reason for showing only the OEC case is that the air-fuel case also shows the same trend along the furnace length, and can be seen in [147]. In this chart, the effect of the convective heat flux in the pre-heating zone is examined further. The specific heat flux in the pre-heating zone reaches the maximum value at the end of the zone. This

correlates to the velocities displayed in Fig. 108, which show the highest values at the end of the pre-heating zone. After the billets enter the heating zone at approximately 8.65 m, the radiative heat flux "jumps" to its maximum level, which is at approximately 11 m. In the pre-heating and soaking zones, the convective heat flux loses its relevance for the transient heating of the steel billets. Almost the entire furnace length showed that the fraction of the radiative heat transfer on the overall heat flux is above 90 %. Only in the first 2 – 3 m after charging did the radiative heat flux drop below 90 %.

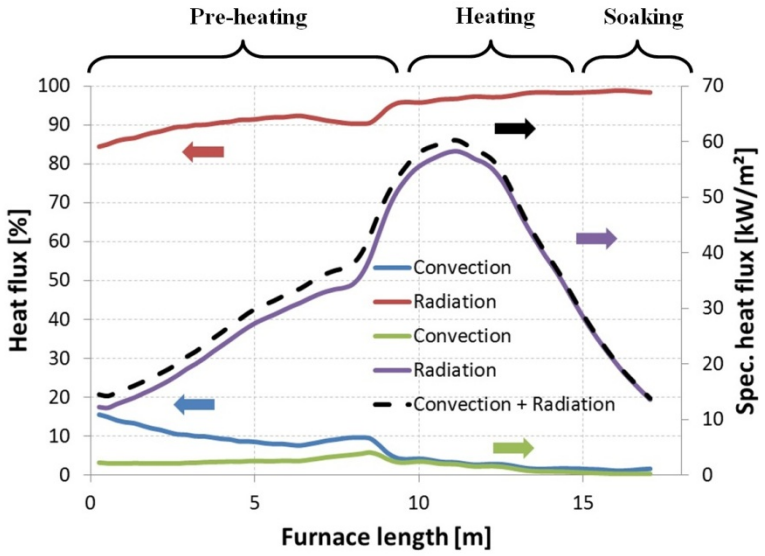

Fig. 109. Distribution of the heat fluxes (radiation and convection) dependent on the furnace length for OEC.

Since the heat fluxes to the steel billets in the furnace were determined in detail, the global energy balance calculated by CFD will now be given in Fig. 110. As a reminder, the operating conditions used for the CFD simulations were related to the same production rate for air-fuel combustion and OEC, where production rate was 47.428 t/h. Therefore, to achieve the desired target temperature of the billets for the chosen production rate, the total heat flux to the billets has to be the same. In Fig. 110, only a small deviation of 0.2 MW can be detected for the heat flux to the billet between air-fuel combustion and OEC. The effect on the temperature distribution and target temperature after the reheating process is considered in Section 7.4. Although the heat flux absorbed by the billets in the CFD simulation was similar, the fuel input was lower than in the OEC case. As a consequence, the enrichment level of 25 % O_2 leads to fuel savings of 8 % compared to the conventional air-fuel combustion case. Such fuel savings are in good agreement to the experimental and numerical results on the lab scale-furnace described in Section 6.5. In the lab-scale furnace, fuel savings of 8.3 % were observed without thermal load, at a temperature level of approximately 1090 °C. The same was detected in the experiments with copper plate inside the lab-scale furnace. In this case, the fuel savings were 8.2 % at a temperature level of 1000 °C.

During furnace operation, the oxygen concentration in the dry flue gas was 0.7 % for both cases. As a consequence of the fuel savings, a lower amount of pre-heated oxidant is necessary for OEC. Therefore, the heat flux through the pre-heated oxidant is reduced from 1.9 MW (air-fuel) to 1.46 MW (OEC).

Considering the heat loss through the walls and flue gas, it is decisive that the use of OEC is beneficial to both the efficiency and safety of the operation. The lower losses through the flue gas are a result of the reduced mass-flow rate of the flue gas and slightly lower outlet temperatures in OEC, which was already investigated in the lab-scale furnace.

Similar to the furnace efficiency defined for the lab-scale furnace, the efficiency was calculated for the walking hearth furnace. Although the pre-heated oxidant represents an additional heat flux to the furnace (see Fig. 110), it was not considered for the calculation of the efficiency. Using Eq. (132), the efficiencies for both operating conditions were determined with values of 57.6 % (air-fuel) and 61.4 % (OEC). Only a minor increase in the oxygen concentration, from 21 to 25 % in the oxidant, is enough to significantly improve the efficiency of the reheating process.

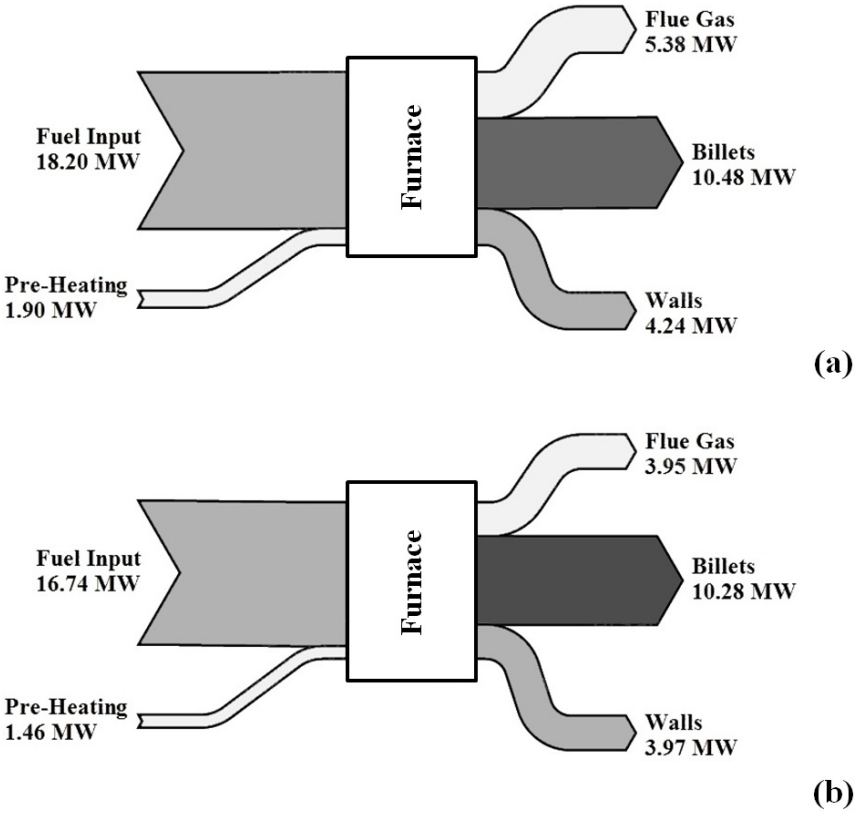

Fig. 110. Sankey charts for the heat fluxes at the furnace for air-fuel combustion (a) and OEC (b).

7.4 Heating characteristics of the steel billets

In this section, the effect of the different heat fluxes on the transient heating of the steel billets is investigated. The calculated heat fluxes in the previous section are used to predict the temperature distribution in the billets depending on their position/residence time in the furnace. The positions of the temperature monitors in the CFD simulation are displayed in Fig. 111, where *L* is the distance from the symmetry plane of the billet. During the transient simulations the temperatures were observed in 9 different positions in the same cross-section of the billet, which were named “t1” to “t9”. In the same cross-section, the temperature is also observed at the top surface position called “t_surf”.

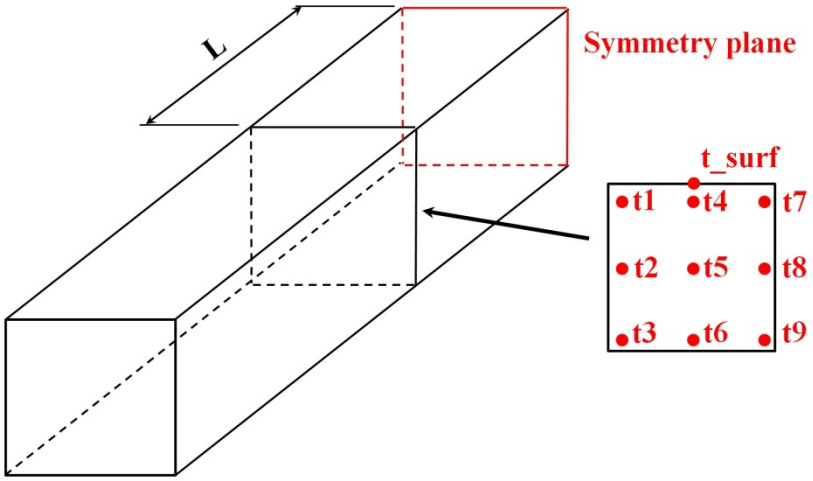

Fig. 111. Position of the temperature monitors in the steel billet during the transient simulation.

In Fig. 112, the temperature trend in the billet is shown for the air-fuel case. The temperature is only given for the air-fuel case because the trend for the OEC case is hardly different from the results in Fig. 112; however, the results of the OEC case will be compared to the air-fuel case in the following figures, and differences will be examined in this section. The temperature trend of t1 to t9 in the pre-heating is quite steady, with a constant increase between the maximum and minimum temperatures. At the end of the pre-heating zone, a maximum temperature difference of 99.9 K was detected between t1 and t6. During the entire process of reheating the steel billets, the maximum temperature difference was found between t1 and t6. Since the highest heat fluxes to the billets were found in the heating zone, a faster increase in the temperature was found. This is more obvious for t1, t4 and t7, because the top surface is exposed to radiative and convective heat fluxes. The lowest temperature increase was detected at t6, where the heat transfer took place due to conduction. At 12.7 m, the temperature gap between t1 and t6 reached a global maximum, and furthermore, the temperature trend of t6 starts to increase rapidly. This can be explained due to the drop in the

specific heat capacity of the steel at a temperature of 830 °C. From Fig. 31, it is possible to see that the specific heat falls from above 1000 to approximately 600 J/kg*K. As a consequence, the steel at position t6 has a higher heating rate after 12.6 m in the furnace.

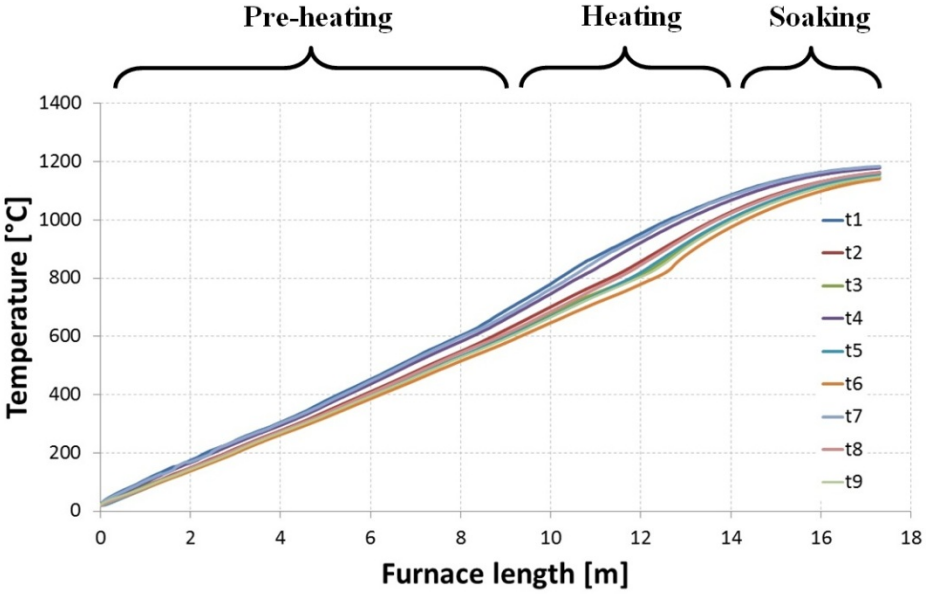

Fig. 112. Temperature trend during the heating process at the temperature monitors for air-fuel combustion (L = 4.875 m).

In Fig. 113, the temperature trend at t_surf is shown by the blue line for the air-fuel combustion case. The trend from the OEC case is not displayed because this line would be barely distinguishable from the air-fuel case in this figure. Instead, the red line represents the temperature difference between the air-fuel and OEC cases at t_surf. Since a higher heat flux in the pre-heating zone for the air-fuel case was observed, the surface temperature increases much faster. Therefore, the difference between the air-fired and OEC cases is at its maximum at 4.6 m with 38.2 K. This is also examined in Fig. 115a. Between 4.6 m and the end of the pre-heating zone (≈ 8.65 m), the temperature difference is quite constant, because the first burners are arranged in this region. The radiation from the flames is slightly higher in OEC and compensates the higher convective heat flux from air-fuel combustion. The global maximum is reached before the billets exit the pre-heating zone. A small peak in the temperature difference is found at 8.5 m, due to the convective heat flux, which is induced by the higher velocities in this region. The reason for that is the water cooled wall, which decreases the cross-section for the gas flow (see Fig. 108). When the billets enter the heating zone, the temperature difference at the surface starts to decrease. This is a result of the higher total and radiative heat flux in OEC. Additionally, the high heat flux in the heating zone promotes the development of high temperature gradients around the corners and edges of the billet in OEC (see Fig. 115d and f). At the end of the reheating process, the temperature

difference between the combustion cases at the surface position was 17.8 K, which is a consequence of the lower total heat flux in OEC of 0.2 MW. At the end of the furnace, the surface temperatures were 1172.8 °C (air-fuel) and 1159 °C (OEC), and thus within the range of the target temperatures mentioned in Section 3.2.

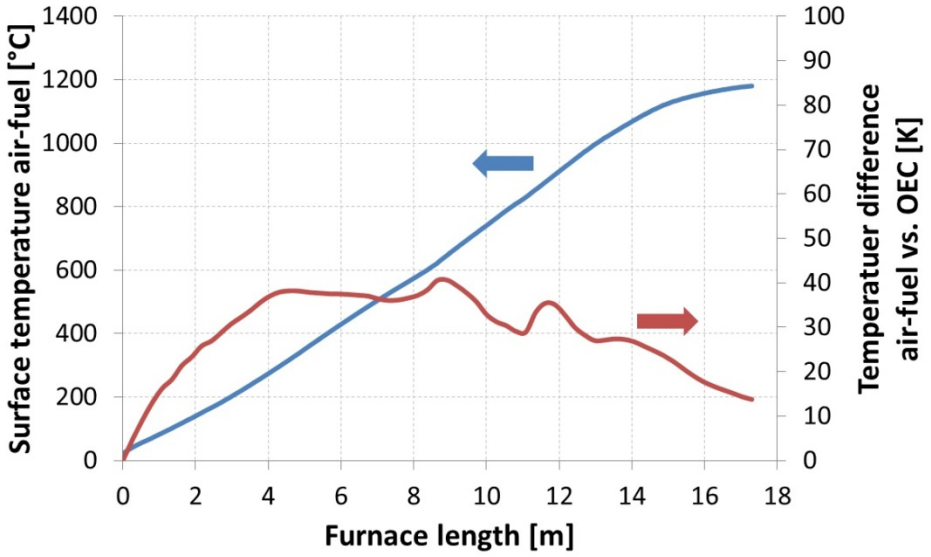

Fig. 113. Surface temperature of the billet for air-fuel combustion (blue) and difference of surface temperatures from air-fuel combustion and OEC (red) at L = 1.4 m.

In addition to the surface temperature, the temperature distribution in the steel billets was also analysed. From the charging to the discharging of the billets, the highest temperature difference within the steel was found between t1 and t6, which is a reference for temperature uniformity in the billet. The difference between these two positions was observed for both cases in Fig. 114. A linear increase in the temperature difference was found in the pre-heating zone. Although the trend was similar for both air-fuel combustion and OEC, the difference was slightly higher when air was used as the oxidant, due to the higher heat fluxes in the pre-heating zone. In the heating zone, the difference in temperature between t1 and t6 starts to increase more quickly, with its maximum at 12.45 m (air-fuel) and 12.75 m (OEC). In this position, the air-fuel combustion showed a maximum temperature deviation of 170.1 K. For the OEC case, the maximum was only 2 K higher. The progress of the heating process leads to a more homogeneous temperature distribution as well as a lower temperature difference between t1 and t6. By the end of the soaking zone, the temperature difference dropped to values of 41.4 K (air-fuel) and 45.6 K (OEC). In the CFD simulations, both operating conditions showed a similar temperature distribution and target temperatures, which are crucial to achieving the desired product quality under OEC.

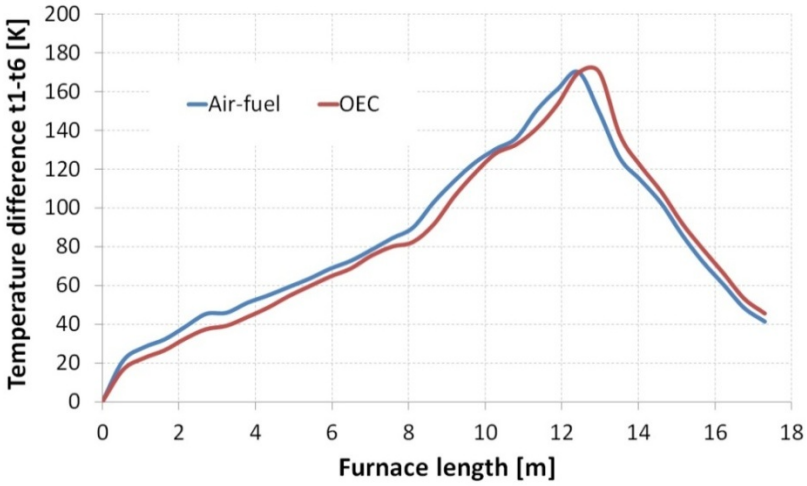

Fig. 114. Temperature difference between t1 and t6 m depending on the position in the furnace for air-fuel combustion and OEC (L = 1.4 m).

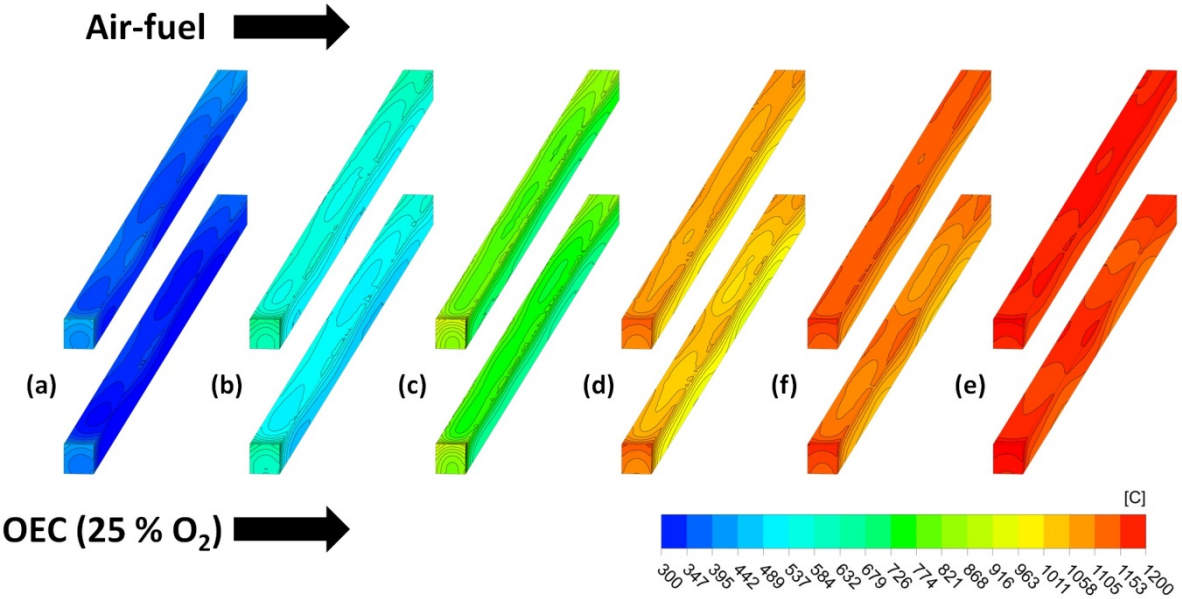

Fig. 115. Contour plots of the temperature at the billets' surface for air-fuel combustion and OEC: (a) 4.9 m, (b) 7.6 m, (c) 10.3 m, (d) 13.8 m, (e) 15.1 m and (f) 17 m.

8 Conclusion and outlook

In this work, OEC was experimentally and numerically investigated for use in industrial processes, such as annealing, melting and reheating applications. Compared to the combustion of coal with pure oxygen in power plants, only a few studies have been published on the combustion of natural gas with oxygen enhanced air in energy demanding processes. Thus, a CFD model was developed, based on experimental data, to investigate the heat transfer and gas phase combustion in OEC of natural gas in industrial furnaces.

In the lab-scale experiments, the benefits of OEC technology compared to air-fuel combustion were examined at different temperature levels, which are significant for high temperature processing. The test runs were carried out in the full range of oxygen enrichment from air-fuel conditions up to 100 % O_2. Experiments without thermal load inside the furnace revealed a significant fuel saving potential when OEC is used. To achieve a constant temperature level of 1090 °C, 18 kW fuel input was necessary under air-fuel conditions. Test runs under OEC conditions, with 25 % and 30 % O_2 in the oxidant, showed a fuel reduction to 16.5 and 16 kW, respectively. Thus, even small additional amounts of oxygen lead to a reasonable increase in the process efficiency. The same effect was determined by experiments with a thermal load (water cooled copper plate) inside the furnace. It was found that fuel input can be decreased with higher oxygen enrichment levels although the heat flux to the thermal load is constant. The biggest effect was highlighted for oxygen enrichment up to 30 % O_2 in the oxidant. Fuel savings of 8.2 % (25 % O_2) and 15.7 % (30 % O_2) were measured, leading to an increase of the furnace efficiency. Using pure oxygen for the combustion process instead of air, the efficiency was increased from 40 % to 53.6 % at a temperature level of 1000 °C. The results of the experiments revealed a significant optimization potential in high temperature processes. High efforts for oxygen production or costs for oxygen supply can be minimized when low oxygen enrichment levels are applied.

Measured temperatures and heat fluxes in the lab-scale furnace were used to validate different combustion, radiation models and turbulence models, as well as reaction mechanisms in order to test their applicability for OEC in high temperature processes.

a) 1D analysis of reaction mechanisms

For the CFD simulations of the combustion processes, four different chemical reaction mechanisms (skeletal25, smooke46, DRM19 and GRI3.0) were tested in 1D analysis for a

laminar counter-flow diffusion flamelet. Temperature and species concentrations in the flamelet were in close accordance for air-fuel conditions without heat loss. Additionally, for oxy-fuel combustion the calculated temperatures and species concentrations were also in good agreement using the smooke46, DRM19 and GR3.0 mechanism. The skeletal25 mechanism showed a significant increase of the predicted temperature at stoichiometric mixture fraction, due to the faster conversion of intermediate species, such as CO, to the products H_2O and CO_2. This accounts for the good prediction of OEC cases.

b) Turbulence modelling

To predict the jet flame in the lab-scale furnace, it was found that the realizable k-epsilon model and the RSM are able to simulate flames under OEC conditions, which was determined by comparison with the measured temperatures in the furnace. Furthermore, the standard k-epsilon model calculated a significantly different flame shape. For the axisymmetric jet, the spreading rate was over-predicted by the standard k-epsilon model, and therefore, the temperature in the vicinity of the burner outlet is too high. Although the RSM and realizable k-epsilon model showed the same results, it is recommended to use the simpler realizable k-epsilon model in air-fuel combustion and OEC because of the lower calculation time. Therefore, it was used in all CFD simulations to test the different radiation and combustion models.

c) Radiation models

It was found that the modelling of the radiative properties of the flue gas can be reduced with the use of standard models, such as WSGGM, and combined with model parameters from Smith et al. [94]. The RTEs were solved using the DOM. In the combustion case with pure oxygen, these models showed the best agreement with measured results in the lab-scale furnace. Additionally, the P1 model was tested to solve the RTEs under OEC conditions. The comparison with the measurement revealed that the P1 model over-predicts the radiation intensity and is not able to predict the measured temperatures in the furnace. Although the lab-scale furnace has a lower mean beam length, where the effect of modelling the radiative properties of the flue gas is minor, the WSGGM can also be used for industrial scale furnaces. Since furnaces for thermal processing have a low volume to surface ratio, the mean beam length is also quite low. Therefore, the DOM and WSGGM can be used for different furnace dimensions and optical thicknesses in OEC.

d) Combustion models and reaction mechanisms

The results of the EDM, EDC model and SFM were compared to measured temperatures in the lab-scale furnace. The EDM approach, which determines the reaction progress by the

turbulent mixing rate, was not suitable to predict an OEC flame. It significantly over-predicts the flame temperature and leads to much shorter flames when the oxygen enrichment level is higher.

In contrast to the EDM, the EDC model, in conjunction with the smooke46 mechanism, was in close accordance with the temperature measurement when pure oxygen is used. Since the EDC model calculates the reaction rate for each chemical reaction by the Arrhenius approach, the prediction of temperature and species concentrations within in the flame was improved compared to the EDM. Additionally, in this thesis, an optimized 3-step global mechanism proposed by Yin et al. [74] showed also good results for oxy-fuel combustion, but failed under air-fuel conditions. When global reaction mechanisms are used in OEC with the EDC, the Arrhenius parameters have to be adapted for each enrichment level. Hence, the application of the EDC with global reaction mechanisms for the full range of OEC is not recommended. As a consequence, detailed reaction mechanisms with several elementary reactions are recommended for OEC. Since the entire reaction mechanism has to be solved for each iteration step, the calculation time increases using the EDC model. This represents a limitation for its application in industrial large scale furnaces.

The SFM offers an opportunity to consider a detailed reaction mechanism without solving the reaction mechanism during the CFD simulation, because the chemistry is reduced to the mixture fraction and its variance. Thus, the chemistry is not explicitly solved during the CFD simulation which reduced the calculation time significantly. It was determined by the simulations that the calculation time with the SFM was 7 to 10 times lower than with the EDC model. The application of the SFM with the different reaction mechanisms showed no significant differences for air-fuel combustion and low oxygen enrichment levels, as it was expected by the 1D analysis of the flamelets. However, at higher oxygen levels in the oxidant, the skeletal25 mechanism predicted different temperatures, species concentrations and flame shapes than the smooke46, DRM19 and GR3.0 mechanisms. Whereas the results with the SFM/skeletal25 were in close accordance to the measurement and results from the EDC in oxy-fuel combustion, the other mechanisms predicted an unreasonable temperature in the vicinity of the burner. Therefore, only the skeletal25 mechanism was suitable, in conjunction with the SFM, for the full range of OEC cases, as well as air-fuel combustion.

Due to the results of the CFD simulations and comparison with measured data, an overall CFD model to predict air-fuel combustion and OEC cases with high accuracy and low computational costs was developed. It is applicable, not only for all oxygen concentrations in

the oxidant, but also for large scale furnaces in industry. The combination of the following sub-models was found to be the most efficient for the investigated combustion cases:

- Steady flamelet model (SFM)
- Discrete ordinates model (DOM)
- skeletal25 reaction mechanism (17 species, 25 reversible reactions)
- Realizable k-epsilon model

The CFD model developed was suitable to predict temperatures, species concentrations and heat fluxes, not only in small scale furnaces, but also in an industrial walking hearth furnace for reheating steel billets. The furnace was operated under air-fuel conditions and OEC (25 % O_2). Good agreement to the measured temperatures was found for the wall and gas temperatures. Small deviations were determined in the pre-heating zone because of some simplifications (e.g. air leaking, thermal conductivity of the wall, etc.) in the CFD model. It was also found that the majority of the heat flux is transported by radiation, particularly when the gas and wall temperatures are high. Although OEC was applied in the furnace investigated, the product quality has to be the same as for the conventional air-fuel combustion. To determine the product quality, the temperature in the steel billets was calculated by means of a transient simulation, which was coupled with the gas phase combustion. The coupling of the gas phase combustion and the transient heating process of the billets was achieved by means of an iterative solution procedure developed for this thesis. The simulated temperature distribution within the billets showed a maximum temperature difference within the billets of below 50 K for both operating conditions. The target temperature of the billets at the end of the reheating process also showed very similar results. The numerical results predicted that both operating conditions can achieve the desired target temperature and temperature uniformity of the billet.

8.1 Outlook

a) Scale formation

The formation of scale layers on the surface of the steel is responsible for mass loss during the reheating process and has to be minimized. In reheating processes, the growth rate of the scale layer formation is dependent on the temperature and the species concentrations at the billet surface. Since all of this data is available in the CFD model developed, the prediction of the scale layer formation can be added to the CFD code. Only experimental data on the scale layer formation under OEC conditions has to be determined.

b) Application of the flamelet generated manifold (FGM) model

Since the SFM has some limitations for low strain rates and flame ignition/extinction modelling, the FGM can overcome these obstacles. During work for this thesis, the FGM was also used to simulate the combustion process in the lab-scale furnace. Contour plots and an iso-surface for 21 % and 45 % O_2 are displayed in Fig. 116 (21 % O_2) and Fig. 117 (45 % O_2). It is possible to see that the FGM fits quite well with the SFM for air-fuel combustion. In contrast, the predicted temperatures with increasing oxygen enrichment levels are far too high, and the energy balance in the CFD simulation shows a high error. To apply the FGM for OEC, this fact should be analysed in a future research project.

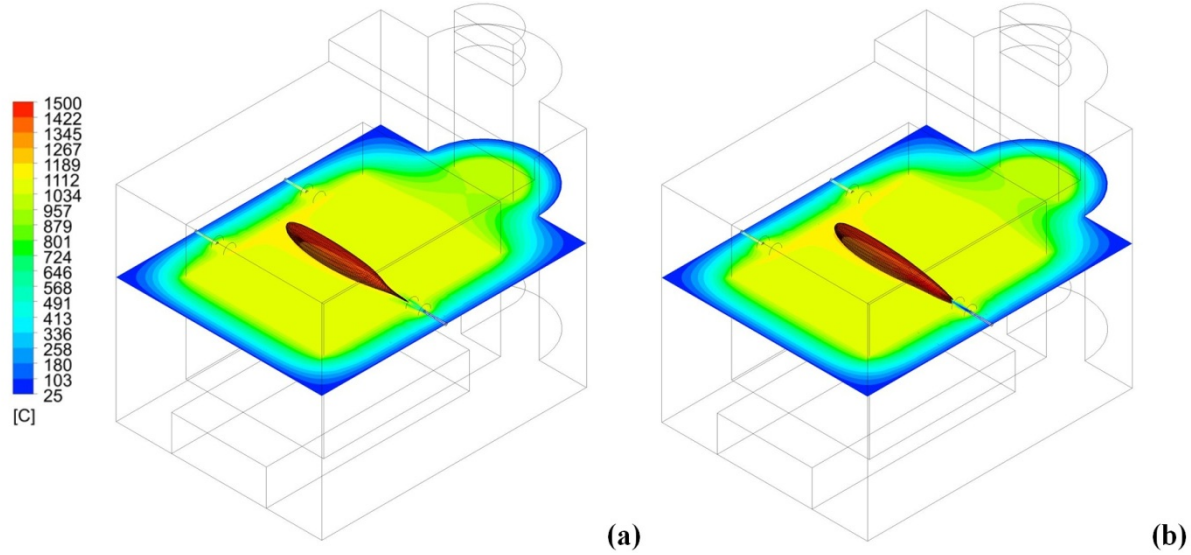

Fig. 116. Contour plots and iso-surface (1200 °C) of the temperature in the lab-scale furnace for 2-OEC_21: (a) SFM, (b) FGM.

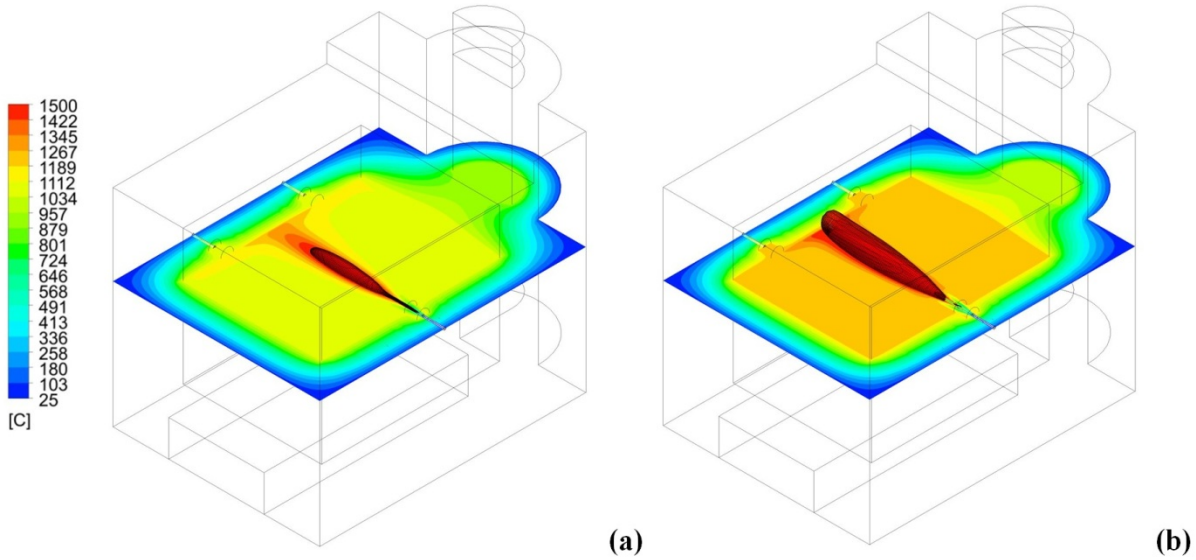

Fig. 117. Contour plots and iso-surface (1200 °C) of the temperature in the lab-scale furnace for 2-OEC_45: (a) SFM, (b) FGM.

9 References

[1] Davison J. Performance and costs of power plants with capture and storage of CO_2. Energy 2007; 32: 1163-1176.

[2] Intergovernmental Panel on Climate Change (IPPC). IPPC special report on carbon dioxide capture and storage. Cambridge, UK and New York, NY, USA: Cambridge University Press; 2005.

[3] Manickam B, Dinkelacker F, Lobe T, Tertychnyy M. Enriched oxygen combustion simulation for rotary kiln application, In: 4th European Combustion Meeting, Vienna, Austria; 2009.

[4] Falcitelli M, Pasini S, Tognotti L. Modelling practical combustion systems and predicting NOx emissions with an integrated CFD based approach. Computers Chem Eng 2002; 26: 1171-1183.

[5] Rabensteiner M, Kinger G, Koller M, Gronald G, Hochenauer C. Pilot plant study of ethylenediamine as a solvent for post combustion carbon dioxide capture and comparison to monoethanolamine. Int J Greenhouse Gas Control 2014; 27: 1-14.

[6] Rabensteiner M, Kinger G, Koller M, Gronald G, Unterberger S, Hochenauer C. Investigation of the suitability of aqueous sodium glycinate as a solvent for post combustion carbon dioxide capture on the basis of pilot plant studies and screening methods. Int J Greenhouse Gas Control 2014; 29: 1-15.

[7] Rabensteiner M, Kinger G, Koller M, Hochenauer C. Three years of working experience with different solvents at a realistic post combustion capture pilot plant. Energy Procedia 2014; 63: 1578-1584.

[8] Cuellar-Franca RM, Azapagic A. Carbon capture, storage and utilisation technologies: A critical analysis and comparison of their life cycle environmental impacts. Journal of CO_2 utilization 2015;9: 82-102.

[9] Ponsich A, Azzaro-Pantel C, Domenech S, Pibouleau L, Pigeonneau F. A systemic approach for glass manufacturing process modeling. Chem Eng Proc: Process Intensification 2009; 48: 1310-1320.

[10] Leicher J, Giese A. O2-Glaswanne: Untersuchungen zur Verbesserung der Energieeffizienz und der Wärmeübertragung in Oxy-Fuel-Glasschmelzwannen (AiF-Nr. 15987 N). Würzburg: Gaswärme-Institut e.V. Essen; 2013.

[11] Stallinger C. Modellierung und Optimierung einer Methan-Reinsauerstoff Verbrennung in einem Glasschmelzofen mittels CFD. Master thesis. Wels: FH Oberösterreich Campus Wels; 2012.

[12] Furu J, Buchholz A, Bergstrøm, HT, Marthinsen K. Numerical modeling of oxy-fuel and air-fuel burners for aluminium melting. In: Light Metals 2012. Hoboken, NJ, USA: John Wiley & Sons, Inc; 2012.

[13] Al-Abbas AH, Naser J. Effect of chemical reaction mechanisms and NOx modeling on air-fired and oxy-fuel combustion of lignite in a 100-kW furnace. Energy Fuels 2012; 26: 3329-3348.

[14] Al-Abbas AH, Naser J. Numerical study of one air-fired and two oxy-fuel combustion cases of propane in a 100 kW furnace. Energy Fuels 2012; 26: 952-967.

[15] Bhuiyan AA, Naser J. Computational modelling of co-firing of biomass with coal under oxy-fuel condition in a small scale furnace. Fuel 2015; 143: 455-466.

[16] Habibi A, Merci B, Heynderickx GJ. Multiscale modeling of turbulent combustion and NO_x emission in steam crackers. AIChE Journal 2007; 53: 2384–2398.

[17] Guihua H, Honggang W, Feng Q. Numerical simulation on flow, combustion and heat transfer of ethylene cracking furnaces. Chem Eng Sci 2011; 66: 1600-1611.

[18] Granados DA, Chejne F, Mejia JM, Gomez CA, Berrio A, Jurado WJ. Effect of flue gas recirculation during oxy-fuel combustion in a rotary cement kiln. Energy 2014; 64: 615-625.

[19] Baukal CE. Oxygen-enhanced combustion. 2nd Edition. Boca Raton: CRC Press; 2013.

[20] Liu H, Saffaripour M, Mellin P, Grip C-E, Yang W, Blasiak W. A thermodynamic study of hot syngas impurities in steel reheating furnaces – Corrosion and interaction with oxide scales. Energy 2014; 77: 352-361.

[21] Sobotka CVF. High temperature oxidation of steel, aluminum and copper alloys under the influence of a sustainable energy-efficient combustion in industrial furnaces. PhD Thesis. Leoben, Austria: Montanuniversität Leoben – University of Leoben; 2014.

[22] Riley MF. Dilute oxygen combustion - Phase 4 report: Optimized reheat furnace design. Report-ID DE-FC36-95ID13331, April 2003, Online: http://www.osti.gov/scitech/servlets/purl/877124.

[23] Jang JH, Lee DE, Kim MY, Kim HG. Investigation of the slab heating characteristics in a reheating furnace with the formation and growth of scale on the slab surface. Int J Heat Mass Trans 2010; 53: 4326-4332.

[24] Jaklic A, Glogovac B, Kolenko T, Zupancic B, Tezak B. A simulation of heat transfer during billet transport. Applied Thermal Eng 2002; 22: 873-883.

[25] Han SH, Chang D, Huh C. Efficiency analysis of radiative slab heating in a walking-beam-type reheating furnace. Energy 2011; 36: 1265-1272.

[26] Kim MY. A heat transfer model for the analysis of transient heating of the slab in a direct-fired walking beam type reheating furnace. Int J Heat Mass Trans 2007; 50: 3740-3748.

[27] Emadi A, Saboonchi A, Taheri M, Hassanpour S. Heating characteristics of billet in a walking hearth type reheating furnace. Applied Thermal Eng 2014; 63: 396-405.

[28] Tan CK, Jenkins J, Ward J, Broughton J, Heeley A. Zone modelling of the thermal performances of a large-scale bloom reheating furnace. Applied Thermal Eng 2013; 50: 1111-1118.

[29] Jang J-Y, Huang J-B. Optimization of a slab heating pattern for minimum energy consumption in a walking-beam type reheating furnace. Applied Thermal Eng 2015; 85: 313-321.

[30] Jaklic A, Vode F, Kolenko T. Online simulation of the slab-reheating process in a pusher-type furnace. Applied Thermal Eng 2007; 27: 1105-1114.

[31] Hottel HC, Sarofim AF. Radiative transfer. New York: McGraw-Hill; 1967.

[32] Hu Y, Niska J, Broughton J, McGee E, Tan CK, Matthew A, Roach P. Zone modelling coupled with dynamic flow pattern for the prediction of transient performance of metal reheating. In: Proceedings of the Iron and Steel Technology Conference (AISTech), Indianapolis, Indiana, US; 2014.

[33] Han SH, Chang D, Kim CY. A numerical analysis of slab heating characteristics in a walking beam type reheating furnace. Int J Heat Mass Trans 2010; 53: 3855-3861.

[34] Han SH, Chang D. Optimum residence time analysis for a walking beam type reheating furnace. Int J Heat Mass Trans 2012; 55: 4079-4087.

[35] Gu MY, Chen G, Liu X, Wu C, Chu H. Numerical simulation of slab heating process in a regenerative walking beam reheating furnace. Int J Heat Mass Trans 2014; 76: 405-410.

[36] Morgado T, Coelho PJ, Talukdar P. Assessment of uniform temperature assumption in zoning on the numerical simulation of a walking beam reheating furnace. Applied Thermal Eng 2015; 76: 496-508.

[37] Singh VK, Talukdar P, Coelho PJ. Performance evaluation of two heat transfer models of a walking beam type reheat furnace. Heat Transf Eng 2015; 36: 91-101.

[38] Singh VK, Talukdar P. Comparisons of different heat transfer models of a walking beam type reheat furnace. Int Communications Heat Mass Trans 2013; 47: 20-26.

[39] Chen WH, Chung YC, Liu JL. Analysis on energy consumption and performance of reheating furnaces in a hot strip mill. Int Communications Heat Mass Trans 2005; 32: 695-706.

[40] Jaklic A, Kolenko T, Zupancic B. The influence of the space between the billets on the productivity of a continuous walking-beam furnace. Applied Thermal Eng 2005; 25: 783-795.

[41] Chen W-H, Lin M-R, Leu T-S. Optimal heating and energy management for slabs in a reheating furnace. Marine Science Technology 2010; 18: 24-31.

[42] Morawe F. Sauerstoffanreicherung des Gebläsewindes im Kupolofen. Giesserei 1930; 17: 132-136.

[43] Prieler R, Demuth M, Hochenauer C. Analysis of natural gas fired furnaces with different oxygen enrichments. In: 15th International Conference on Numerical Combustion, Avignon, France; April 2015.

[44] Spoljaric D, Palmai G. Reducing emissions and improving energy efficiency by oxy-fuel fired glass melting technology – Experiences, limits and expectations. In: Glassman, Istanbul, Turkey; November 2011.

[45] Delabroy O, Louedin O, Tsiava R, Le Gouefflec G, Bruchet P. Oxycombustion for reheat furnaces: major benefits based on ALROLL^{TM}, a mature technology. In: AFRC/JFRC/IEA Joint Int Combustion Symposium, Kauai, Hawaii; 2001.

[46] Bělohradský P, Skryja P, Hudak I. Experimental study on the influence of oxygen content in the combustion air on the combustion characteristics. Energy 2014; 75: 116-126.

[47] Kutne P, Kapadia BK, Meier W, Aigner M. Experimental analysis of the combustion behaviour of oxyfuel flames in a gas turbine model combustor. Proc Combust Inst 2011; 33: 3383-3390.

[48] Abraham BM, Asbury JG, Lynch EP, Teotia APS. Coal-oxygen process provides CO_2 for enhanced recovery. Oil Gas Journal 1982; 80: 68-75.

[49] Horn FL, Steinberg M. Control of carbon dioxide emissions from a power plant (and use in enhanced oil recovery). Fuel 1982; 61: 415-422.

[50] Steinberg M. History of CO_2 greenhouse gas mitigation technology. Energy Conversion Management 1992; 33: 311-315.

[51] Wall T. Fundamentals of oxy-fuel combustion. In: Oxy-fuel Combustion Research Network, Cottbus, Germany; November 2005.

[52] Al-Abbas AH, Naser J, Dodds D. CFD modelling of air-fired and oxy-fuel combustion of lignite in a 100 kW furnace. Fuel 2011; 90: 1778-1795.

[53] Lasek JA, Janusz M, Zuwala J, Glod K, Iluk A. Oxy-fuel combustion of selected solid fuels under atmospheric and elevated pressures. Energy 2013; 62: 105-112.

[54] Chen L, Yong SZ, Ghoniem AF. Oxy-fuel combustion of pulverized coal: Characterization, fundamentals, stabilization and CFD modeling. Prog Energy Comb Sci 2012; 38: 156-214.

[55] Scheffknecht G, Al-Makhadmeh L, Schnell U, Maier J. Oxy-fuel coal combustion—A review of the current state-of-the-art. Int J Greenhouse Gas Control 2011; 5: 16-35.

[56] Wall T, Liu Y, Spero C, Elliott L, Khare S, Rathnam R, Zeenathal F, Moghtaderi B, Buhre B, Sheng C, Gupta R, Yamada T, Makino K, Yu J. An overview on oxyfuel coal combustion—State of the art research and technology development. Chem Eng Res Design 2009; 87: 1003-1016.

[57] Yin C, Yan J. Oxy-fuel combustion of pulverized fuels: Combustion fundamentals and modeling. Applied Energy 2016; 162: 742-762.

[58] Baukal CE. Oxygen-enhanced combustion. 1st Edition. Boca Raton: CRC Press; 1998.

[59] Oliveira FAD, Carvalho JA, Sobrinho PM, de Castro A. Analysis of oxy-fuel combustion as an alternative to combustion with air in metal reheating furnaces. Energy 2014; 78: 290-297.

[60] Kobayashi H. Oxygen enhanced combustion system performance study - Phase 1Interim/Final Report: Volume 1 – Technical and economic analysis. Report-ID 12597, March 1987.

[61] Merlo N, Boushaki T, Chauveau C, Persis SD, Pillier L, Sarh B, Gökalp I. Combustion characteristics of methane-oxygen enhanced air turbulent non-premixed swirling flames. Exp Therm Fluid Sci 2014; 56: 53-60.

[62] Wu KK, Chang ZC, Chen CH, Chen YD. High-efficiency combustion of natural gas with 21-30% oxygen-enriched air. Fuel 2010; 89: 2455-2462.

[63] Belohradský P, Skryja P, Hudak I. The influence of oxygen-enhanced combustion methods on NOx emissions, in-flame temperatures and heat flux distribution. In: 10th European Conference on Industrial Furnaces and Boilers, Gaia (Porto), Portugal; 2015.

[64] Viehböck D. Numerical simulation of oxy-fuel combustion in industrial furnaces with different reaction mechanisms. Master thesis. Wels: FH Oberösterreich Campus Wels; 2015.

[65] Geffroy P-M, Fouletier J, Richet N, Chartier T. Rational selection of MIEC materials in energy production processes. Chem Eng Sci 2013; 87: 408-433.

[66] Biernatzki D. Erzeugung von Reinsauerstoff mit Membranverfahren. Master thesis. Graz: Graz University of Technology; 2014.

[67] Qiu K, Hayden ACS. Increasing the efficiency of radiant burners by using polymer membranes. Applied Energy 2009; 86: 349-354.

[68] Law CK. Combustion physics. Cambridge: Cambridge University Press; 2006.

[69] Joos F. Technische Verbrennung. Berlin, Heidelberg: Springer-Verlag; 2006.

[70] Warnatz J, Maas U, Dibble RW. Combustion. 4rd Edition. Berlin, Heidelberg: Springer-Verlag; 2006.

[71] Liberman MA. Introduction to physics and chemistry of combustion. Berlin, Heidelberg: Springer-Verlag; 2008.

[72] Turns SR. An introduction to combustion. 2nd Edition. Singapore: McGraw-Hill; 2000.

[73] Baukal CE. Industrial burners handbook. Boca Raton: CRC Press; 2003.

[74] Atkins PW, de Paula J. Physikalische Chemie. 5th Edition. Weinheim: Wiley-VCH Verlag; 2013.

[75] Glassman I, Yetter RA. Combustion. 4th Edition. Burlington, MA, US: Academic Press; 2008.

[76] Westbrook CK, Dryer FL. Simplified reaction mechanisms for the oxidation of hydrocarbon fuels in flames. Combust Sci Technol 1981; 27: 31-43.

[77] Yin C, Rosendahl LA, Kær SK. Chemistry and radiation in oxy-fuel combustion: A computational fluid dynamics modeling study. Fuel 2011; 90: 2519-2529.

[78] Jones WP, Lindstedt RP. Global reaction schemes for hydrocarbon combustion. Combust Flame 1988; 73: 233-249.

[79] Frassoldati A, Cuoci A, Faravelli T, Ranzi EM, Candusso C, Tolazzi D. Simplified kinetic schemes for oxy-fuel combustion. In: Proceedings of S4FE2009 - International Conference on Sustainable Fossil Fuels for Future Energy, Rome, Italy; 2009.

[80] Marinov NM, Pitz WJ, Westbrook CK, Lutz AE, Vincitore AM, Senkan SM. Chemical kinetic modeling of a methane opposed-flow diffusion flame and comparison to experiments. In: 27th Symp (Int) on Combustion/The Combustion Institute 1998; 27: 605-613.

[81] Baehr HD, Stephan K. Wärme- und Stoffübertragung. 6th Edition. Berlin, Heidelberg: Springer-Verlag; 2008.

[82] Trinks W. Industrial furnaces. 6th Edition. Hoboken, New Jersey: Jon Wiley & Sons, Inc.; 2004.

[83] Modest MF. Radiative heat transfer. 3rd Edition. Boston: Academic Press; 2013.

[84] Schemberg S, Eichler R, Gripenberg H. Leistungssteigerung von Banddurchlauföfen durch Oxy-Fuel Brennertechnik. Gaswärme International 2015; 1: 67-72.

[85] Chander S, Ray A. Flame impingement heat transfer: A review. Energy Conversion Management 2005; 46: 2803-2837.

[86] EES User Manual, F-Chart Software. http://www.fchart.com/assets/downloads/ees_manual.pdf.

[87] Becher V, Goanta A, Spliethoff H. Validation of spectral gas radiation models under oxyfuel conditions - Part C: Validation of simplified models. Int J Greenhouse Gas Control 2012; 11: 34-51.

[88] Goody RM. A statistical model for water-vapour absorption. Q J R Meteorol Soc 1952; 78: 165–169.

[89] Edwards DK, Balakrishnan A. Thermal radiation by combustion gases. Int J Heat Mass Trans 1973; 16: 25-40.

[90] Becher V, Clausen S, Fateev A, Spliethoff H. Validation of spectral gas radiation models under oxyfuel conditions. Part A: Gas cell experiments. Int J Greenhouse Gas Control 2011; 5: 76-99.

[91] Rothman LS, Gordon IE, Barber RJ, Dothe H, Gamache RR, Goldman A, Perevalov I, Tashkun SA, Tennyson J. HITEMP, the high-temperature molecular spectroscopic database. J Quant Spect Rad Trans 2010; 111: 2139-2150.

[92] Rothman LS, Wattson RB, Gamache R, Schroeder JW, McCann A. HITRAN HAWKS and HITEMP: high-temperature molecular database. In: Proc SPIE 2471, Atmospheric Propagation and Remote Sensing IV; 1995

[93] Rothman LS, Gordon IE, Barbe A, Benner DC, Bernath PF, Birk M, Boudon V, Brown LR, Campargue A, Champion J-P, Chance K, Coudert LH, Dana V, Devi VM, Fally S, Flaud J-M, Gamache RR, Goldman A, Jacquemart D, Kleiner I, Lacome N, Lafferty WJ, Mandin J-Y, Massie ST, Mikhailenko SN, Miller CE, Moazzen-Ahmadi N, Naumenko OV, Nikitin AV, Orphal J, Perevalov VI, Perrin A, Predoi-Cross A, Rinsland CP, Rotger M, Simeckova M, Smith MAH, Sung K, Tashkun SA. The HITRAN 2008 molecular spectroscopic database. J Quant Spect Rad Trans 2009; 110: 533-572.

[94] Rothman LS, Jacquemart D, Barbe A, Benner DC, Birk M, Brown LR, Carleer R, Chackerian C, Chance K, Coudert LH, Dana V, Devi VM, Flaud J-M, Gamache RR, Goldman A, Hartmann J-M, Jucks KW, Maki AG, Mandin J-Y, Massie ST, Orphal J, Perrin A, Rinsland CP, Smith MAH, Tennyson J, Tolchenov RN, Toth RA, Vander Auwera J, Varanasi P, Wagner G. The HITRAN 2004 molecular spectroscopic database. J Quant Spect Rad Trans 2005; 96: 139-204.

[95] Grosshandler W. RADCAL: A narrow-band model for radiation calculations in a combustion environment. Gaitherburg: National Institute of Standards and Technology; 1993.

[96] Soufani A, Taine J. High temperature gas radiative property parameters of statistical narrow-band model for H_2O, CO_2 and CO, and correlated-k model for H_2O and CO_2. Int J Heat Mass Trans 1997; 40: 987-991.

[97] Smith TF, Shen ZF, Friedman JN. Evaluation of coefficients for the weighted sum of gray gases model. J Heat Trans 1982; 104: 602-608.

[98] Bordbar MH, Wecel G, Hyppänen T. A line by line based weighted sum of gray gases model for inhomogeneous CO_2-H_2O mixture in oxy-fired combustion. Combust Flame 2014; 161: 2435-2445.

[99] Johansson R, Andersson K, Leckner B, Thunman H. Models for gaseous radiative heat transfer applied to oxy-fuel conditions in boilers. Int J Heat Mass Transf 2010; 53: 220-230.

[100] Johansson R, Leckner B, Andersson K, Johnsson F. Account for variations in the H_2O to CO_2 molar ratio when modelling gaseous radiative heat transfer with the weighted-sum-of-grey-gases-model. Combust Flame 2011; 158: 893-901.

[101] Kangwanpongpan T, Franca FHR, Correa da Silva R, Schneider PS, Krautz HJ. New correlations for the weighted-sum-of-gray-gases model in oxy-fuel conditions based on HITEMP 2010 database. Int J Heat Mass Transf 2012; 55: 7419-7433.

[102] Krishnamoorthy G. A new weighted-sum-of-gray-gases model for CO_2-H_2O gas mixtures. Int Commun Heat Mass Transf 2010; 37: 1182-1186.

[103] Rehfeldt S, Kuhr C, Ehmann M, Bergins C. Modeling of radiative properties of an oxyfuel atmosphere with a weighted sum of gray gases for variable carbon dioxide and water vapor concentrations. Energy Procedia 2011; 4: 980-987.

[104] Yin C, Johansen LCR, Rosendahl LA, Kær SK. New weighted sum of gray gases model applicable to computational fluid dynamics (CFD) modeling of oxy−fuel combustion: Derivation, validation, and implementation. Energy Fuels 2010; 24: 6275-6282.

[105] VDI-Wärmeatlas. 10th Edition. Berlin, Heidelberg, New York: Springer-Verlag; 2006.

[106] Mullinger P, Jenkins B. Industrial and Process Furnaces. 1st Edition. Oxford, UK: Butterworth-Heinemann; 2008.

[107] Prieler R, Mayr B, Demuth M, Spoljaric D, Hochenauer C. Application of the steady flamelet model on a lab-scale and an industrial furnace for different oxygen concentrations. Energy 2015; 91: 451-464.

[108] Prieler R, Mayr B, Demuth M, Holleis B, Hochenauer C. Prediction of the heating characteristic of billets in a walking hearth type reheating furnace. Int J Heat Mass Trans 2016; 92: 675-688.

[109] JMatPro User Guide, Sente Software. http://cntech.com.nc/down/h000/h13/attach200612011615520.pdf.

[110] Ferziger JH, Peric M. Computational Methods for Fluid Dynamics. 3rd Edition. Berlin, Heidelberg, New York: Springer; 2002.

[111] Poinsot T, Veynante D. Theoretical and Numerical Combustion. 2nd Edition. Philadelphia, US: R.T. Edwards Inc.; 2005.

[112] Moukalled F, Mangani L, Darwish M. The Finite Volume Method in Computational Fluid Dynamics. Cham, Switzerland: Springer International Publishing Switzerland; 2016.

[113] Prieler R, Mayr B, Hochenauer C. Verbrennungssimulation – Ofenmodellierung und Fehlerquellen. In: 43. Fachausschuss für Industrieofenbau – Austrian Society for Metallurgy and Materials, Graz, Austria; October 2015.

[114] Martens S. Lecture notes – Strömungsmechanik und Stoffaustausch. TU Graz, Austria; 2010.

[115] Scharler R. Lecture notes – CFD in Energy Applications. TU Graz, Austria; 2014.

[116] Launder BE, Spalding DB. Lectures in mathematical models of turbulence. London: Academic Press; 1972.

[117] ANSYS Fluent Theory Guide 15.0, 2013. Canonsburg, PA, USA: ANSYS, Inc.

[118] Henkes RAWM, van der Flugt FF, Hoogendoorn CJ. Natural convection flow in a square cavity calculated with low-Reynolds-number turbulence model. Int J Heat Mass Trans 1991; 34: 377-388.

[119] Shih T-H, Liou WW, Shabbir A, Yang Z, Zhu J. A new k-ϵ eddy viscosity model for high reynolds number turbulent flows – model development and validation. Comp Fluids 1995; 24(3): 227-238.

[120] Kim S-E, Choudhury D, Patel B. Computations of complex turbulent flows using the commercial code ANSYS FLUENT, In: Proceedings of the ICASE/LaRC/AFOSR symposium on modeling complex turbulent flows, Hampton, Virginia; 1997.

[121] Reynolds WC. The element potential method for chemical equilibrium analysis: Implementation in the interactive program STANJAN, Department of Mechanical Engineering, Stanford University; 1986.

[122] Launder BE, Reece GJ, Rodi W. Progress in the development of a Reynolds-stress turbulence closure. J Fluid Mech 1975; 68(3): 537-566.

[123] Launder BE. Second-moment closure: present... and future?. Int J Heat Fluid Flow 1989; 10(4): 282-300.

[124] Gibson MM, Launder BE. Ground effects on pressure fluctuations in the atmospheric boundary layer. J Fluid Mech 1978; 86: 491-511.

[125] Magnussen BF, Hjertager BH. On mathematical modeling of turbulent combustion with special emphasis on soot formation and combustion. In: 16th Symposium (Int) on Combustion. The Combust Inst; 1976.

[126] Spalding DB. Mixing and chemical reaction in steady confined turbulent flames. In: 13th Symposium (Int) on Combustion. The Combust Inst; 1970.

[127] Edge P, Gubba SR, Ma L, Porter R, Pourkashanian M, Williams A. LES modelling of air and oxy-fuel pulverised coal combustion—Impact on flame properties. Proc Combust Inst 2011; 33: 2709-2716.

[128] Chui EH, Douglas MA, Tan Y. Modeling of oxy-fuel combustion for a western Canadian sub-bituminous coal. Fuel 2003; 82: 1201-1210.

[129] Karimi HJ, Saidi MH. Heat transfer and energy analysis of a pusher type reheating furnace using oxygen enhanced air for combustion. Iron Steel Research 2010; 17: 12-17.

[130] Magnussen BF. On the structure of turbulence and a generalized eddy dissipation concept for chemical reaction in turbulent flow. In: 19th AIAA Meeting. St. Louis, USA; 1981

[131] Andersen J, Rasmussen CL, Giselsson T, Glarborg P. Global combustion mechanisms for use in CFD modeling under oxy-fuel conditions. Energy Fuels 2009; 23: 1379-1389.

[132] Galletti C, Coraggio G, Tognotti L. Numerical investigation of oxy-natural-gas combustion in a semi-industrial furnace: Validation of CFD sub-models. Fuel 2013; 109: 445-460.

[133] Vascellari M, Cau G. Numerical simulation of pulverized coal oxy-combustion with exhaust gas recirculation. In: 4th Int Conference on Clean Coal Technologies, Dresden, Germany; 2009.

[134] Gran IR, Magnussen BF. A numerical study of a bluff-body stabilized diffusion flame. Part 2. Influence of combustion modeling and finite-rate chemistry. Combust Sci Technol 1996; 119: 191-217.

[135] Pope SB. Computationally efficient implementation of combustion chemistry using in situ adaptive tabulation. Combust Theory Modeling 1997; 1: 41-63.

[136] Peters N. Laminar diffusion flamelet models in non-premixed turbulent combustion. Prog Energy Combust Sci 1984; 10: 319-339.

[137] Peters N. Laminar flamelet concepts in turbulent combustion. In: 21st Symposium (Int) on Combustion/The Combustion Institute. 1986: 1231-1250.

[138] Pitsch H, Peters N. A consistent flamelet formulation for non-premixed combustion considering differential diffusion effects. Combustion Flame 1998; 114: 26-40.

[139] Pitsch H, Barths H, Peters N. Three-dimensional modeling of NOx and soot formation in DI-diesel engines using detailed chemistry based on the interactive flamelet approach. SAE Technical Paper 1996; 962057.

[140] Kim JS, Williams FA. Extinction of diffusion flames with nonunity Lewis numbers. Engineering Mathematics 1997; 31: 101-118.

[141] Jones WP, Whitelaw JH. Calculation methods for reacting turbulent flows: A review. Combust Flame 1982; 48: 1-26.

[142] Mayr B, Prieler R, Demuth M, Hochenauer C. The usability and limits of the steady flamelet approach in oxy-fuel combustions. Energy 2015; 90: 1478-1489.

[143] Yin C. Advanced modeling of oxy-fuel combustion of natural-gas. ForskEL report 2009-1-0256, 2011, Online: http://energinet.dk/SiteCollectionDocuments/Danske%20dokumenter/Forskning%20-%20PSO-projekter/10256%20Advanced%20modeling%20of%20oxy-fuel%20combustion%20of%20natural%20gas.pdf.

[144] Oijen van JA, Goey de LPH. Modelling of premixed laminar flames using flamelet-generated manifolds. Comb Sci Tech 2000; 161: 113-137.

[145] Smith GP, Golden DM, Frenklach M, Moriarty NW, Eiteneer B, Goldenberg, MC, Bowman T, Hanson RK, Song S, Gardiner Jr WC, Lissianski VV, Qin Z. http://www.me.berkeley.edu/gri_mech/.

[146] Kazakov A, Frenklach M. http://combustion.berkeley.edu/drm/.

[147] Smooke MD, Puri IK, Seshadri K. A comparison between numerical calculations and experimental measurements of the structure of a counterflow diffusion flame burning diluted methane in diluted air. In: 21st Symposium (Int) on Combustion/The Combustion Institute. 1988: 1783-1792.

[148] Peeters TWJ. Numerical modeling oft turbulence natural-gas diffusion flames. PhD Thesis. Delft, The Netherlands: Delft Technical University; 1995.

[149] Smooke MD, Giovangigli V. Reduced kinetic mechanisms and asymptotic approximations for methane air flames. Lecture notes in physics 1991; 384: 1-28.

[150] Cheng P. Two-dimensional radiating gas flow by a moment method. AIAA Journal 1964; 2: 1662-1664.

[151] Siegel R, Howell JR. Thermal radiation heat transfer. 3rd Edition. Washington D.C.: Hemisphere Publishing Corporation; 1992.

[152] Chui EH, Raithby GD. Computation of radiant heat transfer on a non-orthogonal mesh using the finite-volume method. Numerical Heat Transfer, Part B: Fundamentals 1993; 23: 269-288.

[153] Raithby GD, Chui EH. A finite-volume method for predicting a radiant heat transfer in enclosures with participating media. J Heat Transf 1990; 112: 415-423.

[154] Richardson LF. The approximate arithmetical solution by finite differences of physical problems involving differential equations, with an application to the

stresses in a masonry dam. Transactions Royal Soc London, Series A 1910; 210: 307-357.

[155] Prieler R, Demuth M, Spoljaric D, Hochenauer C. Evaluation of a steady flamelet approach for use in oxy-fuel combustion. Fuel 2014; 118: 55-68.

[156] Prieler R, Demuth M, Spoljaric D, Hochenauer C. Numerical investigation of the steady flamelet approach under different combustion environments. Fuel 2015; 140: 731-743.

[157] CHEMKIN-PRO, Reaction Design: San Diego, 2008.

[158] Roache PF. Quantification of uncertainty in computational fluid dynamics. Ann Rev Fluid Mech 1997; 29: 123-160.

[159] Prieler R, Bělohradský P, Mayr B, Demuth M, Hochenauer C. Numerical modeling of oxygen enhanced combustion and transient heating characteristics in a reheating furnace. In: Proceedings of the Australian Combustion Symposium. 2015: 236-239.

[160] Prieler R, Mayr B, Demuth M, Holleis B, Hochenauer C. Numerical analysis of the transient heating of steel billets and the combustion process under air-fired and oxygen enriched conditions. Appl Therm Eng 2016; 103: 252-263.

10 Appendix

10.1 Introduction

Table 23
Adiabatic flame temperature and equilibrium mole fractions for a stoichiometric CH_4 flame calculated with CHEMKIN-PRO using the GRI3.0 mechanism.

O_2 in oxidant [%]	Temperature [K]	X_{H_2O} [-]	X_{OH} [-]	X_{CO_2} [-]	X_{CO} [-]	X_{N_2} [-]
21.0	223.1	0.1835	0.0031	0.0857	0.0087	0.7097
25.2	2363.1	0.2028	0.0061	0.0905	0.0158	0.6675
29.3	2458.5	0.2186	0.0096	0.0934	0.0233	0.6291
33.5	2530.2	0.2317	0.0132	0.0953	0.0306	0.5943
37.6	2586.1	0.2427	0.0168	0.0967	0.0373	0.5628
41.8	2630.9	0.2522	0.0202	0.0977	0.0436	0.5342
45.9	2667.6	0.2605	0.0234	0.0986	0.0492	0.5083
50.1	2698.4	0.2678	0.0264	0.0993	0.0544	0.4846
54.3	2724.5	0.2743	0.0292	0.0999	0.0591	0.4603
58.4	2746.9	0.2801	0.0318	0.1004	0.0635	0.4432
62.6	2766.4	0.2854	0.0342	0.1009	0.0674	0.4250
66.7	2783.5	0.2901	0.0365	0.1014	0.0711	0.4082
70.9	2798.7	0.2944	0.0386	0.1018	0.0744	0.3927
75.1	2812.3	0.2984	0.0406	0.1022	0.0775	0.3782
79.2	2824.4	0.3020	0.0424	0.1025	0.0804	0.3648
83.4	2835.4	0.3054	0.0442	0.1028	0.0831	0.3523
87.5	2845.3	0.3085	0.0458	0.1032	0.0855	0.3406
91.7	2854.4	0.3114	0.0473	0.1034	0.0879	0.3297
95.8	2862.7	0.3141	0.0488	0.1037	0.0900	0.3194
100.0	2870.4	0.3166	0.0501	0.1040	0.0921	0.3098

10.2 Combustion principles

10.2.1 EES-Code and results for the adiabatic flame temperature (1-step)

```
"1) chemical reaction"
CH4 + 2 (O2 + y N2) ===> CO2 + 2 H2O + 2*y N2
"2) enthalpy of reactants"
T_o = 298,15                    "Note: the terms below are zero since 298 K is Tref "
h_R = ENTHALPY(CH4;T=T_o)       "+2*ENTHALPY(O2,T=T_o) +2*y*ENTHALPY(N2,T=T_o)"
"3) enthalpy of products"
y = (100-X_o2)/X_o2
h_P = ENTHALPY(CO2;T=T_a)+2*ENTHALPY(H2O;T=T_a)+2*y*ENTHALPY(N2;T=T_a)
"4) energy balance"
h_R = h_P
```

Table 24
Adiabatic flame temperature for a stoichiometric CH_4 flame calculated with EES for a one-step reaction.

O_2 in oxidant [%]	Temperature [K]
21.0	2324.5
23.7	2507.9
26.5	2680.2
29.2	2842.5
31.9	2995.5
34.6	3140.1
37.3	3276.8
40.1	3406.3
42.8	3529.0
45.5	3645.4
48.2	3756.1
51.0	3861.3
53.7	3961.4
56.4	4056.9
59.1	4148.0
61.9	4235.0
64.6	4318.1
67.3	4397.7
70.0	4474.0
72.8	4547.1
75.5	4617.3
78.2	4684.7
80.9	4749.6
83.7	4812.0
86.4	4872.1
89.1	4930.1
91.8	4986.1
94.6	5040.2
97.3	5092.4
100.0	5142.9

10.2.2 EES-Code and results for dissociation of H_2O

```
"Procedure zur Berechnung von h und g einer Spezies S$"
Procedure h&g(S$;T:h;g)
$Common P;
h=enthalpy(S$;T=T)
s=entropy(S$;T=T;P=P)
g:=h-T*s
end h_g

{T=1173}
P=1,023*10^5
R_m=8,314

call h&g('H2O';T:h|o_H2O;g|o_H2O)
call h&g('OH';T:h|o_OH;g|o_OH)
```

call h&g('H';T:h|o_H;g|o_H)

"Standardbildungsenthalpie DELTA|R_g|o"
DELTA|R_g|o=g|o_OH+g|o_H-(g|o_H2O)

*K_p=EXP(-DELTA|R_g|o/(R_m*T))*

*nu_H2O+2*nu_OH=1*
nu_OH=nu_H

"Gleichgewichtskonstante nur abhängig von den Molanteilen Produkte/Edukte"
K_p=(nu_OH^2)/(nu_H2O)

T_deg=ConvertTemp(K;C;T)

Table 25
Chemical equilibrium composition dependent on the temperature for dissociation of H_2O to OH and H.

Temperature [K]	**X_{H2O} [-]**	**X_{OH} [-]**	**X_{H} [-]**
790.35	1.0000	0.0000	0.0000
962.85	1.0000	0.0000	0.0000
1135.25	1.0000	0.0000	0.0000
1307.15	1.0000	0.0000	0.0000
1480.15	1.0000	0.0000	0.0000
1652.15	1.0000	0.0000	0.0000
1825.15	0.9998	0.0001	0.0001
1997.15	0.9989	0.0005	0.0005
2170.15	0.9963	0.0018	0.0018
2342.15	0.9896	0.0052	0.0052
2514.15	0.9744	0.0128	0.0128
2687.15	0.9445	0.0277	0.0277
2859.15	0.8920	0.0540	0.0540
3032.15	0.8094	0.0953	0.0953
3204.15	0.6940	0.1530	0.1530
3376.15	0.5525	0.2237	0.2237
3549.15	0.4030	0.2985	0.2985
3721.15	0.2689	0.3656	0.3656
3894.15	0.1669	0.4166	0.4166
4066.15	0.0993	0.4504	0.4504
4239.15	0.0583	0.4708	0.4708
4411.15	0.0346	0.4827	0.4827
4583.15	0.0210	0.4895	0.4895
4756.15	0.0131	0.4935	0.4935
4928.15	0.0083	0.4958	0.4958
5101.15	0.0055	0.4973	0.4973
5273.15	0.0037	0.4981	0.4981

10.2.3 Material properties of low-alloy steel

Table 26
Thermal conductivity and specific heat of ST52-3 calculated with JMatPro.

Temperature [°C]	Thermal conductivity [W/mK]	Specific heat [J/kgK]
1400	34.27	691.99
1360	33.77	684.69
1320	33.26	677.62
1280	32.76	670.73
1240	32.26	665.20
1220	32.01	665.92
1180	31.52	657.98
1140	31.02	650.44
1100	30.52	645.93
1060	30.02	638.19
1020	29.52	630.93
980	29.02	624.03
940	28.51	617.43
900	28.01	610.99
860	27.51	604.69
820	27.43	1,011.85
800	28.61	1,003.96
780	29.57	991.21
740	31.00	1,090.53
700	32.05	1,014.24
680	33.62	928.78
640	34.01	860.04
600	34.47	805.47
580	34.73	764.80
540	35.29	724.48
520	35.61	706.49
480	36.29	673.97
460	36.67	659.17
420	37.48	631.98
400	37.91	619.44
360	38.85	596.14
340	39.35	585.28
300	40.41	564.94
280	40.98	555.37
240	42.18	537.29
200	43.47	520.36
180	44.15	512.23
140	45.58	496.45
120	46.33	488.69
80	47.91	473.11
40	49.59	456.81
25	50.24	450.29

10.3 Numerical simulation

10.3.1 Reaction mechanisms

10.3.1.1 DRM19

Table 27
Kinetic parameters for the DRM19 mechanism with the units cm, mol, s, cal.

Reaction no.	Reaction	k_0	b	E_A
1	O+H+M --> OH+M	5.00E+17	-1	0
	H2/2.00/ H2O/6.00/ CH4/2.00/ CO/1.50/ CO2/2.00/ C2H6/3.00/ AR/0.70/			
2	O+H2 --> H+OH	5.00E+04	2.67	6290
3	O+HO2 --> OH+O2	2.00E+13	0	0
4	O+CH2 --> H+HCO	8.00E+13	0	0
5	O+CH2(S) --> H+HCO	1.50E+13	0	0
6	O+CH3 --> H+CH2O	8.43E+13	0	0
7	O+CH4 --> OH+CH3	1.02E+09	1.5	8600
8	O+CO+M --> CO2+M	6.02E+14	0	3000
	H2/2.00/ O2/6.00/ H2O/6.00/ CH4/2.00/ CO/1.50/ CO2/3.50/ C2H6/3.00/ AR/0.50/			
9	O+HCO --> OH+CO	3.00E+13	0	0
10	O+HCO --> H+CO2	3.00E+13	0	0
11	O+CH2O --> OH+HCO	3.90E+13	0	3540
12	O+C2H4 --> CH3+HCO	1.92E+07	1.83	220
13	O+C2H5 --> CH3+CH2O	1.32E+14	0	0
14	O+C2H6 --> OH+C2H5	8.98E+07	1.92	5690
15	O2+CO --> O+CO2	2.50E+12	0	47800
16	O2+CH2O --> HO2+HCO	1.00E+14	0	40000
17	H+O2+M --> HO2+M	2.80E+18	-0.86	0
	O2/0.00/ H2O/0.00/ CO/0.75/ CO2/1.50/ C2H6/1.50/ N2/0.00/ AR/0.00/			
18	H+2O2 --> HO2+O2	3.00E+20	-1.72	0
19	H+O2+H2O --> HO2+H2O	9.38E+18	-0.76	0
20	H+O2+N2 --> HO2+N2	3.75E+20	-1.72	0
21	H+O2+AR --> HO2+AR	7.00E+17	-0.8	0
22	H+O2 --> O+OH	8.30E+13	0	14413
23	2H+M --> H2+M	1.00E+18	-1	0
	H2/0.00/ H2O/0.00/ CH4/2.00/ CO2/0.00/ C2H6/3.00/ AR/0.63/			
24	2H+H2 --> 2H2	9.00E+16	-0.6	0
25	2H+H2O --> H2+H2O	6.00E+19	-1.25	0
26	2H+CO2 --> H2+CO2	5.50E+20	-2	0
27	H+OH+M --> H2O+M	2.20E+22	-2	0
	H2/0.73/ H2O/3.65/ CH4/2.00/ C2H6/3.00/ AR/0.38/			
28	H+HO2 --> O2+H2	2.80E+13	0	1068
29	H+HO2 --> 2OH	1.34E+14	0	635
30	H+CH2(+M) --> CH3(+M)	2.50E+16	-0.8	0
	LOW/ 3.2E+27 -3.14 1230.00/			
	TROE/ 0.68 78 1995 5590/			
	H2/2.00/ H2O/6.00/ CH4/2.00/ CO/1.50/ CO2/2.00/ C2H6/3.00/			

	AR/0.70/			
31	H+CH3(+M) --> CH4(+M) LOW/ 2.48E+33 -4.76 2440.00/ TROE/ 0.783 74 2941 6964/ H2/2.00/ H2O/6.00/ CH4/2.00/ CO/1.50/ CO2/2.00/ C2H6/3.00/ AR/0.70/	1.27E+16	-0.63	383
32	H+CH4 --> CH3+H2	6.60E+08	1.62	10840
33	H+HCO(+M) --> CH2O(+M) LOW/ 1.35E+24 -2.57 1425.00/ TROE/ 0.7824 271 2755 6570/ H2/2.00/ H2O/6.00/ CH4/2.00/ CO/1.50/ CO2/2.00/ C2H6/3.00/ AR/0.70/	1.09E+12	0.48	-260
34	H+HCO --> H2+CO	7.34E+13	0	0
35	H+CH2O(+M) --> CH3O(+M) LOW/ 2.20E+30 -4.8 5560.00/ TROE/ 0.758 94 1555 4200/ H2/2.00/ H2O/6.00/ CH4/2.00/ CO/1.50/ CO2/2.00/ C2H6/3.00/	5.40E+11	0.454	2600
36	H+CH2O --> HCO+H2	2.30E+10	1.05	3275
37	H+CH3O --> OH+CH3	3.20E+13	0	0
38	H+C2H4(+M) --> C2H5(+M) LOW/ 1.20E+42 -7.62 6970.00/ TROE/ 0.9753 210 984 4374/ H2/2.00/ H2O/6.00/ CH4/2.00/ CO/1.50/ CO2/2.00/ C2H6/3.00/ AR/0.70/	1.08E+12	0.454	1820
39	H+C2H5(+M) --> C2H6(+M) LOW/ 1.99E+41 -7.08 6685.00/ TROE/ 0.8422 125 2219 6882/ H2/2.00/ H2O/6.00/ CH4/2.00/ CO/1.50/ CO2/2.00/ C2H6/3.00/ AR/0.70/	5.21E+17	-0.99	1580
40	H+C2H6 --> C2H5+H2	1.15E+08	1.9	7530
41	H2+CO(+M) --> CH2O(+M) LOW/ 5.07E+27 -3.42 84350.00/ TROE/ 0.932 197 1540 10300/ H2/2.00/ H2O/6.00/ CH4/2.00/ CO/1.50/ CO2/2.00/ C2H6/3.00/ AR/0.70/	4.30E+07	1.5	79600
42	OH+H2 --> H+H2O	2.16E+08	1.51	3430
43	2OH --> O+H2O	3.57E+04	2.4	-2110
44	OH+HO2 --> O2+H2O	2.90E+13	0	-500
45	OH+CH2 --> H+CH2O	2.00E+13	0	0
46	OH+CH2(S) --> H+CH2O	3.00E+13	0	0
47	OH+CH3 --> CH2+H2O	5.60E+07	1.6	5420
48	OH+CH3 --> CH2(S)+H2O	2.50E+13	0	0
49	OH+CH4 --> CH3+H2O	1.00E+08	1.6	3120
50	OH+CO --> H+CO2	4.76E+07	1.228	70
51	OH+HCO --> H2O+CO	5.00E+13	0	0
52	OH+CH2O --> HCO+H2O	3.43E+09	1.18	-447
53	OH+C2H6 --> C2H5+H2O	3.54E+06	2.12	870
54	HO2+CH2 --> OH+CH2O	2.00E+13	0	0
55	HO2+CH3 --> O2+CH4	1.00E+12	0	0
56	HO2+CH3 --> OH+CH3O	2.00E+13	0	0
57	HO2+CO --> OH+CO2	1.50E+14	0	23600

58	CH2+O2 --> OH+HCO	1.32E+13	0	1500
59	CH2+H2 --> H+CH3	5.00E+05	2	7230
60	CH2+CH3 --> H+C2H4	4.00E+13	0	0
61	CH2+CH4 --> 2CH3	2.46E+06	2	8270
62	CH2(S)+N2 --> CH2+N2	1.50E+13	0	600
63	CH2(S)+AR --> CH2+AR	9.00E+12	0	600
64	CH2(S)+O2 --> H+OH+CO	2.80E+13	0	0
65	CH2(S)+O2 --> CO+H2O	1.20E+13	0	0
66	CH2(S)+H2 --> CH3+H	7.00E+13	0	0
67	CH2(S)+H2O --> CH2+H2O	3.00E+13	0	0
68	CH2(S)+CH3 --> H+C2H4	1.20E+13	0	-570
69	CH2(S)+CH4 --> 2CH3	1.60E+13	0	-570
70	CH2(S)+CO --> CH2+CO	9.00E+12	0	0
71	CH2(S)+CO2 --> CH2+CO2	7.00E+12	0	0
72	CH2(S)+CO2 --> CO+CH2O	1.40E+13	0	0
73	CH3+O2 --> O+CH3O	2.68E+13	0	28800
74	CH3+O2 --> OH+CH2O	3.60E+10	0	8940
75	2CH3(+M) --> C2H6(+M) LOW/ 1.77E+50 -9.67 6220.00/ TROE/ 0.5325 151 1038 4970/ H2/2.00/ H2O/6.00/ CH4/2.00/ CO/1.50/ CO2/2.00/ C2H6/3.00/ AR/0.70/	2.12E+16	-0.97	620
76	2CH3 --> H+C2H5	4.99E+12	0.1	10600
77	CH3+HCO --> CH4+CO	2.65E+13	0	0
78	CH3+CH2O --> HCO+CH4	3.32E+03	2.81	5860
79	CH3+C2H6 --> C2H5+CH4	6.14E+06	1.74	10450
80	HCO+H2O --> H+CO+H2O	2.24E+18	-1	17000
81	HCO+M --> H+CO+M H2/2.00/ H2O/0.00/ CH4/2.00/ CO/1.50/ CO2/2.00/ C2H6/3.00/	1.87E+17	-1	17000
82	HCO+O2 --> HO2+CO	7.60E+12	0	400
83	CH3O+O2 --> HO2+CH2O	4.28E-13	7.6	-3530
84	C2H5+O2 --> HO2+C2H4	8.40E+11	0	3875

10.3.1.2 Smooke46

Table 28
Kinetic parameters for the smooke46 mechanism with the units cm, mol, s, cal.

Reaction no.	Reaction	k_0	b	E_A
1	CH4+M --> CH3+H+M	1.00E+17	0	86000
2	CH4+O2 --> CH3+HO2	7.90E+13	0	56000
3	CH4+H --> CH3+H2	2.20E+04	3	8750
4	CH4+O --> CH3+OH	1.60E+06	2.36	7400
5	CH4+OH --> CH3+H2O	1.60E+06	2.1	2460
6	CH2O+OH --> HCO+H2O	7.53E+12	0	167
7	CH2O+H --> HCO+H2	3.31E+14	0	10500
8	CH2O+M --> HCO+H+M	3.31E+16	0	81000
9	CH2O+O --> HCO+OH	1.81E+13	0	3082
10	HCO+OH --> CO+H2O	5.00E+12	0	0
11	HCO+M --> H+CO+M	1.60E+14	0	14700

12	HCO+H --> CO+H2	4.00E+13	0	0
13	HCO+O --> OH+CO	1.00E+13	0	0
14	HCO+O2 --> HO2+CO	3.00E+12	0	0
15	CO+O+M --> CO2+M	3.20E+13	0	-4200
16	CO+OH --> CO2+H	1.51E+07	1.3	-758
17	CO+O2 --> CO2+O	1.60E+13	0	41000
18	CH3+O2 --> CH3O+O	7.00E+12	0	25652
19	CH3O+M --> CH2O+H+M	2.40E+13	0	28812
20	CH3O+H --> CH2O+H2	2.00E+13	0	0
21	CH3O+OH --> CH2O+H2O	1.00E+13	0	0
22	CH3O+O --> CH2O+OH	1.00E+13	0	0
23	CH3O+O2 --> CH2O+HO2	6.30E+10	0	2600
24	CH3+O2 --> CH2O+OH	5.20E+13	0	34574
25	CH3+O --> CH2O+H	6.80E+13	0	0
26	CH3+OH --> CH2O+H2	7.50E+12	0	0
27	HO2+CO --> CO2+OH	5.80E+13	0	22934
28	H2+O2 --> 2OH	1.70E+13	0	47780
29	OH+H2 --> H2O+H	1.17E+09	1.3	3626
30	H+O2 --> OH+O	2.20E+14	0	16800
31	O+H2 --> OH+H	1.80E+10	1	8826
32	H+O2+M --> HO2+M H2O/21.00/ H2/3.30/ N2/0.00/ O2/0.00/	2.10E+18	-1	0
33	H+O2+O2 --> HO2+O2	6.70E+19	-1.42	0
34	H+O2+N2 --> HO2+N2	6.70E+19	-1.42	0
35	OH+HO2 --> H2O+O2	5.00E+13	0	1000
36	H+HO2 --> 2OH	2.50E+14	0	1900
37	O+HO2 --> O2+OH	4.80E+13	0	1000
38	2OH --> O+H2O	6.00E+08	1.3	0
39	H2+M --> H+H+M H2O/6.00/ H/2.00/ H2/3.00/	2.23E+12	0.5	92600
40	O2+M --> O+O+M	1.85E+11	0.5	95560
41	H+OH+M --> H2O+M H2O/20.00/	7.50E+23	-2.6	0
42	H+HO2 --> H2+O2	2.50E+13	0	700
43	HO2+HO2 --> H2O2+O2	2.00E+12	0	0
44	H2O2+M --> OH+OH+M	1.30E+17	0	45500
45	H2O2+H --> HO2+H2	1.60E+12	0	3800
46	H2O2+OH --> H2O+HO2	1.00E+13	0	1800

10.3.1.3 Skeletal25

Table 29
Kinetic parameters for the smooke46 mechanism with the units cm, mol, s, cal.

Reaction no.	Reaction	k_0	b	E_A
1	H+O2=>O+OH	2.00E+14	0	16800
2	O+OH=>O2+H	1.58E+13	0	690
3	O+H2=>OH+H	1.80E+10	1	8826
4	OH+H=>O+H2	8.00E+09	1	6760
5	H2+OH=>H2O+H	1.17E+09	1.3	3626

6	H2O+H=>H2+OH	5.09E+09	1.3	18588
7	OH+OH=>H2O+O	6.00E+08	1.3	0
8	H2O+O=>OH+OH	5.90E+09	1.3	17029
9	H+O2+M=>HO2+M	2.30E+18	-0.8	0
	CH4/6.50/ H2O/6.50/ CO2/1.50/ CO/0.75/ O2/0.40/ N2/0.40/			
10	H+HO2=>OH+OH	1.50E+14	0	1004
11	H+HO2=>H2+O2	2.50E+13	0	700
12	OH+HO2=>H2O+O2	2.00E+13	0	1000
13	CO+OH=>CO2+H	1.51E+07	1.3	-758
14	CO2+H=>CO+OH	1.57E+09	1.3	22337
15	CH4=>CH3+H	2.30E+38	-7	114360
16	CH3+H=>CH4	1.90E+36	-7	9050
17	CH4+H=>CH3+H2	2.20E+04	3	8750
18	CH3+H2=>CH4+H	9.57E+02	3	8750
19	CH4+OH=>CH3+H2O	1.60E+06	2.1	2460
20	CH3+H2O=>CH4+OH	3.02E+05	2.1	17422
21	CH3+O=>CH2O+H	6.80E+13	0	0
22	CH2O+H=>HCO+H2	2.50E+13	0	3991
23	CH2O+OH=>HCO+H2O	3.00E+13	0	1195
24	HCO+H=>CO+H2	4.00E+13	0	0
25	HCO+M=>CO+H+M	6.00E+14	0	14700
	CH4/6.50/ H2O/6.50/ CO2/1.50/ CO/0.75/ O2/0.40/ N2/0.40/			
26	CH3+O2=>CH3O+O	7.00E+12	0	25652
27	CH3O+H=>CH2O+H2	2.00E+13	0	0
28	CH3O+M=>CH2O+H+M	2.40E+13	0	28812
	CH4/6.50/ H2O/6.50/ CO2/1.50/ CO/0.75/ O2/0.40/ N2/0.40/			
29	HO2+HO2=>H2O2+O2	2.00E+12	0	0
30	H2O2+M=>OH+OH+M	1.30E+17	0	45500
	CH4/6.50/ H2O/6.50/ CO2/1.50/ CO/0.75/ O2/0.40/ N2/0.40/			
31	OH+OH+M=>H2O2+M	9.86E+14	0	-5070
	CH4/6.50/ H2O/6.50/ CO2/1.50/ CO/0.75/ O2/0.40/ N2/0.40/			
32	H2O2+OH=>H2O+HO2	1.00E+13	0	1800
33	H2O+HO2=>H2O2+OH	2.86E+13	0	32790
34	OH+H+M=>H2O+M	2.20E+22	-2	0
	CH4/6.50/ H2O/6.50/ CO2/1.50/ CO/0.75/ O2/0.40/ N2/0.40/			
35	H+H+M=>H2+M	1.80E+18	-1	0
	CH4/6.50/ H2O/6.50/ CO2/1.50/ CO/0.75/ O2/0.40/ N2/0.40/			

10.3.2 Parameters used for the WSGGM

Table 30
Model parameters for the WSGGM.

i	a_i	$b_{\varepsilon,i,1}$	$b_{\varepsilon,i,2} * 10^4$	$b_{\varepsilon,i,3} * 10^7$	$b_{\varepsilon,i,4} * 10^{11}$
Carbon dioxide, $p_{CO_2} \rightarrow 0\ atm$					
1	0.3966	0.4334	2.620	-1.560	2.565
2	15.64	-0.4814	2.822	-1.794	3.274
3	394.3	0.5492	0.1087	-0.3500	0.9123
Water vapour, $p_{H_2O} \rightarrow 0\ atm$					
1	0.4098	5.977	-5.119	3.042	-5.564
2	6.325	0.5677	3.333	-1.967	2.718
3	120.5	1.800	-2.334	1.008	-1.454
Water vapour, $p_{H_2O} = 1\ atm$					
1	0.4496	6.324	-8.358	6.135	-13.03
2	7.113	-0.2016	7.145	-5.212	9.868
3	119.7	3.500	-5.040	2.425	-3.888
Mixture, $p_{H_2O}/p_{CO_2} = 1$					
1	0.4303	5.150	-2.303	0.9779	-1.494
2	7.055	0.7749	3.399	-2.297	3.770
3	178.1	1.907	-1.824	0.5608	-0.5122
Mixture, $p_{H_2O}/p_{CO_2} = 2$					
1	0.4201	6.508	-5.551	3.029	-5.353
2	6.516	-0.2504	6.112	-3.882	6.528
3	131.9	2.718	-3.118	1.221	-1.612

10.3.3 Numerical settings – Lab-scale furnace and walking hearth furnace

Table 31
Numerical settings for the CFD simulations according to the experiments on the lab-scale furnace and walking hearth furnace.

Spatial discretization	
Pressure	PRESTO!
Momentum	Second order upwind
Turbulent kinetic energy	Second order upwind
Turbulent dissipation rate	Second order upwind
Reynolds stresses	Second order upwind
Energy	Second order upwind
Radiation (DOM, P1 model)	First order upwind
Mean mixture fraction	Second order upwind
Mixture fraction variance	Second order upwind
Gradient	Least squares cell-based
Pressure-velocity coupling	SIMPLE
Operating pressure [mbar]	1013.25

Table 32
Under-relaxation factors for the CFD simulations according to the experiments on the lab-scale furnace and walking hearth furnace.

Pressure	0.7
Density	0.5
Body forces	0.5
Momentum	0.3
Turbulent kinetic energy	0.6
Turbulent dissipation rate	0.6
Turbulent viscosity	0.7
Reynolds stresses	> 0.4
Energy	> 0.98
Temperature	> 0.98
Radiation (DOM, P1 model)	> 0.95
Mean mixture fraction	1.0
Mixture fraction variance	1.0

10.4 Data – Grid independency study

Table 33
Calculated temperatures for the Richardson extrapolation.

	Without thermal load		With thermal load	
Position	Temperature fine grid [K]	Temperature coarse grid [K]	Temperature fine grid [K]	Temperature coarse grid [K]
T1	1482.2	1481.0	1540.2	1531.2
T2	1523.5	1522.1	1534.9	1522.8
T3	1480.5	1479.8	1511.7	1504.8
T4	1479.6	1478.7	1488.1	1475.8